Tests of general relativity and Bayesian population studies with gravitational waves from coalescing binaries.

Alexandre Toubiana

École Doctorale 560 :
Sciences de la Terre et de l'Environnement et Physique de l'Univers

Thèse de doctorat

de Université de Paris
préparée au laboratoire Astroparticules et Cosmologie

Tests of general relativity and Bayesian population studies with gravitational waves from coalescing binaries.

présentée par

Alexandre Toubiana

Sous la direction de
Stanislav Babak

et la co-direction de
Enrico Barausse

présentée et soutenue publiquement le 10 Septembre 2021
devant le jury composé de :

Danièle Steer	Professeure des universités (Université de Paris, France)	Présidente du jury
Yanbei Chen	Professor (Caltech, États-Unis)	Rapporteur
Harald Pfeiffer	Professor (AEI Potsdam, Allemagne)	Rapporteur
Alessandra Buonanno	Professor (AEI Potsdam, Allemagne)	Examinatrice
Alberto Sesana	Associate Professor (Université de Milan-Bicocca, Italie)	Examinateur
Alberto Vecchio	Professor (Université de Birmingham, Royaume-Uni)	Examinateur
Stanislav Babak	Directeur de recherche (Université de Paris, France)	Directeur de thèse
Enrico Barausse	Associate Professor (SISSA, Italie)	Co-directeur de thèse

Strange fascination, fascinating me
Ah changes are taking the pace I'm going through

Changes, David Bowie

Abstract

In only six years, gravitational waves have already provided an incredible amount of information on our Universe. For instance, they have allowed us to infer for the first time the properties of the population of compact binaries and provided new tests of general relativity. They have also triggered many questions, and the future of gravitational wave astronomy promises to be very exciting. The sensitivity improvement of current detectors will increase the detection rate and our ability to extract the source parameters. Moreover, the next generation of detectors is already being planned. Among them, the space-based interferometer LISA will complement ground-based detectors and allow us to observe a yet unexplored population of compact binaries. In this thesis, we propose tools to exploit the full potential of gravitational wave observations, and assess what could be learned on astrophysics and fundamental physics from these observations, with a special focus on the LISA mission.

We perform for the first time a full Bayesian analysis on simulated LISA signals of stellar-mass black holes binaries. We determine the accuracy to which the source parameters could be measured and explain the correlations between them. We also show that such observations could be used to probe low-frequency modifications in the gravitational wave phase arising due to deviations from general relativity or to environmental effects. Thus, they will help us constrain modified gravity theories and inform us on the astrophysical environment of the sources.

In addition to that, we propose a phenomenological model for the gravitational wave signal of binaries made of exotic compact objects. We use it to show that next generation detectors could potentially observe such binaries throughout the observable Universe, but that their detection would be difficult with current search pipelines.

On the astrophysical side, we propose a semi-analytical model for the evolution of binaries made of a black hole accreting from a white dwarf, and show that combining it with LISA observations enables the measurement of the masses of both binary components and the distance to the source. This piece of information, which is usually not accessible from gravitational wave observations of galactic binaries, would allow us to identify both components. Thus, LISA could be the first instrument to convincingly detect such binaries.

Finally, we build a pipeline for inferring the population of massive black hole binaries from LISA observations, and discriminating between different scenarios for the formation and evolution of massive black holes. Our pipeline uses the hierarchical Bayesian framework to measure the hyperparameters controlling the population of massive black hole binaries, comparing the observed population to theoretical predictions. We find that our pipeline would allow us to correctly infer the population of massive black hole binaries, but only if the observed data set is similar enough to the predictions of the model we compare it

against. We highlight important challenges to be tackled in the next few years, both on the data analysis and the astrophysical modelling side.

Keywords: Gravitational waves, general relativity, gravitational wave astronomy, black holes, astrophysics, tests of general relativity, data analysis

Résumé

En à peine six ans, les ondes gravitationnelles nous ont déjà beaucoup appris sur l'Univers. Elles nous ont offert de nouveaux tests de la relativité générale, et nous ont permis d'inférer pour la première fois la population de binaires compactes dans l'Univers. Ces détections ont aussi amené leur lot de nouvelles questions, et le futur de l'astronomie gravitationnelle s'annonce prometteur. Les détecteurs actuellement en marche verront leur sensibilité s'améliorer au cours des prochaines années, augmentant ainsi le nombre de détections et la précision avec laquelle nous mesurerons les paramètres des sources. Par ailleurs, la prochaine génération de détecteurs est déjà en préparation. Parmi eux, l'interféromètre spatial LISA viendra complémenter les détecteurs terrestres et nous permettra d'observer une nouvelle population d'objets compacts. Dans cette thèse, nous développons des outils qui nous permettront d'exploiter au maximum le potentiel des futures observations d'ondes gravitationnelles, et explorons ce qu'elles pourraient nous enseigner sur l'astrophysique et la physique fondamentale, avec un focus sur LISA.

Nous effectuons pour la première fois une analyse bayésienne complète sur des signaux simulés de binaires de trous noirs de masse stellaire dans LISA. Notre travail nous a menés à déterminer la précision avec laquelle les paramètres de la source pourront être mesurés et à expliquer les corrélations entre eux. Nous montrons également que de telles observations pourront être utilisées pour sonder les modifications à basse fréquence de la phase des ondes gravitationnelles dues à des écarts par rapport à la relativité générale ou à des effets environnementaux. Ainsi, elles nous permettront de contraindre les théories de gravité modifiée et nous renseigneront sur l'environnement astrophysique des sources.

Par ailleurs, nous proposons un modèle phénoménologique pour le signal d'ondes gravitationnelles émis par des binaires constituées d'objets compacts exotiques. Nous l'utilisons pour montrer que les futurs détecteurs pourraient observer pratiquement toutes les binaires de ce genre dans l'Univers, mais que leur détection serait difficile avec les méthodes de recherche de signaux actuellement utilisées.

En astrophysique, nous proposons un modèle semi-analytique pour l'évolution de binaires constituées d'un trou noir accrètant la matière d'une naine blanche, et nous montrons que son association avec les observations de LISA permettra de mesurer les masses des deux composants de la binaire ainsi que la distance à la source. Ces informations, qui ne sont généralement pas accessibles à partir d'observations d'ondes gravitationnelles de binaires galactiques, nous permettraient d'identifier les deux composants. Ainsi, LISA pourrait être le premier instrument à apporter la preuve de l'existence de telles binaires.

Enfin, nous proposons une méthode pour inférer la population de binaires de trous noirs massifs à partir des observations de LISA, nous permettant ainsi de distinguer parmis dif-

férents scénarios pour la formation et l'évolution de trous noirs massifs. Notre méthode s'appuie sur l'analyse bayésienne hiérarchique afin de mesurer les hyperparamètres contrôlant la population de binaires de trous noirs massifs, en confrontant la population observée aux prévisions théoriques. Notre méthode permettrait de déduire correctement la population de binaires de trous noirs massifs, mais seulement si les observations sont sufisamment similaires aux prédictions du modèle auquel nous les confrontons. Nous mettons en évidence des défis importants à relever dans les prochaines années, tant du côté de l'analyse de données que du côté de la modélisation astrophysique.

Mots-clés: Ondes gravitationnelles, relativité générale, astronomie gravitationnelle, trous noirs, astrophysique, tests de la relativité générale, analyse de données

Acknowledgements

First of all I wish to thank Stas for his guidance during these 3 years. Although the level of our voices would gradually increase during our discussions so that people would think we were fighting, you were always very patient and supportive. Oscillating between intuition and mathematical rigour, you taught me how to interpret data and to keep calm whenever I think I might have found a deviation from GR! I will dearly remember the cachaça, vodka and other drinks we had after each academic success! Next, I thank Enrico for advising me and providing me a more theoretical background. Despite your apparent grumpiness you have been very kind to me, in particular during my visits at Trieste, from where I have very nice memories. So much I even wanted to buy an appartment there! You also provided me the opportunity to expand my horizon, and thanks to you I got to meet many new working partners and friends.

I think of course of Laura, who turned into both to me. I am very proud we could carry out our silly idea on accreting binaries to the end, with many headaches and fun along the way, and I hope we'll have many other projects like this in the near future! Moreover, thank you for taking me on a cinematographic tour through Rome and Tuscany! I also thank Kaze for making me familiar with hierarchical Bayesian analyses and for taking me around in Baltimore. I wish to thank the other mentors I had during my thesis: Cole, Emanuele, John, Jon, Luis, Paolo, Stephen. A very special thanks goes to Sylvain, who, unofficially, turned into my third advisor. Thank you for your precious advices and for sharing with me your code, without which much of this thesis would not have been possible! A big thanks to Harald and Yanbei for carefully reviewing my manuscript. Finally, I also thank all the people I met when doing my academia world tour, thanks to who I have so many nice memories: Alexandru, Ana, Benji, Daniel, Max, Pablo, Poutine, Tim, Ramiro, Andrea, Félix, Thomas, Vishal. And of course I am grateful to my "Mexican family" in Waterloo who hosted me so well I felt like home!

Going back home, I am very happy to have done my thesis in such a friendly environment as APC. I am indebted to the administrative and informatic services for their availability. I thank Chiara and Stefano for their support as members of my comité de suivi, and to the former, thank you for our discussions on restaurants in the 14ème! I am grateful to the gravitation group at APC for their support. I wish to address a special thanks to Nikos, who always encouraged me a lot, in particular in the early stages of my thesis, and who made me discover the Athenian nightlife. By chance I was given with the opportunity to spend most of my PhD in the best room of the lab, 312B, where our legendary coffee breaks, "Les jeudis du 312B", will echo through eternity. Thank you Baptiste, Clara, Dominic, Hamza, Marc, Jean-Baptiste (aka Rooftop) and the newbies Julien, Magdy and Arianna. I also wish

to thank the other PhD students for the animated lunches, seminars, beers etc: Aurélien, Bastien, Calum, Guilaume, Hugo, Konstantin, Léon, Louise, Marion, Mikel, Nam, Pierre, Raphaël, Roxane, Thomas, Thibault.

Ces 3 années de thèse auront été une véritable aventure humaine, et je souhaite remercier les personnes qui bien qu'extérieures à mon travail ont été cruciales dans ma réussite (souvent sans s'en rendre compte!). Dans l'ordre chronologique. Merci Fanny de ta présence indéfaillible. Même si nos occupations respectives nous éloignent parfois, on se soutient toujours dans nos galères. Je repense avec beaucoup de plaisir à tous nos faux "moments de couple"! Même si tu t'en moques d'être là, merci Matthieu de tout ton calme, ta sérénité et ta disponibilité à m'écouter me plaindre... Tu arrives toujours à me changer les idées et je sais à chaque fois que je vais passer un super moment en ta compagnie. Je te dois la découverte de plusieurs des bars que j'aime à Paris et je vais maintenant suivre tes pas à Berlin! Merci également à Charles, François, Hugo, Marie, Olivier, Pacôme, Pierre, Philippe. Je remercie Tallulah pour son amitié et pour la réalisation d'une des figure icôniques de cette thèse! Une autre partie importante de ma vie aura été mes années à Centrale, où j'ai eu la chance de rencontrer tant de personnes qui me sont chères. Un grand merci à Centrale Wakarimasen. Malgré tous nos voyages avortés on arrive quand même à passer de super moments ensemble. Certes je ne sais toujours pas comment dire "trou noir" en japonais, mais je m'y entraînerai pour 2024! Muito obrigado aussi à Pedro, pour toutes nos sorties culturelles, nos discussions pseudo-philosophiques et nos voyages "roots hardcore". J'ai hâte de découvrir les ronds-points de Pologne et d'Algérie! Un grand merci au "3H", pour toutes nos bouffes, nos voyages, nos foots etc. Notre campagne BdE reste un de mes plus beaux souvenirs et je suis heureux que cela nous ai menés aussi loin! Bien entendu, j'en remercie particulièrement deux illustres membres: mes colocs qui forment la team "fond du couloir" (sans ordre particulier). Vous aurez été les témoins privilégiés de ces 3 années de thèse et plus d'une fois votre amitié et votre attention m'aura permis de franchir des obstacles. Je me considère chanceux d'avoir traversé cette période si particulière en votre compagnie. Je garde en mémoire nos repas gargantuesques du samedi soir, nos ateliers bricolages, le couscous, la halvanniversaire, les tennis, le bivouac aux Dolomites et tant d'autres choses! Malgré tout... merci Adélie pour tes conseils avisés et ton soutien lorsque je voulais me réorienter en physique. Merci à Yann pour toutes nos sorties ciné, les visites de Montpellier et Teyran (même si on s'y est surtout reposés) et pour m'aider à cambrioler mon propre vélo! Finalement, je remercie mes collègues de NPAC et en particulier Dany, aux côtés de qui je retrouve un peu de ma latinité!

Infelizmente, tive que passar grande parte desses 3 anos longe do Brasil, mas sempre guardo o Brasil no meu coração e sei que posso contar com o apoio de muita gente. Primeiramente, agradeço o Felipe Canto, meu primeiro orientador, o primeiro a acreditar em mim e que me deu confiança para prosseguir uma carreira na física. Um agradecimento especial vai para o João, que conheço praticamente desde que nasci e que sempre me apoiou de sua forma no meu percurso. Obrigado "Grupão" por sempre proporcionar grandes momentos, e em particular Ana Lê, Alan, Bruno, Bruna, Caio, Daniel, David, Gil, Lucas, Maria, Paulo. Graças a vocês aprendi a desfrutar plenamente do Rio de Janeiro. Agradeço ao Felipe, meu amigo de infância, e tenho um grande pensamento para a Suely, que sempre demonstrou muito carinho por mim e foi muito importante em um dos momentos mais difíceis da minha vida. Lamento imensamente não poder compartilhar esse momento com você. Agradeço à Fernanda, nossa amizade foi do Humaitá para a Europa. Você foi a melhor parceira para

explorar Paris. Só vamos evitar fazer trilha juntos de agora em diante. Mesmo que ela esteja tão distante, agradeço à minha família mineira, Vovó e Titia, que sempre me deram tanto amor. Também tenho a sorte de ter uma família de coração no Rio. Sei que apesar de não entender grande coisa vocês teriam adorado estar aqui para comemorar comigo. Tenho um grande pensamento para minha madrinha Charlotte, você sempre estimulou minha curiosidade e me deu vontade de explorar o mundo. Agradeço igualemnte à Margarette. Vou para Berlim com vocês no coração. Agradeço à Malu, minha madrinha com manias de vampiro, e seus brownies, pães de queijo etc. Mesmo longe, você sempre consegue me transmitir seu apoio e carinho. Um grande abraço para meu querido Alceste. Tenho muita sorte de contar entre meus amigos com alguém tão brilhante e carinhoso. Agradeço igualmente Naro, Wânderlei, Gegena e Rubem com muita saudade dos almoços do domingo e das feijoadas. Muito obrigado à Josane, minha bahiana preferida (na frente de Gil e Caetano!), pela sua amizade e as fofocas. Finalemente, agradeço à Sossô, minha segunda mãe, minha cúmplice, que me viu crescer e sempre me deu tanto amor. Sempre me divirto muito ao seu lado.

Bien évidemment, je suis profondément reconnaissant à la famille Toubiana. La pub Subway disait "on ne choisit pas sa famille mais on choisit son sandwich", heuresement que je n'ai pas choisi ma famille car je n'aurais pas su faire mieux! Des apéros du samedi au 138 aux fêtes juives, tant de beaux moments que nous partageons toujours dans la joie et l'allégresse. Mais surtout, vous êtes d'une générosité sans faille et toujours prêts à aider. Je remercie Pépé et Mémé d'avoir construit une si belle famille. Finalement, en tout manque d'originalité, je remercie du fond du coeur mes parents. Il me faudrait écrire plus que cette thèse pour lister tout ce dont je vous suis reconnaissant donc je me contenterai de vous remercier pour tout ce que vous m'avez appris depuis que je suis enfant, de m'avoir toujours aidé dans mes choix et de votre soutien sans faille dans les moments les plus difficiles, dus à la thèse ou autres. Certains diront qu'avec des parents comme vous il était inévitable que je devienne chercheur, mais si je suis arrivé là c'est surtout parce que vous avez toujours stimulé ma curiosité. C'est tout naturellement que je vous dédie cette thèse.

Résumé étendu

En à peine six ans, les ondes gravitationnelles nous ont déjà beaucoup appris sur l'Univers. Elles nous ont offert de nouveaux tests de la relativité générale, et nous ont permis d'inférer pour la première fois la population de binaires compactes dans l'Univers. Ces détections ont aussi amené leur lot de nouvelles questions, et le futur de l'astronomie gravitationnelle s'annonce prometteur. Les détecteurs actuellement en marche verront leur sensibilité s'améliorer au cours des prochaines années, augmentant ainsi le nombre de détections et la précision avec laquelle nous mesurerons les paramètres des sources. Par ailleurs, la prochaine génération de détecteurs est déjà en préparation. Parmi eux, l'interféromètre spatial LISA viendra complémenter les détecteurs terrestres et nous permettra d'observer une nouvelle population d'objets compacts. Dans cette thèse, nous développons des outils qui nous permettront d'exploiter au maximum le potentiel des futures observations d'ondes gravitationnelles, et explorons ce qu'elles pourraient nous enseigner sur l'astrophysique et la physique fondamentale, avec un focus sur LISA.

Les ondes gravitationnelles sont une prédiction fondamentale de la théorie de la relativité générale. Mathématiquement, elles sont obtenues en développant la métrique autour d'une géométrie Minkowskienne, $g_{\mu\nu} = \eta_{\mu\nu} + h_{\mu\nu}$, et en gardant uniquement les termes d'ordre linéaire en $h_{\mu\nu}$ dans l'équation d'Einstein pour le champ gravitationnel, ce qui nous donne

$$\Box_\eta \bar{h}_{\mu\nu} = -16\pi T_{\mu\nu}, \tag{1}$$

où $\bar{h}_{\mu\nu} = h_{\mu\nu} - \frac{1}{2}\eta_{\mu\nu}h$ et $T_{\mu\nu}$ est le tenseur énergie-moment. Einstein dériva cette équation l'année suivant sa formulation de la théorie de la relativité générale, mais il fallut attendre près de 40 ans pour donner une interprétation physique aux ondes gravitationnelles. On sait depuis que les ondes gravitationnelles sont véritablement l'analogue des ondes électromagnétiques pour l'interaction gravitationnelle, et peuvent extraire de l'énergie et du moment angulaire d'un système. Tout comme en électromagnétisme, il existe deux polarisations pour les ondes gravitationnelles, notées h_+ et $h_\times$, et il est possible d'écrire le flux d'ondes gravitationnelles sous la forme d'une décomposition en harmoniques sphériques, à la différence près que cette expansion commence à l'ordre quadripolaire dû à la conservation de la quantité de mouvement. Les ondes gravitationnelles ne sont émises que par des systèmes non stationnaires, tel qu'un système de deux corps orbitant l'un autour de l'autre. Dans cette thèse nous nous intéressons particulièrement aux binaires de trous noirs telles qu'illustré sur la figure 1.

m_1 et m_2 sont les masses des trous noirs, $M = m_1 + m_2$ la masse totale, $\mu_{\rm red} = m_1 m_2/M$ la masse réduite et $q = m_1/m_2 \geq 1$ est la raison des masses. Deux autres combinaisons s'avèrent particulièrement utiles: la raison symétrique des masses $\eta = \mu_{\rm red}/M$ et la "chirp

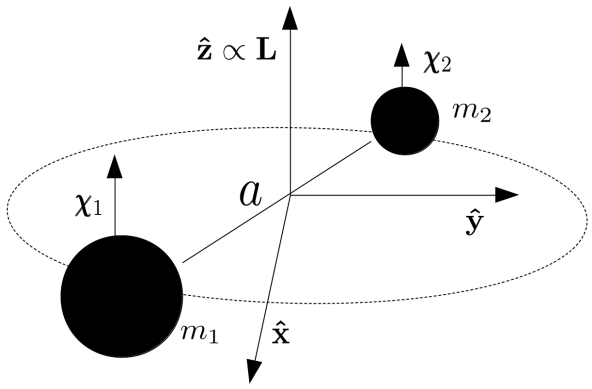

Figure 1: Représentation schématique d'une binaire de trous noirs. Nous adoptons la convention $m_1 \geq m_2$, et nous limitons au cas où les spins des trous noirs ($\boldsymbol{\chi_1}$ et $\boldsymbol{\chi_2}$) sont alignés ou anti-alignés avec le moment cinétique orbital $\mathbf{L}$.

mass" $\mathcal{M}_c = (m_1^3 m_2^3/(m_1+m_2))^{1/5} = M\eta^{3/5}$. Nous nous limitons au cas de binaires sur des orbites circulaires et où les spins des trous noirs ($\boldsymbol{\chi_1}$ et $\boldsymbol{\chi_2}$) sont alignés ou anti-alignés avec le moment cinétique orbital $\mathbf{L}$. Nous définissons les combinaisons de spins $\chi_{+,-} = \frac{m_1\chi_1 \pm m_2\chi_2}{m_1+m_2}$ où $\chi_{1,2} = \boldsymbol{\chi_{1,2}} \cdot \mathbf{L}$. L'émission d'ondes gravitationnelles entraîne le rapprochement des trous noirs pendant la phase "inspiralante" et ceux-ci finissent par fusionner et former un unique trou noir. Ce trou noir est initialement dans un état perturbé et atteint l'équilibre en émettant des ondes gravitationnelles. Cette dernière étape est appelée le "ringdown". En première approximation, le signal lors de la phase inspiralante est donné par

$$h_+ = \frac{4\mathcal{M}_c}{R} \left(\mathcal{M}_c \omega_{\rm orb}(t)\right)^{2/3} \frac{1+\cos^2(\iota)}{2} \cos\left(2(\phi_{\rm orb}(t)+\varphi)\right), \tag{2}$$

$$h_\times = \frac{4\mathcal{M}_c}{R} \left(\mathcal{M}_c \omega_{\rm orb}(t)\right)^{2/3} \cos(\iota) \sin\left(2(\phi_{\rm orb}(t)+\varphi)\right), \tag{3}$$

où R est la distance entre l'observateur et la source, ι est l'angle entre le moment cinétique orbital et la direction d'émission de l'onde, $\omega_{\rm orb}$ est la vitesse orbitale du système binaire, $\phi_{\rm orb}(t) = \phi_c - \int_t^{t_c} \omega_{\rm orb}(t)\mathrm{d}t$, ϕ_c est la "phase de coalescence", t_c est le temps restant avant la coalescence et φ est une constante. Le signal total est illustré sur la figure 2. Par la suite, il sera particulièrement utile de travailler avec la transformée de Fourier du signal: $\tilde{h}(f) = \int_{-\infty}^{+\infty} h(t) e^{2i\pi f t} \mathrm{d}t$.

Il est malheureusement impossible de résoudre exactement les équations d'Einstein et il est nécessaire de faire appel à différentes méthodes d'approximation. Lors de la phase inspiralante, le développement post-Newtonien permet d'obtenir itérativement une solution sous la forme d'une expansion en puissances de v/c, où v est la vitesse relative des trous noirs. Près de la fusion, seules de coûteuses simulations numériques permettent de résoudre les équations d'Einstein. Finalement lors du ringdown, la théorie de perturbations linéaires des trous noirs permet d'obtenir le signal gravitationnel, qui peut s'écrire comme une superposition de sinus amortis dont les fréquences et temps caractéristiques dépendent uniquement des propriétés du trou noir final. Le signal complet peut être obtenu en assemblant ces trois méthodes. Une importante propriété des ondes gravitationnelles permet par ailleurs

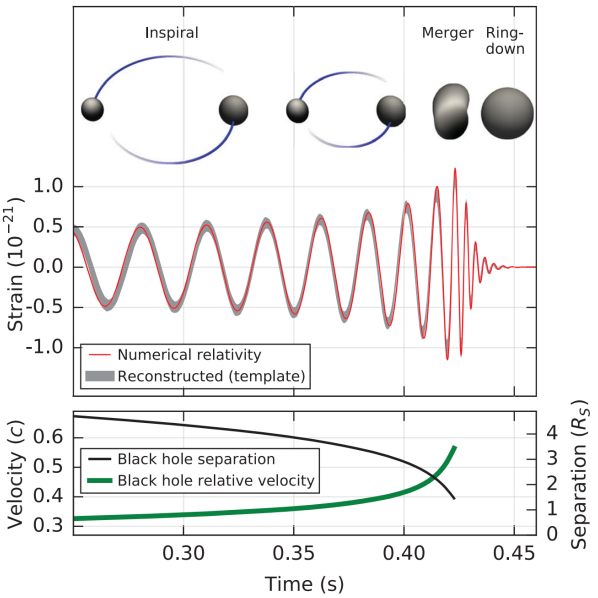

Figure 2: Représentation schématique du premier évenement détecté, GW150914. Sur le panneau du haut figurent la prédiction théorique pour le signal gravitationnel et sa reconstruction à partir des données, en rouge et gris respectivement. Sur le panneau du bas figurent l'évolution de la séparation et la vitesse relative entre les trous noirs au cours de l'évolution.

de simplifier le calcul: les signaux temporels h/M et fréquentiels $\tilde{h}/M^2$ peuvent s'écrire en fonction de t/M et Mf, respectivement, sans aucune autre dépendance en M. Ainsi, l'échelle de masse du système n'intervient pas dans les calculs. Par ailleurs, cela implique que plus un système est massif, plus il émet à des basses fréquences. Dans cette thèse nous utilisons des formes d'onde phénoménologiques construites directement dans le domaine de Fourier, PhenomD et PhenomHM. Cette dernière, inclut l'effet des harmoniques autres que le quadrupôle, contrairement à PhenomD.

Les ondes gravitationnelles peuvent être détectées à travers leur effet sur la matière. En effet, la distance propre entre deux objets immobiles varie selon $\Delta L/L = h/2$ lors du passage d'une onde gravitationnelle. Une des principales méthodes de détection est l'interférométrie et consiste à mesurer le déphasage entre deux faisceaux lasers dont la longueur varie dû au passage d'une onde gravitationnelle. Cette technique est actuellement utilisée par les détecteurs LIGO et Virgo, dont les bras font 4 et 3 km de long respectivement, et sera également exploitée par les futurs détecteurs terrestres (Einstein Telescope et Cosmic Explorer) et spatiaux, LISA. Ce dernier sera composé de trois navettes spatiales suivant la Terre sur son orbite autour du Soleil, reliées par des lasers de 2.5 millions de kilomètres. Tandis que les détecteurs terrestres sont sensibles à des systèmes binaires de masse totale de l'ordre de 1-100 $M_\odot$, tels que des binaires de trous noirs de masses stellaires ou des binaires d'étoiles à neutrons, LISA cherchera à observer des binaires de trous noirs massifs, de masse totale allant de $\sim 10^4$ à 10^9 $M_\odot$. LISA sera également capable de détecter le signal émis par des binaires Galactiques. Ces systèmes, constitués essentiellement de naines blanches mais aussi d'étoiles à neutrons et de trous noirs, formeront un signal stochastique dominant

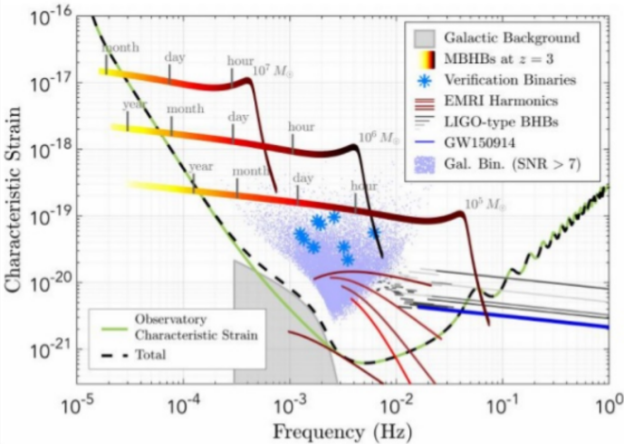

Figure 3: Principales sources de LISA comparées au niveau de bruit dans le détecteur.

sur le bruit de l'instrument. Par ailleurs, quelques dizaines de milliers de ces sources devraient être détectables individuellement. Finalement, LISA pourra également observer des binaires de trous noirs de masses stellaires lors de leur phase inspiralante, quelques semaines avant que les détecteurs terrestres n'observent leur fusion. Sur la figure 3, nous représentons l'amplitude des principales sources de LISA ainsi que le niveau de bruit dans le détecteur, mesuré par la densité spectrale de puissance du bruit, $S_n(f)$.

La présence de bruit dans les détecteurs peut grandement compromettre la détection de signaux. La technique du "matched filtering" permet d'y remédier. Tout d'abord, définissons le produit scalaire entre deux formes d'ondes:

$$(a|b) = 4\mathcal{R}e\left(\int_0^{+\infty} \frac{\tilde{a}(f)\,\tilde{b}^*(f)}{S_n(f)}\mathrm{d}f\right). \tag{4}$$

Notons θ l'ensemble des paramètres d'un système binaire. Le "matched filtering" consiste à trouver un θ maximisant le ratio signal sur bruit (signal to noise ratio, SNR, en anglais), défini comme

$$\mathrm{SNR}[\theta] = \frac{(d|h(\theta))}{\sqrt{(h(\theta)|h(\theta))}}, \tag{5}$$

où d est la série de données mesurée par le détecteur. On considère qu'un signal est détecté lorsque le SNR dépasse un seuil prédéfini. Ce seuil est fixé de telle sorte que la probabilité que le bruit du détecteur puisse produire un signal semblable à celui observé soit suffisamment faible (typiquement de l'ordre de 10^{-3}). Pour un seul détecteur, le seuil en SNR est alors de l'ordre de 8. Une fois un signal détecté on procède à l'estimation des paramètres. Pour cela, les paramètres du système sont traités comme une variable aléatoire dont la distribution de probabilité est estimée à l'aide du théorème de Bayes:

$$p(\theta|d,\mathcal{H}) = \frac{p(d|\theta,\mathcal{H})p(\theta|\mathcal{H})}{p(d|\mathcal{H})}. \tag{6}$$

où $\mathcal{H}$ représente l'ensemble des hypothèses faites dans l'analyse, $p(\theta|d,\mathcal{H})$ est la "posterior distribution", $p(d|\theta,\mathcal{H})$ la vraisemblance, $p(\theta|\mathcal{H})$ la "prior distribution" et $p(d|\mathcal{H})$ l'évidence.

Ce dernier terme peut être utilisé pour comparer différents modèles (des $\mathcal{H}$ différents), mais peut être considéré comme une simple constante de normalisation lors de l'estimation des paramètres. Puisque nous n'effectuons pas de comparaison entre modèles, nous omettons le terme $\mathcal{H}$ par la suite. Sous l'hypothèse que le bruit dans le détecteur est gaussien, la vraisemblance s'écrit

$$p(d|\theta) = \exp\left[-\frac{1}{2}(d - h(\theta)|d - h(\theta))\right]. \tag{7}$$

La difficulté dans l'estimation des paramètres réside dans la haute dimensionnalité de θ, 11 dans notre cas (les masses, les spins, la distance à la source, l'inclinaison de la source, la phase de polarisation, la latitude, la longitude, le temps de coalescence/la fréquence initiale, la phase de coalescence/phase initiale). Cela requiert d'explorer l'espace des paramètres efficacement. La technique la plus répandue est d'utiliser un algorithme "Markov chain Monte-Carlo" (MCMC). Un des principaux buts de cette thèse a été de développer un algorithme MCMC permettant d'effectuer des estimations de paramètres sur des signaux simulés de binaires de trous noirs de masses stellaires dans LISA. Il s'agit plus spécifiquement d'un algorithme Metropolis-Hastings MCMC (MHMCMC). Notre algorithme s'appuie sur le calcul de la matrice de Fisher afin d'explorer efficacement l'espace des paramètres. Cette dernière est définie à travers la relation

$$F_{ij}(\theta) = (\partial_i h|\partial_j h)|_\theta\,. \tag{8}$$

et son inverse fournit une approximation (optimiste) de la matrice de covariance des paramètres. Dans cette thèse nous ne traitons pas de la détectabilité des signaux, nous nous focalisons sur des systèmes à suffisamment haut SNR et effectuons l'estimation des paramètres.

Nous avons utilisé notre algorithme pour effectuer une étude à large échelle de l'estimation des paramètres de binaires de trous noirs de masses stellaires observées avec LISA. Jusque-là toutes les études portant sur ce sujet avaient utilisé la matrice de Fisher pour l'estimation des paramètres et ne prenaient pas en compte la réponse complète de LISA au signal gravitationnel. Au contraire, nous effectuons des analyses bayésiennes complètes sur des signaux réalistes de LISA. À partir d'un système compatible avec le premier événement observé, GW150914, (dit système *Fiducial*) nous définissons d'autres systèmes en variant un ou deux paramètres à la fois, afin de comprendre comment varient l'erreur sur les paramètres et les corrélations entre eux à travers l'espace des paramètres. Nous explorons également l'importance du temps d'observation et du choix de prior. Le principal résultat est que l'estimation des paramètres intrinsèques (masses et spins) dépend énormément du stade de l'évolution du système pendant lequel il est observé. Cela peut être vu sur la figure 4, où nous montrons la posterior distribution pour le système *Fiducial* pour des durées de la mission de 4 et 10 ans, sachant que l'observation du système démarre 8 ans avant sa coalescence. Dans le cas où la mission ne dure que 4 ans, nous n'observons que la phase inspiralante et seule la chirp mass peut être précisément mesurée, avec quand même une forte corrélation avec la raison symétrique des masses. Nous montrons que la posterior des autres paramètres intrinsèques est dominée par le choix de prior. Dans le deuxième cas, nous observons le début du "chirp", la corrélation entre $\mathcal{M}_c$ et η est partiellement brisée et il est possible de mesurer le spin effectif χ_+. Par ailleurs, nous montrons que la position dans le ciel est toujours bien estimée, typiquement au-dessous de 1 deg^2, ce qui permettrait à des futurs observatoires électromagnétiques tels qu'Athena et SKA de chercher une contrepartie élec-

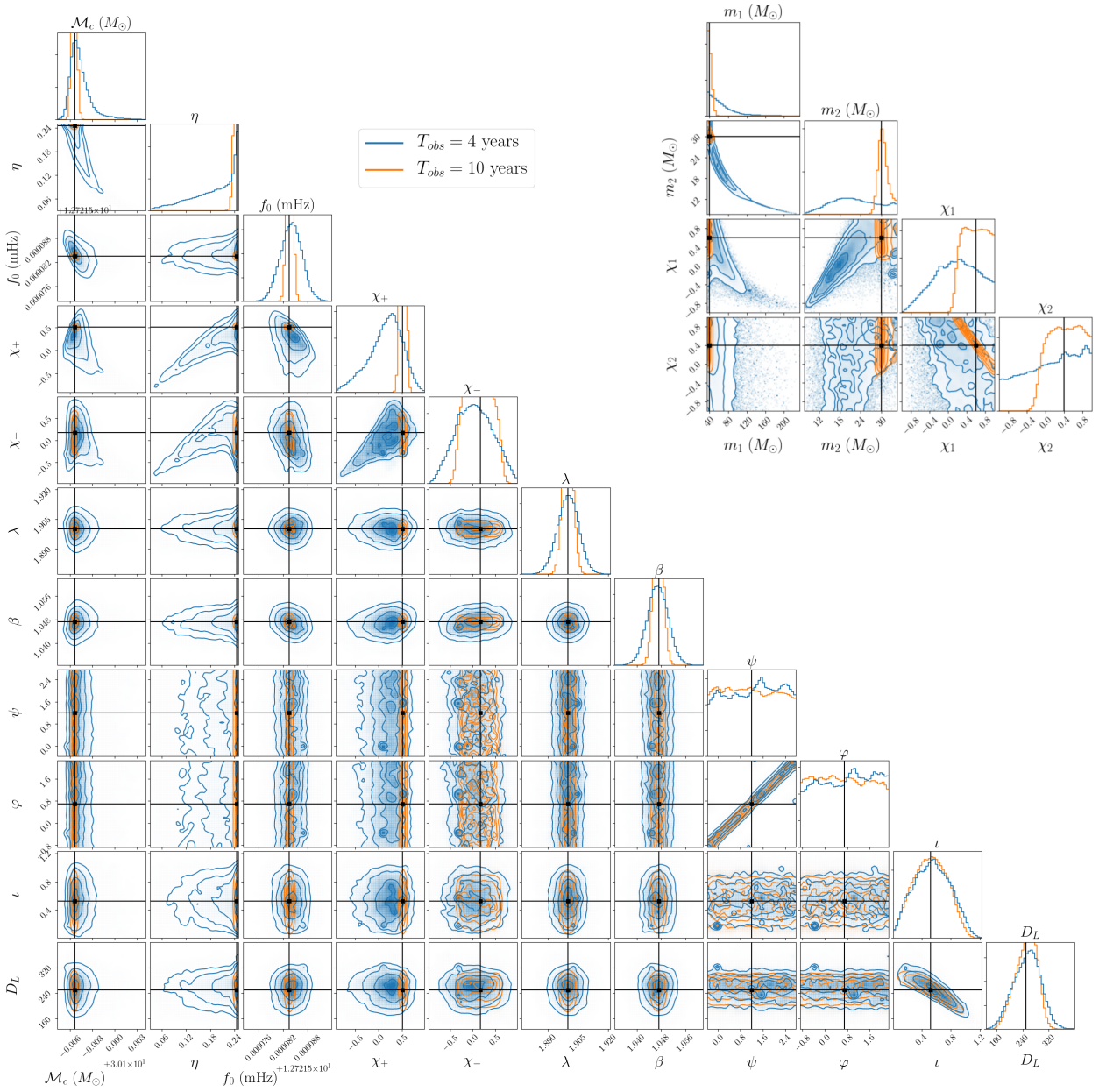

Figure 4: Distributions des paramètres inférées pour le système *Fiducial* dans le cas où la mission dure 4 ans (bleu) et 10 ans (orange). Les valeurs des paramètres du signal injectées sont indiquées par des lignes noires. Les masses sont dans le référentiel du détecteur.

tromagnétique. Nous proposons également une amélioration de l'estimation des paramètres basée sur la matrice de Fisher, produisant des résultats compatibles avec l'analyse bayésienne. L'amélioration consiste en l'ajout d'une matrice à la matrice de Fisher afin de prendre en compte l'étendue finie du prior sur les spins et corriger la trop grande erreur prédite sur la distance, due à la forte corrélation avec l'inclinaison. Finalement, nous comparons l'effet de l'approximation "long wavelength" pour la réponse sur l'estimation des paramètres. Nous concluons que celle-ci à peu d'impact si les données sont générées avec cette même approximation, mais qu'elle peut entraîner des biais dans le cas plus réaliste où la réponse complète est prise en compte. En conclusion, notre travail sert de base à l'exploitation scientifique de l'observation des binaires de trous noirs de masses stellaires avec LISA et pourra être utilisé dans le futur afin de mettre en place des outils de recherche de tels signaux.

L'existence d'ondes gravitationnelles est également prédite par les théories de gravité modifiée. Ces théories, visant à expliquer la matière noire, l'énergie noire et/ou concilier la gravitation avec les phénomènes quantiques, modifient l'équation d'Einstein et donc les solutions d'ondes gravitationnelles. Celles-ci sont émises dans un régime où le champ gravitationnel est fort et dynamique, où les écarts par rapport à la relativité générale sont potentiellement plus grands. Ainsi, les observations d'ondes gravitationnelles constituent un excellent moyen de tester les théories de gravité modifiée. Malheureusement, il est encore plus difficile de résoudre les équations du champ gravitationnel dans ces théories, et peu de

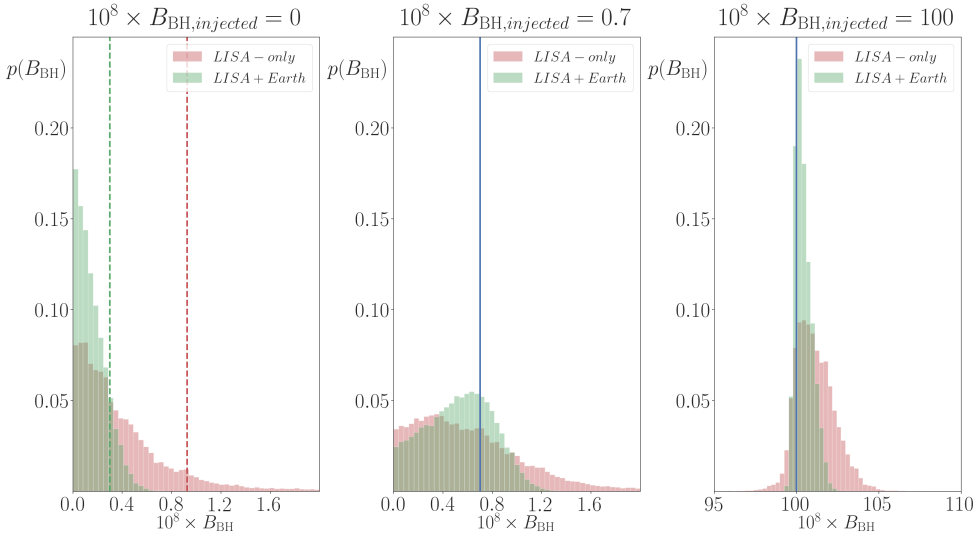

Figure 5: Distribution de l'amplitude de la radiation dipolaire pour un système similaire à GW150914 avec LISA (rouge) et LISA+détecteurs terrestres (vert). Sur le panneau de gauche, la valeur injectée est nulle et les lignes en pointillées indiquent la borne supérieure que l'on pourrait placer sur B_{BH} (correspondant à l'intervalle de confiance de 90%). Dans les deux scénarios, la contrainte est bien inférieure à celle actuelle (4×10^{-2}). Sur les panneaux du milieu et de droite, la valeur injectée est 0.7×10^{-8} et 1.0×10^{-6} respectivement, comme indiquée par la ligne bleue. Puisque zéro n'appartient pas au support de la posterior sur le panneau de droite, il serait possible dans ce cas d'identifier avec certitude la présence d'une modification de la relativité générale, contrairement au cas sur le panneau du milieu.

résultats de formes d'ondes en gravité modifiée sont actuellement disponibles. Il est alors utile de se tourner vers des tests agnostiques, ne ciblant pas des théories spécifiques. Par exemple, une prédiction commune à plusieurs théories est la présence de radiation dipolaire dans des binaires de trous noirs. Cet effet entraîne une modification de la phase de l'onde gravitationnelle à basses fréquences, dont l'amplitude est proportionnelle à l'amplitude de la radiation dipolaire $B_{\rm BH}$. On s'attend donc à ce que l'observation de binaires de trous noirs de masses stellaires à basses fréquences avec LISA permette de contraindre cet effet. À l'aide d'une analyse bayésienne, nous obtenons en effet que l'observation d'un système semblable à GW150914 permettrait de contraindre $B_{\rm BH}$ à moins de 10^{-8}, et un ordre de magnitude moins si le système est ensuite observé avec des détecteurs terrestres (voir figure 5), ce qui représente une amélioration de 7 ordres de magnitude par rapport aux contraintes actuelles. Nous considérons également la possibilité de contraindre la masse du graviton. Une masse non nulle entraîne une modification de la relation de dispersion et ainsi une dépendance de la vitesse des ondes gravitationnelles avec la fréquence. Cette dépendance crée un décalage en phase apparaissant à plus hautes fréquences. Nous obtenons que LISA pourrait légèrement améliorer les contraintes actuelles sur la masse du graviton mais nous nous attendons à ce que LIGO et Virgo améliorent leur contrainte d'ici le lancement de LISA.

Ensuite, nous nous intéressons à des modifications survenant proche de la fusion lors de la coalescence d'objets compacts exotiques. L'existence de ces objets est prédite par de nombreuses théories au-delà du modèle standard et de la relativité générale, l'exemple le mieux étudié étant les étoiles à bosons. Ces objets ont une compacité (raison adimensionnelle entre la masse et le rayon) allant de ~ 0.1 à 0.5 et peuvent mimer le comportement gravitationnel des trous noirs et des étoiles à neutrons, rendant leur identification difficile. En nous basant sur des résultats analytiques et de simulations numériques, nous identifions les principales différences qu'exhiberait le signal gravitationnel émis par de tels systèmes avec une binaire

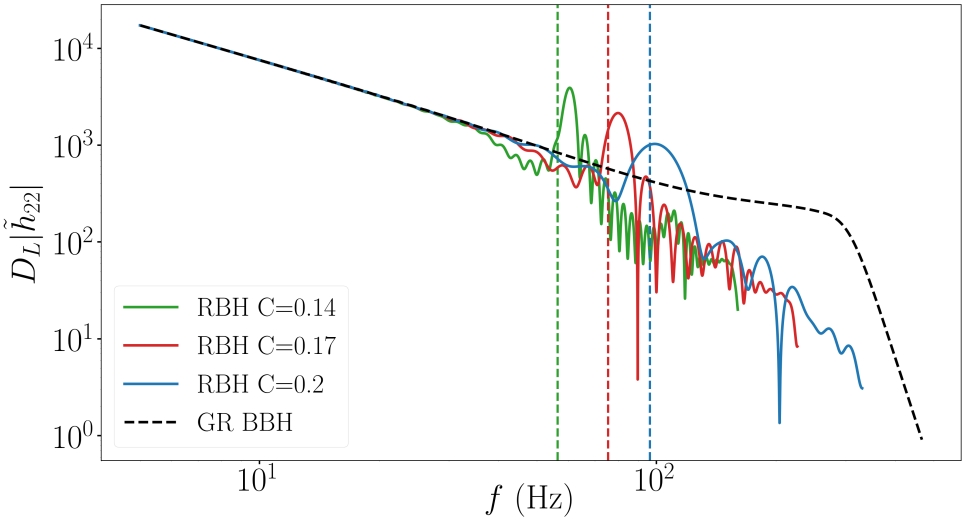

Figure 6: Amplitude du signal dans le domaine de Fourier pour un type de binaires d'objets compacts exotiques de masses 30 $M_\odot$, pour différentes valeurs de la compacité. En noir nous représentons le signal correspondant à une binaire de trous noirs de mêmes masses, sans spins.

de trous noirs. Nous identifions trois issues possibles à la fusion de ces objets: formation prompte d'un trou noir, formation d'une étoile "supermassive" qui finit par collapser en un trou noir ou qui finit par former un objet compact exotique de la même nature que les objets dans le système binaire. De plus, dans ce dernier cas la quantité de moment cinétique angulaire retenue lors de la coalescence dépend fortement de la nature de l'objet. Nous nous concentrons sur les cas où une étoile supermassive est formée et proposons un modèle simplifié pour la dynamique du système suite à la fusion, dans le cas où les objets n'ont pas de spin, ont la même masse et ont une compacité comprise entre 0.14 et 0.2. Nous calculons ensuite les signaux gravitationnels émis dans chaque configuration, en incluant les effets de marée lors la phase inspiralante et en utilisant notre modèle pour le signal fusion/post-fusion. Un exemple de signal est donné sur la figure 6. Nous utilisons ces signaux dans le but d'étudier la détectabilité et l'indiscernabilité de telles binaires. Nous obtenons que LIGO ne peut les détecter que jusqu'à $z \sim 1$ mais que LISA et Einstein Telescope pourront détecter pratiquement toutes les binaires de ce genre dans l'Univers et potentiellement les discerner de binaires de trous noirs. De plus, nous montrons que des recherches de signaux basées sur le matched filtering pourraient perdre jusqu'à 60% de SNR si seules des formes d'ondes de binaires de trous noirs sont utilisées, ce qui compromettrait grandement nos chances de détecter ces signaux. Finalement, nous estimons qu'il est peu vraisemblable que les signaux détectés par LIGO et Virgo lors des deux premières périodes de prises de données soient issus de binaires d'objets compacts exotiques telles que celles que nous considérons. Notre modèle pourrait être amélioré afin d'inclure d'autres modifications au signal d'une binaire de trous noirs lors de la phase inspiralante, dues par exemple à une structure multipolaire différente, et une plus grande variété de comportements post-fusion. Il pourrait être utilisé afin de mettre en place des outils d'analyse de données cherchant à identifier des modifications à la relativité générale proche de la fusion.

L'environnement astrophysique dans lequel évolue un système binaire peut également entraîner des modifications à basse fréquence de l'onde gravitationnelle. C'est par exemple le cas si les trous noirs accrètent de la matière, se déplacent dans de la matière subissant une force visqueuse ou orbitent un objet massif. De telles modifications seraient potentiellement dégénérées avec des modifications dues à des écarts par rapport à la relativité générale, difficultant les tests de la relativité générale, et doivent donc être soigneusement pris en compte. Les circonstances décrites auparavant sont réunies dans le cas où le système se trouve au centre d'une galaxie active, tel qu'il a été spéculé pour l'événement GW190521 détecté par LIGO et Virgo. Ce système présente la particularité d'être très massif ($M \sim 150\ M_\odot$), avec au moins un des deux composants dans le "gap de masse" prédit par la théorie de l'évolution stellaire. En effet, on s'attend à ce que des étoiles avec une masse de l'ordre de 120-260 $M_\odot$ se désintègrent complètement, sans laisser de trou noir derrière elles. Ainsi, des trous noirs de masse entre 60 et 130 $M_\odot$ ne devraient pas pouvoir êtres formés suite à l'effondrement gravitationnel d'une étoile d'après les modèles d'évolution stellaire standard. Une alternative serait que ces trous noirs (du moins le plus massif) soient de "seconde génération", c'est-à-dire des trous noirs formés suite à la fusion de deux trous noirs plus petits, formés eux suite à l'effondrement gravitationnel d'étoiles. La formation de binaires où au moins l'un des trous noirs est de seconde génération est favorisée dans des régions denses telles que le centre d'une galaxie active. De plus, le télescope optique et infrarouge Zwicky Transient Facility a détecté un candidat pour une contrepartie électromagnétique qui aurait été provoqué par

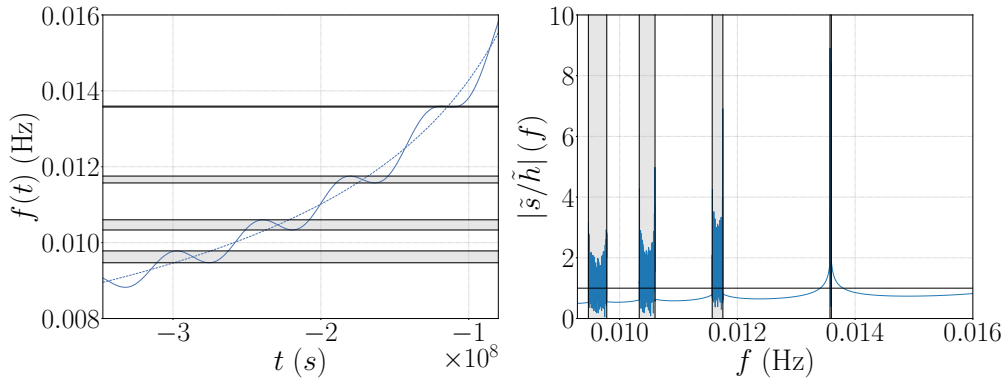

Figure 7: Modulation Doppler du signal gravitationnel due au mouvement de la binaire autour du trou noir massif central. Le panneau de gauche représente l'évolution de la fréquence de l'onde au cours du temps pour des signaux avec (ligne continue) et sans (ligne pointillée) modulation (la coalescence est à $t = 0$). Le panneau de droite représente le ratio des amplitude du signal gravitationnel dans le domaine de Fourier avec et sans modulation. La ligne horizontale est à 1. Dans les deux panneaux, les bandes grisées indiquent les bandes de fréquence où la relation temps-fréquence n'est pas bijective.

le déplacement du trou noir final dans le disque d'accrétion autour de trou noir massif au centre de la galaxie J124942.3+344929. Grâce à sa large masse totale, un tel système serait potentiellement détectable par LISA. Ainsi, nous nous penchons sur ce que LISA pourrait nous apprendre sur les effets environnementaux dans des binaires de trous noirs de masses stellaires et des binaires de trous noirs de masses intermédiaires ($M \sim 10^2$-$10^3\ M_\odot$). Nous nous sommes d'abord intéressés à l'effet de l'accrétion. Nous considérons que chaque trou noir accrète au même taux $\dot{m} = f_{\rm Edd}\dot{m}_{\rm Edd}$ où $\dot{m}_{\rm Edd}$ est le taux d'Eddington, une limite théorique sur le taux d'accrétion d'un trou noir et $f_{\rm Edd}$ est un paramètre libre. Nous montrons que cela entraîne une modification à basses fréquences proportionnelle à $f_{\rm Edd}$ et qu'il est possible de détecter son effet pour des accrétions de niveau supra-Eddington ($f_{\rm Edd} \sim 10$) dans des binaires de trous noirs de masses stellaires et de niveau Eddington dans des binaires de trous noirs de masses intermédiaires ($f_{\rm Edd} \sim 1$). Dans ce dernier cas, nous estimons de plus qu'il serait possible d'observer une contrepartie électromagnétique en rayons X avec Athena et dans le domaine radio avec SKA. Nous nous concentrons ensuite sur des systèmes semblables à GW190521, à cheval entre une binaire de trous noirs de masses stellaires et une binaire de trous noirs de masses intermédiaires. Nous considérons les trois effets décrits précédemment: accrétion, friction dynamique, accélération (constante) autour d'un trou noir massif et évaluons dans quelles configurations ces effets sont détectables. Nous estimons que l'effet de l'accrétion serait détectable pour $f_{\rm Edd} \gtrsim 6$, celui de la friction dynamique pour une densité du gaz dans le disque d'accrétion supérieure à 10^{-12}g.cm^{-3} (soit 100 fois moins que celle estimée par Zwicky Transient Facility) et celui de l'accélération pour un rayon orbital inférieur à 0.4 pc pour un trou noir central ayant une masse de $10^8\ M_\odot$. Finalement, nous considérons l'effet du mouvement du système binaire autour du trou noir dans le cas où le rayon orbital est trop petit pour que l'accélération puisse être considérée constante. Dans ce cas, comme illustré sur la figure 7, la fréquence du signal gravitationnel n'est plus une fonction croissante du temps, avec des modulations dues à l'effet Doppler. Cela

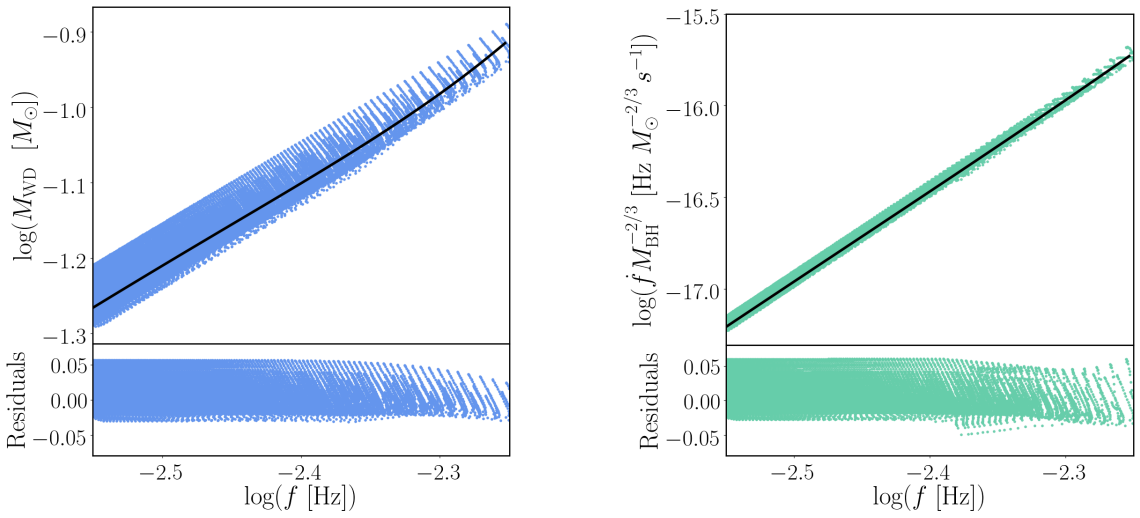

Figure 8: Relations entre la fréquence du signal gravitationnel, sa dérivée et les masses du trou noir et de la naine blanche obtenues à partir de simulations numériques

.

entraîne une modification non perturbative du signal comme il est possible de constater sur le panneau droit de cette même figure. Nous sommes actuellement en train d'estimer dans quelle mesure cet effet pourrait nous renseigner sur les propriétés de la galaxie où se trouve le système binaire. Par ailleurs, la capacité de LISA à identifier précisément la position de la source faciliterait la recherche de contreparties électromagnétiques telle que celle identifiée par Zwicky Transient Facility.

Nous nous intéressons ensuite aux effets de l'accrétion au sein d'un système binaire, plus particulièrement à des systèmes composés d'un trou noir accrétant la matière d'une naine blanche. Les modèles de synthèse de population Galactique prédisent un taux au moins 100 fois moins élevé pour ces systèmes que pour des binaires de naines blanches et leur existence n'a pas encore été confirmée malgré quelques candidats. De tels systèmes émettent un signal quasi monochromatique dans la bande du mHz et seraient des sources potentielles pour LISA. Nous proposons un modèle semi-analytique pour l'évolution de ces systèmes à partir du moment où l'accrétion se met en place, quand le rayon de la naine blanche dépasse celui de son lobe de Roche. Notre modèle repose sur la conservation du moment cinétique angulaire et utilise des approximations analytiques pour le taux d'accrétion, le rayon d'une naine blanche et le rayon du lobe de Roche. Nous considérons de plus que la naine blanche est synchronisée avec la période orbitale du système ("tidal lock") et que le trou noir ne subit pas d'effets de marée. Nous montrons que, comme dans le cas de binaires de naines blanches, il existe une étroite relation entre la fréquence de l'onde gravitationnelle (f) et la masse de la naine blanche ($M_{\rm WD}$), indépendante des conditions initiales, comme illustré sur le panneau gauche de la figure 8. Nous mettons en évidence pour la première fois une relation entre la fréquence de l'onde gravitationnelle, sa dérivée ($\dot{f}$) et la masse du trou noir ($M_{\rm BH}$), illustrée sur le panneau droit de la figure 8. L'observation de tels systèmes avec LISA nous permettrait de mesurer f, $\dot{f}$ et l'amplitude de l'onde, et ces relations nous

permettraient d'inférer les masses du trou noir et de la naine blanche, ainsi que la distance à la source. L'information des masses, qui n'est généralement pas accessible à travers des observations d'ondes gravitationnelles de binaires Galactiques, nous permettrait d'identifier sans ambigüité les deux composants du système binaire. Ainsi, LISA pourrait être le premier instrument à confirmer l'existence de tels binaires. Dans notre modèle nous utilisons une approximation pour le rayon de la naine blanche à température zéro. Or celle-ci peut être chauffée par les radiations du trou noir. En estimant la température de la naine blanche à l'aide de la formule de Stefan-Boltzmann pour les corps noirs et en utilisant des résultats de simulations numériques pour la relation masse-rayon de naines blanches à température finie, nous estimons que la naine blanche ne serait pas chauffée suffisamment pour que les effets de température finie deviennent importants. Par ailleurs, nous prévoyons d'explorer dans quelle mesure nos résultats sont robustes si une relation masse-rayon différente ou une autre approximation pour le rayon de lobe de Roche sont utilisées.

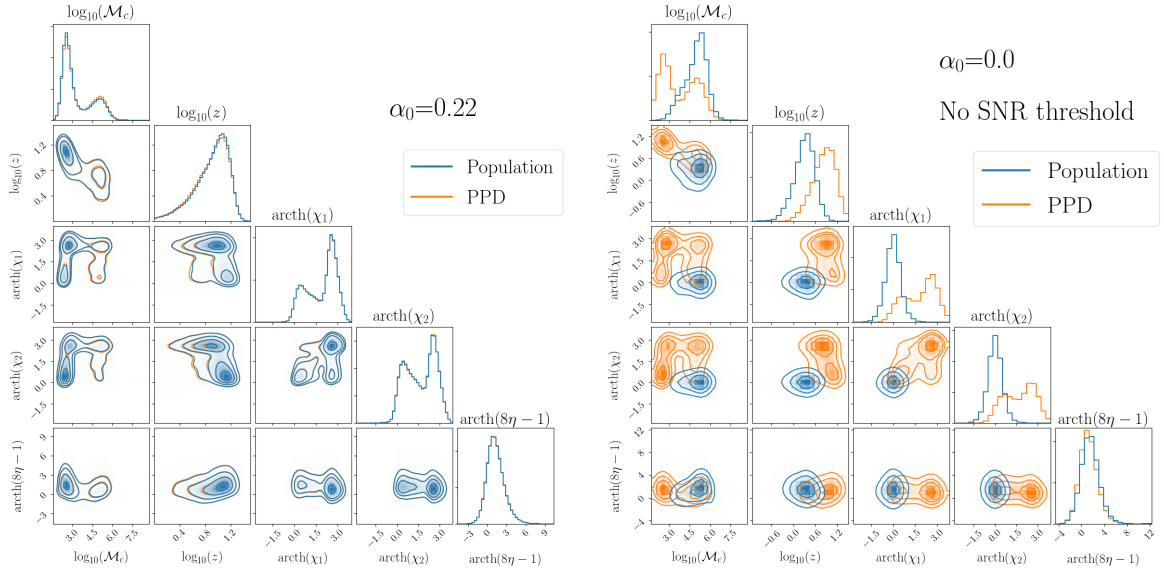

(a) (b)

Figure 9: Inférence de la population de trous noirs massifs à partir d'observations de LISA. Sur le panneau de gauche nous avons simulés des donnés en utilisant le même modèle astrophysique que celui utilisé dans l'analyse hiérarchique. Sur le panneau de droite nous utilisons des modèles différents et, contrairement au premier cas, notre inférence de la population de trous noirs (PPD) est en désaccord avec la population sous-jacente. α_0 est la valeur du coefficient de mélange entre les deux variantes du modèle.

Après avoir exploré ce qui pourrait être appris à partir de détections individuelles, nous nous intéressons à ce que les observations de LISA dans leur ensemble pourrait nous enseigner. Nous nous intéressons à la capacité de LISA d'inférer la population de binaires de trous noirs massifs dans l'Univers. Celle-ci étant le résultat de la longue évolution des trous noirs depuis $z \sim 20$ jusqu'à aujourd'hui, mesurer la distribution de binaires de trous noirs massifs nous informerait sur les processus régissant la formation et l'évolution des trous noirs massifs. Nous utilisons les résultats de simulations semi-analytiques pour modéliser la popu-

lation de binaires de trous noirs massifs. Les modèles que nous utilisons ont deux variantes: l'une où les trous noirs sont formés à partir des étoiles "Pop III", les premières étoiles de l'Univers, et l'autre où ceux-ci sont formés par l'effondrement de disques protogalactiques. Dans le premier cas les trous noirs sont originalement peu massifs ($\sim 10^2\ M_\odot$), contrairement au deuxième cas ($\sim 10^5\ M_\odot$). Puisqu'il est peu vraisemblable que l'Univers puisse être décrit par un seul modèle, nous introduisons un coefficient de mélange entre ces deux variantes que nous traitons comme un hyperparamètre contrôlant la population de binaires de trous noirs massifs. Nous étudions avec quelle précision ce coefficient de mélange pourrait être mesuré à partir des observations de LISA, en effectuant une analyse bayésienne hiérarchique sur des données simulées. Cette analyse cherche à déterminer la valeur du coefficient de mélange pour laquelle les observations peuvent le mieux être décrites par notre modèle théorique. Nous vérifions tout d'abord que notre analyse ne comporte pas de biais systématiques et que la détermination du coefficient de mélange s'améliore avec le nombre d'observations. Nous montrons ensuite que cette méthode permet de déterminer précisément la population de binaires de trous noirs massifs, mais seulement dans le cas où les observations sont suffisamment proches du modèle théorique auquel elles sont comparées (voir figure 9). Afin de pallier cela, nous sommes actuellement en train de travailler sur un modèle plus flexible pour la population de binaires de trous noirs massifs, où celle-ci serait contrôlée par des hyperparamètres ayant une plus grande signification physique, tels que la distribution initiale de masse ou les délais entre la fusion de galaxies et la fusion des trous noirs massifs centraux. Par ailleurs, nous commentons sur l'importance d'avoir suffisamment de points fournis par les simulations numériques, sous peine d'entraîner des biais systématiques dans l'analyse. Finalement, nous nous penchons sur des systèmes pour lesquels nous avons effectué une analyse bayésienne et la distribution des paramètres intrinsèques est multimodale lorsque les harmoniques au-delà de l'harmonique dominant sont inclus. Nous montrons que cela est dû au fait que ces harmoniques ont des SNRs suffisamment élevés pour réduire l'erreur sur les paramètres par rapport au cas où seul l'harmonique dominant est pris en compte, mais pas assez pour briser certaines dégénérescences. Étudier ces systèmes est pertinent du point de vue astrophysique puisqu'ils proviennent de simulations numériques, mais la plupart des cas où nous observons une multimodalité est pour des systèmes ayant de larges spins et des raisons de masses bien au-dessus de 1. Cela renforce l'importance d'avoir des formes d'ondes dans ce régime plus fiables que celles dont nous disposons actuellement.

Ainsi, dans cette thèse j'ai fait de mon mieux pour apporter des réponses à des questions qui me semblaient importantes pour la communauté des ondes gravitationnelles. Ce processus a amené de nouvelles questions tout aussi pertinentes auxquelles j'espère être capable d'apporter une réponse dans un futur proche.

Contents

List of Figures

List of Tables

Acronyms

AGN active galactic nuclei

BBH binary black hole

BNS binary neutron star

CE Cosmic Explorer

ECO exotic compact object

EOB effective-one-body

ET Einstein Telescope

FF fitting factor

GB galactic binaries

HS heavy seed

IMBHB intermediate-mass black hole binary

ISCO innermost stable circular orbit

KDE kernel density estimation

KL Kullback-Leibler

LIGO Laser Interferometer Gravitational-Wave Observatory

LISA Laser Interferometer Space Antenna

LS light seed

LVC LIGO-Virgo Collaboration

MCMC Markov chain Monte Carlo

MHMCMC Metropolis-Hastings Markov chain Monte Carlo

MBHB massive black hole binary

PN post-Newtonian

SBHB stellar-mass black hole binary

SKA Square Kilometer Array

SNR signal-to-noise ratio

SSB Solar System barycentre

TDI time delay interferometry

TT transverse-traceless

WDBH white dwarf-black hole

Symbol	Meaning	Expression
m_1	Mass of the primary black hole	/
m_2	Mass of the secondary black hole	/
$\mathcal{M}_c$	Chirp mass	$\mathcal{M}_c = \left(\frac{m_1^3 m_2^3}{m_1+m_2}\right)^{1/5}$
η	Symmetric mass ratio	$\eta = \frac{m_1 m_2}{(m_1+m2)^2}$
q	Mass ratio	$q = \frac{m_1}{m_2} \geq 1$
M	Total mass	$M = m_1 + m_2 = \mathcal{M}_c \eta^{-3/5}$
$\mu_{\rm red}$	Reduced mass	$\mu = \frac{m_1 m_2}{m_1+m_2}$
δ_m	Relative mass difference	$\delta_m = \frac{m_1-m_2}{m_1+m_2}$
χ_1	Spin of the primary black hole along the orbital angular momentum	/
χ_2	Spin of the secondary black hole along the orbital angular momentum	/
χ_+	Effective spin	$\chi_+ = \frac{m_1\chi_1+m_2\chi_2}{m_1+m_2}$
χ_-	Antisymmetric mass-weighted spin	$\chi_+ = \frac{m_1\chi_1-m_2\chi_2}{m_1+m_2}$
χ_s	Symmetric spin	$\chi_a = \frac{\chi_1+\chi_2}{2}$
χ_a	Antisymmetric spin	$\chi_a = \frac{\chi_1-\chi_2}{2}$
$\chi_{\rm PN}$	1.5 PN spin combination	$\chi_{\rm PN} = \frac{\eta}{113}[(113q+75)\chi_1 + (\frac{113}{q}+75)\chi_2]$
f_0	Initial frequency	/
t_c	Time to coalescence	/
λ	Longitude	/
β	Latitude	/
ψ	Polarisation angle	/
φ	Initial phase	/
φ_c	Coalescence phase	/
ι	Inclination	/
D_L	Luminosity distance in Mpc	/
z	Redshift	$z(D_L)$ [1]

Table 1: Parameters used throughout the manuscript and their explicit expressions when necessary.

Introduction

In 2015, the Laser Interferometer Gravitational Wave Observatory (LIGO) [2] observed for the first time the gravitational wave signal emitted by a coalescing binary [3]. The detection of GW150914, named after its detection date, came forty years after the indirect observation of gravitational waves in binary pulsars [4], and definitively confirmed Einstein's 1916 finding [5]. Since then, LIGO has been joined by Virgo [6] and the LIGO/Virgo collaboration (LVC) has issued two catalogues of the gravitational wave sources identified during the first and second observing runs [7] and during the first half of the third run [8], counting in total 50 events. These observations of gravitational waves in the 10–1000 Hz band have inaugurated the era of gravitational wave astronomy and opened a new window to the Universe.

The latter expression is not a mere figure of style. For instance, gravitational waves offer complementary means of observing neutron stars. A first *multimessenger* event occurred during the second observing run, when LIGO and Virgo detected the coalescence of a binary neutron star (BNS) [9] and a coincident electromagnetic counterpart was observed [10]. Moreover, unlike electromagnetic telescopes, gravitational wave detectors can observe black holes in binary systems without any need for matter surrounding them. All observations so far being in good agreement with the prediction of general relativity for the gravitational wave emission of binary black holes (BBHs) [11, 12, 13], they make a strong case for the existence of black holes. As the observations accumulate, we become able to infer the astrophysical properties of BBHs with total mass in the range $\sim 10 - 100\ M_\odot$, dubbed stellar-mass black hole binaries (SBHBs) [14, 15]. In parallel, following Karl Popper's theory of falsification [16], one should always challenge the standard paradigm and try to prove it wrong. Therefore, the possibility that in the near future we might observe some exotic compact objects (ECOs) rather than black holes and/or that general relativity might fail cannot be discarded. Gravitational waves probe the strong field dynamical regime, where putative deviations from the general relativity BBH behaviour are stronger, offering exciting perspectives.

The improvement of gravitational wave detectors in the next years will increase our reach and allow us to perform more and more precise tests. LIGO and Virgo should reach their design sensitivity by 2024, they will be joined by KAGRA [17, 18] and shortly after by LIGO India [19]. In the next decade, the Einstein Telescope (ET) [20, 21, 22] and Cosmic Explorer (CE) [23] will improve our sensitivity in the Hz band and observe all coalescing SBHBs and BNSs in the Universe. On the other end of the frequency spectrum, pulsar timing arrays [24, 25] are currently looking for the signal emitted by inspiralling massive black hole binaries (MBHBs) in the nHz band [26], and a promising candidate signal has recently been reported [27]. In the late 2020s, the Square Kilometer Array (SKA) [28] will improve

our sensitivity in the nHz band by a factor 10. Finally, the Laser Antenna Space Antenna (LISA) [29], scheduled for launch in 2034, will observe gravitational waves in a different frequency band (the mHz band) and, therefore, complement ground-based detectors and pulsar timing arrays. The strongest anticipated gravitational wave sources in the LISA data will be merging MBHBs, with total mass in the range 10^4–10^9 $M_\odot$ [30], and galactic binaries (GBs) comprising mostly white dwarves, but also neutron stars and black holes [31]. SBHBs with a total mass as large as those observed by LIGO and Virgo could also be detected by LISA during their early inspiral phase, long before entering the frequency band of ground-based detectors and merging [32]. This great variety of sources make LISA a science rich instrument.

The goal of this thesis is to assess what could be learned from gravitational waves observations with next generation detectors, and more specifically with LISA, from the fundamental physics and astrophysical point of view. This manuscript is organised as follows.

In chapter 1, we give a brief overview of the history of general relativity, gravitational waves and black holes. We then give a short introduction to the theory of gravitational waves within general relativity and modified gravity theories, the main sources of gravitational waves and the detection methods. In that chapter, we introduce some key notions that we use in this work.

Chapter 2 introduces the main aspects of data analysis used in this manuscript. First, we describe how the presence of a signal can be identified in the data stream of gravitational wave detectors, and then how the parameters of the source are estimated from the detected signal.

In chapter 3, we focus on the parameter estimation of SBHBs. We introduce the Markov chain Monte Carlo algorithm we developed for this purpose, and apply it to simulated LISA data. We scan the parameter space of SBHBs and describe how does the parameter estimation evolve across it. This chapter is based on the results published in [33].

Chapter 4 is dedicated to tests of general relativity. Using our Markov chain Monte Carlo algorithm, we show that LISA will be able to improve current constraints on deviations from general relativity by observing SBHBs. These results were published in [34]. We also propose a phenomenological model of ECOs, and use it to show that such exotic signals could be missed with current data analysis pipelines, as was published in [35].

In chapter 5, we move to the use of gravitational waves for astrophysical purposes. We present the results published in [36, 37], where using our Markov chain Monte Carlo algorithm, we show that LISA will be able to provide information on the astrophysical environment of SBHBs, e.g. if the binary is orbiting a massive black hole, if it is accreting etc. Echoing the last point, we present a semi-analytical model for the evolution of binaries made of a black hole accreting from a white dwarf companion, and show that LISA could be the first instrument to unambiguously identify them. There, we reproduce the results published in [38].

Finally, chapter 6 is dedicated to the use of LISA to discriminate between different models for the formation and evolution of massive black holes. We propose a pipeline based on the hierarchical Bayesian framework and using results from astrophysical simulations to infer the population of massive black holes from LISA observations, and discriminate between different scenarios. This chapter is based on a submitted work [39].

Chapter 1

Introduction to gravitational waves

1.1 A short history of general relativity, gravitational waves and black holes

By the beginning of the 20th century, Newton's law of gravitation had passed several tests, and was seen as a solid theoretical basis for mechanics. It provided a unified framework to explain from Earth-based experiments to the motion of planets in the Solar System. Nevertheless, a few observational and theoretical discrepancies motivated the search for a gravitational theory beyond Newton's one.

Since the mid 19th century, the orbit of Mercury was known to deviate from the Newtonian prediction. Its orbit around the Sun precesses, causing the perihelion to "advance" by 43 arc-seconds per century. This is (exaggeratedly) illustrated in figure 1.1. Astronomers initially followed Adams and Le Verrier's successful approach in explaining the irregularities in the motion of Uranus, which led to the discovery of Neptune, and postulated the existence of unobserved celestial bodies that perturbed Mercury's orbit. Le Verrier himself suggested the existence of a planet named *Vulcain*. However, no observation over the years was able to prove them right, and the possibility that Newton's theory was failing became concrete, leading physicists to work on a new theory of gravitation.

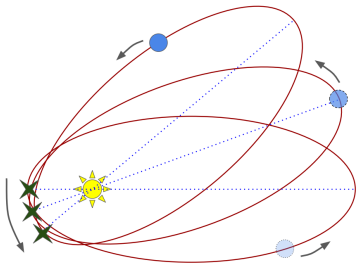

Figure 1.1: Exaggerated illustration of the advance of the perihelion (green star). Mercury's (blue) orbit around the Sun (yellow) precesses, causing its perihelion to shift between succesive passages. Extracted from [40].

On a theoretical level, Newton's theory predicts that the gravitational interaction between two bodies at any distance is instantaneous. This is a major conceptual difference with

Maxwell's theory of electromagnetism, which was already considered one of the greatest achievements of modern physics. Maxwell's theory predicts a delay between an action and its consequences due to finite speed of light. On a one hand, if we include an ad hoc finite propagation speed to Newton's theory, Solar System orbits are substantially modified, unless the speed of gravity is orders of magnitude above the one of the light [41]. On the other hand, given all the parallels between gravitation and electromagnetism, it seemed odd that gravitation could propagate instantaneously. Moreover, in 1905 Einstein formulated his theory of *special relativity*, of which one of the two postulates is that nothing propagates faster than the speed of light in vacuum [42]. Special relativity progressively became a well accepted theory, and efforts concentrated in proposing a relativistic theory of gravitation.

Thanks to collaborations with notable mathematicians and physicists of his time, Einstein managed to formulate his theory of general relativity in 1915 [43]. The driving idea of general relativity is well explained in the words of Wheeler "spacetime tells matter how to move; matter tells spacetime how to curve." [44], and is contained in Einstein's field equations for the metric $g_{\mu\nu}$ [45]:

$$R_{\mu\nu} - \frac{1}{2}R = \frac{8\pi G}{c^4}T_{\mu\nu}, \tag{1.1}$$

where $R_{\mu\nu} = g^{\alpha\beta}R_{\alpha\mu\beta\nu}$ is the Ricci tensor, $R = g^{\mu\nu}R_{\mu\nu}$ is its trace, $R_{\alpha\mu\beta\nu}$ is the Riemann curvature tensor computed from the Christoffel symbols $\Gamma^{\mu}_{\alpha\beta}$, and $T_{\mu\nu}$ is the stress-energy tensor. The explicit expressions of these quantities as functions of the metric can be found in classical textbooks [46, 47, 48]. The Riemann tensor encodes the geometry of spacetime, and vanishes only for a flat spacetime. It is clear from equation (1.1) that the curvature of spacetime is sourced by matter/energy ($T_{\mu\nu}$). The conservation of energy and momentum reads $\nabla_\mu T^{\mu\nu} = 0$, where ∇_μ is the covariant derivative, and leads to the relativistic generalisation of Newton's second law, the geodesic equation [49]:

$$\frac{\mathrm{d}^2x^\mu}{\mathrm{d}\tau^2} + \Gamma^{\mu}_{\alpha\beta}\frac{\mathrm{d}x^\alpha}{\mathrm{d}\tau}\frac{\mathrm{d}x^\beta}{\mathrm{d}\tau} = 0, \tag{1.2}$$

where τ is the proper time. The geodesic equation describes how free-falling test masses move in spacetime, the effect of curvature being imprinted in the Christoffel symbols. An immediate success of general relativity was to correctly account for the precession of the perihelion of Mercury's orbit [50]. The theory also provided a framework for computing the motion of massless particles in a gravitational field, an ill-defined limit in Newtonian gravitation. Einstein computed the deflection of light by the Sun, twice as large as the Newtonian result, and in 1919 a team led by Eddington experimentally confirmed his prediction [51]. These successes established general relativity as the new theory of gravitation physicists had been looking for.

Since then, general relativity has passed many tests from Solar System to cosmological scales with flying colours [52, 53, 54]. Nevertheless, we face today a situation similar to the one a hundred years ago. In order to explain cosmological observations, dark matter and dark energy need to be introduced in the standard model of cosmology [55, 56, 1]. Those could be a new form of matter/energy, or perhaps the manifestation that general relativity fails at large scales. Moreover, from a theoretical perspective, we need a theory of gravity that accounts for quantum effects in order to be able to describe the very early Universe

and solve the information paradox [57, 58]. As a fundamental prediction of gravity theories, gravitational waves provide us with new means to explore beyond general relativity.

As soon as 1916, Einstein "discovered" gravitational waves when looking for an approximate solution to his field equations [5], and two years later he derived the quadrupole formula for the generation of gravitational waves [59]. Some contemporary physicists saw them as a coordinates' artefact, Einstein himself changed his mind many times, and the physical reality of these waves was the object of a controversy that lasted until the late 1950's, when it was shown that they carry energy and angular momentum and do have a physical meaning [60, 61, 62]. Crucially, a few years later, Hulse and Taylor observed for the first time a pulsar in a binary system [63]. Evolving in the strong field regime, this system allowed us to perform unprecedented tests of general relativity. By following its evolution over many years it was possible to measure the predicted decay of the orbital period due to gravitational radiation [4], and additional binary pulsar systems complemented this remarkable observation along the years [64, 65]. The final proof for the existence of gravitational waves came with their direct detection by the LVC in 2015 [3], which was awarded with the Nobel prize in 2017.

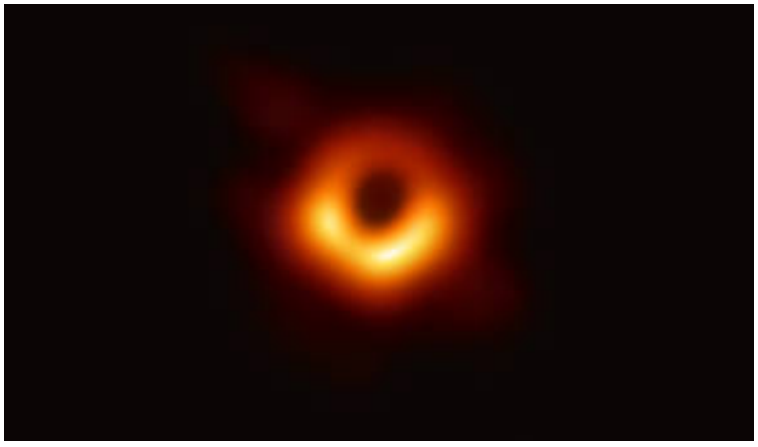

Figure 1.2: Shadow of M87*, the massive black hole at the centre of the M87 galaxy. The dark central part corresponds to the region where photons cannot escape the gravitational attraction of the black hole and are absorbed. Thus, no light can be emitted from this region. This fist "image" of a black hole is in very good agreement with the general relativity prediction for the shadow of a black hole. Credits: Event Horizon Telescope collaboration.

GW150914 has also been considered to be the first direct observation of black holes, almost one century after Schwarzschild derived its famous solution to Einstein's equations [66]. This solution, obtained for the exterior metric of a spherical symmetric star of mass m in vacuum, predicted the existence of a "horizon" beyond which the escape velocity is higher than the speed of light. Remarkably, the same result can be obtained in Newtonian mechanics, and astronomer Michell had already postulated the existence of "dark stars" in 1783 [67]. For a horizon to exist, the star's radius must be smaller than the *Schwarzschild radius*, $2Gm/c^2$. For a star of same mass as the Sun, this is equal to ~ 3 km, less than the radius of Paris! Therefore, it was thought that no such object could exist, and that the horizon was nothing but a mathematical curiosity. In the 1930's, work by Chandrasekhar [68], Tolman, Oppenheimer and Volkoff [69, 70] suggested that such objects could form from

the gravitational collapse of stars too massive to end as white dwarves or neutron stars. The first observational evidence came in the 1960's, with the first observation of a quasar [71] and the understanding that an accreting "black hole", a denomination popularised by Wheeler in that same decade, provided the best explanation [72]. By the same time, Kerr derived his metric for axisymmetric spacetime [73], and work by Hawking and Penrose provided theoretical motivation for the existence of black holes [74]. The latter was awarded with the Nobel prize in 2020 for his work on black holes. The prize was shared with Ghez and Genzel whose observations of the motion of stars at the centre of the Milky Way allowed us to infer the existence of a massive black hole of $\sim 4 \times 10^6 M_\odot$ at the centre of our galaxy, Sagittarius A* [75, 76]. These observations helped unveil the mystery on the nature of the massive objects at the centre of galaxies, and were complemented by the GRAVITY collaboration in the past few years [77]. Soon after the first LIGO/Virgo detection, the Event Horizon Telescope collaboration published the first "image" of a black hole, shown in figure 1.2, by reconstructing the shadow of the massive object at the centre of the M87 galaxy [78]. They obtained a very good agreement with the general relativity prediction for the shadow of a black hole.

The electromagnetic observation of black holes is very challenging because it requires the presence of some sort of matter (stars, gas) around them, unlike gravitational wave observations. Thus, black holes are finally starting to show themselves to us, and gravitational wave astronomy provides us powerful means to better understand the properties of these still very mysterious objects and of the underlying theory of gravity, as we will argue in this manuscript.

Following this brief historical review, we give a short introduction to gravitational waves: their theoretical description, within general relativity and then in modified gravity theories, the main sources of gravitational waves and the detection principle. In the remaining of this manuscript, Greek indices run from 0 to 3 and Latin indices from 1 to 3. The notation ∂_μ (∂^μ) denotes partial derivation of a quantity with respect to x^μ (x_μ). We work in units of $G = c = 1$. The detailed steps for the derivation of the results presented in the next section can be found in classical textbooks [46, 47, 48].

1.2 Theory of gravitational waves

Gravitational waves are often called "ripples of spacetime " because they appear as a perturbation propagating on top of a background geometry. Let us start from a flat background, described by a Minkowskian metric $\eta_{\mu\nu} = (-1, 1, 1, 1)$, and add a perturbation $h_{\mu\nu}$ such that the total metric is given by

$$g_{\mu\nu} = \eta_{\mu\nu} + h_{\mu\nu}. \tag{1.3}$$

We will work to linear order in $h_{\mu\nu}$. The covariance principle ensures that the laws of physics are the same in any coordinate system, therefore we can choose a specific one where Einstein's field equations take a simpler form. When transforming from a coordinate system x^μ to x'^μ, the metric transforms as $g'_{\mu\nu} = \partial_\mu x'^\alpha \partial_\nu x'^\beta g_{\alpha\beta}$. Applying this to the metric given by equation (1.3) for an infinitesimal transformation $x^{\mu\prime} = x^\mu + \zeta^\mu$, and keeping only terms linear in ζ, we get $h'_{\mu\nu} = h_{\mu\nu} - (\partial_\mu \zeta_\nu + \partial_\nu \zeta_\mu)$. Therefore, by choosing the appropriate transformations, we can work in a *harmonic* gauge, where $h_{\mu\nu}$ is divergenceless (to linear order in

the perturbations the covariant derivative is simply the partial derivative):

$$\partial_\nu h^{\mu\nu} = 0. \tag{1.4}$$

Then, by computing the Christoffel symbols and the Ricci tensor for this metric, keeping only terms linear in $h_{\mu\nu}$, we obtain the linearised Einstein's equations

$$\Box_\eta \bar{h}_{\mu\nu} = -16\pi T_{\mu\nu}, \tag{1.5}$$

where $\bar{h}_{\mu\nu} = h_{\mu\nu} - \frac{1}{2}\eta_{\mu\nu}h$, $h = \eta^{\mu\nu}h_{\mu\nu}$ and $\Box_\eta = \eta^{\mu\nu}\partial_\mu\partial_\nu$ is the flat d'Alembert operator. Thus, we find that $\bar{h}_{\mu\nu}$ follows the equation for a wave propagating at the speed of light, sourced by the stress-energy field.

1.2.1 Propagation in vacuum

Transverse-traceless gauge

Let us consider a wave propagating in vacuum ($T_{\mu\nu} = 0$). After imposing the harmonic gauge condition, we still have the freedom to impose four constraints on $h_{\mu\nu}$ by considering infinitesimal coordinates transformations $x^{\mu\prime} = x^\mu + \zeta^\mu$ such that $\Box_\eta \zeta_\mu = 0$. In vacuum, we can impose $h_{0,i} = h^\mu{}_\mu = 0$. Imposing these conditions defines the *transverse-traceless* gauge (denoted by TT). Together with equation (1.4), this implies $\partial_0 h^{00} = 0$, and we can set $h_{00} = 0$, since time independent terms do not affect the propagation of a wave. In the transverse-traceless frame, a gravitational wave propagating along the $\hat{\mathbf{z}}$-axis can be written as

$$h^{\mathrm{TT}}_{\mu\nu} = \begin{pmatrix} 0 & 0 & 0 & 0 \\ 0 & h_+ & h_\times & 0 \\ 0 & h_\times & -h_+ & 0 \\ 0 & 0 & 0 & 0 \end{pmatrix}_{\mu\nu} \cos(\omega(t-z)), \tag{1.6}$$

where $\omega/2\pi$ is the frequency of the wave. Similarly to electromagnetic waves, gravitational waves can have two polarisation states, usually denoted by h_+ and $h_\times$. In the more general case of a wave travelling in a direction $\hat{\mathbf{n}}$, expressed in some coordinate system, we can transform it into the transverse-traceless gauge by use of projection operators:

$$h^{\mathrm{TT}}_{ij} = \Lambda_{ij,kl} h_{kl}, \tag{1.7}$$

$$\Lambda_{ij,kl} = P_{ik}P_{jl} - \frac{1}{2}P_{ij}P_{kl}, \tag{1.8}$$

$$P_{ij} = \delta_{ij} - n_i n_j. \tag{1.9}$$

Physical effect of gravitational waves

Let us now describe the effect of gravitational waves on test particles. For definiteness, we consider a wave propagating in the $\hat{\mathbf{z}}$ direction. For a particle initially at rest, $\frac{\mathrm{d}x^\mu}{\mathrm{d}\tau}\big|_{\tau=0} = \delta^{\mu 0}$, and the geodesic equation reads

$$\left.\frac{\mathrm{d}^2 x^\mu}{\mathrm{d}\tau^2}\right|_{\tau=0} = -\Gamma^\mu_{00}. \tag{1.10}$$

$$\tag{1.11}$$

At linear order in $h_{\mu\nu}$, $\Gamma^\mu_{00} = \frac{1}{2}(2\partial_0 h^\mu{}_0 - \partial^\mu h^{00})$. In the transverse-traceless frame, all the terms inside the parenthesis are zero, so $\Gamma^\mu_{00} = 0$. Therefore, particles initially at rest will still be at rest a moment later, and the same argument applies later on. Thus, the transverse-traceless frame is "comoving" with the wave.

Now, let us consider a gauge invariant quantity: the proper distance. Consider two particles at a distance L_0 in the absence of any gravitational wave. For simplicity, we take them to be along the $\hat{\mathbf{x}}$-axis in the transverse-traceless frame, at $z = 0$, and suppose that L_0 is much smaller than the length scale on which the gravitational wave varies. The distance L between the two test particles when the gravitational wave passes can be computed as

$$\begin{aligned} L &= \left[g_{\mu\nu}\Delta x^\mu \Delta x^\nu\right]^{1/2} \\ &= \left[(\eta_{11} + h_{11})\Delta x^1 \Delta x^1\right]^{1/2} \\ &= L_0 \left[1 + \frac{h_+ \cos(\omega t)}{2}\right], \end{aligned} \tag{1.12}$$

where in the last line we performed a Taylor expansion. Thus, we see that the gravitational wave makes the distance between the test particles vary as

$$\frac{\Delta L}{L} = \frac{h_+ \cos(\omega t)}{2}. \tag{1.13}$$

It is this variation in distance, induced by their passage, that allows us to detect gravitational waves, as we will see in section 1.5.

Effect on a ring of test particles

Finally, in order to understand the meaning of the two different polarisation states, let us consider the effect of this same gravitational wave on a ring of test particles initially lying in the $z = 0$ plane. We call O the centre of the ring, and assume that the ring of particles is small enough so that we can work in an inertial frame attached to O (i.e. smaller than the length scale on which the gravitational wave varies), defining $t = 0$ as the moment the gravitational wave reaches O. We parametrise the test particles on the ring by their spatial coordinates relative to O in that frame, ξ^i. Given an initial condition ξ^i_0 at $t = 0$, the evolution of ξ^i as the gravitational wave passes by is driven by the equation of geodesic deviation:

$$\frac{\mathrm{D}^2\xi^i}{\mathrm{D}\tau^2} = -R^i_{\nu\rho\sigma}\xi^\rho \frac{\mathrm{d}x^\nu}{\mathrm{d}\tau}\frac{\mathrm{d}x^\sigma}{\mathrm{d}\tau}, \tag{1.14}$$

where $\frac{\mathrm{D}\xi^i}{\mathrm{D}\tau}$ is the covariant derivative of ξ^i along the worldline of the particle. In this local inertial frame, all Christoffel symbols vanish, so the covariant derivative is the regular partial derivative with respect to proper time. Moreover, working at linear order in the perturbations $h_{\mu\nu}$ to flat spacetime, the Riemann tensor is a gauge invariant quantity, so we can use its expression in any frame to evaluate equation (1.14), in particular in the transverse-traceless frame, where it takes a simple form. Last, for test particles initially at rest we have $\frac{\mathrm{d}x^\nu}{\mathrm{d}\tau} = \delta^{\nu 0}$. We then get

$$\ddot{\xi}^i = \frac{1}{2}\ddot{h}^{\mathrm{TT}}_{ij}\xi^j. \tag{1.15}$$

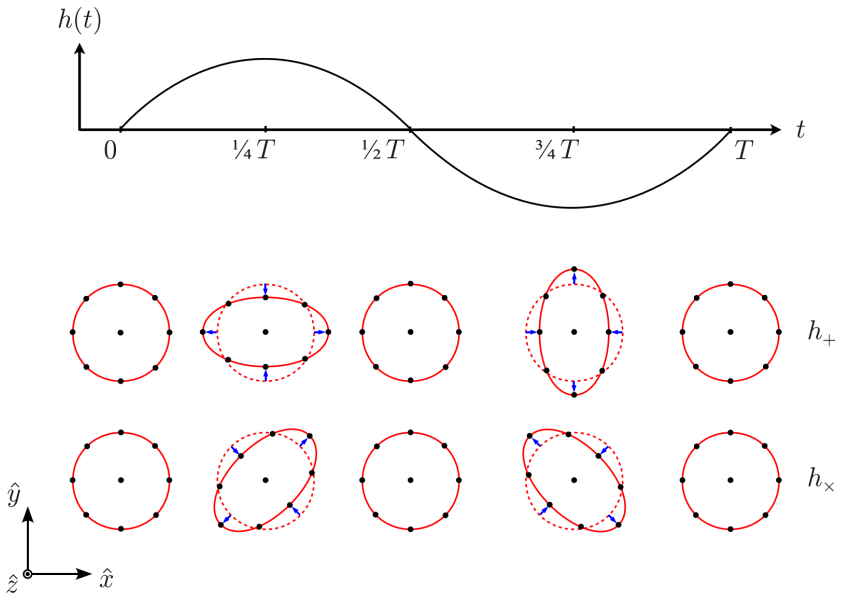

Figure 1.3: Effect of a monochromatic gravitational wave on a ring of test particles lying in a plane transverse to its direction of propagation. $T = 2\pi/\omega$ is the period of the wave. The effect of each polarisation state is shown separately. Extracted from [79].

For weak displacements, a solution to equation (1.15) at linear order in $h_{\mu\nu}$ is given by

$$\xi^x = \xi_0^x + \frac{1}{2}h_+ \cos(\omega t)\xi_0^x + \frac{1}{2}h_\times \cos(\omega t)\xi_0^y, \tag{1.16}$$

$$\xi^y = \xi_0^y + \frac{1}{2}h_\times \cos(\omega t)\xi_0^x - \frac{1}{2}h_+ \cos(\omega t)\xi_0^y, \tag{1.17}$$

$$\xi^z = 0. \tag{1.18}$$

Note that in this locally inertial frame $g_{\mu\nu} = \eta_{\mu\nu} + \mathcal{O}(x^\mu x^\nu)$, so coordinate distances do correspond to proper distances, and equation (1.16) yields the same result as equation (1.13). Moreover, these equations show that gravitational waves induce a displacement only in the plane transverse to their direction of propagation.

Let us now consider the effect of each polarisation individually. First, consider the case $h_+ \neq 0$ and $h_\times = 0$. The displacement is then given by

$$\xi^x = \xi_0^x \left(1 + \frac{1}{2}h_+ \cos(\omega t)\right), \tag{1.19}$$

$$\xi^y = \xi_0^y \left(1 - \frac{1}{2}h_+ \cos(\omega t)\right). \tag{1.20}$$

$$\tag{1.21}$$

We see that first ξ^x increases while ξ^y decreases, and then the opposite. Therefore, as the gravitational wave travels through it, the ring of test particles will successively be stretched in the $\hat{\mathbf{x}}$ and $\hat{\mathbf{y}}$ direction, as illustrated in figure 1.3. Next, consider the case $h_\times \neq 0$ and

$h_+ = 0$. It is helpful to define $\xi'^{x,y} = \frac{1}{\sqrt{2}}(\xi^x \pm \xi^y)$. These new coordinates verify

$$\xi'^x = \xi'^x_0 + \frac{1}{2} h_\times \cos(\omega t) \xi'^x, \tag{1.22}$$

$$\xi'^y = \xi'^y_0 - \frac{1}{2} h_\times \cos(\omega t) \xi'^x, \tag{1.23}$$

$$\tag{1.24}$$

which are similar to equations (1.19) and (1.20). Since the primed coordinates are related to the original ones by a simple rotation of $\pi/4$ around the $\hat{\mathbf{z}}$-axis, we see that the effect of the $\times$ polarisation is to stretch the ring of test particles along axes rotated by $\pi/4$ with respect to the original $\hat{\mathbf{x}}$ and $\hat{\mathbf{y}}$-axis, as illustrated in figure 1.3.

It is now easy to understand that the names of the individual polarisations come from the deformation patterns each of them induces. In the general case, gravitational waves are a superposition of these two polarisation states. When writing equation (1.6), we implicitly choose a basis in the plane orthogonal to the direction of propagation. If we rotate this basis by an angle ψ around the direction of propagation, the polarisations transform as

$$h'_+ = h_+ \cos(2\psi) - h_\times \sin(2\psi) \tag{1.25}$$

$$h'_\times = h_+ \sin(2\psi) + h_\times \cos(2\psi) \tag{1.26}$$

The relative angle between the basis in which the polarisations of a gravitational wave are computed (the so called "radiative frame") and the one used to measure the wave is called the polarisation angle.

1.2.2 Generation

Quadrupole formula

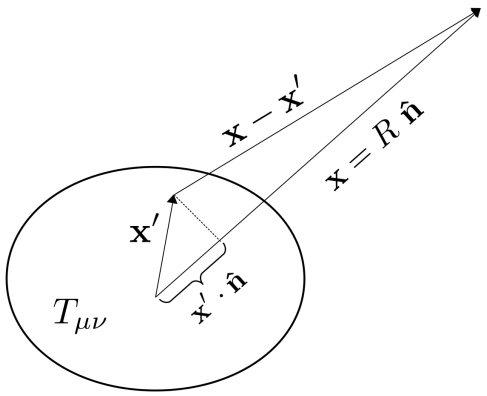

Figure 1.4: Graphical illustration of the gravitational wave source. Adapted from [48].

Let us now turn to the generation of gravitational waves. Consider some matter distribution, described by a stress-energy tensor $T_{\mu\nu}$, and attach a coordinate system x^μ to an observer far from the source (i.e. at a distance much larger than the typical length scale of

the source), as illustrated in figure 1.4. We can solve equation (1.5) using the method of Green's function, and get

$$\bar{h}_{\mu\nu}(t,\mathbf{x}) = 4\int \mathrm{d}^3\mathbf{x}' \frac{1}{|\mathbf{x}-\mathbf{x}'|} T_{\mu\nu}(t-|\mathbf{x}-\mathbf{x}'|,\mathbf{x}'). \tag{1.27}$$

The integral is performed over the whole space, but $T_{\mu\nu}$ is assumed to be nonzero only in a limited region. Since the observer is far from the source, $|\mathbf{x}-\mathbf{x}'| \sim |\mathbf{x}| - \mathbf{x}'\cdot\hat{\mathbf{n}} = R - \mathbf{x}'\cdot\hat{\mathbf{n}}$ where R is the distance to the source and $\hat{\mathbf{n}}$ is a unit vector pointing in its direction. Then, as in electromagnetism, we can perform an expansion of the source term around $t-R$, leading to a multipolar expansion with mass and current moments. To the lowest order, using the conservation of the stress-energy tensor ($\nabla_\mu T^{\mu\nu} = 0$), we obtain the quadrupole formula

$$h_{ij}^{\mathrm{TT}} = \frac{2}{R}\ddot{Q}_{ij}^{\mathrm{TT}}(t-R/c), \tag{1.28}$$

where Q_{ij} is the quadrupole moment defined as

$$Q^{ij} = \int \mathrm{d}^3x\ T^{00}(t,\mathbf{x})(x^i x^j - \frac{1}{3}\delta^{ij}x^2), \tag{1.29}$$

and Q_{ij}^{TT} is the transverse-traceless part of it, obtained by using the projection operator defined in equation (1.8). In the full multipolar expansion, factors of v^2 establish a hierarchy between the successive terms, v being the characteristic velocity within the source (in units of c).

Just like electromagnetic waves, gravitational ones carry energy and angular momentum, which are extracted from the source. Within the quadrupole approximation, the radiated power and angular momentum are given by

$$P_{\mathrm{GW}} = \frac{1}{5} < \dddot{Q}_{ij}\dddot{Q}_{ij} >, \tag{1.30}$$

$$\dot{J}^i_{\mathrm{GW}} = \frac{2}{5}\varepsilon^{ikl} < \ddot{Q}_{ka}\dddot{Q}_{la} >, \tag{1.31}$$

where ε^{ikl} is the fully antisymmetric Levi-Civita tensor and $<>$ denotes average over one characteristic time scale of the source. An important property that can be read from these equations is that stationary distributions do not emit gravitational waves.

Let us comment on the absence of dipole radiation in general relativity. The dipole moment reads

$$D^i = \int \mathrm{d}^3x\ T^{00}(t,\mathbf{x})x^i. \tag{1.32}$$

In the Newtonian limit, for a set of point-like masses m_a, $T^{00}(t,\mathbf{x}) = \sum_a m_a\delta^{(3)}(\mathbf{x}-\mathbf{x_a}(t))$ and the dipole moment becomes

$$D^i = \sum_a m_a x_a^i(t). \tag{1.33}$$

We have seen that the gravitational wave emission is related to the second derivative of moments, and from Newton's second law: $\ddot{D}^i = \sum_a m_a \ddot{x}_a^i(t) = 0$ for an isolated system. A similar calculation shows that mass conservation implies that there is no monopole radiation neither, just as it is forbidden in electromagnetism because Maxwell's equations imply the conservation of the electric charge.

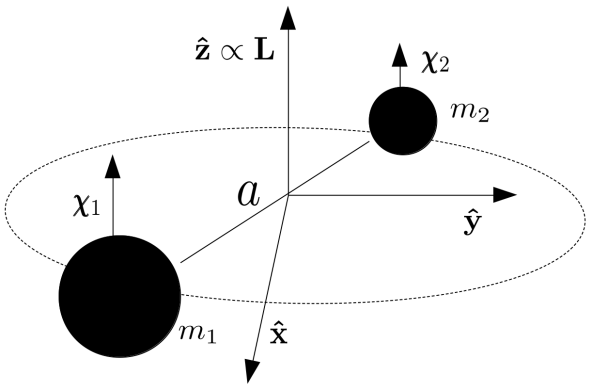

Figure 1.5: Schematic representation of a BBH on a quasicircular orbit. We adopt the convention $m_1 \geq m_2$, and focus on the case where the spins of the black holes ($\boldsymbol{\chi_1}$ and $\boldsymbol{\chi_2}$) are aligned or anti-aligned with the orbital angular momentum $\mathbf{L}$.

Black hole binaries

To give a concrete example, let us consider one of the main sources of gravitational waves, of particular importance in the context of this thesis: a coalescing BBH. The specific configuration we are interested in is illustrated in figure 1.5. m_1 and m_2 are the masses of the black holes, $M = m_1 + m_2$ is the total mass, $\mu_{\rm red} = m_1 m_2 / M$ the reduced mass and $q = m_1/m_2 \geq 1$ the mass ratio. We will need two additional mass combinations: the symmetric mass ratio $\eta = \mu_{\rm red}/M$ and the chirp mass $\mathcal{M}_c = (m_1^3 m_2^3/(m_1+m_2))^{1/5} = M\eta^{3/5}$. For easier reference, in table 1 we list the parameters used throughout this manuscript, together with their explicit expressions. Some of these combinations will be introduced later in the manuscript. We focus on a circular binary, and attach an orthonormal basis to it, taking the axis around which the binary rotates to be the third component of the basis. The dimensionless black hole spins ($\boldsymbol{\chi_1}$ and $\boldsymbol{\chi_2}$) do not enter at the first order approximation considered in this section.

In the Newtonian description, noting a the relative separation of the bodies, the total energy of the system is

$$E_{\rm tot} = -\frac{m_1 m_2}{2a}. \tag{1.34}$$

Moreover, Kepler's third law tells us that

$$\omega_{\rm orb} = \sqrt{M/a^3}, \tag{1.35}$$

where $\omega_{\rm orb}$ is the orbital angular velocity. Let us now compute the gravitational waves emitted in a direction $\hat{\mathbf{n}}$ by this system. We note ι and φ the polar and azimuthal angles of $\hat{\mathbf{n}}$ in the basis attached to the binary. The angle ι is called the inclination of the source. The geodesic equation is used to obtain the trajectory of the black holes, which at first order is Keplerian. Using the point-particle approximation, as for the dipole moment in the previous

section, the quadrupole formula (equation (1.28)) yields

$$h_+ = \frac{4\mathcal{M}_c}{R}\left(\mathcal{M}_c\omega_{\rm orb}\right)^{2/3}\frac{1+\cos^2(\iota)}{2}\cos(2(\omega_{\rm orb}t+\varphi)), \tag{1.36}$$

$$h_\times = \frac{4\mathcal{M}_c}{R}\left(\mathcal{M}_c\omega_{\rm orb}\right)^{2/3}\cos(\iota)\sin(2(\omega_{\rm orb}t+\varphi)), \tag{1.37}$$

where we used our freedom in the definition of initial time and phase to cancel the R term in the argument of sin and cos. Hence, at zeroth order, a binary system emits monochromatic gravitational waves at twice its orbital frequency, i.e. $f = \omega_{\rm orb}/\pi$.

It is necessary to account for the backreaction of gravitational waves, which extract energy of the system. From equations (1.29) and (1.30), the radiated power is $P_{\rm GW} = \frac{32}{5}\omega_{\rm orb}^6\mu_{\rm red}a^2$. Here, the relevant time scale for averaging is the orbital period of the binary. Together with Kepler's third law, the energy balance equation $\dot{E}_{\rm tot} = -P_{\rm GW}$ gives a differential equation for $\omega_{\rm orb}$,

$$\dot{\omega}_{\rm orb} = \frac{96}{5}\omega^{11/3}\mathcal{M}_c^{5/3}. \tag{1.38}$$

Using the angular momentum balance equation yields the same equation. The solution can be written as

$$\mathcal{M}_c\omega_{\rm orb}(t) = \left(\frac{5\mathcal{M}_c}{256(t_{\rm c}-t)}\right)^{3/8}, \tag{1.39}$$

where t_c is a (finite) time, which measures the time remaining to coalescence for given initial conditions, and at which the orbital angular velocity diverges (at the first order approximation we work in). From Kepler's third law, we see that the separation of the binary decreases due to emission of gravitational waves, and according to these results it would go to zero in a finite time. The binary is then said to be "quasicircular". The gravitational waves emitted by the system become

$$h_+ = \frac{4\mathcal{M}_c}{R}\left(\mathcal{M}_c\omega_{\rm orb}(t)\right)^{2/3}\frac{1+\cos^2(\iota)}{2}\cos\left(2(\phi_{\rm orb}(t)+\varphi)\right), \tag{1.40}$$

$$h_\times = \frac{4\mathcal{M}_c}{R}\left(\mathcal{M}_c\omega_{\rm orb}(t)\right)^{2/3}\cos(\iota)\sin\left(2(\phi_{\rm orb}(t)+\varphi)\right), \tag{1.41}$$

where $\phi_{\rm orb}(t) = \phi_c - \int_t^{t_c}\omega_{\rm orb}(t)\mathrm{d}t$ and ϕ_c is the phase at coalescence. Hence, the amplitude of gravitational waves increases as the orbit tightens.

Although our results do predict the qualitative behaviour of the binary correctly, they are valid only when the black holes are far apart, and cannot be used to describe the whole evolution of the binary. In reality, the orbit tightens during the so called *inspiral* regime, but the black holes *merge* and form a perturbed black hole before reaching a zero separation. The latter relaxes to a steady Kerr black hole by emitting gravitational waves, during the *ringdown* stage. The evolution of the binary and the gravitational wave signal are illustrated in figure 1.6. Although three different regimes are clearly distinguishable, there is no sharp transition between them. Inspired by the motion of test masses around black holes, one possibility is to define the inspiral-merger transition as the moment the binary reaches the *innermost stable circular orbit* (ISCO). Following the effective-one-body (EOB) approach (see section 1.2.3 below), we can map the spacetime of the binary when it is about to merge

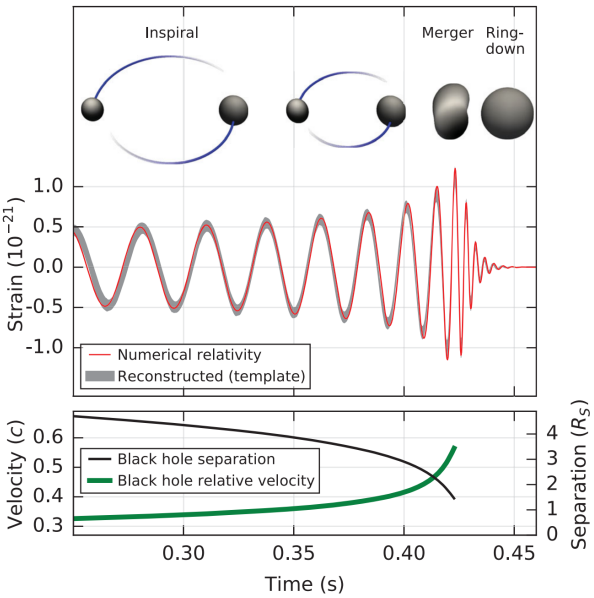

Figure 1.6: Schematic representation of the first gravitational wave event, GW150914. The upper panel shows the theoretical and the reconstructed gravitational wave signal, in red and gray respectively. The lower panel shows the evolution of the separation and the velocity as the evolution proceeds. Extracted from [3].

to the one of the final black hole, with mass $\sim M$ (part of the mass is emitted in the form of gravitational waves). The ISCO is the closest distance at which a massive test particle can orbit a black hole, and below it the *plunge* ensues. As an approximation, we can use its value for the Schwarzschild metric ($6M$) and from Kepler's law, we get an estimate of the merger frequency

$$f_{\rm merger} \sim \frac{1}{\sqrt{6}\pi M}. \tag{1.42}$$

Interestingly, the start of the ringdown phase has been the subject of much debate recently. It is usually measured with respect to the peak in the amplitude of the gravitational wave signal, but authors disagree on how long after the peak (from 0 to 15 M) and how to perform the matching to the inspiral-merger signal [80, 81, 82, 83].

Before moving to the next section, let us define the number of cycles in the gravitational wave signal, $\mathcal{N}$. Over a small amount of time, the fraction of cycle in the signal is $\mathrm{d}\mathcal{N} = f\mathrm{d}t$. Thus, the total number of cycles in the gravitational wave signal when evolving from $f_{\rm min}$ to $f_{\rm max}$ is

$$\mathcal{N} = \int_{f_{\rm min}}^{f_{\rm max}} \frac{f}{\dot{f}} \mathrm{d}f. \tag{1.43}$$

As an approximation, we use can use equation (1.39), and get

$$\mathcal{N} = \frac{1}{32\pi} \left[(\pi \mathcal{M}_c f_{\rm min})^{-5/3} - (\pi \mathcal{M}_c f_{\rm max})^{-5/3} \right]. \tag{1.44}$$

1.2.3 Waveform approximants

In order to extract the maximum information from gravitational wave observations, it is necessary to have accurate theoretical models that we can compare with. We will now discuss how realistic signals (waveforms) for BBHs are computed, focusing on quasicircular binaries with moderate mass ratio ($q \lesssim 20$) and component spins aligned (or anti-aligned) with the orbital angular momentum (without precession). A gravitational wave signal emitted in the direction $\hat{\mathbf{n}}$ can be decomposed in spin-weighted spherical harmonics as

$$h_+ - ih_\times = \sum_{l\leq 2}\sum_{m=-l}^{l} {}_{-2}Y_{lm}(\iota,\varphi)h_{lm}. \tag{1.45}$$

The expression of the ${}_{-2}Y_{lm}(\iota,\varphi)$ can be found in [84]. The (l,m) harmonic is emitted at m times the orbital frequency of the binary. For nonprecessing binaries, we have $h_{l,-m} = (-1)^l h^*_{lm}$. There is a hierarchy between the harmonics: the dominant term is the $(2,\pm 2)$ harmonic, which corresponds to the quadrupole term, and higher harmonics are suppressed by factors of v and $\delta_m = (m_1 - m_2)/M$. However, higher harmonics can be important, in particular near the merger and for highly asymmetric systems (asymmetric in masses and/or spins).

In the following, it will be convenient to work with the Fourier-transform of the signal

$$\tilde{h}_{lm}(f) = \int_{-\infty}^{+\infty} h_{lm}(t)e^{2i\pi ft}\mathrm{d}t \tag{1.46}$$

$$= A_{lm}(f)e^{-i\Psi_{lm}(f)}. \tag{1.47}$$

The Fourier-transform can be approximated using the stationary phase approximation [85, 86, 87]. Writing $h_{lm}(t) = \hat{A}_{lm}(t)e^{-im\phi_{\rm orb}(t)}$, where the hat serves to indicate that it is the time domain amplitude, we have

$$\tilde{h}_{lm}(f) = \int_{-\infty}^{+\infty} \hat{A}_{lm}(t)e^{2i\pi ft - im\phi_{\rm orb}}\mathrm{d}t. \tag{1.48}$$

The main contribution to the integral comes from the stationary points, i.e. where the derivative of the phase of the integrand vanishes: $\dot{\phi}_{\rm orb}(t) = 2\pi f/m$. This defines an equation on t, of which we note t_f the solution (the solution exists only for positive f, since $\dot{\phi}_{\rm orb} = \omega_{\rm orb} > 0$). By expanding the phase of the integrand around the stationary point up to second order, and taking the amplitude to be a slowly varying function of time, we get

$$\tilde{h}_{lm}(f) = \hat{A}_{lm}(t_f)e^{2i\pi ft_f - im\phi_{\rm orb}(t_f)}\int_{-\infty}^{+\infty} e^{-i\frac{m}{2}\ddot{\phi}_{\rm orb}(t_f)(t-t_f)^2}\mathrm{d}t \tag{1.49}$$

$$= \sqrt{\frac{2\pi}{m\ddot{\phi}_{\rm orb}(t_f)}}\hat{A}_{lm}(t_f)e^{2i\pi ft_f - im\phi_{\rm orb}(t_f) - i\frac{\pi}{4}}. \tag{1.50}$$

Finally, we can write

$$t_f = t_c - \int_f^{+\infty} \frac{1}{\dot{f}'} \mathrm{d}f', \tag{1.51}$$

$$\phi_{\mathrm{orb}} = \phi_c - \frac{2\pi}{m} \int_f^{+\infty} \frac{f'}{\dot{f}'} \, \mathrm{d}f', \tag{1.52}$$

$$f = \frac{m\omega_{\mathrm{orb}}}{2\pi}. \tag{1.53}$$

Once we solve for the dynamics of the binary, we can plug-in the expressions for the time domain phase and amplitude in the above equations to get the Fourier domain signal.

As the black holes get closer, non-linear terms in $h_{\mu\nu}$ become important, and need to be properly accounted for in Einstein's equations. Moreover, corrections to the Newtonian equations of motion need to be taken into account [88, 89]. This is done through the post-Newtonian (PN) formalism [84], where the solution is computed iteratively as an expansion in powers of v, the latter being the velocity of the binary. This approach is valid as long as v is "small" (in units of c). Terms at nPN order are suppressed by a factor v^{2n} relative to the leading order solutions, equations (1.35), (1.39), (1.41) and (1.40). Using the stationary phase approximation, we obtain a Fourier-domain post-Newtonian expansion of the gravitational wave signal. For the (2,2) harmonic, it reads

$$\begin{aligned}\Psi_{22}(f) = &- \Big[2\pi f t_c - 2\phi_c - \frac{\pi}{4} \\ &+ \frac{3}{128}(\pi\mathcal{M}_c f)^{-5/3} \sum_i \Psi_i^{22} (\pi\mathcal{M}_c f)^{i/3} + \Psi_{L,i}^{22} (\pi\mathcal{M}_c f)^{i/3} \ln(\pi\mathcal{M}_c f) \Big], \end{aligned} \tag{1.54}$$

$$A_{22}(f) = \sqrt{\frac{2}{3}} \frac{\mathcal{M}_c^2}{R} \sum_i A_i^{22} (\pi\mathcal{M}_c f)^{i/3}, \tag{1.55}$$

Terms with a power $(\pi\mathcal{M}_c f)^{2n/3}$ relative to the leading order term correspond to the nth-PN order. The coefficients Ψ_i^{22}, $\Psi_{L,i}^{22}$ and A_i^{22} are functions of the black holes spins and the mass ratio (see, e.g., [84]), and we have $\Psi_0^{22} = 1$, $\Psi_{L,0}^{22} = 0$. These expressions put in evidence a very important property: $h/\mathcal{M}_c$ and $\tilde{h}/\mathcal{M}_c^2$ are, respectively, functions of $t/\mathcal{M}_c$ and $\mathcal{M}_c f$ only. This is a consequence of general relativity not having any preferred mass scale, and allows us to factor out the mass when doing analytical and numerical computations. Moreover, this implies that the frequencies of the gravitational waves emitted by a system decrease with the chirp mass. The post-Newtonian formalism provides an accurate description of the inspiral, but breaks down when the black holes are about to merge, using Kepler's law we can estimate that $v \sim 0.4$ at the ISCO.

The last stage of the evolution, the ringdown, can be described by linear perturbation theory [90, 91]. The signal is well approached by a sum of damped sinusoids, with frequency and damping times given by the quasinormal modes of the final black hole [92]. As for the merger, numerical simulations are needed to solve Einstein's equations [93]. Due to the extraordinary mathematical complexity of this problem, it is only since 2005 that we are able to solve the full Einstein's equations [94, 95, 96]. In principle numerical simulations

could be used to obtain the full gravitational wave signal for any binary, but, so far, they are too computationally expensive to be extended to the early inspiral, and to be used in data analysis pipelines. The longest numerical waveform to date has 350 cycles and took 8 months to run [97]. Using equations (1.44) and (1.42) we can estimate that a MBHB of individual masses $10^5\ M_\odot$ entering the LISA frequency band at 10^{-4} Hz will spend $\sim 10^4$ cycles in band before merging. Moreover, millions of waveform evaluations are needed for data analysis. Thus, we need to resort to waveform approximants.

Time domain approximants

The EOB approach is a relativistic extension of the Newtonian treatment of the two bodies problem [98]. The Hamiltonian of the binary, which is expanded in a post-Newtonian series, is mapped to an effective Hamiltonian, describing a perturbed black hole and a test mass of mass $\mu_{\rm red}$ orbiting it through a canonical transformation. The same mapping is applied to the post-Newtonian expanded gravitational wave flux, in order to obtain the dissipative Hamilton's equations for the effective problem. We then solve for the dynamics of the test particle, which allows us to compute the gravitational wave signal emitted by the system. Remarkably, it allows us to solve for the waveform up to the merger [99], and quasinormal modes can then be attached to obtain the full signal [100, 101]. We can improve the accuracy of the model by including corrections due to the non-circularity of the orbit and calibrating unknown post-Newtonian terms in the expansion of the gravitational wave flux to numerical simulations [102, 103, 104].

A more recent class of approximants, surrogate models follow a different approach and interpolate between numerical relativity waveforms [105, 106]. The interpolants are extended to the early inspiral by hybridising with EOB waveforms [107]. Currently, these waveforms are available only up to mass ratio 8. Up to date, these are the most accurate waveforms.

Frequency domain approximants

The Phenom family of templates [108, 109, 110] follows a phenomenological approach to compute the frequency domain signal of BBHs. Of particular importance for this thesis, PhenomD [111, 112] provides the $(2, \pm 2)$ harmonic for quasicircular binaries with spins aligned (or anti-aligned) with the orbital angular momentum. The inspiral signal is given by equations (1.54) and (1.55) up to 3.5PN, with additional terms calibrated against Fourier-transformed EOB-extended numerical relativity waveforms. Phenomenological fits to these waveforms are used for the merger and the ringdown. PhenomHM [113] builds on PhenomD and uses the relative phases and amplitudes between the different harmonics and the $(2, \pm 2)$ one, obtained with post-Newtonian expansions and computations of quasinormal modes, to include the $(2, \pm 1)$, $(3, \pm 2)$, $(3, \pm 3)$, $(4, \pm 3)$ and $(4, \pm 4)$ harmonics for quasicircular binaries with aligned or anti-aligned spins. Although not derived from first principles, the Phenom templates have the advantage of being fast to compute, and thus they can be used to speed-up the data analysis.

Finally, to account for the expansion of the Universe, R has to be replaced by the luminosity distance D_L. An additional subtlety, is that the time and the frequency measured by

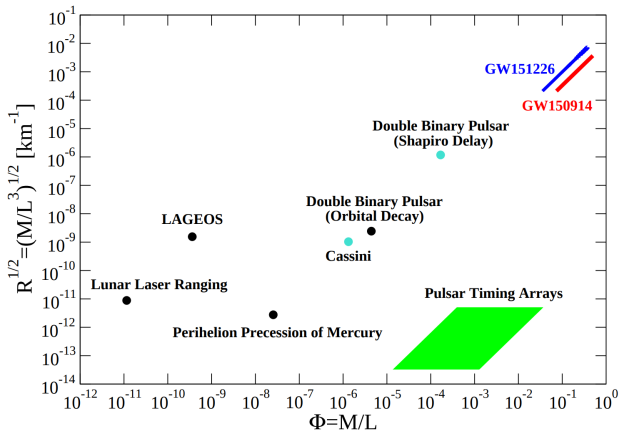

Figure 1.7: Diagram of the curvature-potential phase space, and the regime probed by different gravitational experiments. Gravitational waves probe a regime where both the curvature and the potential are strong, but also dynamical, as indicated by the finite range the lines of GW150914 and GW151226 (the second event [117]) swap. Extracted from [118].

an observer (obs) are related to the ones at the source (src) through the cosmological redshift: $\Delta t_{\rm obs} = (1+z)\Delta t_{\rm src}$ and $f_{\rm obs} = f_{\rm src}/(1+z)$. Since waveforms depend on t and f only through the combinations $t/\mathcal{M}_c$ and $\mathcal{M}_c f$, the cosmological redshift can be reabsorbed by defining redshifted (or detector-frame) masses $m_d = (1+z)m_s$, where m_s is the source-frame mass. The expression for the gravitational wave signal remains the same, but with redshifted time/frequency and masses. In the remaining of this paper, unless stated otherwise, m will be the detector frame mass, and we adopt the cosmology reported by the Planck mission (2018) [1].

So far we have discussed only the case of binaries made of black holes, which are objects with no internal structure. For binaries containing other objects, such as white dwarves or neutron stars, the same framework can be used to describe the inspiral, although additional energy loss channels could be present. For instance, in the case of BNSs and neutron star-black hole binaries, tidal effects lead to a correction starting at 5PN [114, 115, 116], which accelerates the evolution. When the bodies can no longer be treated as point particles, astrophysical mechanisms can radically modify the dynamics, and therefore the gravitational wave emission, as we will see in the case of mass-transferring binaries in chapter 5.

1.3 Gravitational waves in modified gravity theories

Although general relativity has been very successfully tested from Solar System to cosmological scales [52, 53, 54], the need to explain dark matter/dark energy and to have a unified theory of quantum gravity provide motivations to go beyond general relativity. As illustrated in figure 1.7, gravitational waves offer us the first opportunity to probe the strong field dynamical regime, where putative deviations from general relativity are expected to be stronger.

A standard path for building beyond general relativity theories is to modify the Einstein-

Hilbert action. Because of Lovelock's theorem [119, 120], general relativity is the only theory that can be derived from a local action containing up to second derivatives of the metric field in four dimensions. Therefore, any modified gravity theory built from an action must break one of these assumptions. We will briefly illustrate how gravitational waves differ in the Fierz-Jordan-Brans-Dicke theory [121, 122, 123], where an additional scalar field is introduced in the action. Although this theory is strongly constrained by Solar System experiments [124], it will provide us with a base to discuss beyond general relativity effects. The following results are extracted from [125] and [126], to which we refer for more details.

1.3.1 Fierz-Jordan-Brans-Dicke theory

The action for a generic scalar-tensor theory reads

$$\mathcal{S} = \frac{1}{16\pi}\int \mathrm{d}^4x\sqrt{-g}\left[(\Phi R - \omega(\Phi)\partial_\mu\Phi\partial^\mu\Phi\right] + \mathcal{S}_{\rm matter}(g_{\mu\nu}, \Upsilon_{\rm matter}), \tag{1.56}$$

where R is the Ricci scalar, Φ is a scalar field, $\omega(\Phi)$ is a scalar coupling and $\Upsilon_{\rm matter}$ stands for the matter fields. The Fierz-Jordan-Brans-Dicke theory is realised in the special case where the scalar coupling is constant, noted $\omega_{\rm BD}$. Within the Fierz-Jordan-Brans-Dicke theory, G is no longer a constant, it is given by $G = \Phi^{-1}(4+2\omega_{\rm BD})/(3+2\omega_{\rm BD})$. General relativity is recovered in the limit $\Phi \to cst$, $\omega_{\rm BD} \to +\infty$. Note that Φ does not enter the matter action so that the weak equivalence principle holds, i.e. the universality of free-fall is preserved [127]. Φ is said to be minimally coupled to matter. By varying the action with respect to the metric and the scalar field, we obtain the field equations for the Fierz-Jordan-Brans-Dicke theory:

$$R_{\mu\nu} - \frac{1}{2}R = 8\pi\Phi^{-1}T_{\mu\nu} + \omega_{\rm BD}\Phi^{-2}(\partial_\mu\Phi\partial_\nu - \frac{1}{2}g_{\mu\nu}\partial_\lambda\Phi\partial_\lambda) + \Phi^{-1}(\nabla_\mu\nabla_\nu\Phi - g_{\mu\nu}\Box\Phi), \tag{1.57}$$

$$\Box\Phi = \frac{8\pi}{3+2\omega_{\rm BD}}\left(T - 2\Phi\frac{\partial T}{\partial\Phi}\right), \tag{1.58}$$

where $T_{\mu\nu} = \frac{-2}{\sqrt{-g}}\frac{\partial\sqrt{-g}\mathcal{S}_{\rm matter}}{\partial g^{\mu\nu}}$ and $T = g^{\mu\nu}T_{\mu\nu}$.

For a system of gravitating point-like masses m_a, the matter action reads $\mathcal{S}_{\rm matter} = \sum_a \int \mathrm{d}\tau_a m_a$. If we now consider bodies of finite size, such as stars, the interior solution will depend on Φ. Since the equations for Φ are of second order, by imposing continuity the interior solution will depend on the value of the scalar field and its gradient outside the body. Thus, within the Fierz-Jordan-Brans-Dicke theory, the universality of free-fall does not apply to objects of finite size, and the strong equivalence principle is violated. It is the so called "Nordtvedt effect" [128, 129, 130]. This can be accounted for in the matter action by doing the replacement $m_a \to m_a(\Phi)$ [128]. The dependence of the mass on the scalar field is parametrised by the sensitivity $s_a = -\frac{\partial\ln(m_a)}{\partial\ln(\Phi)}|_{\Phi_0}$, where Φ_0 is the asymptotic value of the scalar field. A different way of understanding that the strong equivalence principle is violated is through the modified geodesic equation

$$\nabla_\nu T^{\mu\nu} = \frac{\partial T}{\partial\Phi}\partial^\mu\Phi. \tag{1.59}$$

The term on the left hand is actually the same as in general relativity, but the dependence of the stress-energy tensor of finite bodies on the scalar field leads to a (system dependent) "fifth force" that affects their trajectory.

For small perturbations, we can write $g_{\mu\nu} = \eta_{\mu\nu} + h_{\mu\nu}$, $\Phi = \Phi_0 + \Phi$. Defining $\tau_{\mu\nu} = h_{\mu\nu} - \frac{1}{2}h\eta_{\mu\nu} - (\Phi/\Phi_0)\eta_{\mu\nu}$, and imposing the gauge condition $\nabla_\mu \tau^{\mu\nu} = 0$, the field equations read:

$$\Box_\eta \tau^{\mu\nu} = -\frac{16\pi}{\Phi_0}\left(T^{\mu\nu} + t^{\mu\nu}\right), \tag{1.60}$$

$$\begin{aligned}\Box_\eta \Phi = &\frac{16\pi}{6+4\omega_{\rm BD}}\left(T - 2\Phi\frac{\partial T}{\partial \Phi}\right)\left(1 - \frac{1}{2}\tau - \frac{\Phi}{\Phi_0}\right) \\ &+ \left(\partial_\mu\partial_\nu \Phi \tau^{\mu\nu} + \frac{1}{\Phi_0}\partial_\mu \Phi \partial^\mu \Phi\right) + \mathcal{O}(\tau^3, \tau^2\Phi, \tau\Phi^2, \Phi^3),\end{aligned} \tag{1.61}$$

where $t^{\mu\nu}$ if a function of quadratic and higher-order in $\tau^{\mu\nu}$. Thus, we recover wave equations for $\tau_{\mu\nu}$ and Φ. To solve for the perturbations, the machinery described in the previous section can be applied, i.e. use the method of the Green function, and then perform a multipolar expansion, accounting for the modified geodesic equation. As expected, changes in the field equations lead to a different gravitational wave signal. In particular, from equation (1.59) it is clear that the stress-energy tensor of the point particles system is no longer conserved, and therefore, dipole radiation is allowed in the Fierz-Jordan-Brans-Dicke theory. For a binary system, its amplitude is proportional to $(s_1 - s_2)^2$, where s_i are the sensitivities of the objects. This distinctive prediction has been tested in binary pulsars, and failing to detect it has allowed us to place lower bounds on $\omega_{\rm BD}$ [128, 125, 131, 132, 133, 134] competitive with Solar System constraints obtained with the Cassini spacecraft [124]. On the other hand, owing to the "no-hair" theorem [135], all black holes have the same sensitivity ($\frac{1}{2}$), and dipole radiation is cancelled in BBHs. This powerful theorem states that black hole solutions (obtained by setting $T^{\mu\nu} = 0$) in the Fierz-Jordan-Brans-Dicke theory are identical to the ones in general relativity, and therefore, any stationary black hole is described by three quantities: its mass, angular momentum and electrical charge (the latter is believed to be zero for astrophysical black holes). The no-hair theorem has been demonstrated for the broader class of scalar-tensor theories [136], but recently it has been found that it could be circumvented in more involved theories (e.g. Einstein-dilaton-Gauss-Bonnet theories, Einstein-Maxwell-dilaton theories etc) [137, 138, 139, 140, 141, 142, 143], where they can even become significantly large ("nonperturbative") in specific situations [140, 141], and even in the Fierz-Jordan-Brans-Dicke theory if the assumption of asymptotic flatness is relaxed (e.g. due to cosmological boundary conditions or the presence of nearby matter) [144, 145, 146]. Binaries of "hairy" black holes emit a different gravitational wave signal with respect to the general relativity prediction, e.g. dipole emission is expected. Therefore, gravitational waves offer a unique possibility of identifying these extra hairs, and more broadly to discriminate between different theories of gravity, as we will see in chapter 4.

1.3.2 State of the art

In principle, the way of computing waveforms described in the previous section (post-Newtonian expansions for the inspiral, numerical simulations for the merger, quasinormal

modes for the ringdown) could be applied to any theory. However, even in the Fierz-Jordan-Brans-Dicke theory, the simplest extension to general relativity, the field equations are much more complicated, and so are gravitational wave computations, even for the inspiral. Moreover, the large number of candidate theories with no clear preference from data dilutes the efforts. Thus, only recently full numerical simulations of BBHs in modified gravity theories have become available, in scalar-tensor [144, 146], $f(R)$ [147], Einstein-Maxwell-dilaton [148], Einstein-dilaton-Gauss-Bonnet [149, 150], and dynamical Chern-Simons [151] theories. Similarly, quasinormal modes for gravitational perturbations have been computed only in Einstein-dilaton-Gauss-Bonnet [152, 153] and dynamical Chern-Simons [154, 155] theories. As for the inspiral, waveforms have been obtained up to 2PN for scalar tensor theories [156, 157], in the case of binaries where the components have no spin. We have provided the examples we are aware of, and the previous list might not be exhaustive. Nonetheless, it illustrates that very few results are available for waveforms beyond general relativity. An alternative is to consider phenomenological modifications to general relativity, which could be present in several theories, e.g. dipole radiation, and compute how the gravitational wave signal is modified. This will be further discussed in chapter 4.

Modified gravity theories also predict additional polarisation states, up to six states could exist. Intuitively, this corresponds to the dimensionality of the vectorial space formed by 3×3 symmetric matrices, to which the gravitational wave tensor belongs. For a discussion of the physical effect of the different polarisation states, see, e.g. [89]. Finally, compact objects other than black holes and neutron stars can also arise in modified gravity theories, we will say more on that in the next section.

1.4 Gravitational wave sources

Gravitational waves interact very weakly with matter, the gravitational fine-structure constant ($m_e^2/\hbar$, where m_e is the electron mass) is 33 orders of magnitude smaller than the weak interaction one. Therefore, they travel almost unaffected from the source to the observer, and constitute very clean messengers that can be used to infer the properties of the source. As mentioned in section 1.2, BBHs are one of the main sources of gravitational waves. Although from the general relativity point of view BBHs at all mass scales are described identically, astrophysically speaking a distinction exists, and gravitational wave detections can inform us on astrophysics happening at different scales. Moreover, gravitational wave observations are not all about black holes, and a variety of sources (not only binary systems) are predicted. Let us now review the main expected sources, and the physics that could be done with such observations. The characteristic strain ($f|\tilde{h}(f)|$) of some of these sources, together with the level (root-mean-square) of noise in different detectors is shown in figure 1.8.

1.4.1 Stochastic background and cosmological sources

Several sources, of cosmological or astrophysical origin, generate gravitational waves that are too weak to be detected individually, but their superposition forms a stochastic background that could be loud enough to be detected. Astrophysical sources contributing to the stochastic background will be mentioned in the following. An example of cosmological source

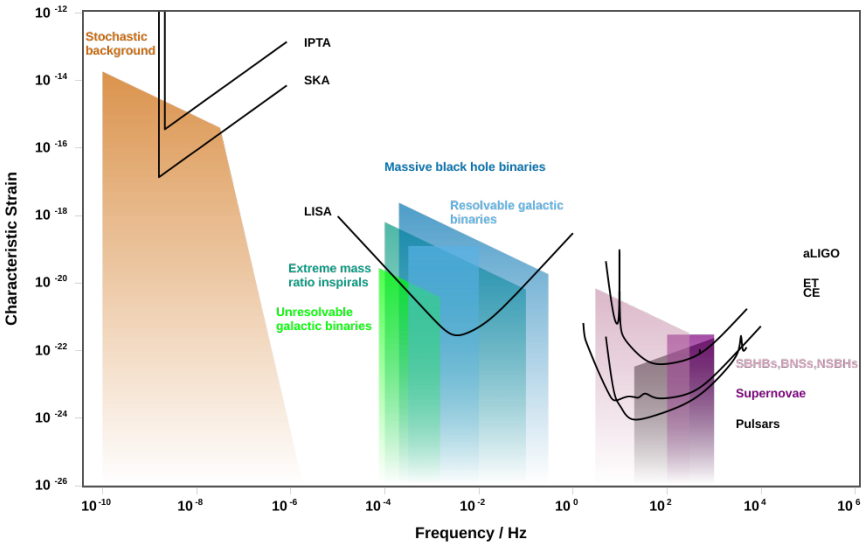

Figure 1.8: Noise level of current and future gravitational wave detectors ($\sqrt{fS_n(f)}$, where $S_n(f)$ is formally defined in section 1.5), together with the characteristic strain ($f|\tilde{h}(f)|$) of some of the main expected sources, as a function of frequency [169, 170].

is topological defects, such as cosmic strings [158, 159, 160]. Moreover, stochastic cosmological processes occurring during the early Universe, such as inflation/reheating and phase transitions that occurred as the Universe cooled down (e.g. the electroweak phase transition) [160], form a relic signal. It can be seen as the analogue of the cosmic microwave background for gravitational waves, and contributes to the stochastic background. By measuring the properties of the stochastic background, i.e. its amplitude and its frequency dependence, we can reverse engineer the problem and obtain information on these sources. The separation between astrophysical and cosmological sources is difficult and requires the use of dedicated methods [161]. No stochastic background has been detected by the LVC nor pulsar timing arrays so far, putting constraints on these processes [162, 163, 164, 165]. However, it has been argued that the candidate signal reported by pulsar timing arrays [27] could be a first piece of evidence for cosmic strings [166, 167, 168]. By probing a different frequency range, LISA will provide yet another opportunity to detect the stochastic cosmological background [160].

1.4.2 Continuous waves

Stars with a bumpy surface have a time varying quadrupole momentum, and therefore emit gravitational waves. Because these signals are fairly constant and monochromatic (dominantly at twice the rotation frequency of the star), they are called continuous waves. Ground-based detectors aim at detecting rapidly spinning neutron stars (pulsars) [171], but no signal has been detected so far [172, 173]. By targetting known pulsars, the lack of detection allows us to place an upper limit on the amount of *spin-down* due to gravitational radiation. These deformed pulsars contribute to the stochastic background.

1.4.3 Galactic binaries

According to population synthesis models, the Milky Way contains a multitude of compact binaries emitting monochromatic gravitational waves in the mHz band [174]. These are the end product of the evolution of stellar binaries. They are so numerous that they will form a stochastic foreground signal (confusion noise) dominating over the LISA instrumental noise, and a fraction of them ($\sim 10^4$) will be individually resolvable [31]. In particular, a few tens of *verification binaries* that have already been observed with electromagnetic instruments are expected to be detected by LISA [175] and will serve to ensure that LISA is operating correctly. Most GBs are formed of white dwarves, but they could also comprise neutron stars and stellar-mass black holes [174].

These binaries will be observed both in the mass-accreting and in the detached phase and could be targeted by other surveys in the electromagnetic band, such as Gaia [176]. The detection of such a large number and wide range of GBs will allow the Milky Way to be mapped [177, 178, 179], to explore Milky Way satellites [180, 181], measure the influence of tidal couplings [182, 183], test binary population models [184] and even test general relativity [185]. We will discuss one specific kind of GBs, white dwarf-black hole binaries, in chapter 5.

1.4.4 Stellar-mass black hole binaries

Massive stars end their lives as black holes, but due to pair instability, a mass gap for black holes is thought to exist between $\sim 60-120\ M_\odot$ [186, 187, 188, 189]. We refer to black holes below this gap as stellar-mass black holes. Pair instability consists in the total disintegration of the star through a supernova explosion, with no remnant left to form a black hole. In short, it is due to the annihilation of photons into electron/positron pairs, which reduces the radiative pressure, gravitational pressure then compresses the star, and accelerates the burning, causing a runaway explosion. The spontaneous production of electron/positron pairs from photons requires very hot temperatures ($\sim 10^9 K$) that can be reached when the helium core is massive enough $\sim 40-60\ M_\odot$. Pair instability is not expected to occur for high metallicity stars, but such stars tend to form lighter black holes ($\lesssim 40\ M_\odot$) because they loose a larger amount of mass through stellar winds. Note that the gap could be filled by the remnants of previous mergers, but, according to standard theories, not by the end product of stellar evolution. For this reason, the recent detection of a binary with (at least) one component in the mass gap, GW190521, has received a lot of attention [190]. Furthermore, observations suggest that a lower mass-gap between $\sim 3-5\ M_\odot$ could exist between neutron stars and stellar-mass black holes [191, 192, 193]. Unlike the higher mass gap, there is no *a priori* theoretical motivation for a dearth of black holes in this range, and it could be the effect of observational bias.

SBHBs are the most numerous sources for Earth-based detectors. The loudest of them could also be detected by LISA years before they merge in ground-based detectors band, offering the opportunity to perform *multiband* detections [32]. The remaining of them will contribute to the astrophysical stochastic background [32], as illustrated in figure 1.9. Several scenarios have been suggested for the formation of SBHBs, such as stellar evolution of field binaries or dynamical formation channels [194, 195]. As an alternative, the pos-

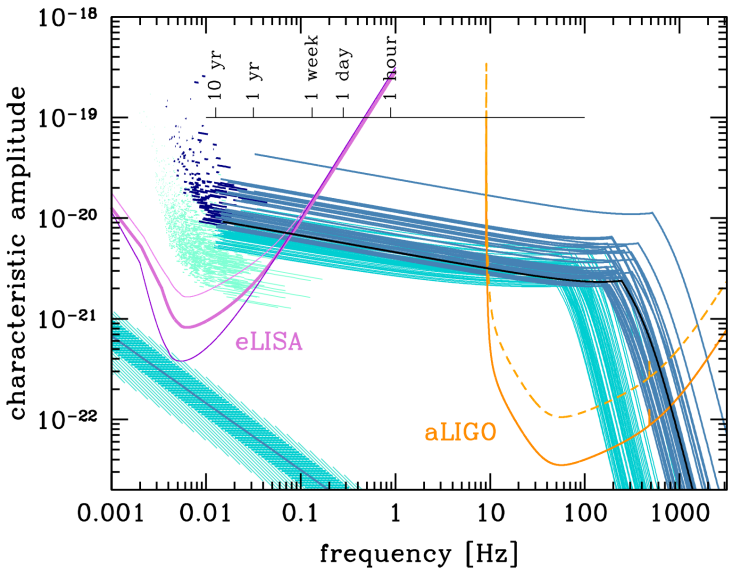

Figure 1.9: Illustration of multiband gravitational wave astronomy. The orange and purple curves indicate the level of noise in LIGO and LISA respectively, and the blue lines the characteristic strain of SBHBs. Dark blue ones correspond to binaries that could be individually resolved by LISA and that would merge within ten years in ground-based detectors band. Light blue lines correspond to unresolved binaries contributing to the stochastic background. Extracted from [32]. The black line is the characteristic strain of GW150914.

sibility that some stellar-mass black holes are of primordial origin [196, 197] cannot be completely discarded. The various possible formation channels typically predict different distributions for the parameters of SBHBs, especially spin orientation/magnitude and eccentricity [198, 199, 200, 201], providing discriminating power in astrophysical model selection. With the accumulation of observations in the last few years, we are starting to discriminate between these scenarios [202, 203, 204, 205]. However, ground-based detectors can hardly measure the eccentricity of SBHBs, since by the time they reach the frequency band of ground-based detectors they have circularised. Thus, LISA could help discriminate between the different formation scenarios [206, 207, 208, 209, 210]. In chapters 3, 4 and 5 we will discuss of how accurately could LISA infer the parameters of SBHBs, and how their observation with LISA could be used to constraint modified theories of gravity and inform us on astrophysical effects.

1.4.5 Intermediate-mass black hole binaries

Intermediate-mass black holes have masses in the range $10^2 - 10^4\ M_\odot$, and are also good candidates for multiband detections [211, 212]. The existence and the formation mechanisms for these black holes are still unclear due to the small number of observations. Several candidates have been observed electromagnetically [213], and they have been proposed as an explanation for ultra-luminous X-ray sources [214]. The end product of GW190521 has proven that a young population of intermediate-mass black holes could form through succes-

sive mergers [215]. Finally, they are thought to provide seeds for the growth of the massive black holes that are ubiquitously observed in the local Universe [213, 216]. We will discuss of how LISA observations can inform us on the astrophysical environment of intermediate-mass black hole binaries (IMBHBs) in chapter 5.

1.4.6 Massive black hole binaries

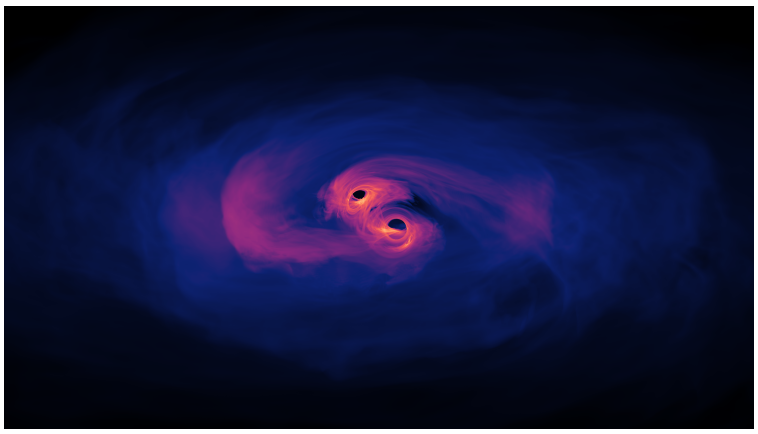

Figure 1.10: Numerical simulation of the merger of two massive black holes surrounded by accretion disks. Credits: NASA's Goddard Space Flight Center.

Black holes in the mass range $10^7 - 10^9\ M_\odot$ (the ones originally observed in quasars) are sometimes called supermassive black holes, but since they come from the same evolutionary path as black holes in the mass range $10^4 - 10^7\ M_\odot$, we will use the denomination massive black holes for the whole mass range $10^4 - 10^9\ M_\odot$. The seeds for massive black holes are thought to form at $z \sim 15 - 20$ and grow through mergers and accretion of matter [217], and their evolution has been found to be correlated with the one of their host galaxies [218]. Over the last 60 years, electromagnetic observations have provided strong evidence for the existence of massive black holes in the centre of galaxies. Massive black holes accreting from matter surrounding them are thought to power the active galactic nuclei (AGNs) [219], observed up to $z \sim 7$ [220]. Binaries of massive black holes form following the merger of their host galaxies [221]. The merger of massive black holes surrounded by matter, illustrated in figure 1.10, is likely to produce an electromagnetic counterpart [222], making them strong candidates for multimessenger observations [223]. The events for which we observe a counterpart will have independent redshift and luminosity distance measurements, and thus could be used as "standard sirens" (in analogy to standard candles). Detecting standard sirens up to high redshift ($z \sim 7$), would allow us to measure the expansion of the Universe [224]. MBHBs constitute the main target of the LISA mission, and we expect to detect a few tens per year, up to $z \sim 20$ [225]. The observation of many MBHBs with LISA will allow us to infer the population of massive black holes in the Universe. In chapter 6, we will discuss how this can be used to discriminate between different formation and evolution scenarios. Finally, while LISA will observe MBHBs when they are about to merge, pulsar timing arrays look for the signal in the nHz band formed by the superposition of the inspiral

emission of MBHBs with total mass $\geq 10^8\ M_\odot$ [26]. Similarly to GBs in the LISA band, we expect to detect a stochastic signal on top of which the loudest inspiralling MBHBs could be resolved. Both the stochastic and resolved signals could be used to inform us on the population of massive black holes, complementing LISA observations. This stochastic signal is the favoured hypothesis for explaining the candidate signal reported by pulsar timing arrays [27].

1.4.7 Extreme mass ratio inspirals

Extreme mass ratio inspirals form as the result of N-body interactions in stellar cusps surrounding massive black holes leading to the capture of compact objects, typically neutron stars or stellar-mass black holes, by the massive black hole [226]. For massive black holes with $10^5 - 10^6\ M_\odot$, these systems emit in the mHz band, and LISA is expected to resolve from a few to a few thousands of such sources, while others will contribute to the stochastic background [227, 228]. Due to the large asymmetry of the system, the compact object can spend a long time close to the massive black hole, typically $\sim 10^5$ orbits, before plunging [229]. Thus, the modelling of these sources is very challenging, since numerical relativity cannot be used to compute all the inspiral signal and post-Newtonian computations are not accurate at such short separations. We need to resort to perturbation theory to compute their waveforms, using the mass ratio as an expansion parameter [230]. On the other hand, by orbiting the massive black hole for so many orbits, the compact object will map its spacetime to high precision, allowing us to extract the parameters of the source accurately [228], and to perform exquisite tests of general relativity [231, 228].

1.4.8 Binary neutron stars

Similarly to SBHBs, binaries of neutron stars can form either through the evolution of isolated stellar binaries in galactic fields or dynamical encounters in globular/nuclear clusters [232, 233]. Coalescing BNSs are one of the main targets for ground-based detectors. The internal structure of neutron stars plays a role in the final stages of the evolution (late inspiral/merger), thus gravitational waves from BNSs can be used to probe the equation of state of nuclear matter [114, 234, 235]. Alternatively, the accumulation of observations will inform us on the maximum mass of neutron stars, providing a constraint on the equation of state [236]. The coalescence of BNSs is expected to be associated with electromagnetic and neutrino counterparts [237, 238, 239, 240], allowing us to perform multimessenger astronomy, as with GW170817 [10]. A single candidate BNS was reported during the first half of the third observing run, but no electromagnetic counterpart to it was detected [241]. With third generation detectors, we expect to detect more BNSs as well as more counterparts, thanks to an improved sky localisation [242]. BNSs are therefore excellent candidates for standard sirens [243].

1.4.9 Neutron star-black hole binaries

Similarly to SBHBs and BNSs, neutron star-black hole binaries can form as the end product of stellar evolution or through dynamical encounters [244, 245, 246, 247]. A candidate was

reported by the LVC during the third observing run [248]. Due to its intermediate mass, 2.6 $M_\odot$, the nature of the secondary is uncertain, making it either the heaviest neutron star or the lightest black hole ever observed. The non-detection of an electromagnetic counterpart does not dismiss the possibility of the secondary being a neutron star. First, we might have missed it given the large uncertainty on the sky location measured by the LVC. Second, depending on the black hole's mass and spin, the neutron star could be tidally disrupted or swallowed by the black hole, and we expect an electromagnetic counterpart only in the latter case [249, 250]. Pictorially, the neutron star is disrupted if the tidal disruption radius lies outside the ISCO of the black hole, therefore it is more likely to occur for light and rapidly spinning black holes [249, 250]. Neutron star-black hole binaries remain valuable candidates for standard sirens, since thanks to the higher mass of black holes, they could be observed up to higher redshift than BNSs.

1.4.10 Exotic compact objects

In the standard astrophysical paradigm, the only compact objects (with compactness $C = m/r \gtrsim 0.1$ where m is the mass of the object and r its radius) are black holes ($C \geq 0.5$) and neutron stars ($C \sim 0.14 - 0.2$). Among these, black holes are the only ones that can have mass above 3 $M_\odot$. However, extensions of general relativity and/or of the standard model can give rise to ECOs. Examples of such objects are boson stars, see [251] and references therein, gravastars [252, 253], wormholes [254], fuzzballs [255] and firewalls [256]; see also [257, 258, 259, 260] for further possibilities and [261] for a review. ECOs can have masses ranging from $\mathcal{O}(1\ M_\odot)$ to $\mathcal{O}(10^9\ M_\odot)$ and compactnesses ranging from 0.1 to 0.5, thus mimicking the gravitational behaviour of black holes and neutron stars to various degrees. ECOs have not been detected yet, but if binaries of such objects can form, their gravitational wave signal would offer a unique opportunity to identify them, as we will discuss in chapter 4. Due to the wide mass range allowed, these exotic binaries are potential sources for both space-based and ground-based detectors.

1.4.11 Bursts

Bursts are short signals leading to an excess of power in detectors. Coalescing binaries are an example of bursts, but many other candidates have been proposed. For instance, galactic supernovae explosions emit gravitational waves in the Hz band that could be detected by ground-based detectors [262, 263, 264, 265]. However, the intrinsically low rate of supernovae in the Milky Way (1 to 3 per century [266]), our lack of knowledge on the fraction of energy liberated in the form of gravitational waves and the difficulty in detecting poorly modelled signals makes their detection very challenging [267]. Besides contributing to the stochastic background, cosmic strings are potential burst sources for both LISA and ground-based detectors [268], but have not been detected yet [163]. Furthermore, compact objects on eccentric orbits around a massive black hole emit significant gravitational waves only close to the periapsis, resulting in a succession of burst-like signals for LISA [269]. We expect LISA to detect one of these extreme mass ratio bursts per year [269]. Finally, bursts could also be generated by yet unknown sources.

1.5 Gravitational wave detectors

Figure 1.11: Aerial view of the Virgo detector. Credits: the Virgo collaboration.

The first attempt to detect gravitational waves was made by Weber in the 1960s, using resonant bars [270]. His idea was to observe gravitational waves through the vibrations they would induce in the bars. By the end of that decade, he claimed having detected a coincident signal from the Milky Way with two independent detectors [271]. His claim pushed many groups around the world to build their own resonant detectors, but no other group confirmed the detection. By the same time, it was argued [272] that, given the sensitivity of its detector, in order for Weber to observe such a galactic signal, a lot of stellar-mass had to be converted into gravitational waves, and that at this rate the Milky Way would already have dispersed long ago! Despite its apparent failure, Weber's attempt made the idea of observing gravitational waves concrete.

In the meantime, Russian theorists Gertsenshtein and Pustovoit proposed to use laser interferometry for detecting gravitational waves [273]. The idea was independently proposed a few years later by Weber and Weiss [274] and after more than two decades the construction of the two LIGO instruments started near Hanford and Livingston. The two detectors ran from 2002 to 2010 but no signal was observed. From 2010 to 2015, the detectors were upgraded, and *advanced* LIGO was able to directly detect gravitational waves for the first time in 2015 [3]. In Europe, the laser interferometer Virgo, shown in figure 1.11, started being built in 1996 and took data from 2007 to 2011. It was then upgraded, and the *advanced* Virgo detector was operational in 2017, playing an important role in the first multimessenger observation of a BNS [9].

In the 1990s appeared the idea of a space-based gravitational waves detector, LISA. Thanks to the absence of seismic noise, it would be sensitive to low-frequency gravitational waves, allowing us to observe the merger of massive black holes. Following the first observation of gravitational waves, and the success of the test mission LISA Pathfinder [275, 276] in 2015, the LISA mission was adopted and is scheduled for launch in 2034. Although it also uses laser interferometry, LISA is a very different instrument, not "LIGO in space".

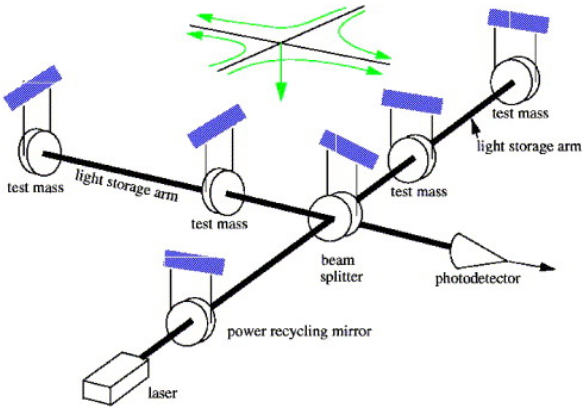

Figure 1.12: Scheme of a LIGO detector. Gravitational waves induce an unequal length shift in each arm, leading to a measurable phase offset between the lasers. Extracted from [277].

Following this historical review, we will now present the operational principle of ground-based detectors, taking the opportunity to introduce some general notions about gravitational wave detectors, and then of LISA. Finally, we will briefly comment on pulsar timing arrays, which use a different detection principle.

1.5.1 Ground-based detectors

The principle of laser interferometry is to measure the variation of length induced by a gravitational wave. Figure 1.12 shows a simplified scheme of a LIGO detector. The beam splitter divides the emitted beam in equal fractions, which are transmitted in two arms of equal length. The beams are then reflected by the test masses and recombined. When a gravitational wave passes, the length travelled by light in each arm is not equal anymore, resulting in a measurable phase offset. The response of a detector to an incoming gravitational wave is [278, 279]

$$h = F_+(\lambda, \beta, \psi)h_+ + F_\times(\lambda, \beta, \psi)h_\times, \tag{1.62}$$

where F_+ and $F_\times$ are the antenna pattern functions

$$F_+ = \frac{1}{2}\left(1 + \sin^2(\beta)\right)\cos(2\lambda)\cos(2\psi) - \sin(\beta)\sin(2\lambda)\sin(2\psi), \tag{1.63}$$

$$F_\times = \frac{1}{2}\left(1 + \sin^2(\beta)\right)\cos(2\lambda)\sin(2\psi) + \sin(\beta)\sin(2\lambda)\cos(2\psi), \tag{1.64}$$

which vary between -1 and 1. The angles λ and β are the longitude and latitude of the source, and ψ is the polarisation angle of the gravitational wave. LIGO's arms are 4 km long and Virgo's 3 km. As an example, GW150914 had masses $m_1 \simeq 40\ M_\odot$ and $m_2 \simeq 32\ M_\odot$, and was at a distance $D_L = 400$Mpc [3], from equation (1.13), we compute that $h \sim 10^{-21}$. Thus, it was necessary to measure variations in distance of the order of 10^{-18}m to detect it, much below the radius of the nucleus of an atom!

The level of noise in a detector is measured by the *power spectral density* $S_n(f)$. We denote by $n(t)$ the noise time series in a detector, and $\tilde{n}(f)$ its Fourier transform. Assuming

noise to be stationary, noise in different frequency bins is uncorrelated, and we get

$$< n(f)n^*(f') >= \delta(f - f')\frac{S_n(f)}{2}, \tag{1.65}$$

where <> denotes the average over different realisations. By virtue of the ergodic theorem, this amounts in averaging over successive periods of time. As a first approximation, noise is usually considered to be Gaussian (i.e. at each moment it is generated by a stochastic process following a normal distribution) with zero mean:

$$< n(t) >=< \tilde{n}(f) >= 0. \tag{1.66}$$

The main sources of noise in LIGO and Virgo are seismic noise at lower frequencies, thermal noise (due to motion of the test masses and mirror coating) at intermediate frequencies and photon shot noise (due to quantum fluctuations in the number of emitted laser photon) at high frequencies [280]. The Japanese detector KAGRA is experimenting with cryogenic technologies and is built underground to reduce thermal and seismic noise [17, 18]. Third generation detectors will also implement cryogeny, and will explore quantum technologies to reduce the high frequency noise. CE will keep the L-shape of LIGO detectors, but with 40 km long arms [23], while ET will be an equilateral triangle of 10 km long arms, amounting to three detectors [20, 21, 22]. Figure 1.8 shows the noise amplitude ($\sqrt{fS_n(f)}$) for current and future detectors. Besides increasing the overall sensitivity of the detector network, having more detectors allows us to resolve the polarisation of gravitational waves, and to test for additional polarisation states that are predicted in modified gravity theories [89, 281]. The issue of extracting a gravitational wave signal from noise and interpreting it will be discussed in chapter 2.

1.5.2 Space-based detector: LISA

LISA is composed of three spacecraft forming an equilateral triangle with 2.5 Gm long arms, following the Earth on its orbit around the Sun, as illustrated in figure 1.13. Each pair of spacecraft is connected by two lasers, and each spacecraft contains a test mass in free fall that drives its motion. The gigantic dimensions of LISA prevent from using one single laser that would go back and forth between two spacecraft due to power loss. The passage of a gravitational wave will make the spacecraft deviate, inducing a frequency shift. If not removed properly, the intrinsic laser frequency noise will dominate the measurement. Moreover, an important difference of LISA with respect to ground-based detectors is that the arms' lengths are not constant, because the spacecraft revolve in a central potential. These issues are dealt with by taking time-delayed linear combinations of the measurements to form the time delay interferometry (TDI) observables A, E and T (see, e.g., [282]), which play the role of the strain h for ground-based detectors. This laser frequency noise is naturally cancelled in ground-based detectors because the arms' lengths (in the absence of signal) are fixed and the lasers in both arms come from the same source and are recombined (the lasers are said to be "phase locked"). After subtraction of the laser frequency noise, the LISA noise budget is dominated by acceleration noise (due to deviations from geodesic motion of the test masses) below 3 mHz, and photon shot noise above [29]. We now give a short review of

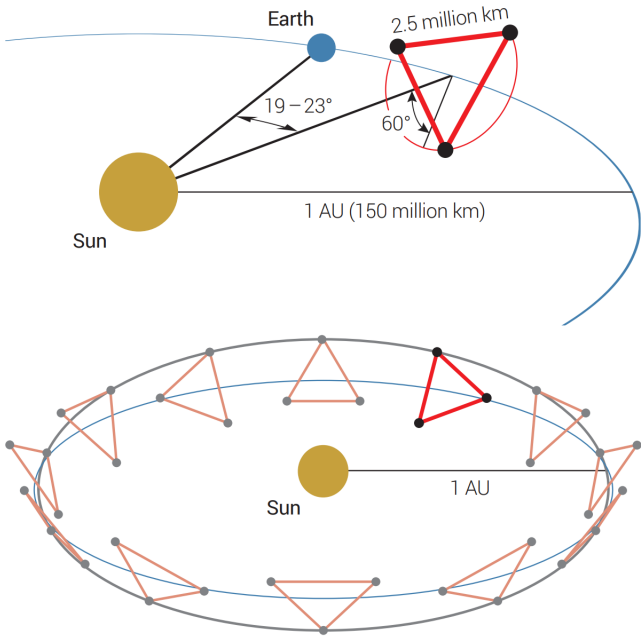

Figure 1.13: Scheme of LISA. The three spacecraft forming LISA will follow the Earth on its orbit around the Sun. Gravitational waves will be measured thanks to the frequency shift they induce by modifying the geodesic motion of the spacecraft in free fall. Extracted from [29].

how the LISA response to an incoming gravitational wave is computed, considering only the $(2, \pm 2)$ harmonics, and refer to [283, 284] for a more extensive discussion.

Let y_{slr} be the single-link observables that measure the laser frequency shift due to an incoming gravitational wave across link l between the sender spacecraft s and the receiver spacecraft r. Exploiting the mode symmetry $h_{l,-m} = (-1)^l h^*_{lm}$ (valid only for nonprecessing systems), the signal can be expressed in terms of h_{22} only. Working in Fourier domain, the single-link observables can be written with a transfer function

$$\tilde{y}_{slr} = \mathcal{T}^{22}_{slr} \tilde{h}_{22}. \tag{1.67}$$

Working under the hypothesis that the radiation-reaction timescale ($\sim \sqrt{1/\dot{f}}$) is short with respect to LISA's orbital motion timescale (i.e. at leading order in separation of timescales in the formalism of [283]), the transfer function is given by:

$$\mathcal{T}^{22}_{slr} = G^{22}_{slr}(f, t^{22}_f), \tag{1.68}$$

$$\begin{aligned} G^{22}_{slr}(f,t) = {} & \frac{i\pi f L}{2} \mathrm{sinc}\left[\pi f L (1 - \hat{\mathbf{n}} \cdot \mathbf{n}_l)\right] \\ & \times \exp\left[i\pi f \left(L + \hat{\mathbf{n}} \cdot (\mathbf{p}^L_r + \mathbf{p}^L_s)\right)\right] \\ & \times \exp(2i\pi f \hat{\mathbf{n}} \cdot \mathbf{p}_0)\, \mathbf{n}_l \cdot \mathbf{P}_{22} \cdot \mathbf{n}_l, \end{aligned} \tag{1.69}$$

$$t^{22}_f = -\frac{1}{2\pi} \frac{\mathrm{d}\Psi_{22}}{\mathrm{d}f}, \tag{1.70}$$

where $\hat{\mathbf{n}}$ is the unit gravitational wave propagation vector, $\mathbf{n}_l(t)$ is the link unit vector pointing from the spacecraft s to r, $\mathbf{p}_0(t)$ is the position vector of the centre of the LISA constellation in the Solar System barycentre (SSB) frame, $\mathbf{p}_r^L(t)$ is the position of spacecraft r measured from the centre of the LISA constellation, $\mathbf{P}_{22}$ is the polarisation tensor defined in [284] and the convention $\mathrm{sinc}(x) = \sin(x)/x$ is adopted. We dropped the t dependence in equation (1.69) for more clarity. The global factor $\exp(2i\pi f \hat{\mathbf{n}} \cdot \mathbf{p}_0)$ is the Doppler modulation in gravitational wave phase and the $\mathbf{n}_l \cdot \mathbf{P}_{22} \cdot \mathbf{n}_l$ term is the projection of the gravitational wave tensor on the interferometer links. Note that both terms are time dependent due to LISA's motion. Moreover, they depend on the sky position of the source, so that the annual variation in the phase and amplitude allows us to localise the source. The transfer function is evaluated at the time t_f^{22}, which is defined by the time-frequency mapping of the stationary phase approximation. The TDI observables A, E and T are then obtained as time-delayed linear combinations of the $\tilde{y}_{slr}$. They constitute noise-uncorrelated datasets.

1.5.3 Pulsar timing arrays

Pulsars are rapidly rotating neutron stars of high regularity, emitting a beam of electromagnetic radiation along their magnetic axis. We receive their light when their beam points towards us, with a regularity (on long timescales) comparable to atomic clocks. Thus, the time delay in the time of arrival induced by a gravitational wave can be used to detect it. The confirmation of the recently reported candidate signal [27] would be a major breakthrough and offer bright perspectives for pulsar timing arrays, especially with the advent of SKA in the late 2020s [28], which will have an improved sensitivity by a factor 10, as shown in figure 1.8.

Chapter 2

Data analysis

In this short chapter, we start by describing techniques used to search for gravitational waves. Since this is not the topic of this thesis, we will only introduce some basic notions that will be useful later. Then, we lay down the basics of the Bayesian framework that we will use for parameter estimation, i.e. the reconstruction of the properties of the source from observed data.

2.1 Signal detection

Data measured by gravitational wave detectors (d) consists in a superposition of gravitational wave signals (s) and noise: $d = s + n$. The instantaneous amplitude of gravitational wave signals is often much lower than noise, making their detection very challenging[1]. For signals of known shape, we can dig them out from noise by searching for a specific pattern in the data series. This is the process of *matched filtering*, a technique initially developed for the analysis of time series in engineering [285, 286], later applied to gravitational wave data analysis [287].

Define an inner product between two frequency series as

$$(a|b) = 4\mathcal{R}e\left(\int_0^{+\infty} \frac{\tilde{a}(f)\ \tilde{b}^*(f)}{S_n(f)}\mathrm{d}f\right), \tag{2.1}$$

where $S_n(f)$ is the power spectral density, defined through equation (1.65). The idea of matched filtering is to find the signal s that maximises the matched filter signal-to-noise ratio (SNR)

$$\mathrm{SNR}[s] = \frac{(d|s)}{\sqrt{(s|s)}}. \tag{2.2}$$

In practice we do not know the signal s itself, but rather an approximation to it: a template h. For instance, in the case of BBHs, h could be one of the waveform approximants discussed in section 1.2.3. Therefore, s is replaced by h when computing matched filter SNRs. We define the optimal SNR as $\sqrt{(h|h)}$. Averaging over noise realisations, it would be equal to

[1] With the important exception of MBHB and GB signals in the LISA band, which will typically be far above the instrumental noise.

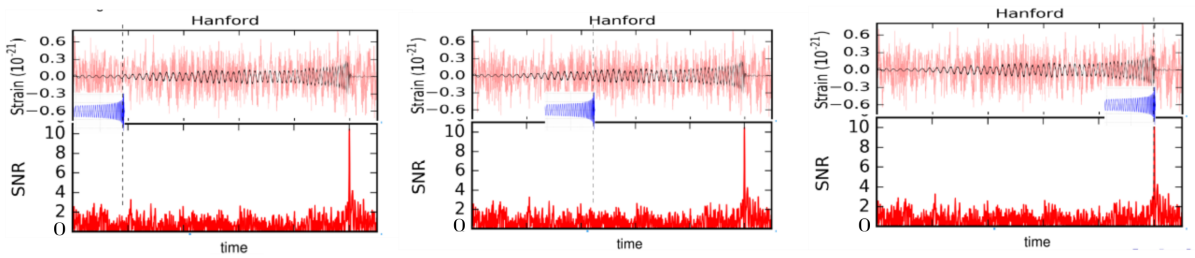

Figure 2.1: Illustration of matched filtering. The matched filter SNR is computed for different chunks of data and for different templates. A detection is claimed when it exceeds a threshold. The time series shown in this figure is the data measured by LIGO Hanford at the time of GW151226 [117].

the matched filter SNR if our template could perfectly reproduce the signal (which is usually not the case due to mismodelling). As illustrated in figure 2.1, the search for a signal is done by computing the matched filter SNR for different chunks of data and for different templates, and a detection is claimed when it exceeds a predetermined threshold ρ_*. Note from equation (2.2) that the overall amplitude of the template cancels when computing the matched filter SNR, it is really the coherence in phase between data and template that maximises it.

In order to speed up computation, the templates used to perform the search are predetermined, forming a *template bank*. They are chosen in order to ensure a good coverage of the parameter space. This can be quantified by the overlap between two templates:

$$\mathcal{O}(h_1, h_2) = \frac{(h_1|h_2)}{\sqrt{(h_1|h_1)(h_2|h_2)}}. \tag{2.3}$$

$$\tag{2.4}$$

Template banks are built using stochastic placement algorithms [288, 289, 290] so that the overlap between neighbouring templates is no less than 0.97 [291, 292]. As an example, we show the template bank used for the detection of GW150914 in figure 2.2.

The SNR threshold is set by the requirement that the probability of noise fluctuations by themselves (i.e. in the absence of a gravitational wave signal) leading to a value of the matched filter SNR higher than ρ_* is small. This is called the *false-alarm probability*, and we typically require it to be below 10^{-3}. For a given false-alarm probability $\mathcal{F}$, the corresponding SNR threshold can be approximated as [293]

$$\rho_* = \sqrt{2(\ln(N_t) - \ln(\mathcal{F}))}, \tag{2.5}$$

where N_t is the size of the template bank. It is clear that decreasing the false-alarm probability requires a higher threshold. The size of the template bank depends on the "coarseness" of the grid (i.e. the overlap between neighbouring templates) and the dimensionality of the parameter space [293]. In practice, the dimensionality can be reduced by maximising over the phase, the time to coalescence and the amplitude. Moreover, the goal of the search is not to faithfully estimate the parameters of the source, but rather to detect the presence of a signal. Therefore, not all the parameters of a targeted signal need to be used in the search, only the ones the waveform is the most sensitive to. This allows us to further reduce

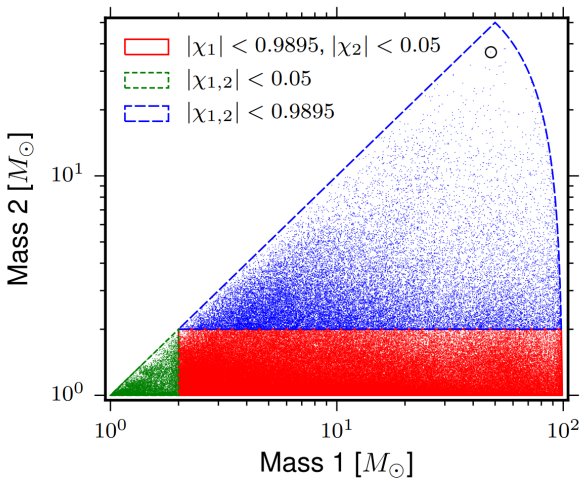

Figure 2.2: Template bank used for the detection of GW150914. A minimum overlap of 0.97 between neighbouring templates is required. The grid seems sparser at higher masses because larger difference in masses lead to a smaller dephasing between templates as the mass increases. The circle marks the template that triggered the detection of GW150914. Extracted from [295].

the dimensionality, and therefore the computational cost. As an example, for typical values $N_t = 10^{15}$ and $\mathcal{F}_{\rm tot} = 10^{-3}$ [293, 294], we get $\rho_* = 9.1$.

In general, additional statistics are computed in order to assess the significance of a candidate detection [296, 297, 298, 299, 300], in particular to account for non-stationarity and non-Gaussianity of noise. Furthermore, model independent search algorithms are also used [301]. They look for an excess of power in time-frequency bins relative to the detector noise. Although the SNR with these methods is smaller than the matched filter SNR, the threshold for detection is usually lower (for a given false-alarm probability), thus they can be more efficient in detecting short burst-like signals. Moreover, they allow us to prospect for unknown signals. On the other hand, they are less sensitive to longer and quieter signals, which require tracking coherently the phase over many cycles. Finally, when several noise-independent measurements are performed, the total SNR is the quadratic sum of the individual SNRs

$$\rho_{\rm tot} = \sqrt{\sum_o \rho_o^2}, \tag{2.6}$$

where o runs over the different (noise-independent) measurements such as LIGO Hanford, LIGO Livingston and Virgo or the three TDI channels A, E and T for LISA. In the remaining of this manuscript, we will use the SNR to decide of the detectability of an event and consider that the search has already been performed when running parameter estimation.

2.2 Parameter estimation

The parameter estimation is performed within a Bayesian framework, treating the set of parameters of the source, θ, as random variables. Bayes' theorem states that given the

observed data d, the posterior distribution $p(\theta|d)$ is given by

$$p(\theta|d,\mathcal{H}) = \frac{p(d|\theta,\mathcal{H})p(\theta|\mathcal{H})}{p(d|\mathcal{H})}. \tag{2.7}$$

On the right-hand side of this equation, $p(d|\theta)$ is the likelihood, $p(\theta)$ is the prior distribution and $p(d)$ is the evidence. $\mathcal{H}$ stands for all the underlying hypothesis in the analysis, e.g. that noise is Gaussian and stationary, that general relativity is correct (or not), the template family used in the analysis etc. The evidence allows us to compare between different hypothesis and decide which one is favoured by data. As we will not be performing model selection based on individual measurements, the evidence can be seen as a normalisation constant that does not need an explicit calculation, and we will drop $\mathcal{H}$ in the following expressions. Under the assumption that noise is stationary and Gaussian, the likelihood is given by

$$\mathcal{L} = p(d|\theta) = \prod_o \exp\left[-\frac{1}{2}(d_o - h_o(\theta)|d_o - h_o(\theta))\right], \tag{2.8}$$

where o runs over all noise-independent observation sets (e.g. the TDI observables A, E and T). The templates depend on o because of the response of the detector.

In order to speed up the computation, we will work in the zero-noise approximation: $n = 0$, so that $d = s$. Moreover, we will consider only one source at a time and neglect all possible systematic errors due to signal mismodelling: $s = h(\theta_0)$, with θ_0 the parameters of the gravitational wave source. In this approximation, the matched filter SNR is equal to the optimal SNR. The addition of noise to the gravitational wave signal is not expected to drastically affect the parameter estimation, leading at most to a displacement of the centroid of the posterior distribution within the confidence intervals (with the probability defined by the confidence interval). Moreover, by virtue of equation (1.66), this can be seen as an averaging over noise realisations [302]. Note that we still account for the finite sensitivity of the detector through the power spectral density, which appears in the inner product (equation (2.1)). Thus, the analysis of the posterior distribution itself should remain representative in the presence of noise (still assuming Gaussianity). Under these simplifications, the log-likelihood is given by

$$\ln\mathcal{L} = -\frac{1}{2}\sum_o (h_o(\theta_0) - h_o(\theta)|h_o(\theta_0) - h_o(\theta))\,. \tag{2.9}$$

The goal of parameter estimation is to compute the posterior distribution. The difficulty resides in the high dimensionality of the parameter space, an efficient way to explore the parameter space is needed. This can be done by means of a Markov chain Monte Carlo (MCMC) algorithm [303]. As an example, in the next chapter we will describe the code we developed to perform parameter estimation on simulated LISA data of SBHBs. A less costly alternative for forecast studies is to use the parameter estimation based on the Fisher information matrix.

2.2.1 Fisher information matrix

In the Fisher matrix approach, the likelihood is approximated by a multivariate Gaussian distribution [304]:

$$p(d|\theta) \propto e^{-\frac{1}{2}F_{ij}(\theta_0)\Delta\theta_i\Delta\theta_j}, \tag{2.10}$$

where $\Delta\theta = \theta - \theta_0$ and F is the Fisher information matrix given by:

$$F_{ij}(\theta) = (\partial_i h|\partial_j h)|_\theta \,. \tag{2.11}$$

The inverse of F is the Gaussian covariance matrix of the parameters, which gives an estimate of the error on each parameter. The Fisher approach is often used in forecast studies thanks to its simplicity. However, for systems with low SNR, the Fisher approximation might not be valid [304] and a full Bayesian analysis is needed. Fisher matrices are often prone to numerical instabilities. In order to mitigate this, we split between the phase and amplitude contribution to the waveform derivative:

$$F_{ij}(\theta) = 4\mathcal{R}e\left(\int_0^{+\infty} \frac{(\partial_i A + iA\partial_i\Psi)(\partial_j A - iA\partial_j\Psi)}{S_n(f)}\mathrm{d}f\right)\Bigg|_\theta . \tag{2.12}$$

The Fisher matrix has an alternative interpretation: it can be seen as a metric on the parameter space associated with the distance between two nearby templates defined by the inner product (2.1):

$$\begin{aligned} ||h(\theta+\delta\theta) - h(\theta)||^2 =& (h(\theta+\delta\theta) - h(\theta)|h(\theta+\delta\theta) - h(\theta)) \\ \simeq& (\partial_i h\ \delta\theta^i|\partial_j h\ \delta\theta^j)\big|_\theta \\ =& F_{ij}(\theta)\delta\theta^i\delta\theta^j. \end{aligned} \tag{2.13}$$

We exploit this property in our MCMC sampler.

Chapter 3

Observations of stellar-mass black hole binaries with LISA

SBHBs with a total mass as large as those observed by LIGO and Virgo could also be detected by LISA during their early inspiral phase, long before entering the frequency band of ground-based detectors and merging [32]. Although SBHBs are not LISA's main target, the scientific potential of multiband observations with LISA and ground-based detectors is considerable, as argued in this chapter and chapters 4 and 5. In this chapter, we focus on the parameter estimation of resolvable SBHBs, one of the best candidates for multiband observations [32]. We reproduce the analysis published in [33][1].

LISA will observe MBHBs somewhere between a few days and few months before their merger, i.e., in their final, rapidly evolving inspirals [30]. On the contrary, GBs are slowly evolving, almost monochromatic sources, and they will remain in band during the whole LISA mission [305]. Resolvable SBHB signals will fall in between these two behaviours: they are long-lived sources but are not monochromatic and some SBHBs can chirp and leave the LISA band. In addition, all resolvable SBHBs are clustered at the high end of LISA's sensitive band. Thus, SBHBs will produce very peculiar signals of great diversity. In this work we do not address the question of how to detect those sources, although it has been argued to be challenging [294]. Instead, we assume that we have at our disposal an efficient detection method, and we focus on inferring the parameters of the detected signals. The parameter estimation study presented here will serve as a basis for characterising the scientific potential of LISA observations of SBHBs. It will also be valuable in building search tools as we discuss at the end of the chapter.

Most previous studies of parameter estimation for SBHBs with LISA relied on the Fisher approach, and used simple approximations to LISA's response to gravitational wave signals. While a quick and efficient method for forecasting studies, the Fisher approach might not be suited for the systems with low SNR and non-Gaussian parameter distributions [304]. In ad-

[1]My part in this paper has been to develop the MCMC code for the Bayesian analysis, to run it for the different systems considered here, and to interpret the results, under the supervision of my collaborators. This task was eased by the fast LISA response generation and likelihood computation developed by Sylvain Marsat, John Baker and Tito Dal Canton [283, 284] that I use in all Bayesian analyses of SBHBs and MBHBs presented in this and the next chapters. Figure 3.3 is to be credited to Sylvain Marsat. I produced the remaining figures.

dition, SBHBs signals are long-lived and emit at wavelengths comparable to LISA's size. As a result, the commonly used long-wavelength approximation, also called low-frequency approximation [306], might not hold and could seriously bias the parameter estimation [307, 308]. We simulate LISA data using the full LISA response as described in section 1.5.2, and perform a full Bayesian analysis in zero noise of all the systems we consider. We perform a systematic scan of the parameter space by varying a few parameters at a time and investigating their qualitative impacts on the parameter estimation. We also provide a comparison to Fisher-matrix-based parameter estimation and briefly comment on the impact of using the long-wavelength approximation. Here and in the next chapters, we consider quasicircular binaries consisting of spinning black holes, with the spins aligned or anti-aligned with the orbital angular momentum,

3.1 Data simulation

Since LISA will only observe the inspiral phase of these binaries, the dominant $(2, \pm 2)$ harmonic is expected to be sufficient, and we neglect the contribution of all other subdominant harmonics. We use PhenomD to generate $\tilde{h}_{2\pm2}$, and compute the LISA response as described in section 1.5.2 to generate the TDI observables A, E, and T. The sources are parametrised by their initial frequency and phase at the start of the observation, instead of the time to coalescence and phase at coalescence (more suitable in LIGO/Virgo data analysis or for MBHBs with LISA). The initial time is defined as the moment LISA starts observing the system. A system is characterised by (i) five intrinsic parameters: the masses (m_1 and m_2), the gravitational wave frequency at which LISA starts observing the system (f_0) and the projections of spins on the orbital axis (χ_1 and χ_2); and (ii) six extrinsic parameters (those depending on the relative orientation of the source to the observer): the position in the sky defined in the SSB frame (λ and β), the polarisation angle (ψ), the azimuthal angle of the observer in the source frame (φ), the inclination of the orbital angular momentum with respect to the line of sight (ι) and the luminosity distance to the source (D_L). Only two out of the six general spin parameters are needed to describe the system because spins are assumed to be aligned (or anti-aligned) with the orbital angular momentum.

The LISA sampling rate is assumed to be 1 Hz so the Nyquist frequency is $f_{\rm Ny} = 0.5$ Hz. When computing inner products given by equation (2.1), templates are generated from f_0 up to $f_{\rm max} = \min(f_{\rm Ny}, f_{T_{\rm obs}})$ where $f_{T_{\rm obs}}$ is the frequency reached by the system after the observation time $T_{\rm obs}$. We consider two mission durations: $T_{\rm obs} = 4$ yr and $T_{\rm obs} = 10$ yr. Details on fast LISA response generation and likelihood computation are given in [284]. The parameter estimation is performed using the Metropolis-Hastings MCMC (MHMCMC) [309] we have developed for this purpose.

3.2 Metropolis-Hastings MCMC

The *target* distribution $p(\theta|d)$ is sampled by means of a Markov chain, generated from a transition function $P(\theta, \theta')$ satisfying the detailed balance condition:

$$p(\theta|d)P(\theta, \theta') = p(\theta'|d)P(\theta', \theta). \tag{3.1}$$

The transition function is built from a proposal function π such that $P(\theta, \theta') = \pi(\theta, \theta') r_{\rm acc}(\theta, \theta')$ where $r_{\rm acc}(\theta, \theta')$ is the acceptance ratio defined as

$$r_{\rm acc}(\theta, \theta') = \begin{cases} \min\left(1, \frac{p(\theta'|d)\pi(\theta', \theta)}{p(\theta|d)\pi(\theta, \theta')}\right) & \text{if } \pi(\theta, \theta') \neq 0 \\ 0 \text{ otherwise.} \end{cases} \tag{3.2}$$

It is easy to verify that P satisfies the detailed balance condition for any choice of π. In practice, a jump from a point θ to θ' is proposed using the function $\pi(\theta, \theta')$ and the new point is accepted with probability $r_{\rm acc}(\theta, \theta')$. If the point is not accepted, the chain remains at θ. In both cases, the current state of the chain is recorded. By repeating this procedure, we obtain a sequence of samples of the target distribution. From the expression of the acceptance ratio it is clear that points with higher posterior density are more likely to be accepted, thus the chain will tend to move towards regions of higher posterior density, exploring all regions of the parameter space compatible with the observed data. In theory, the chain should converge regardless of the proposal function and starting point of the chain, but in practice it may take an inconveniently large time to do so unless the proposal and starting points are chosen wisely. Since we are interested in high posterior regions, we start the chain from the true signal parameters, i.e. the maximum-likelihood point. The maximum-likelihood point coincides with the maximum posterior point if all priors are flat, but this is not true in general and the maximum posterior point can depend on the adopted prior distribution. Even though the posterior does not depend on the proposal, the convergence, efficiency and resolution of tails of the distribution do very strongly depend on the particular choice; ideally, an efficient proposal should closely resemble the target posterior distribution. Thus, most of the work goes into building an efficient proposal function. Note that for a symmetric proposal ($\pi(\theta, \theta') = \pi(\theta', \theta)$), the acceptance ratio is simply given by the ratio of the posterior distributions. This specific case is called Metropolis MCMC [310] and is the one we consider.

For building the proposal, we work with a set of sampling parameters for which the posterior distribution is expected to be a simple function, i.e. close to either a uniform or Gaussian distribution, based on the properties of post-Newtonian inspiral waveforms [84, 311, 312]. These parameters are $\theta = (\mathcal{M}_c, \eta, f_0, \chi_+, \chi_-, \lambda, \sin(\beta), \psi, \varphi, \cos(\iota), \log_{10}(D_L))$, where $\chi_+ = \frac{m_1\chi_1 + m_2\chi_2}{m_1+m_2}$ is the effective spin (often denoted $\chi_{\rm eff}$ in the literature) and $\chi_- = \frac{m_1\chi_1 - m_2\chi_2}{m_1+m_2}$ is an antisymmetric mass-weighted spin combination. We remind that the list of parameters used throughout this manuscript is listed in table 1.

The runs are done in two steps: first a short MCMC chain ($\simeq 10^5$ points) is run to explore the parameter space and then the covariance matrix of the points obtained from this chain are used to build a multivariate Gaussian proposal that is used in a longer chain. During the first stage, called burn-in, a block diagonal covariance matrix is used. The set of parameters is split in three groups: intrinsic parameters ($\mathcal{M}_c$, η, f_0, χ_+, χ_-), angles except the inclination (λ, $\sin(\beta)$, ψ, φ) and inclination distance ($\cos(\iota)$, $\log_{10}(D_L)$). Each block is computed inverting the Fisher matrix of that group of parameters. This separation was based on the intuition, well verified in practice, that the stronger correlations are within these groups of parameters and is intended to avoid numerical instabilities that may arise when dealing with full Fisher matrices. Note that by making this choice, possible correlations between parameters of different groups are not discarded; they are simply not taken into account when proposing points based on the Fisher matrix. If those correlations exist, they

should appear in the resulting covariance matrix that is used to build a proposal for the main chain. Failing to include existing correlations could reduce the efficiency of our sampler in its exploratory, or burn-in, phase; however the splitting can easily be adapted if needed.

The current state vector θ is rotated to the basis of the covariance matrix's eigenvectors. In this basis, the covariance matrix is diagonal, formed by the eigenvalues of the covariance matrix in the original basis. Because for some parameters the distribution is very flat, the eigenvalues of the covariance matrix predicted by Fisher can be very large, reducing the efficiency of the sampler. This is usually the case for poorly constrained but bounded parameters like $\cos(\iota)$ and spins. To avoid this issue, the eigenvalue of the $(\cos(\iota),\log_{10}(D_L))$ matrices are truncated and we define an effective Fisher matrix accounting for the finite extent of the prior on spins: $F_{\rm eff} = F + F^{\rm p}$. We take $F^{\rm p}_{\chi_+,\chi_+} = F^{\rm p}_{\chi_-,\chi_-} = \frac{1}{\sigma^2}$ with $\sigma = 0.5$. This choice will be motivated in section 3.4.3.

In order to improve the sampling efficiency in the event of complicated correlations between intrinsic parameters, the metric interpretation of Fisher matrix is exploited and occasionally the covariance matrix for the first group of parameters is recomputed with a given probability. By doing so, the balance equation might be violated, but this is only done during the burn-in stage (exploration of the parameter space); the resulting points are then discarded from the analysis.

The convergence of the chains is tested by running multiple chains with different random number generator seeds, checking that they all give similar distributions and computing the Gelman-Rubin diagnosis [313] for all the parameters. Potential scale reduction factors below 1.2, as the ones of these chains, indicate that the chains converged [313]. For each chain 10^3–10^4 independent samples are accumulated (by thinning the full chain by the autocorrelation length) which takes 4–7 hours on a single CPU thanks to the fast likelihood computation and LISA response generation presented in [284].

3.3 Setups

3.3.1 Systems

Despite the ongoing effort to infer the astrophysical formation channel of the SBHBs observed by LIGO/Virgo, a huge uncertainty still remains. Thus, instead of working with a randomised catalogue of sources, we start from a fiducial system with masses and spins compatible with GW150914, labelled *Fiducial* system, and perform a systematic scan of the parameter space by varying a few parameters at a time. The parameters of the *Fiducial* system are given in table 3.1 along with its SNR assuming LISA mission lifetimes $T_{\rm obs} = 4$yr and $T_{\rm obs} = 10$yr. Note that $T_{\rm obs}$ is the mission duration, not the time spent by the system in the LISA band. We assume an ideal 100% duty cycle. The initial frequency is derived from the time to coalescence from the beginning of LISA observation (t_c) that we fix to eight years for the *Fiducial* system. Thus, with $T_{\rm obs} = 4$ yr the *Fiducial* system is observed for a fraction of its inspiral, while with $T_{\rm obs} = 10$ yr the same system is observed for eight years before exiting the LISA band and coalescing. The sky location is given in the SSB frame. In the following, subscripts f refer to the *Fiducial* system.

We list all the systems we consider in the following subsections, specifying what are the

m_1 ($\mathrm{M}_\odot$)	40	
m_2 ($\mathrm{M}_\odot$)	30	
$m_{1,s}$ ($\mathrm{M}_\odot$)	36.2	
$m_{2,s}$ ($\mathrm{M}_\odot$)	27.2	
t_c (yrs)	8	
f_0 (mHz)	12.7215835397	
χ_1	0.6	
χ_2	0.4	
λ (rad)	1.9	
β (rad)	$\pi/3$	
ψ (rad)	1.2	
φ (rad)	0.7	
ι (rad)	$\pi/6$	
D_L (Mpc)	250	
z	0.054	
T_{obs} (yrs)	4	10
SNR	13.5	21.5

Table 3.1: Parameters of a representative SBHB system labelled *Fiducial*. The masses and spins of this system are compatible with GW150914 [319]. The initial frequency is computed such that the system is merging in eight years from the start of LISA observations. We consider two possible durations of the LISA mission: four and ten years (in the latter case, the signal leaves the band after eight years, at coalescence). Subscripts s denote quantities in the source frame, bare quantities are in the detector frame. The sky location is given in the SSB frame.

changes with respect to the *Fiducial* system and the corresponding labels. For all systems we consider the two possible mission durations quoted above, unless another choice is specified. In table 3.2 we show the considered systems and their respective SNR. Note that we chose to use the LISA proposal noise level [29], which does not include a 50% margin introduced to form the "science requirements" SciRDv1 [314]. The SNRs would thus be significantly lower with SciRDv1. From the point of view of the parameter estimation, using one or the other noise model amounts to a constant rescaling of the noise power spectral density S_n, with the same effect as rescaling the distance to the source. Although it has a minor impact on our analysis, we include the confusion noise due to GBs [315]. Note that the detection of SBHBs with LISA could be a challenge, at least for the traditional method of template banks [294], and that some mergers might only be detectable retroactively after being discovered by third generation ground based detectors [316, 317, 318]. We will not address this question, and simply consider that systems with SNR above 8, as the ones here, could be detected.

Intrinsic parameters

Unless specified we take $t_c = 8$ years, the initial frequency is computed according to the chosen t_c. Changing t_c (or equivalently f_0) amounts in shifting the gravitational wave signal in frequency and also defines its frequency bandwidth (within the chosen observation time). We consider the following variations in the intrinsic parameters:

- Time left to coalescence at the beginning of LISA observations:

  Earlier: $t_c = 20$ yr,

  Later: $t_c = 2$ yr

- Chirp mass keeping the mass ratio unchanged:

  Heavy: $\mathcal{M}_c = 1.5\mathcal{M}_{c,f}$, $q = q_f$, $D_L = 445$ Mpc

  Light $\mathcal{M}_c = \frac{\mathcal{M}_{c,f}}{1.5}$, $q = q_f$, $D_L = 150$ Mpc

- Mass ratio, keeping the chirp mass unchanged:

  q3: $q = \frac{m_1}{m_2} = 3$, $\mathcal{M}_c = \mathcal{M}_{c,f}$

  q8: $q = \frac{m_1}{m_2} = 8$, $\mathcal{M}_c = \mathcal{M}_{c,f}$

- Spins:

  SpinUp: $\chi_1 = 0.95$, $\chi_2 = 0.95$

  SpinDown: $\chi_1 = -0.95$, $\chi_2 = -0.95$

  SpinOp12: $\chi_1 = 0.95$, $\chi_2 = -0.95$

  SpinOp21: $\chi_1 = -0.95$, $\chi_2 = 0.95$.

For the *Heavy* and *Light* systems we scaled the distance so that the SNR remains the same as for the *Fiducial* system in the case $T_{\rm obs} = 10$yr. Changing spins or mass ratio barely affects the SNR, so we do not change the distance for those systems. Since the *Earlier* system merges in two years, increasing the observation time from four to ten years has no impact.

Extrinsic parameters

Changes in extrinsic parameters do not affect the time to coalescence, so all systems below have the same initial frequency as the *Fiducial* system. We consider the following variations in the extrinsic parameters:

- Sky location in the SSB frame:

  Polar: $\beta = \frac{\pi}{2} - \frac{\pi}{36}$, $\lambda = \lambda_f$

  Equatorial: $\beta = \frac{\pi}{36}$, $\lambda = \lambda_f$

- Inclination:

  Edgeon: $\iota = \frac{\pi}{2} - \frac{\pi}{36}$, $D_L = 150$ Mpc, $T_{\rm obs} = 10$yr

	$T_{\rm obs} = 4$yr	$T_{\rm obs} = 10$yr
Fiducial	13.5	21.1
Earlier	10.3	17.2
Later	11.8	/
Heavy	12.8	20.9
Light	14.1	21.1
q3	13.5	21.1
q8	13.5	21.1
SpinUp	13.5	21.1
SpinDown	13.5	21.1
SpinOp12	13.5	21.1
SpinOp21	13.5	21.1
Polar	12.8	20.1
Equatorial	14.9	23.1
Edgeon	/	14.7
Close	17.8	/
Far	/	15.1
Very Far	/	10.6

Table 3.2: SNR of all systems considered, computed with the LISA proposal noise level given in [29] and using the *Full* response. Different systems are derived from the *Fiducial* system, varying a few parameters at once.

- Distance:

  Close: $D_L = 190$ Mpc, $T_{\rm obs} = 4$yr

  Far: $D_L = 350$ Mpc, $T_{\rm obs} = 10$yr

  Very Far: $D_L = 500$ Mpc, $T_{\rm obs} = 10$yr

The drop in SNR being very large for an almost edge-on system, we decrease the distance of the *Edgeon* system to maintain a reasonably high SNR. For the same reason, we use only $T_{\rm obs} = 10$yr in this case. The goal of the variation in distance is to assess the impact of the SNR on the parameter estimation, all other things being equal. This also mimics the effect of varying the noise level and the duty cycle. For the *Close* system we only consider the $T_{\rm obs} = 4$yr case and for the *Far* and *Very Far* systems we only consider the $T_{\rm obs} = 10$yr case.

3.3.2 Prior

Regarding the Bayesian analysis, we take our fiducial prior to be flat in m_1 and m_2 with $m_1 \geq m_2$, flat in spin magnitude between -1 and 1, flat in initial frequency, volume uniform for the source location and flat in the source orientation, its polarisation and its initial phase. For phase and polarisation, since only 2φ (restraining to the (2,2) harmonic) and 2ψ intervene, we restrict to an interval of π. The prior probability density function in terms of

the sampling parameters is obtained by computing the Jacobian of the transformation from $(m_1, m_2, \chi_1, \chi_2, D_L)$ to $(\mathcal{M}_c, \eta, \chi_+, \chi_-, \log_{10}(D_L))$, which gives

$$p_f(\theta) = \begin{cases} N \frac{\mathcal{M}_c \eta^{-11/5} D_L^3}{\sqrt{1-4\eta}} \text{ if } 0.05 \leq \eta \leq 0.25\,, \\ 0 \text{ otherwise.} \end{cases} \tag{3.3}$$

Just like the evidence in equation (2.7), N acts only as a normalisation constant and thus it is of no importance in this study. The lower limit for η was set according to the maximum mass ratio up to which PhenomD is calibrated ($q = 16$) [111, 112]. The range of chirp mass, initial frequency and distance are orders of magnitude larger than the posterior support, so they do not affect the posterior. We label this prior as *Flatphys* and use it by default unless some other choice is specified. For example, we will consider two additional priors:

- *Flatmag*: uniform prior for the spins orientation and magnitude
- *Flatsampl*: flat prior in $\mathcal{M}_c$, η and $\log_{10}(D_L)$.

In the *Flatmag* case, we start from a full 3D spin prior, uniform in [0,1] for the spins amplitude and uniform on the sphere for the spins' orientation. We then consider only the spin projections on the orbital momentum, thus ignoring the in-plane spin components. The resulting prior is $p(\chi_i) = -\frac{1}{2}\ln(|\chi_i|)$. The *Flatmag* probability density function is: $p(\theta) = p_f(\theta)p(\chi_1)p(\chi_2)$ where $p_f(\theta)$ is given in equation (3.3). This is the prior generally used by the LVC [7, 8].

The *Flatsampl* probability density function is given by

$$p_{fs}(\theta) = \begin{cases} N \frac{1}{\eta} \text{ if } 0.05 \leq \eta \leq 0.25\,, \\ 0 \text{ otherwise.} \end{cases} \tag{3.4}$$

This prior has no astrophysical motivation; we will use it to compare the Fisher-based parameter estimation to the full Bayesian inference in section 3.4.3.

It is instructive to illustrate how the nontrivial priors look like. As we will show later in section 3.4, the chirp mass can be constrained by a Bayesian analysis to a fractional error of 10^{-4}, so a narrow constraint on the prior can be imposed. The chirp mass is nontrivially coupled to other parameters (as we will show in great details in the following sections), and constraining it to the narrow interval introduces nonlinear slicing in other parameters. Note that the imposed interval (10^{-3} in relative terms) is still much broader than the typical measurement error. Figure 3.1 displays the *Flatphys*, *Flatmag* and *Flatsampl* prior distributions for η, χ_+, and χ_- obtained by restraining the chirp mass to the specified interval. The remarkable features of the fiducial prior, the *Flatphys* prior, are the double peak at $\eta = 0.25$ and $\eta = 0$ and the bell-like shape for the χ_+ and χ_- priors with almost zero support at extreme values. The *Flatmag* is singled out by the strong peak at $\chi_{+,-} = 0$. As we will discuss in section 3.4, these non-trivial shapes of the priors can strongly affect the resulting posterior distributions in some cases.

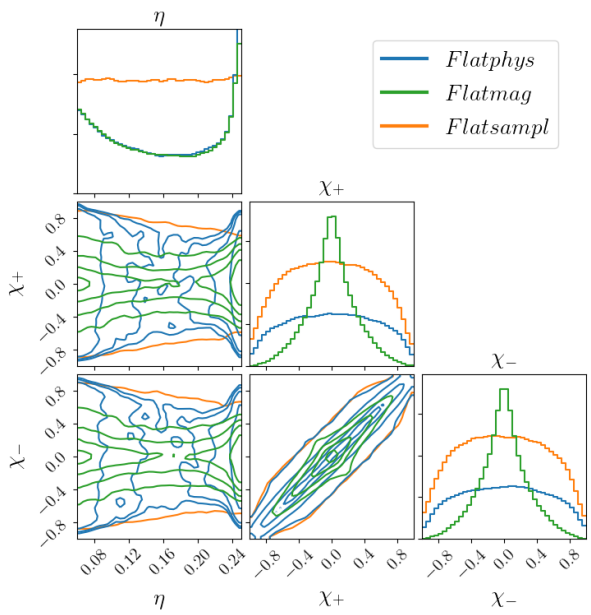

Figure 3.1: Comparison between the *Flatphys* (blue), *Flatmag* (green) and *Flatsampl* (orange) priors for η, χ_+, and χ_-.

3.3.3 LISA response

All our results are obtained using the full LISA response (see section 1.5.2), but we also assess the impact of using the long-wavelength approximation, a simplified version of the LISA response [306]. In this approximation, LISA is somewhat similar to two LIGO/Virgo-type detectors rotated one with respect to the other by $\pi/4$, and with angles of $\pi/3$ between the arms. It is obtained by taking the $2\pi fL \ll 1$ limit in the LISA response so that

$$G^{22}_{slr}(f,t) = \frac{i\pi fL}{2}\exp(2i\pi f\mathbf{k}\cdot\mathbf{p_0})\mathbf{n}_l\cdot\mathbf{P}_{22}\cdot\mathbf{n}_l. \tag{3.5}$$

The sinc function appearing in equation (1.69) leads to a damping of the signal amplitude at high frequencies. However, in the long-wavelength approximation, it is replaced by 1, leading to unrealistically high SNRs. To compensate for this, inspired by the computation of the sky-averaged sensitivity [320], we introduce a degradation function that multiplies the gravitational wave amplitude

$$R(f) = \frac{1}{1+0.6(2\pi fL)^2}. \tag{3.6}$$

To explore the validity of this approximation for SBHBs, we will compare the parameter estimation for the *Fiducial*, *Polar* and *Equatorial* systems using the full response and the long-wavelength approximation, labelled *Full* and *LW* respectively.

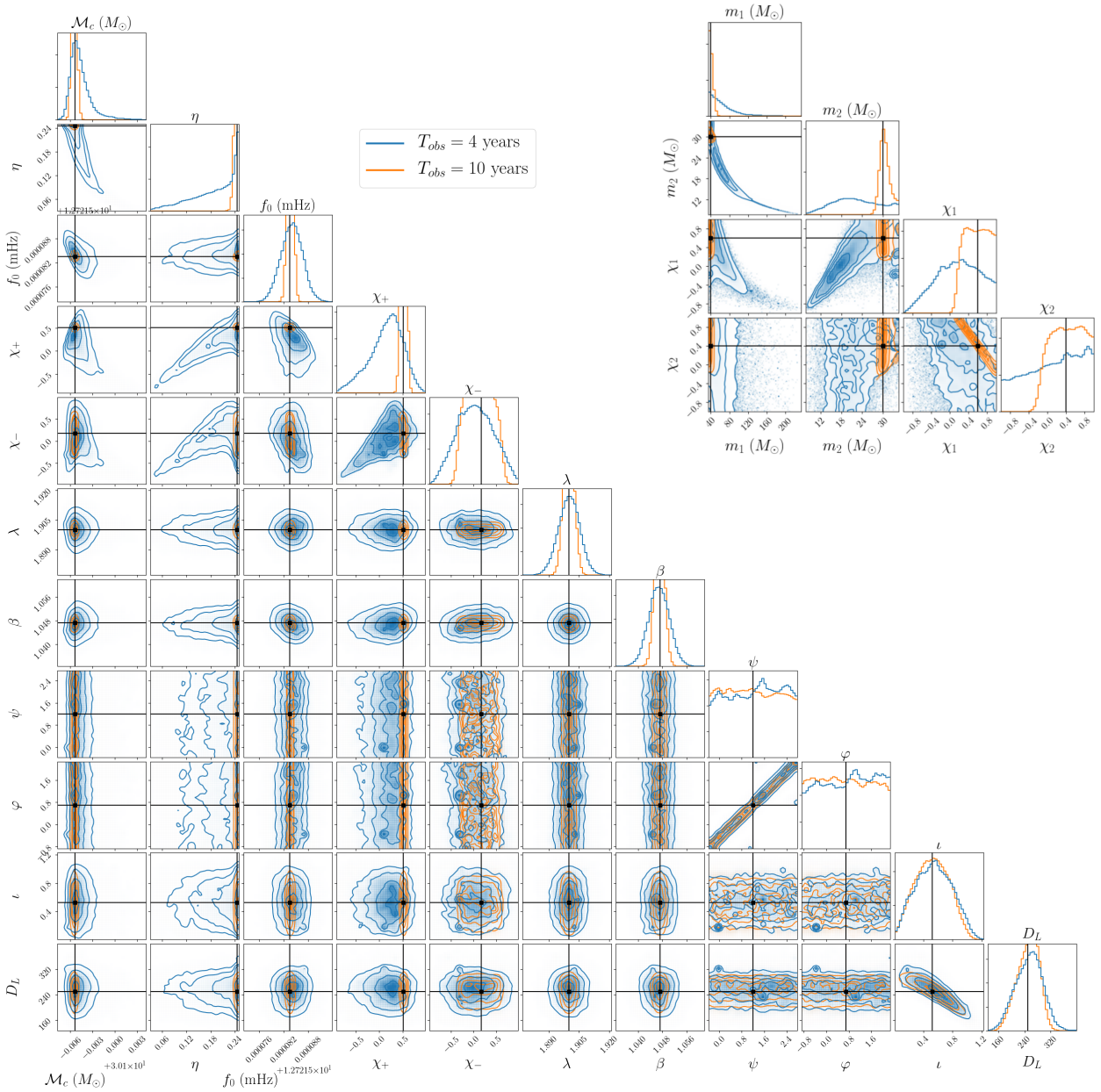

Figure 3.2: Inferred parameter distribution for the *Fiducial* system, both in the $T_{\rm obs} = 4$yr case (blue) and the $T_{\rm obs} = 10$yr case (orange). The true parameters are indicated by black lines and squares. Masses are in the detector frame.

3.4 Parameter estimation of SBHBs

In order to test the performance of our MHMCMC sampler we compared it to the well tested parallel tempering MCMC code `PTMCMC` [2]. The similarity of two distributions p_1 and p_2 can be quantified by computing their Kullback-Leibler (KL) divergence [321]:

$$D_{KL} = \sum_{\theta} p_1(\theta) \ln \left(\frac{p_1(\theta)}{p_2(\theta)} \right). \tag{3.7}$$

The KL divergence is zero if two distributions are identical. We computed D_{KL} for the marginalised distributions of each parameter obtained with two samplers using the *Flatsampl* prior, and assuming four and ten years of observation. Apart from the polarisation and the initial phase, all divergences were below 0.1 for four years of observation and below 0.01 for ten years of observation, showing a very good agreement between samplers. For ψ and φ, less well determined in general, we got slightly higher values (up to $\simeq 0.6$) but still showing a good agreement. The results presented in this section were obtained with our MHMCMC code, and, unless otherwise specified, we use the *Flatphys* prior and the *Full* response. We give the full "corner plot" [322] for the *Fiducial* system, comparing results for the two observation times in figure 3.2, this plot shows pair-wise correlation between parameters and the fully marginalised posterior for each parameter. The inset in the right top of the figure shows posterior distributions for $(m_1, m_2, \chi_1, \chi_2)$.

It would be difficult to represent the posterior distributions for all possible variations (deviations from the *Fiducial*) discussed above. Instead, we will summarise the results by underlining qualitative differences whenever we observe them and show comparative corner plots only when necessary. We start by discussing the structure of correlation between intrinsic parameters, move to extrinsic parameters, then compare the full Bayesian analysis with predictions from the Fisher matrix, and finally show the effect of the *LW* approximation to the response.

3.4.1 Intrinsic parameters

One of the main features appearing in figure 3.2 is the strong correlation between intrinsic parameters, in particular the one between $\mathcal{M}_c$ and η, which is especially pronounced for four years of observation. The main reason for this degeneracy is the limited evolution of the gravitational wave frequency: in four years of observation the *Fiducial* system spans a very narrow range from $f_0 = 12.7$ mHz to $f_{4\mathrm{yr}} = 16.5$ mHz.

First, it will be instructive to consider the magnitude of the different post-Newtonian orders appearing in the phasing (see [84] for a review). The phase of the (2,2) harmonic can be written as

$$\Psi_{22}(f) = \frac{3}{128\eta v^5} \sum_i a_i v^i, \tag{3.8}$$

where $v = (\pi M f)^{1/3}$ and where the a_i are post-Newtonian coefficients (we scaled out the leading term, so that $a_0 = 1$) that depend on the mass ratio and on the spins, and can be

[2] https://github.com/JohnGBaker/ptmcmc

separated between nonspinning terms (NS), spin-orbit terms (SO), and spin-square terms (SS). It was argued in [323] that most SBHBs would require terms up to 2PN order (terms going as $v\ln(v)$ are not considered in equation (3.8) because they enter at 2.5PN). Figure 3.3 shows the magnitude of the known post-Newtonian terms in the phasing for the *Fiducial* system, noted $\Delta\Psi_n$. In general, the magnitude of phase contributions is delicate to interpret because of the alignment freedom, as part of the phasing error can typically be absorbed in a time and phase shift. In figure 3.3 the contributions are individually aligned at f_0 with a zero phase and zero time according to equation (1.70). For $T_{\rm obs} = 4$yr, post-Newtonian orders beyond 1.5PN appear negligible due to the limited chirping in frequency, while more terms become relevant for $T_{\rm obs} = 10$yr, where much higher frequencies are reached. We also grey out the area ($f > 123$ mHz) beyond which the signal contributes less than 1 in SNR^2, which we take as a somewhat conventional limit to indicate that ignoring the signal beyond this point would not affect the log-likelihood (equation (2.9)) and therefore the parameter estimation.

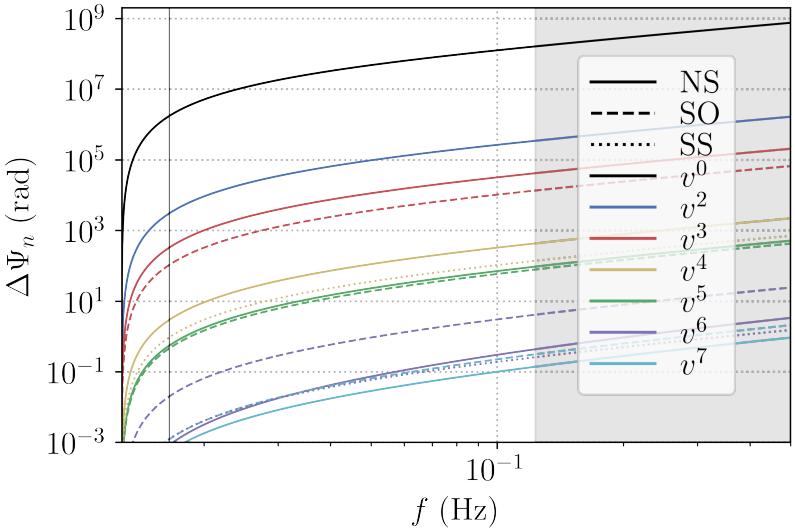

Figure 3.3: Individual post-Newtonian phase contributions $\Delta\Psi_n$ for the *Fiducial* system. The linestyle indicates the nature of the term, nonspinning (NS), spin-orbit (SO) or spin-spin (SS), while the colour indicates the post-Newtonian order. Note that these contributions are individually aligned at f_0, as explained in the text, and that interpreting the magnitude of these terms is not easy due to the alignment freedom. The vertical line shows $f_{4\rm yr}$, and the greyed area shows the frequency range contributing less than 1 in SNR^2.

In order to provide an explanation for the strong correlation between chirp mass and symmetric mass ratio, we consider a simplified problem by reducing the dimensionality: we fix f_0, χ_+, χ_- and all extrinsic parameters to the injected values and investigate the correlation between the chirp mass and the symmetric mass ratio for the *Fiducial* system. Keeping these parameters fixed will collapse some degeneracies seen in the full analysis, but this exercise will serve as an illustration of the differences between a chirping and a nonchirping system.

Since for $T_{\rm obs} = 4$yr the gravitational wave frequency changes little from f_0 to $f_{4\rm yr}$, the

phase can be Taylor expanded around f_0:

$$\Psi_{22}(f) \simeq \Psi_{22}(f_0) + \left.\frac{\mathrm{d}\Psi_{22}}{\mathrm{d}f}\right|_{f_0} (f - f_0) + \frac{1}{2} \left.\frac{\mathrm{d}^2\Psi_{22}}{\mathrm{d}f^2}\right|_{f_0} (f - f_0)^2. \tag{3.9}$$

Consider the inner product between the data $d = A_d(f)e^{i\Psi_d(f)}$ and the template $h = A_h(f)e^{i\Psi_h(f)}$. With the adopted conventions, the initial phase at f_0 is the same, $\Psi_d(f_0) = \Psi_h(f_0)$. The initial time is zero at f_0, so the stationary phase approximation (equation (1.70)) gives $\frac{\mathrm{d}\Psi_{22}}{\mathrm{d}f}|_{f_0} = 0$. The inner product becomes

$$\begin{aligned}(d|h) &= 4\mathrm{Re}\int_{f_0}^{f_{4\mathrm{yr}}} df \frac{A_d(f)A_h(f)e^{i(\Psi_d(f)-\Psi_h(f))}}{S_n(f)}\mathrm{d}f \\ &\simeq A_d(f_0)A_h(f_0)\ 4\mathrm{Re}\left[\int_{f_0}^{f_{4\mathrm{yr}}} \frac{df}{S_n(f)} e^{i(\frac{\mathrm{d}^2\Psi_d}{\mathrm{d}f^2}|_{f_0} - \frac{\mathrm{d}^2\Psi_h}{\mathrm{d}f^2}|_{f_0})\frac{(f-f_0)^2}{2}}\right],\end{aligned} \tag{3.10}$$

where we used the fact that the amplitude is a slowly varying function of the frequency. The overlap is maximised when the template is in phase with the data, making the integrand nonoscillating. In our quadratic approximation to the dephasing, this defines a curve in the $(\mathcal{M}_c, \eta)$ plane according to

$$\left.\frac{\mathrm{d}^2\Psi_{22}}{\mathrm{d}f^2}\right|_{f_0} = \left.\frac{\mathrm{d}^2\Psi_{22}(\mathcal{M}_{c,0}, \eta_0)}{\mathrm{d}f^2}\right|_{f_0}. \tag{3.11}$$

In figure 3.4 we display in blue (orange) dots points from the sampling in the $(\mathcal{M}_c, \eta)$ plane in the $T_{\mathrm{obs}} = 4\mathrm{yr}$ ($T_{\mathrm{obs}} = 10\mathrm{yr}$) case and overplot (in orange dotted line) the curve obtained by solving (3.11). The true (injection) value is indicated by black dashed lines. The curve closely follows the shape obtained from parameter estimation in the $T_{\mathrm{obs}} = 4\mathrm{yr}$ case. The green dashed line is obtained by solving (3.11) truncating the phase to 1.5PN order. We verified that adding higher post-Newtonian terms does not produce any noticeable changes, which is in a good agreement with [323] and figure 3.3.

The degeneracy can even better be reproduced by minimising the phase difference between injection and template over the whole frequency range spanned by the injected signal. More specifically, defining

$$\delta_I\Psi(\mathcal{M}_c, \eta) = \mathrm{max}_I|\Psi_{22}(\mathcal{M}_{c,0}, \eta_0)(f) - \Psi_{22}(\mathcal{M}_c, \eta)(f)|, \tag{3.12}$$

for each value of $\mathcal{M}_c$ we find η such that $\delta_I\Psi$ is minimised. Note that all parameters are kept fixed in the dephasing measure used here, in particular there is no optimisation over a constant phase or time shift. The subscript I stands for the frequency interval and this curve is plotted for $I = [f_0, f_{4\ \mathrm{years}}]$ in figure 3.4. One can see that the shape of the correlation between the chirp mass and the symmetric mass ratio in the $T_{\mathrm{obs}} = 4\mathrm{yr}$ case is almost perfectly reproduced. In the $T_{\mathrm{obs}} = 10\mathrm{yr}$ case, the system evolves until it leaves the band so it spans a broader frequency range. Figure 3.5 shows the value of the minimised $\delta_I\Psi$ for $I = [f_0, f_{4\mathrm{years}}]$ and for $I = [f_0, f^{\mathrm{LISA}}_{\mathrm{max}}]$ with $f^{\mathrm{LISA}}_{\mathrm{max}} = 0.5$ Hz taken at the conventional end of the LISA frequency band. In practice, in the latter case the maximal dephasing occurs typically around ~ 0.1 Hz. For the observation span of four years, $\delta_I\Psi$ can be found to be

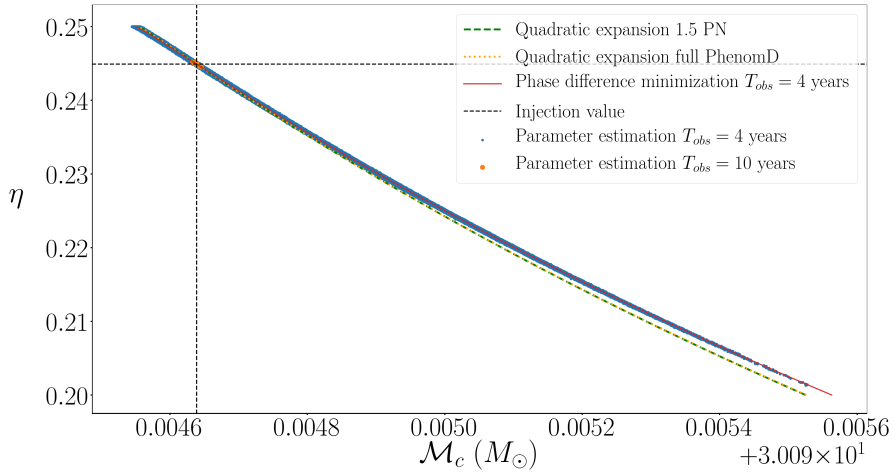

Figure 3.4: Analysis of the degeneracy between $\mathcal{M}_c$ and η. The blue (orange) dots were obtained running a parameter estimation on the *Fiducial* system in the $T_{\rm obs} = 4$yr ($T_{\rm obs} = 10$yr) case allowing only $\mathcal{M}_c$ and η to vary. The injection point is indicated by the black dashed lines. The orange dotted and the green dashed curves are given by (3.11) using the full PhenomD phase and the 1.5PN truncation of the phase respectively. The red solid line was obtained by minimising the phase difference between the injected signal and templates over the whole frequency range spanned over four years of observation.

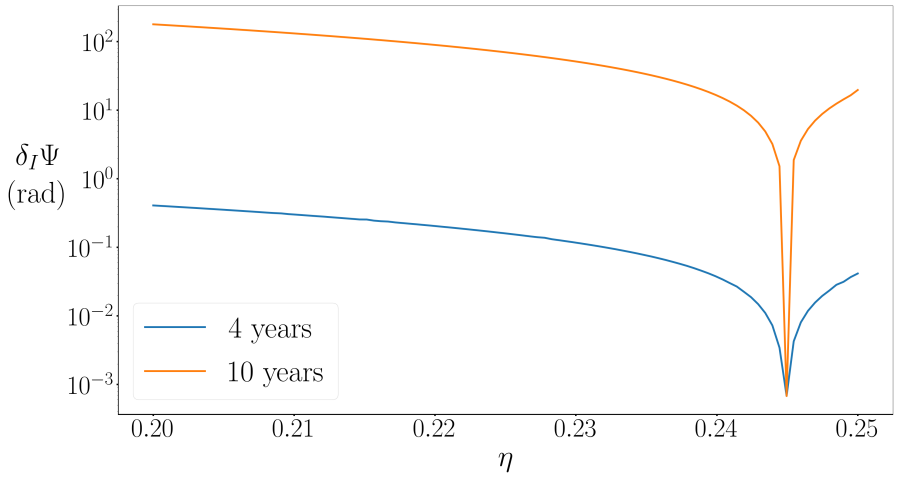

Figure 3.5: Value of $\delta_I\Psi$ along the curve in the $(\mathcal{M}_c, \eta)$ plane that minimises it for $I = [f_0, f_{4\ \rm years}]$ (blue) and $I = [f_0, f_{\rm max,LISA}]$ (orange). When LISA observes the system at low frequencies, the phase difference can be kept small over an extended region far from the injection. When LISA observes the chirp of the system, the phase difference becomes very large immediately at the vicinity of the injection point, reducing the extent of the degeneracy between $\mathcal{M}_c$ and η.

quite small (< 0.5 rad) over a large range of η. As the bandwidth of the signal becomes broader, changes in the chirp mass cannot be efficiently compensated by varying η, which results in a significant reduction of the degeneracy and a great improvement in measuring those two parameters, as seen by the narrower region covered by the orange dots in figure 3.4.

Let us now come back to the full Bayesian analysis and consider the estimation of the black holes' spins. Following [324, 112] we introduce the 1.5PN spin combination:

$$\chi_{\rm PN} = \frac{1}{113}\left(94\chi_+ + 19\frac{q-1}{q+1}\chi_-\right) \tag{3.13}$$

$$= \frac{\eta}{113}\left((113q+75)\chi_1 + (\frac{113}{q}+75)\chi_2\right). \tag{3.14}$$

This term defines how the spins enter the gravitational wave phase at the leading (1.5PN) order [84], and, therefore, should be the most precisely measured spin combination. We found this to be indeed the case. As an illustration, we plot samples obtained for the *q3*, *q8*, *SpinUp*, *SpinDown*, *SpinOp12* and *SpinOp21* systems in the $T_{\rm obs} = 10$yr case in figure 3.6. The points are the samples obtained in the Bayesian analyses and the lines show $\chi_{\rm PN} = \chi_{\rm PN,0}$ (fixing the mass ratio to its true value) for all those systems in the (χ_1, χ_2) plane. In all these cases $\chi_{\rm PN}$ is extremely well measured, within 10^{-2}, but the combination of spins orthogonal to $\chi_{\rm PN}$ is constrained only by the prior boundaries.

For slowly evolving binaries, only terms up to 1.5PN in the gravitational wave phase are found to be relevant. At this order a strong correlation between the 1.5PN spin combination and the symmetric mass ratio is expected: any change in $\chi_{\rm PN}$ can be efficiently compensated by a change in η such that the 1.5PN term $(-16\pi+1133\chi_{\rm PN})\eta^{-3/5}$ is kept (almost) constant. We have verified this by plotting the curve $(-16\pi + 1133\chi_{\rm PN})\eta^{-3/5} = \text{const}$ on top of the samples obtained for the *Fiducial* system and reproducing the shape formed by the posterior samples. Thus, we obtained and explained the three-way correlation between chirp mass, mass ratio and spins for the mildly relativistic systems spanning a narrow frequency band during the observation time. The increase in the observation time allows further chirping of the system, making the contribution of the 1 and 1.5PN corrections in the phasing significant, thus breaking strong correlations between intrinsic parameters. However, the effect of higher-order post-Newtonian terms is weak, consistently with [323] and figure 3.3, which leads to only the 1.5PN spin combination being measured. This study also suggests that $\chi_{\rm PN}$, being the most relevant mass-weighted spin combination for parameter estimation, should be used as sampling parameter. The component of $\chi_{\rm PN}$ along χ_+ is always much larger than the one along χ_- (at least by a factor $\frac{94}{19} \simeq 5$), so χ_+ is also measured reasonably well. The effective spin χ_+ is frequently used in the gravitational wave literature and has a clear astrophysical interpretation, as opposed to the 1.5PN spin combination; therefore, we will alternate between $\chi_{\rm PN}$ and χ_+ in the next discussions.

In order to further quantify the dependence of parameter estimation on the frequency bandwidth spanned by the signal during the observation time, let us consider the *Earlier*, *Fiducial* and *Later* systems, which differ in the initial frequency chosen so that the SBHBs merge in 20, 8 and 2 years respectively. We compute the KL divergence between the marginalised posterior and the marginalised prior for each intrinsic parameter, and report

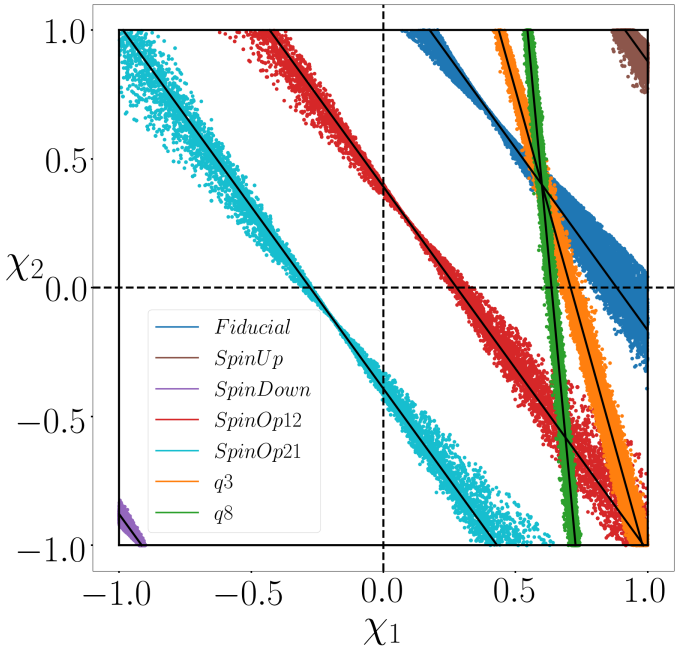

Figure 3.6: Samples of χ_1 and χ_2 obtained for different systems (defined in Sec. 3.3) in the $T_{\rm obs} = 10$yr case. The black solid lines indicates the boundaries of the physically allowed region $-1 \leq \chi_{1,2} \leq 1$ and the $\chi_{\rm PN} = \chi_{\rm PN,0}$ lines. The samples follow the $\chi_{\rm PN} = \chi_{\rm PN,0}$ lines, showing that this is the specific combination of spins that can be measured. The orthogonal combination of spins is constrained only due to the boundaries of the physically allowed region. Due to the orientation of the $\chi_{\rm PN} = $ const lines, χ_1 is better constrained than χ_2. High values of spins with same (opposite) sign are the better (worse) constrained.

the values in table 3.3. The larger values of D_{KL} indicate that knowledge has been gained from the gravitational wave observations as compared to the prior. The results show a strong dependence on the observation time (therefore on the frequency bandwidth), especially for spins, for which the D_{KL} varies by an order of magnitude. For the *Earlier* system only the chirp mass measurement is truly informative. Note that the longer frequency evolution plays a bigger role than the SNR. For instance, *Later*, which leaves LISA after two years with SNR = 11.8, is more informative than *Earlier* with $T_{\rm obs} = 10$yr, which has an SNR = 17.2. We repeated this analysis using the *Flatmag* and *Flatsampl* priors for the *Fiducial* system. For all choices of prior, the KL divergences are similar, proving the η, χ_+, χ_- distributions are prior dominated when observing slowly evolving systems. Notice that KL divergences for spins are slightly smaller when using the *Flatmag* prior, meaning that the posterior is even more dominated by the prior. This is because the *Flatmag* prior peaks strongly at $\chi_+ = \chi_- = 0$ as discussed in section 3.3.2. Note that the values of D_{KL} are always larger for $\chi_{\rm PN}$ than for the other spin combinations, reflecting the fact that it is the best measured spin combination. Still, for systems evolving through a narrow frequency interval, the $\chi_{\rm PN}$ distribution is also prior dominated. The effect of the prior is especially well seen for the

		Fiducial					*Earlier*					*Later*				
		$\mathcal{M}_c$	η	χ_+	χ_-	$\chi_{\rm PN}$	$\mathcal{M}_c$	η	χ_+	χ_-	$\chi_{\rm PN}$	$\mathcal{M}_c$	η	χ_+	χ_-	$\chi_{\rm PN}$
Flatphys	$T_{\rm obs} = 4$yr	3.6	0.4	0.2	0.1	0.3	2.7	0.04	0.04	0.03	0.04	6.1	1.7	3.1	0.4	3.6
	$T_{\rm obs} = 10$yr	7.6	2.5	3.7	0.5	4.3	4.5	0.7	0.5	0.2	0.6	/	/	/	/	/
Flatmag	$T_{\rm obs} = 4$yr	3.4	0.6	0.07	0.04	0.08	/	/	/	/	/	/	/	/	/	/
	$T_{\rm obs} = 10$yr	7.5	2.5	4.4	0.4	4.8	/	/	/	/	/	/	/	/	/	/
Flatsampl	$T_{\rm obs} = 4$yr	3.7	0.4	0.3	0.2	0.3	/	/	/	/	/	/	/	/	/	/
	$T_{\rm obs} = 10$yr	7.3	3.2	3.7	0.5	4.4	/	/	/	/	/	/	/	/	/	/

Table 3.3: KL divergences between the marginalised posterior and prior distribution of the intrinsic parameters for different systems and choices of prior. When observing the system at low frequencies, only $\mathcal{M}_c$ shows a sensible deviation from the prior. The likelihood is informative on η and χ_+ (and $\chi_{\rm PN}$) only for chirping systems. Different choices of prior give similar results.

Fiducial system and $T_{\rm obs} = 4$yr in figure 3.7: the strong peak of the symmetric mass ratio at 0.25 is what is expected due to prior (see section 3.3.2). The same peak is also observed for the *Later* system (predominantly due to low SNR) but η is much better constrained for this system: the likelihood is informative enough to reduce the width of the distribution, but not large enough to suppress the prior. *Let us reiterate this important finding: for intrinsic parameters beyond the chirp mass, the chirping (extent of the frequency evolution) of the observed SBHB has stronger influence on parameter estimation than the SNR or observation time per se.*

We note that, although the frequency is slowly evolving, the signal is far from monochromatic, unlike most of galactic binaries (e.g. double white dwarf binaries). As an element of comparison, using the quadrupole formula to compute the frequency derivative at f_0, for the *Earlier* system we find $\dot{f}_0 = 1.9 \times 10^{-11}$ Hz^2, which is four orders of magnitude higher than the fastest evolving galactic binaries [31]. Thus, despite the strong correlation between intrinsic parameters, the chirp mass is always well measured, with a relative error of order 10^{-4} for the *Earlier* system when observing for four years and below 10^{-6} for chirping systems. The tight constraint on $\mathcal{M}_c$ leads to the banana-like shape correlation between m_1 and m_2 seen in the top right part of figure 3.2. As a result, individual masses can be determined (within 20–30%) only for chirping systems.

The 90% confidence intervals for the parameters of the *Fiducial* system are given in table 3.4. Whenever the marginalised distribution of a given parameter is leaning against the upper (lower) boundary of the prior as for m_1 (m_2) we define the 90% confidence interval as the value between the 0.1 and 1 quantile (0 and 0.9). Otherwise, in all other situations we define the 90% confidence interval as the values between the 0.05 and 0.95 quantiles. In all cases we report the median as a point estimate.

Systems with a higher mass ratio (*q3* and *q8*, keeping the chirp mass the same as for *Fiducial*) give an error on the chirp mass similar to the *Fiducial* system, but the mass ratio is better determined. This is because, when keeping the chirp mass fixed, the post-Newtonian expansion of the gravitational wave phase features negative powers of η, notably in the 1PN

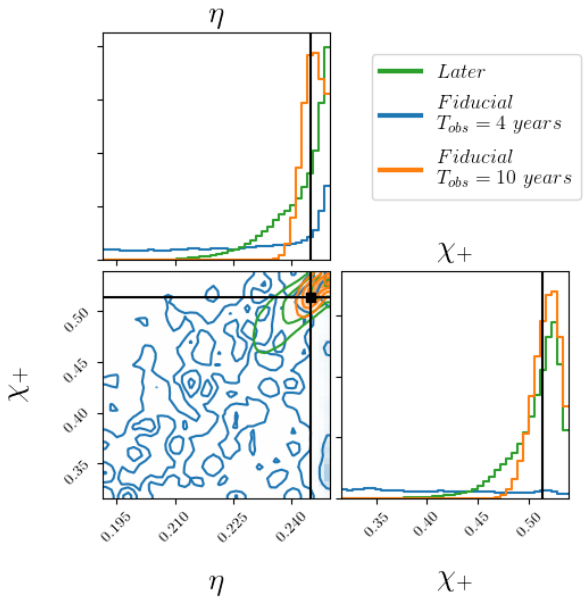

Figure 3.7: Distribution of η and χ_+ for the *Later* system ($t_c = 2$yr) and the *Fiducial* system ($t_c = 8$yr) for both observation times ($T_{\rm obs} = 4$yr and $T_{\rm obs} = 10$yr). Since LISA observes the *Later* system chirping, the determination of η and χ_+ is much better than for the *Fiducial* system in the $T_{\rm obs} = 4$yr case. But because of its low SNR (SNR = 11.8), the posterior distribution still peaks at $\eta = 0.25$, as an effect of the prior. This is in contrast to the *Fiducial* system in the $T_{\rm obs} = 10$yr case (SNR = 21.1), which peaks at the injected value.

term. Moreover, what should matter is the derivative of the phase with respect to η, which contains only negative powers ($\eta^{-7/5}, \eta^{-2/5}$), making it more sensitive to the small mass ratio as compared to equal-mass systems. For an observation time of four years, the uncertainty on individual masses is still of order of 100%, but for an observation time of ten years, it reaches below 10% and 1% for the *q3* and *q8* system, respectively.

We now discuss the effect of priors on parameter estimation for high-spin systems. Consider *SpinUp* system in the $T_{\rm obs} = 4$yr case shown in figure 3.8. As discussed above, in this case the spins, the mass ratio and the chirp mass are correlated. The posterior reflects the interplay between the symmetric mass ratio and effective spin priors, which push samples towards $\eta = 0.25$ and $\chi_+ = 0$, and the likelihood, which peaks at the true value of χ_+ (0.95). This, together with the correlation between parameters, leads to the resulting posterior distribution which has double peak in η and broad distribution for χ_+ (the 2D histogram is more informative). The distribution (overall) is shifted away from the true values (well evident in the right panel of figure 3.8), though they are still contained within the 90% confidence interval. In the case of $T_{\rm obs} = 10$yr, the system chirps, so the information provided by the likelihood dominates over the prior, therefore, this bias is corrected and most of the degeneracies (at least partially) broken. In general, the posterior for the spins for weakly chirping systems are badly constrained and closely resemble the priors. For chirping systems, the determination of spins can be understood from figure 3.6. Because of the orientation of lines $\chi_{\rm PN} = $ const, χ_1 is better constrained than χ_2. As the mass ratio increases, the slope

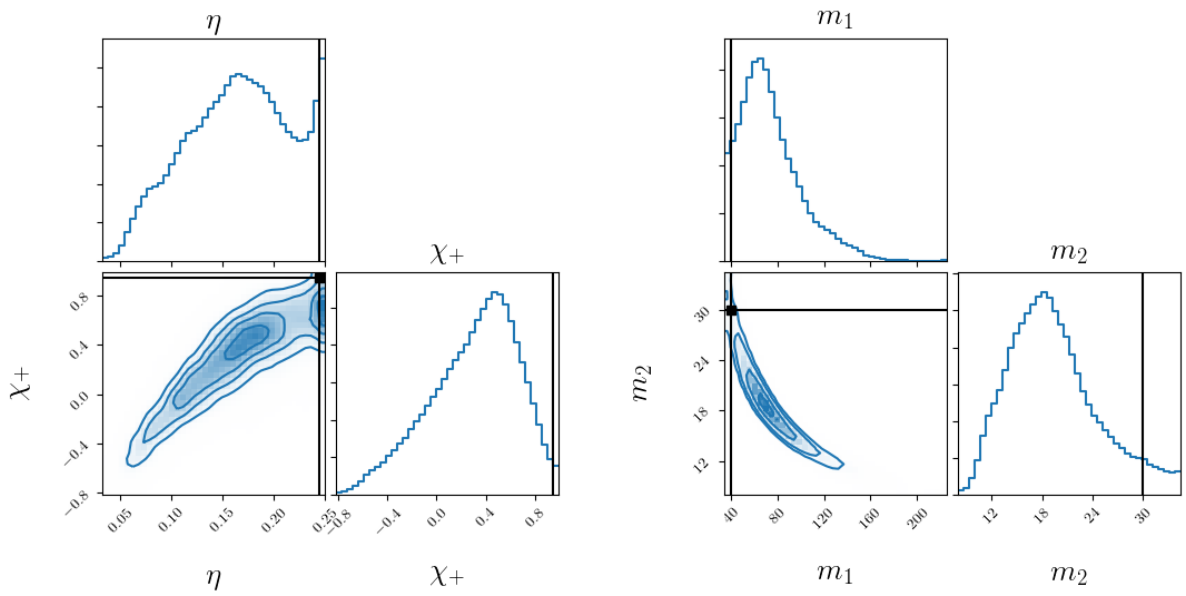

Figure 3.8: The left panel shows the inferred distribution on η and χ_+ for the *SpinUp* system. Because of a "competition" between the prior and the likelihood the distributions of η and χ_- peak away from the true value. The $\mathcal{M}_c$ distribution, not shown, is marginally affected. Because of the bias in η, the inferred distribution of masses is significantly biased. However, with the adopted definition of confidence interval, the true value is within the 90% confidence interval.

of these lines changes, accentuating this difference. Spins of same (opposite) sign, are better (worse) determined as their magnitude increase because of the narrowing (broadening) of the allowed region. For the *Fiducial* system, the error on the spin of the primary black hole is quite large, but we can infer that the spin is positive, with 0 (and negative values) being outside the 90% confidence interval given in table 3.4. The effective spin is measured within 0.1 for chirping systems.

All results (for masses) so far were for redshifted masses. Since $\mathcal{M}_{c,s} = \mathcal{M}_c/(1+z)$,

$$\frac{\Delta\mathcal{M}_{c,s}}{\mathcal{M}_{c,s}} = \frac{\Delta z}{1+z} + \frac{\Delta\mathcal{M}_c}{\mathcal{M}_c}. \tag{3.15}$$

As we will discuss in section 3.4.2, D_L is typically measured within 40–60%, which implies a measurement of the redshift z within $\sim$ 40–60% (at the low redshifts considered here, D_L and z are linearly related). Thus, the second term on the right-hand side of equation (3.15) is clearly subdominant and the error on the source frame chirp mass is dominated by the error on redshift, as a result

$$\frac{\Delta\mathcal{M}_{c,s}}{\mathcal{M}_{c,s}} \simeq \frac{0.5z}{1+z}. \tag{3.16}$$

This error is typically of the order of a few percent for systems detectable by LISA (up to $z \sim \mathcal{O}(10^{-1})$), which is better than current LIGO/Virgo measurements [7, 8]. This estimate is in good agreement with the results presented in table 3.4. The errors for individual masses

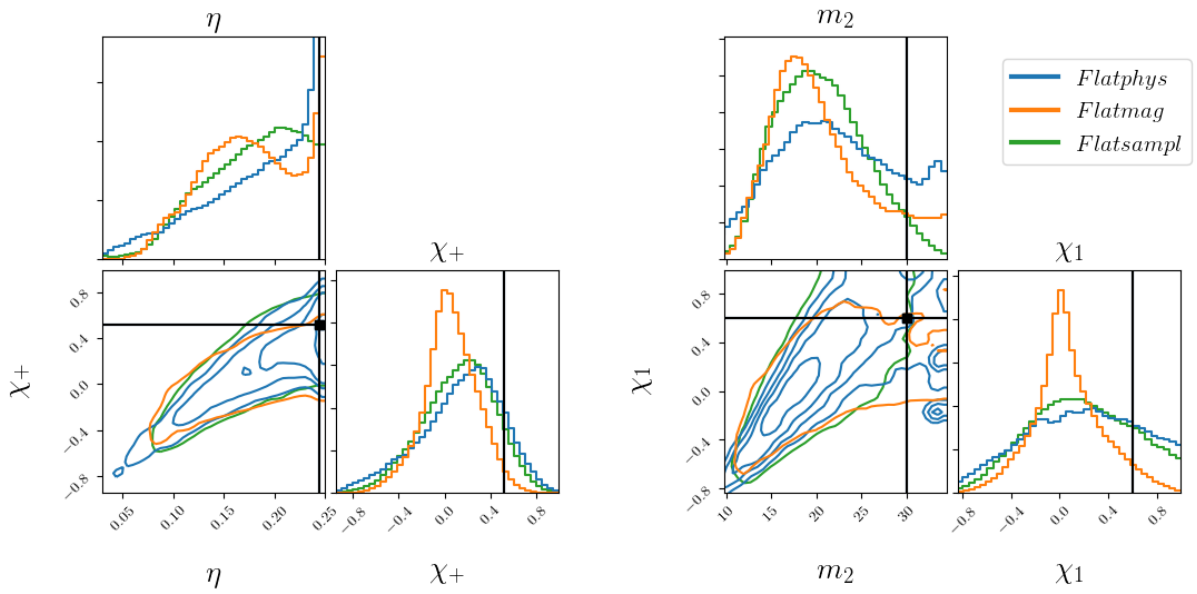

Figure 3.9: Effect of the prior on the parameter estimation. The left (right) panel shows the inferred distribution on η and χ_+ (m_2, χ_1) for the *Fiducial* system using the *Flatphys*, *Flatmag* and *Flatsampl* priors. Under the effect of the prior, the posterior distribution can be significantly shifted away from the true value.

in the source frame are dominated by the error on the masses (like the second term on the left-hand side of equation (3.15)) due to the poor constrain on the mass ratio.

The initial frequency is always extremely well determined, with relative errors below 10^{-5}. Its determination improves for chirping systems due to reduction of correlation with other intrinsic parameters. The frequency of the system at the beginning of the LISA observations is coincidental, as it is directly linked to the time that is left for the system to coalesce. The time to coalescence is inferred by applying the stationary phase approximation (equation (1.70)) to the full gravitational wave phase. This transformation involves all intrinsic parameters, so the error on t_c is typically smaller for chirping systems. The error is of the order of 1 day for systems far from merger, while for more strongly chirping systems t_c can be determined to within 30 s.

Increasing or decreasing the total mass of the system (while preserving the SNR) as in the *Heavy* and *Light* systems has little consequence for the estimation of intrinsic parameters. The error on spins and symmetric mass ratio are the same as in the *Fiducial* case. The relative error on chirp mass and initial frequency is slightly smaller for lighter systems (factor $\simeq 1.4$ between the *Heavy* and *Light* systems) because of the larger number of cycles. However, we do not find a simple scaling with the chirp mass of the system for a fixed level of SNR. In particular, we do not find the error on the chirp mass to scale with $\mathcal{M}_c^{5/3}$ as computed in [325, 85]. This was to be expected, since as discussed in this section the error on intrinsic parameters depends crucially on the frequency interval through which LISA observes the binary.

Finally, the choice of prior only marginally affects the posterior distribution for chirping systems. On the other hand, it can have a significant impact for nonchirping systems as can

be seen in figure 3.9. For example, the *Flatmag* prior completely dominates the posterior distribution of spins as the KL divergences suggested and shown in figure 3.9. Because of the noted correlations, the prior on spins propagates into the determination of mass ratio and individual masses.

	$T_{\rm obs} = 4$yr	$T_{\rm obs} = 10$yr
$\mathcal{M}_c/\mathcal{M}_{c,0}$	$1^{+1\times10^{-4}}_{-4\times10^{-5}}$	$1^{+2\times10^{-6}}_{-1\times10^{-6}}$
$\mathcal{M}_{c,s}/\mathcal{M}_{c.s,0}$	$0.99^{+0.01}_{-0.01}$	$1.00^{+0.01}_{-0.01}$
q	$2.6^{+4.7}_{-1.6}$	$1.3^{+0.1}_{-0.3}$
$m_1/m_{1,0}$	$1.4^{+1.1}_{-0.6}$	$0.99^{+0.04}_{-0.13}$
$m_2/m_{2,0}$	$0.7^{+0.4}_{-0.3}$	$1.06^{+0.14}_{-0.04}$
$m_{1,s}/m_{1,s,0}$	$1.5^{+1.2}_{-0.6}$	$0.99^{+0.04}_{-0.13}$
$m_{2,s}/m_{2,s,0}$	$0.7^{+0.5}_{-0.3}$	$1.06^{+0.15}_{-0.04}$
χ_+	$0.2^{+0.5}_{-0.7}$	$0.52^{+0.01}_{-0.02}$
χ_-	$0.03^{+0.7}_{-0.6}$	$0.1^{+0.4}_{-0.4}$
$\chi_{\rm PN}$	$0.2^{+0.4}_{-0.7}$	$0.433^{+0.008}_{-0.009}$
χ_1	$0.2^{+0.8}_{-0.6}$	$0.6^{+0.4}_{-0.3}$
χ_2	$0.2^{+0.7}_{-1.0}$	$0.4^{+0.6}_{-0.5}$
Δt_c (s)	10^4	20
$\Delta\Omega$ (deg^2)	0.41	0.07
$D_L/D_{L,0}$	$1.1^{+0.2}_{-0.3}$	$1.0^{+0.2}_{-0.2}$
z	$0.060^{+0.012}_{-0.014}$	$0.055^{+0.009}_{-0.012}$

Table 3.4: 90% confidence intervals on the parameters of the *Fiducial* system, whose parameters are given in table 3.1, using the *Flatphys* prior. For masses and distance, the relative errors are given. The redshifted chirp mass is extremely well determined for both mission durations but individual masses can be measured only if the mission is long enough and LISA can observe the system chirping. The measurement of the source frame chirp mass is worse, being dominated by the error on the distance measurement and therefore the redshift in (3.15). The error on individual masses is dominated by their intrinsic degeneracy. For chirping systems, $\chi_{\rm PN}$ can also be measured, which translates into a good constraint on the effective spin χ_+. The error on individual spins remains large for the chirping system, the spin of the primary BH can be mildly constrained (in this example, excluding negative values). As a consequence of the overall improvement in the determination of the intrinsic parameters, the inference of the time to coalescence improves drastically. The sky location (given by equation (3.17)) is very well determined for both mission durations, within the field of view of next generation electromagnetic instruments like Athena and SKA [326, 327].

3.4.2 Extrinsic parameters

Sky location

The sky location of the source is very well determined and, except for systems close to the equator, its posterior distribution is very similar to a Gaussian unimodal distribution.

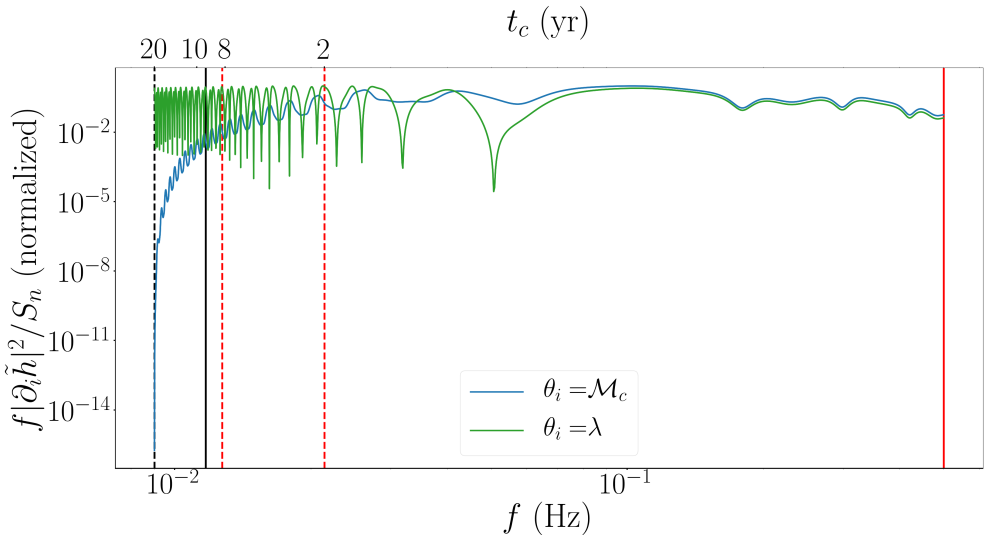

Figure 3.10: Relative contribution to the determination of $\mathcal{M}_c$ and λ as a function of frequency. As discussed in section 3.4.1, most of the information on intrinsic parameters comes from the high end of the frequency band, whereas the contribution to sky parameters mainly comes from the low frequencies.

Following [306], we define the p quantile for the solid angle as

$$\Delta\Omega = -2\ln(1-p)\pi\sqrt{(\Sigma^{\lambda,\lambda})(\Sigma^{\sin(\beta),\sin(\beta)}) - (\Sigma^{\lambda,\sin(\beta)})^2}\,, \tag{3.17}$$

where Σ is the covariance matrix. The 90 % confidence interval is obtained for $p = 0.9$. The error for the *Fiducial* system, reported in table 3.4, is below 0.4 deg^2, which is within the field of view of most planned electromagnetic instruments such as Athena and SKA [326, 327]. Except for the *Equatorial* system, the sky position is constrained with a similar precision for all systems considered in this work. The good localisation comes from the complicated modulations imprinted in the signal by the orbital motion of LISA, according to equation (1.69). To understand how the sky localisation evolves as a function of the frequency band LISA observes a system, figure 3.10 shows $f|\partial_\lambda\tilde{h}|^2/S_n$ (normalised with respect to its maximum value) as a function of the frequency. The quantity $f|\partial_i\tilde{h}|^2/S_n$ is the integrand entering the computation of the diagonal elements of the Fisher matrix (2.11) and indicates (for each parameter) the most informative frequency range. Using a logarithmic scale for frequencies, the factor f ensures that we can visualise the contributions to the integral as the area under the curve (up to a normalisation factor). The corresponding values of the time to coalescence t_c are indicated in the upper x-axis. We indicate the initial (dashed line) and end (solid line) frequencies of the *Later* (red), *Fiducial* (red) and *Early* (black) systems for $T_{\rm obs} = 10$yr. The behaviour for $\sin(\beta)$ is similar to λ. For comparison the same quantity is shown for the chirp mass, the behaviour for other intrinsic parameters is similar. As discussed in the previous section, most of the information on intrinsic parameters comes from high frequencies. On the other hand, there is more information on the sky location at low frequencies, where a given range of frequencies corresponds to more orbital cycles of the LISA constellation. However, this is to be balanced with the narrower frequency range

	$\Delta\Omega$ (deg^2)	
	$T_{\rm obs} = 4$yr	$T_{\rm obs} = 10$yr
Fiducial	0.41	0.07
Earlier	1.6	0.46
Later	0.11	/
Polar	0.32	0.05
Equatorial	6.3	0.55

Table 3.5: Solid angle around the injection point corresponding to a 90 % confidence region, computed with (3.17). The sky localisation is slightly better for the *Polar* sky position ($\beta \simeq \pm\pi/2$), but much worse for the *Equatorial* sky position ($\beta \simeq 0$). The sky localisation is better for the *Later* system than for the *Earlier* system (despite a lower SNR in the $T_{\rm obs} = 10$yr case) due to the broader frequency range spanned during its observation.

spanned by systems evolving at lower frequencies, for a fixed observation time. For this reason, the *Later* system gives a better localisation than the *Earlier* system even in the $T_{\rm obs} = 10$yr case as reported in table 3.5 (0.05 against 0.2 deg^2).

There are two main effects in the LISA response (equation (1.69)) that give information about the sky localisation: the time dependency (through t_f, see equation (1.70)) of the response reflects the orbital cycles of LISA, and the Doppler modulation $\exp(2i\pi f \mathbf{k}\cdot\mathbf{p}_0)$ of the phase. The Doppler modulation shows this time dependency, but also scales with f, so this term is larger for chirping signals reaching high frequencies. The sky localisation is better for lighter systems: $\Delta\Omega_{Light} < \Delta\Omega_{Fiducial} < \Delta\Omega_{Heavy}$ (ranging from 0.23 to 0.69 deg^2 in the $T_{\rm obs} = 4$yr case and from 0.05 to 0.11 deg^2 in the $T_{\rm obs} = 10$yr case). This is a result of keeping fixed the time to coalescence t_c and the SNR (by adjusting the distance) for those systems. The gravitational wave signal from the lighter and heavier systems is displaced at higher and lower frequencies, since the evolution rate of the inspiral depends primarily on the chirp mass. Namely, $f_0 = 9.9,\ 12.7,\ 16.4$ mHz for *Heavy*, *Fiducial*, and *Light*, respectively. Since the SNR is kept fixed in this comparison, this means that the lighter system has a stronger sky-dependent Doppler modulation of the phase, helping with the localisation.

When comparing the *Polar*, *Fiducial* and *Equatorial* systems, a direct comparison of the sky localisation could be quite misleading because the metric on a sphere depends on the latitude, with a singularity at the pole. This issue can be evaded by defining a system of coordinates on the sphere (μ, γ) such that the injection point is always on the equator. The transformation from the ecliptic coordinates to this frame is source dependent. The spherical coordinates at the equator are locally Cartesian and simplify the comparison of the results. Results of the sky localisation are shown in figure 3.11 for the *Polar*, *Equatorial* and *Fiducial* systems in the (μ, γ) frame and for $T_{\rm obs} = 4$yr. All three systems recover μ (azimuthal angle) similarly well but the determination of γ worsens as $\beta \to 0$. Furthermore, for the *Equatorial* system we find a tail extending all the way to a secondary sky position corresponding to $\beta \to -\beta$. This behaviour is due to the dominant Doppler phase in the frequency response, which goes as $\cos(\beta)$: although the amplitude of the effect itself is maximised, its variation with the latitude is minimal as $\cos(\beta)$ is flat for $\beta = 0$. For $T_{\rm obs} = 10$yr, this partial

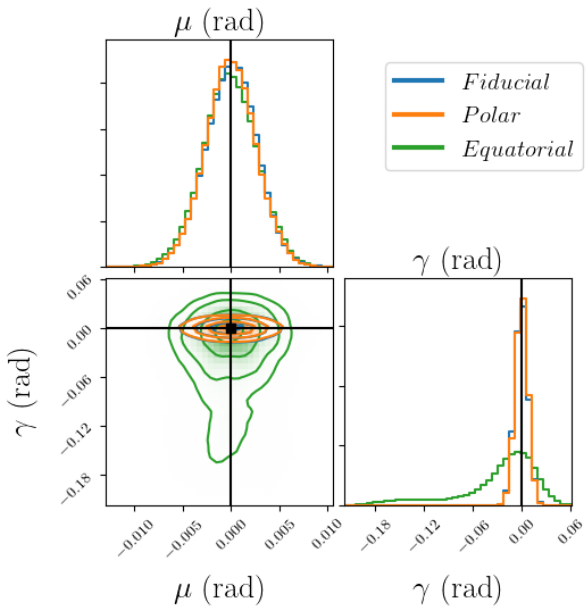

Figure 3.11: Inferred distribution on the angles parametrising the position of the source for the *Polar*, *Fiducial* and *Equatorial* systems, with $T_{\rm obs} = 4$yr. As explained in the main text, to avoid coordinate effects near the pole we do not compare the angles in the SSB frame (λ, β) but transformed angles (μ, γ) defined by placing the injection point at the equator in each case (note that the scale of the two axis is not the same). The injection corresponds to $\mu = \gamma = 0$ as indicated by the black solid lines and squares. μ is equally well recovered in the three cases. For the *Equatorial* system, there is a tail extending to the position $\beta \to -\beta$.

degeneracy is broken thanks to a combination of effects: there are more cycles of LISA's orbit contributing, the signal reaches high frequencies where the f dependent terms in the response (see equation (1.69)) are larger, and the total SNR itself is larger. The solid angle for the *Equatorial* system is larger than for the other systems (as reported in table 3.5), but remains much tighter than the current sky localisation with ground-based observatories [7, 8].

Other extrinsic parameters

Our results show strong correlations between inclination and distance, and between the polarisation and the initial phase. These degeneracies are commonly seen in the analysis of LIGO/Virgo sources when using only the dominant $(2, \pm 2)$ harmonic in the analysis. In this case, the gravitational wave in the radiation frame is given as

$$\tilde{h}_+(f) = \tilde{A}(f)\frac{1+\cos^2(\iota)}{2}e^{2i\varphi}e^{-i\Psi_{22}(f)}\,, \tag{3.18a}$$

$$\tilde{h}_\times(f) = i\tilde{A}(f)\cos(\iota)e^{2i\varphi}e^{-i\Psi_{22}(f)}\,, \tag{3.18b}$$

where $\tilde{h}_{22}(f) = A_{22}(f)\exp(-i\Psi_{22}(f))$ is the frequency domain amplitude and phase decomposition of the h_{22} harmonic, with $\tilde{A} \equiv \sqrt{5/16\pi}A(f)$ absorbing conventional factors. We

refer to [284] for notation; in particular we exploit the symmetry between h_{22} and $h_{2,-2}$ for nonprecessing systems to write the waveform in terms of h_{22} only. Going to the SSB frame we rotate by the polarisation angle ψ:

$$\tilde{h}_+^{\rm SSB} = \tilde{h}_+ \cos(2\psi) - \tilde{h}_\times \sin(2\psi)\,, \tag{3.19a}$$
$$\tilde{h}_\times^{\rm SSB} = \tilde{h}_+ \sin(2\psi) + \tilde{h}_\times \cos(2\psi)\,. \tag{3.19b}$$

For a face-on system, $\iota = 0$ leading to

$$\tilde{h}_+^{\rm SSB}(f) = \tilde{A}(f) e^{2i(\varphi-\psi)} e^{-i\Psi_{22}(f)}\,, \tag{3.20a}$$
$$\tilde{h}_\times^{\rm SSB}(f) = i\tilde{A}(f) e^{2i(\varphi-\psi)} e^{-i\Psi_{22}(f)}\,. \tag{3.20b}$$

Thus, the initial phase and the polarisation appear only through the combination $\psi - \varphi$, yielding a true degeneracy corresponding to $\psi - \varphi = \text{const}$. For systems close to face-on/face-off, like the *Fiducial* system, this gives the strong correlation between ψ and φ well observed in figure 3.2. For edge-on systems ($\iota = \pi/2$) instead

$$\tilde{h}_+^{\rm SSB}(f) = \tilde{A}(f) \cos(2\psi) e^{2i\varphi} e^{-i\Psi_{22}(f)}\,, \tag{3.21a}$$
$$\tilde{h}_\times^{\rm SSB}(f) = \tilde{A}(f) \sin(2\psi) e^{2i\varphi} e^{-i\Psi_{22}(f)}\,, \tag{3.21b}$$

and the degeneracy between ψ and φ is then broken, as also shown in figure 3.12. This figure compares the distributions of ψ, φ, ι and D_L for the *Edgeon* system to the *Far* system (which is almost face-on). Those systems have similar SNR. When the degeneracy between ψ and φ is broken, we observe a correlation between the initial phase and the initial frequency. This is an artificial correlation due to relating φ to the value of the phase at f_0 for each template. Using a fixed reference frequency, such as the initial frequency of the injected signal for example, eliminates this correlation.

In figure 3.12 we also plot distance and inclination, which show a significant correlation for the *Far* system that is absent for the *Edgeon* system. Distance and inclination are purely extrinsic parameters, and the degeneracy features when subdominant (higher order) harmonics are negligible appear in the same way for LIGO/Virgo and LISA. For LISA, see, e.g., a discussion in the context of galactic binaries in [328]. In short, in the limit of face-on/off systems the inclination acts as a scaling factor over a rather broad range of inclination values, thus changes in $\cos(\iota)$ can be compensated by changes in D_L. For close to edge-on systems, the $\times$ polarisation of the wave is suppressed (in the wave-frame, before transforming to the SSB frame as in equation (3.19)). The important point is that this suppression of $h_\times$ depends itself quite rapidly on the inclination, so that reproducing the injected signal leads to a rather tight constraint on ι, and, as a consequence, on D_L. For MBHB observations with LISA, higher harmonics play an important role and help break these degeneracies [284]; but SBHBs are observed by LISA far from coalescence and higher harmonics are negligible for these signals.

Figure 3.13 shows the effect of the distance prior on the posterior distribution for $\cos(\iota)$ and D_L using the *Flatphys* and *Flatsampl* priors for $T_{\rm obs} = 4$yr. The former favours larger distances and, to keep the correct overall signal amplitude, compensates by preferring the face-on configuration. In the case of the *Flatsampl* prior, the posterior distribution of $\cos(\iota)$

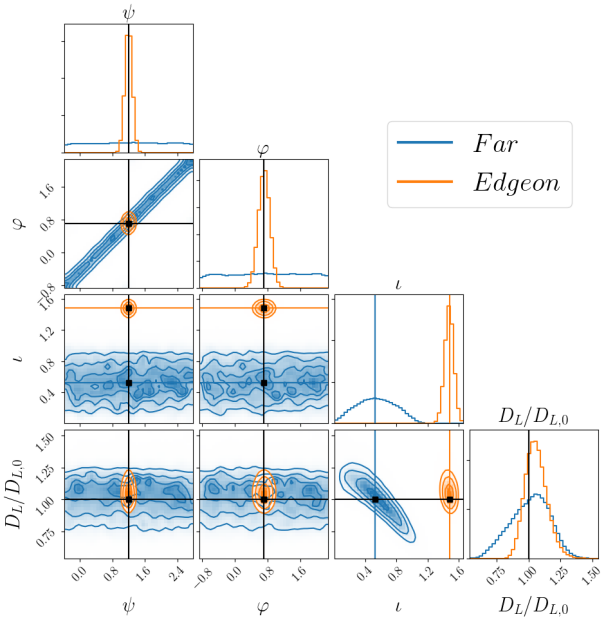

Figure 3.12: Comparison of the inferred distribution on ψ, φ, ι and D_L for the *Far* and *Edgeon* systems, both have similar SNR. The distance is normalised to the injection value. Black lines and squares indicate the true values common for both systems and coloured lines and squares the value of ι for each system. For the *Edgeon* system the degeneracies between φ and ψ and between ι and D_L are broken giving a better estimation of each of these parameters. However, close to edge-on systems will usually have much lower SNR. Indeed, in order to keep a comparable SNR the distance to the *Edgeon* is less than half the distance to the *Far* system.

is flat because the likelihood itself is very flat around $\iota = 0, \pi$ ($\cos(\iota)$ is a slowly varying function around its extrema). Thus, the choice of prior shifts the peak of the posterior, but the 90% confidence interval still contains the true value and its width is barely affected.

Among all the cases considered, D_L can be at best determined within 40%, except for the *Edgeon* system for which it can be determined within 20%. However, the edge-on systems will have lower SNR for a fixed distance to the source, and, therefore there is an observational selection effect where the face-on/off systems are preferred (that is what we observe with LIGO/Virgo). Fixing all other parameters of the *Fiducial* system and setting $\iota = \pi/2 - \pi/36$, the SNR drops from 21 to 9 for $T_{\rm obs} = 10$yr. For the fixed inclination, time to coalescence and source position, the error on intrinsic parameters, distance and sky position scale, in first approximation, as 1/SNR.

3.4.3 Fisher matrix analysis

In this subsection we consider parameter estimation using a slightly improved version of Fisher information matrix analysis, inspired by [304]. We have introduced the Fisher matrix in section 2.2.1 and discussed its augmented version, the effective Fisher, in section 3.2 for computing the covariance matrix. As we mentioned in section 3.2 and showed in section

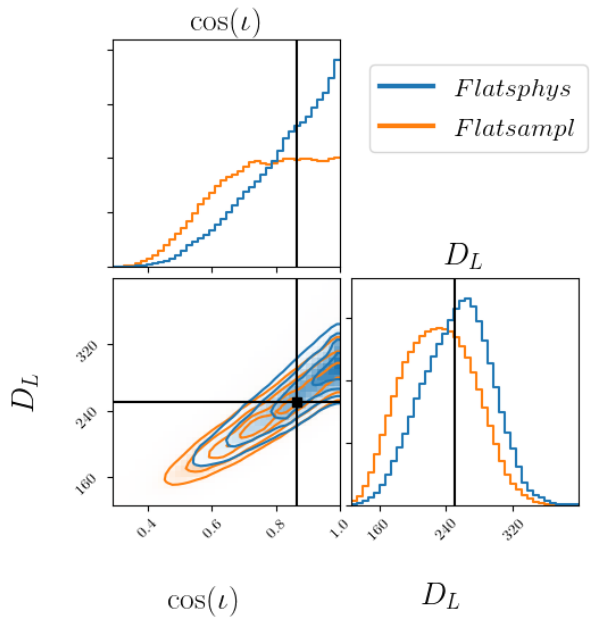

Figure 3.13: Distribution of $\cos(\iota)$ and D_L using the *Flatphys* and *Flatsampl* priors for $T_{\rm obs} = 4$yr. Although the distributions look rather different, the width of the 90% confidence interval for D_L is barely affected and the true point is well within the confidence interval.

3.4.2, the likelihood is very flat around $\iota = 0, \pi$ leading Fisher-based-parameter estimation to overestimate the errors on $\cos(\iota)$ and D_L. To correct for this, we add a term (F^t) to the effective Fisher matrix: $F_{\rm eff} = F + F^{\rm p} + F^{\rm t}$ where F is the "original" Fisher matrix given by equation (2.11) and $F^{\rm p}$ is introduced to account for the prior on spins. Empirically, we found the choice $F^{\rm t}_{\cos(\iota),\cos(\iota)} = \frac{1}{(0.2(20/{\rm SNR}))^2}$ and 0 elsewhere to give good results for $\cos(\iota)$ and $\log_{10}(D_L)$. The prior matrix $F^{\rm p}$ does more than truncating the error on spins: it mimics the nontrivial prior on χ_+ and χ_-. Indeed, requiring the spins to be in the physically allowed range $(-1 \leq \chi_{1,2} \leq 1)$ leads to a parabola-shaped prior on $\chi_{+,-}$ as seen in figure 3.1. We treat this nontrivial prior by a Gaussian distribution centred at $\chi_{+,-} = 0$ with standard deviation $\sigma = 0.5$. We invert the effective Fisher matrix to obtain the covariance matrix and use it to draw points from a multivariate Gaussian distribution. To fully account for the effect of the prior on spins, the point at which the Gaussian distribution is centred is shifted to $\theta_{\rm eff} = F^{-1}_{\rm eff} F\theta_0$. We only keep points within the boundaries given in equation (3.4). For ψ and φ we draw points in an interval of width π around the central value. In figures 3.14 and 3.15 we compare our Fisher analysis to the inferred distribution for the *Fiducial* system using the *Flatsampl* prior.

Despite the rather low SNR of this system, especially in the $T_{\rm obs} = 4$yr case, there is a good agreement between the two analysis. In particular, the sky localisation is the same for the full parameter estimation and the effective Fisher analysis. Naturally, this method cannot reproduce the secondary maximum we found for the *Equatorial* system, but it does predict a higher error as the system approaches the equatorial plane. The good agreement for χ_+ and χ_- and for $T_{\rm obs} = 4$yr is because the effective Fisher and posterior distribution are both prior dominated. For $\mathcal{M}_c$ and η, Fisher agrees with the full parameter estimation on a

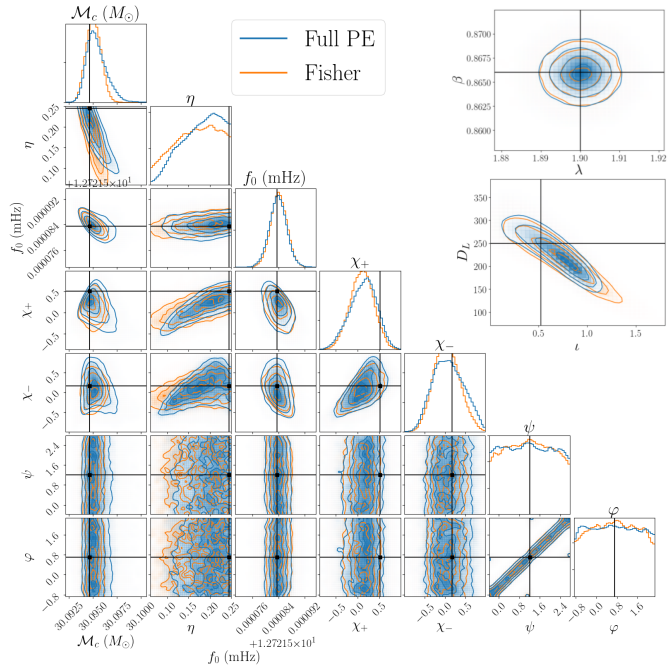

Figure 3.14: Comparison between the inferred distribution for the *Fiducial* system using the *Flatsampl* prior and our Fisher analysis with $T_{\rm obs} = 4$yr. PE stands for parameter estimation.

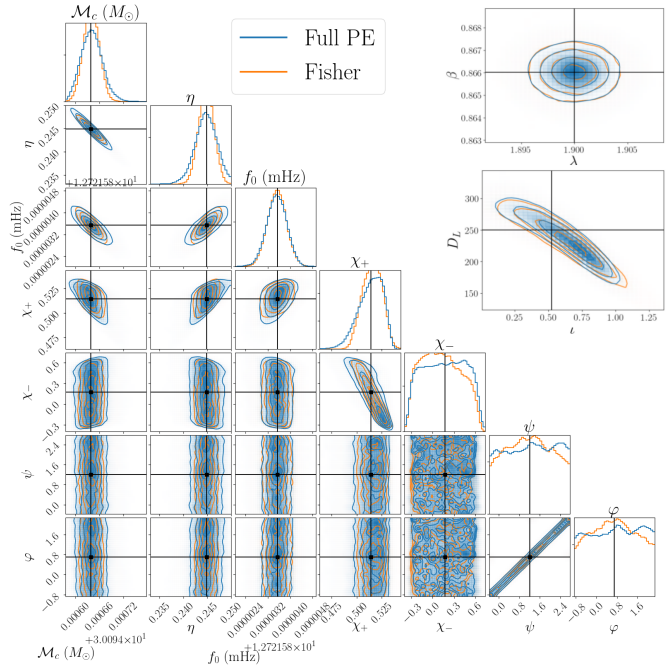

Figure 3.15: Similar to figure 3.14 but with $T_{\rm obs} = 10$yr.

2-sigma level but cannot reproduce the banana-like correlation. In case of $T_{\rm obs} = 10$yr, the likelihood becomes more informative for the effective spin, reducing the error predicted by the "original" Fisher while the χ_- distribution is still prior dominated. Without adding $F^{\rm t}$ to

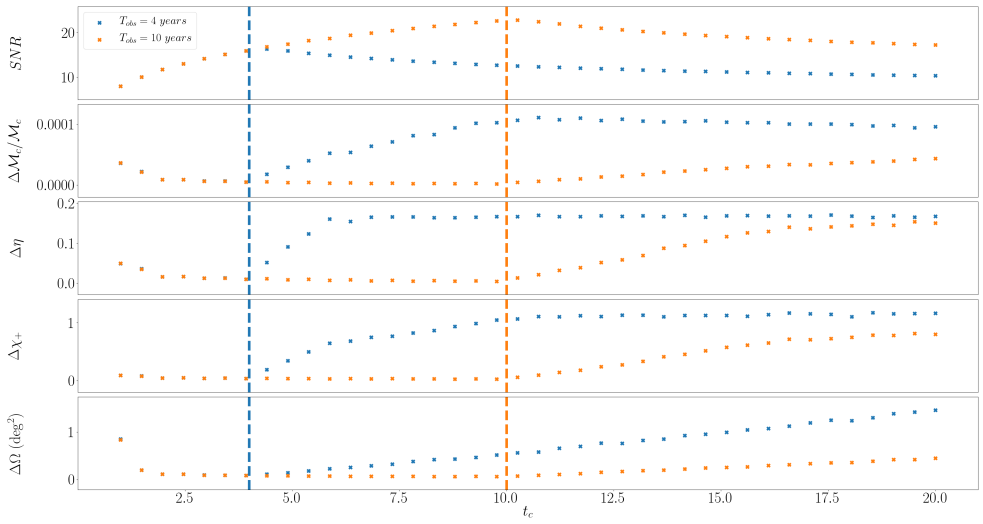

Figure 3.16: Evolution of the error as function of the time before merger LISA starts observing the system in the $T_{\rm obs} = 4$yr and $T_{\rm obs} = 10$yr cases. The SNR is given in the upper panel. The errors on $\mathcal{M}_c$, η, and χ_+ correspond to the width of the 90% confidence intervals, and $\Delta\Omega$ is defined in (3.17).

the effective Fisher, the direction for the correlation between $\cos(\iota)$ and D_L is predicted well but the Fisher matrix severely overestimates the error for nearly face-on/face-off systems. For the *Edgeon* system, the likelihood is not so flat, so the error predicted by the "original" Fisher is already small (in agreement with the Bayesian analysis) and adding $F^{\rm t}$ does not affect the parameter estimation.

Based on the rather good agreement we found with Bayesian parameter estimation, we can exploit the simplicity of the Fisher analysis to further explore how does the parameter estimation evolve with the time (left) to coalescence. In figure 3.16, assuming $T_{\rm obs} = 4$yr and $T_{\rm obs} = 10$yr, we plot the errors on $\mathcal{M}_c$, η, χ_+ and $\Delta\Omega$ as a function of the time to coalescence t_c, keeping all the parameters of the *Fiducial* system fixed but varying the initial frequency in accordance with the chosen t_c. The corresponding evolution of the SNR is shown in the top panel, with the lowest SNR of 8 being reached for $t_c \simeq 1$yr. Dashed lines mark $t_c = T_{\rm obs}$ in each case, which corresponds to the maximum achievable SNR given the observation time, and it also corresponds to the best estimation of parameters. Note two different regimes on the two sides of the dashed line: to the left, the parameter estimation is governed by the decrease in the signal duration in LISA band and reduction in SNR, while to the right the parameter estimation is determined mainly by the bandwidth of the signal spanned over the observation time. As discussed in section 3.4.2 the sky localisation comes mainly from modulations caused by the motion of LISA, therefore it worsens rapidly if the system spends too little time in band (below 1 year).

As a conclusion to this subsection, let us mention that the code developed to perform this improved Fisher analysis is currently being used in the computation of *figures of merit* for LISA[3]. The goal of figures of merit is to characterise the performance of LISA for different

[3]https://gitlab.in2p3.fr/LISA/lisa-fom

	$T_{\rm obs} = 4$yr		$T_{\rm obs} = 10$yr	
	Full	*LW*	*Full*	*LW*
Fiducial	13.5	12.9	21.1	21.4
Polar	12.8	12.2	20.1	20.0
Equatorial	14.9	14.2	23.1	23.4

Table 3.6: Comparison between the SNRs for the *Fiducial*, *Polar* and *Equatorial* systems using the *Full* and the *LW* response.

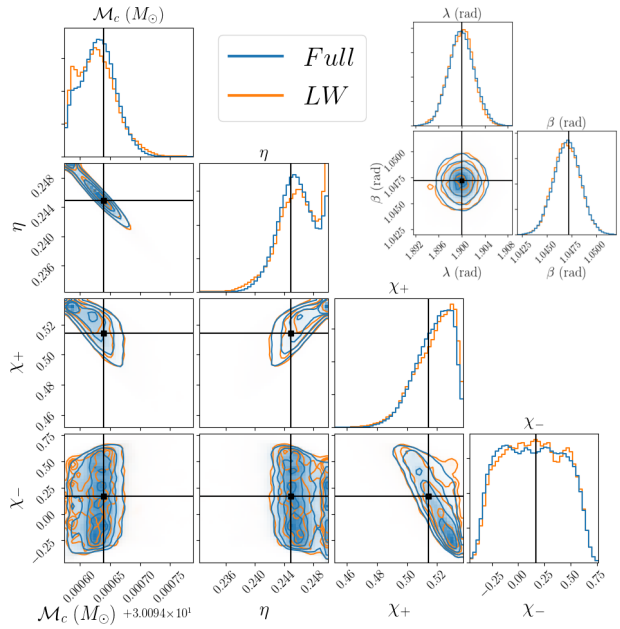

Figure 3.17: Comparison of inferred distributions of intrinsic parameters and sky location using the *Full* and *LW* responses for the *Fiducial* system in the $T_{\rm obs} = 10$yr case.

configurations, and quantify the science goals of the mission.

3.4.4 Long-wavelength approximation

Let us now assess the impact of using the long-wavelength approximation on the parameter estimation. In table 3.6 we show the SNR for the *Fiducial*, *Polar* and *Equatorial* systems using the *Full* and *LW* responses for two observation times. Accounting for the degradation at high frequencies (equation (3.6)), the long-wavelength approximation has little impact on the SNR and seems to barely affect the parameter estimation, as can be seen in figure 3.17. The behaviour is similar for the *Polar* and *Equatorial* systems. Some care is needed in interpreting this result: this comparison shows that the high frequency terms neglected in the long-wavelength approximation have little impact on the posterior of the sky position if the likelihood is computed self-consistently (signal and template are produced using same response, either *LW* or *Full*). However, when analysing real data these high frequency terms cannot be neglected.

	$T_{\rm obs} = 4$yr			$T_{\rm obs} = 10$yr		
	$\ln \mathcal{L}(\theta_0)$	$\max(\ln \mathcal{L})$	$\tilde{\rho}$	$\ln \mathcal{L}(\theta_0)$	$\max\ (\ln \mathcal{L})$	$\tilde{\rho}$
Fiducial	-50	-2	0.99	-268	-38	0.91
Polar	-45	-3	0.99	-234	-30	0.92
Equatorial	-55	-2	0.99	-288	-34	0.94

Table 3.7: Loglikelihood at the true point, maximum likelihood and relative SNR (defined in equation (3.22)) when using the *LW* response in the Bayesian analysis for data generated with the *Full* response.

In other words, these effects in the full response can indeed be subdominant in the parameter recovery, if more information comes from other effects like the LISA motion and the main Doppler modulation, while not being negligible in the signal itself. To illustrate this, we simulate data for the *Fiducial*, *Polar* and *Equatorial* systems using the full response and perform a Bayesian analysis using the long-wavelength approximation to compute templates. In table 3.7, we give the log-likelihood evaluated at the true point, the maximum likelihood and the maximum overlap

$$\tilde{\rho} = \max_h \left(\frac{(d|h)}{\sqrt{(d|d)(h|h)}} \right). \tag{3.22}$$

In practice, we compute the maximum overlap by optimising over the samples. The quantity $1 - \tilde{\rho}$ indicates how much SNR would be lost if wrong templates were used for the detection of signal. Up to $\sim 10\%$ of the SNR could be lost, given the already low SNR of SBHBs in LISA this would severely compromise our chances of detecting such sources. The very small value of the likelihood at the true point by itself shows that using the long-wavelength approximation will have an impact on the parameter estimation. Figure 3.18 compares the posterior distributions obtained by using templates generated with the *Full* or *LW* response while analysing the *Fiducial* system, with $T_{\rm obs} = 10$yr and generated with the *Full* response. This system has a significant bandwidth and the *LW* template cannot fit simultaneously the low and high frequency content of the signal, causing severe biases in the parameter estimation and loss of SNR. The same system but with $T_{\rm obs} = 4$yr, shows different result, the *LW* template is effectual enough to fit the signal rather well with the largest bias appearing only in $\psi - \varphi$ distribution as a compensation for terms neglected in the response and with a mild drop in the SNR. However, those signals are quite weak, and we do not have the luxury to lose even a small portion of SNR. Thus, these findings seem to validate the long-wavelength approximation for prospective parameter estimation studies, if it is used consistently for injecting and recovering the signal, while it would be inappropriate to analyse real data. However, we should remember that we did not explore the full parameter space, while equation (3.6) is valid as an average over orientations, so a different choice of parameters could yield worse results. We also note that the full response (equation (1.69)) is actually quite simple and not more expensive computationally, while being unambiguous and eliminating the need for the averaging entering equation (3.6).

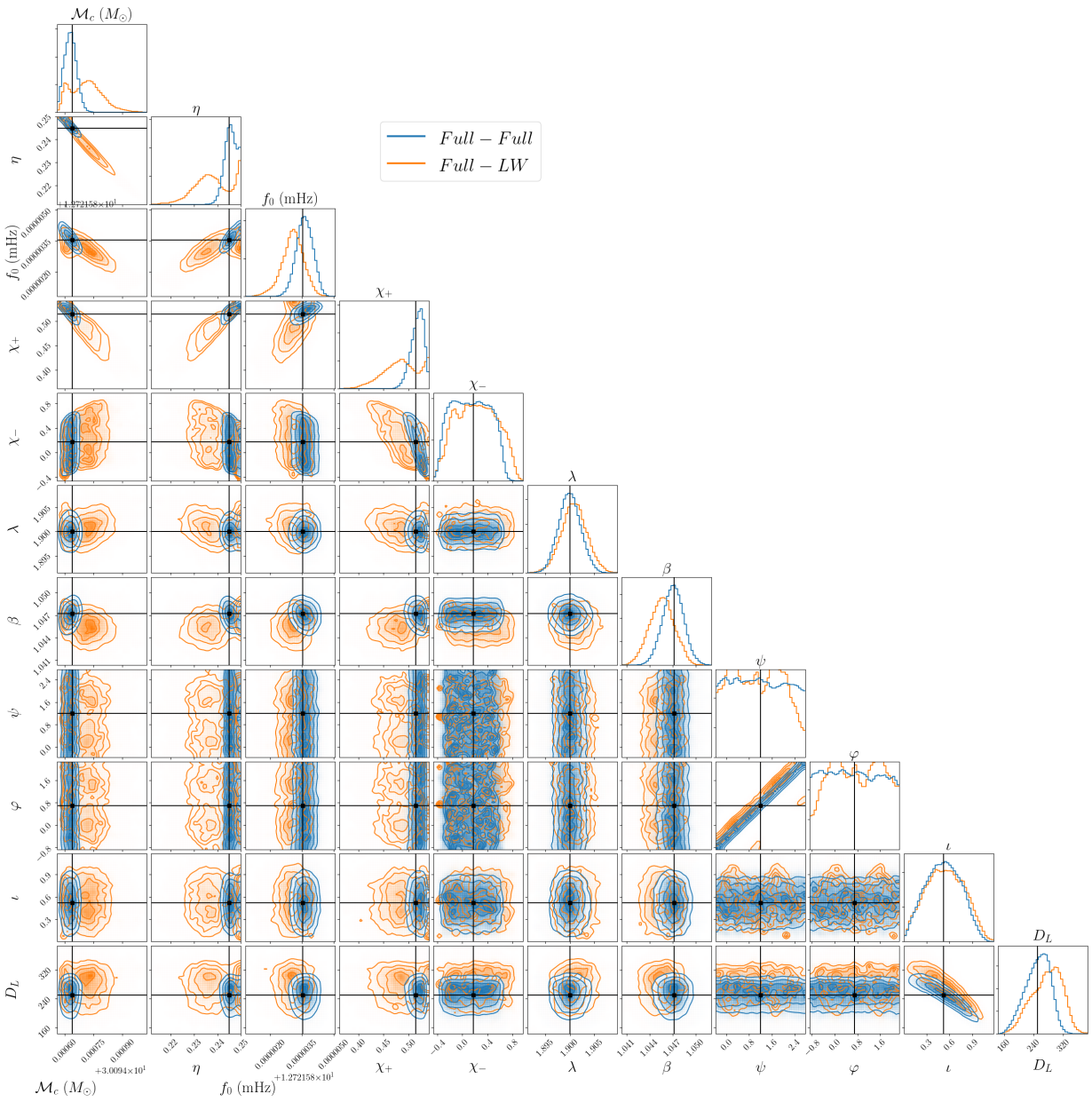

Figure 3.18: Comparison of the inferred distributions for the *Fiducial* system in the $T_{\rm obs}$ = 10yr case using the *Full* and the *LW* response in the Bayesian analysis. In both cases, data was generated with the *Full* response.

3.5 Discussion

In this chapter we explained how the parameter estimation for the observation of SBHBs with LISA evolves across the parameter space. To do so, we simulated LISA data and performed a Bayesian analysis for many systems, starting from a GW150914-like system and varying the parameters of the system in turn. The main finding is that parameter estimation results are most sensitive to the frequency span of the gravitational wave and its

extent within LISA sensitivity region given the observation duration, or in other words, how much the signal chirps during the observation time. The chirp mass and the sky location are always well recovered (typically within 10^{-4} relative and 1 deg^2 respectively), but the effective spin and the individual masses can only be measured for chirping systems. These results are expected to extend to more massive systems such as "light" IMBHBs, i.e. with component masses $\mathcal{O}(10^2 M_\odot)$ and systems similar to the massive binary recently announced by the LIGO/Virgo collaboration [190, 37].

The knowledge and understanding obtained in the study of parameter estimation can be utilised for the development of search tools: (i) the parameter estimation for these systems is mainly unimodal, with secondary modes appearing either in special cases (like the *Equatorial* system) or under the effect of priors where the likelihood is weakly informative (like the symmetric mass ratio for nonchirping systems); (ii) the chirp mass and the sky coordinates are the best measured parameters, so we can make a hierarchical search starting with those parameters and taking into account the correlations, which are explored and understood in section 3.4; (iii) the effective Fisher is an efficient proposal for a Bayes-based search once we start to find indications for a candidate gravitational wave signal in the data. In addition, we can perform an incremental analysis starting with a half-year-long data segment and progressively increasing it. This works as a natural annealing scheme and should help in detecting (especially) chirping systems.

A major improvement to this work would be the inclusion of orbital eccentricity. Astrophysical formation models predict that binaries formed dynamically should have large eccentricities [199, 200]. However, by the time these binaries reach the frequency band of ground-based detectors, they have circularised. Thus, LISA could play an important role in the discrimination between different formation channels [206, 207, 208, 209, 210]. Furthermore, neglecting eccentricity could affect the parameter estimation and detection efficiency. We are currently limited by the lack of fast eccentric waveforms, but work is ongoing in this direction [329, 330, 331, 332, 333]. Concerning spins, binaries formed dynamically are expected to have misaligned spins [198], causing the binary's orbit to precess. The system might endure a sizeable number of precession cycles over the lifetime of LISA, albeit with a small opening angle of the precession cone for a binary in its early inspiral. Precession effects can become more important close to merger and therefore should be considered carefully when relating the signal in the LISA band with the signal in the ground-based detectors band. The investigation of precession effects is left for future work.

Detection of even few SBHBs by LISA that merge somewhat later with a very high SNR in the band of ground-based detectors [198] will constitute "golden events". Beyond all the benefits of multiband detections *per se*, the information provided by LISA itself will be very valuable. The good estimate on the time to coalescence and the sky location could be used for electromagnetic follow-up of the source as we will discuss in chapter 5. These measurements could be used to tighten the constraints on the Hubble constant (H_0) even if no electromagnetic counterparts are detected, using galaxy catalogues [334, 335, 336]. Finally, the observation of SBHBs during their early inspiral will allow us to probe low-frequency modifications due to deviations from general relativity and/or environmental effects with high precision, as we will discuss in the next two chapters.

Chapter 4

Tests of general relativity with gravitational waves

Gravitational wave observations provide an excellent opportunity to test general relativity in the strong field dynamical regime, but due to the complexity of the task, few full results derived from first principles are currently available (see section 1.3). As an alternative, we can assess how theoretically-motivated phenomenological modifications to the generation and/or propagation of gravitational waves affect the detected signal. In this chapter we reproduce the results of [34] and [35][1].

First, we focus on modifications to the inspiral evolution of BBHs. Black holes are purely gravitational objects, therefore BBHs are very "clean" systems (i.e. with no matter effects as long as they are in vacuum) that can be used to probe deviations from general relativity. Since LISA will observe SBHBs in the long low-frequency inspiral phase up to several years, these observations will be very sensitive to any dephasing affecting the low-frequency regime and will allow us to probe deviations from general relativity. Previous works on this topic [337, 338, 339, 340, 341, 342] used Fisher matrices to perform parameter estimation, and the long-wavelength approximation for the LISA response. We introduce the parametrised post-Einsteinian formalism [343], which provides a unified framework to capture deviations from general relativity during the inspiral, and use it to assess how LISA observations will allow us to constrain the presence of dipole radiation in BBHs and the mass of the graviton, using the full Bayesian analysis presented in the previous chapters. We also estimate the improvement thanks to multiband observations.

Next, we consider a different kind of test of general relativity: probing the nature of compact objects. For this purpose, we inspect the coalescence of binaries made of ECOs. Detecting such objects would be a smoking gun for beyond general relativity/standard model physics. As these objects have a gravitational behaviour very similar to neutron stars and black holes, specific gravitational wave templates are needed to identify putative ECO binaries. Unfortunately, the vast majority of models of ECOs are not yet complete enough to construct their corresponding gravitational wave templates, especially in the binary merger case, except for (some types of) binary boson stars (BBSs). Furthermore, even for BBSs,

[1] I derived all the results and, except for figure 4.4, I realised all the figures in this chapter, with the help of my collaborators. Figure 4.4 is a courtesy of a friend of mine, Tallulah Frapier.

full solutions are available only in few cases [344, 345, 346]. The lack of templates beyond the standard paradigm could spoil our chances of observing these systems, because the SNR is highest with matched filtering techniques (see section 2.1). In order to fully exploit the potential of gravitational wave observations and ready the analysis required to discern ECOs through the full inspiral, merger and post-merger phases, we propose a toy model aiming to capture the main features of the full signal emitted by such binaries. We then use it to assess the detectability of ECO binaries and our ability to distinguish them from standard compact binaries with current and future gravitational wave detectors.

4.1 Theory-agnostic inspiral tests of general relativity with LISA

4.1.1 Parameterised post-Einsteinian formalism

A theory-agnostic phenomenological framework to describe and classify deviations from general relativity, at least during the low-frequency inspiral, is provided by the parametrised post-Einsteinian formalism [343]. A similar formalism is applied in the TIGER pipeline [347] used in LIGO/Virgo tests of general relativity [12, 13]. In these approaches the general relativistic phase and amplitude are modified as

$$\tilde{h}(f) = \tilde{h}_{GR}(1 + a_1(\pi\mathcal{M}_c f)^{a_2})e^{-ib_1(\pi\mathcal{M}_c f)^{b_2}}\,, \tag{4.1}$$

where $\tilde{h}_{GR}$ is the frequency domain waveform of general relativity, while the deviations from general relativity are described by the dimensionless parameters a_1, b_1, a_2 and b_2. Since interferometers are mostly sensitive to the phase of gravitational waves, we will neglect the amplitude modifications and set $a_1 = 0$. This approximation has been discussed and justified in [348], to which we refer for further details. Different values of b_1 and b_2 correspond to distinct physical effects (see, e.g., [340, 349, 138, 350, 351, 352, 353, 354, 355, 342] for some specific modifications of general relativity and their mapping to the parametrised post-Einsteinian parameters b_1 and b_2). Note that these physical effects could be common to different theories, and measuring nonzero values of some of these parameters might not allow to unambiguously identify the "correct" theory of gravity. However, this could be used as a smoking gun to identify the presence of beyond general relativity effects. We will focus on two specific examples: one affecting the generation of gravitational waves (dipolar gravitational wave emission) and one affecting their propagation (nonzero mass for the graviton).

In section 1.3, we saw that the presence of dipole radiation is a generic prediction of modified gravity theories, and that it is related with violations of the strong equivalence principle. We will now compute how it affects the gravitational wave signal. Obeying the relative ordering of terms in the multipolar expansion, the dipolar gravitational wave energy flux must come with a factor v^{-2} (v being the relative velocity in the binary) relative to the leading order quadrupolar term. Following [356] we write the total energy flux during the early inspiral regime as

$$P_{\rm tot} = P_{\rm GR}(1 + Bv^{-2}), \tag{4.2}$$

where $P_{\rm GR}$ is the general relativity quadrupole flux (see equation (1.30)), and B (which vanishes in general relativity) is a theory and system dependent parameter that characterises

dipole emission. As discussed in section 1.3, B typically goes as the difference of sensitivities (to additional fields in the action) squared. Using the energy balance equation and Kepler's law as in section 1.2.2, we get a modified equation for the orbital speed of the binary

$$\dot{\omega}_{\rm orb} = \frac{96}{5}\mathcal{M}_c^{5/3}\omega_{\rm orb}^{11/3} + \frac{96}{5}\eta^{2/5}\mathcal{M}_c B\omega_{\rm orb}^3. \tag{4.3}$$

Using the stationary phase approximations (equations (1.50), (1.51), (1.52), (1.53)), and assuming B to be small ($B(\pi\mathcal{M}_c f)^{-2/3} \ll 1$), we get for the phase of the (2,2) harmonic

$$\Psi_{22}(f) = -\left[2\pi f t_c - 2\phi_c - \frac{\pi}{4} + \frac{3}{128}(\pi\mathcal{M}_c f)^{-5/3} - \frac{3}{224}B\eta^{2/5}(\pi\mathcal{M}_c f)^{-7/3}\right]. \tag{4.4}$$

Thus, comparing this equation with (1.54), we see that dipole radiation leads to a -1PN modification that can be described within the parametrised post-Einsteinian framework with [356]

$$b_1 = -\frac{3}{224}\eta^{2/5}B \tag{4.5}$$

$$b_2 = -7/3. \tag{4.6}$$

Because of the violation of the strong equivalence principle, the value of B might depend on the nature of the system. To make it explicit that we are considering dipole radiation in black hole systems, we will use the symbol $B_{\rm BH}$ for the rest of this manuscript.

The propagation of gravitational waves could be altered due to a modified dispersion relation for the graviton [357, 355]:

$$E^2 = p^2c^2 + \mathbb{A}_{\alpha_d}p^{\alpha_d}\,, \tag{4.7}$$

where E and p are the graviton's energy and linear momentum, while $\mathbb{A}$ and α_d are free parameters. For example, Hořava gravity predicts the presence of terms with both $\alpha_d = 4$ and $\alpha_d = 6$ [358, 359], while the case $\alpha_d = 0$ corresponds to a massive graviton [121]. From equation (4.7), at first order in $\mathbb{A}$ the graviton's velocity reads

$$v_g^2 = 1 - \mathbb{A}E^{\alpha_d - 2}\,. \tag{4.8}$$

By measuring the time delay between the gravitational waves and light emitted by GW170817, it is possible to bound the fractional difference between the speed of gravitational waves and that of light to less than 10^{-15} [360]. A modified dispersion relation also deforms the shape of the gravitational wave signal as it propagates, since each frequency travels at a different (phase and group) speed [355]. This allows for testing modified dispersion relations even in the absence of electromagnetic counterpart, as is expected to be the case for SBHBs. This is the technique by which the LVC has obtained graviton mass bounds [12, 11, 13] competitive with Solar System observations [361].

In more detail, it was shown in [355] that a modified dispersion relation like equation (4.7) changes the phase of the gravitational wave signal, and this modification corresponds to parametrised post-Einsteinian coefficients [355]

$$b_1 = -\frac{\pi^{2-\alpha_d}}{1-\alpha_d}\frac{D_{\alpha_d}\mathcal{M}_c^{1-\alpha_d}}{(1+z)^{1-\alpha_d}}\frac{\mathbb{A}}{(hc)^2}, \tag{4.9}$$

$$b_2 = \alpha_d - 1\,, \tag{4.10}$$

where D_{α_d} is a distance variable given by $D_{\alpha_d} = \frac{(1+z)^{1-\alpha_d}}{H_0}\int_0^z \frac{(1+z')^{\alpha_d-2}}{\sqrt{\Omega_m(1+z')^3+\Omega_\Lambda}}\mathrm{d}z'$. In this expression, z is the cosmological redshift of the source, H_0 is the Hubble constant and Ω_m and Ω_Λ are the matter and dark energy density parameters respectively.

In this manuscript we will focus on the case of a massive graviton, $\alpha_d = 0$ and $\mathbb{A} = m_g^2c^4$, where m_g is the graviton's mass. As can be seen in equations (4.9) and (4.10), a nonzero graviton mass leads to a 1PN modification and the phase shift increases with chirp mass and distance. Thus, we may expect the best gravitational wave constraints on this effect to come not from GW170817, but from more massive and distant systems [362]. For a given source, though, distance also reduces the SNR, so experimental bounds are defined by the interplay of those two factors.

4.1.2 Method

We want to assess the sensitivity of LISA to modifications of general relativity. To that purpose, we work in a full Bayesian framework and consider two different MCMC experiments. The first one consists of simulating the signal predicted by general relativity, for a few astrophysical systems, and trying to recover it with templates where either dipole radiation or a massive graviton is allowed. Our goal is to place upper bounds on $B_{\rm BH}$ and m_g, i.e. to determine how well gravitational wave observations can constrain those deviations, accounting also for possible correlations between parameters. The second experiment consists of simulating signals containing a modification to general relativity, for the same astrophysical systems, and estimating how well can we detect this modification.

In order to obtain an estimate of how much multiband observations could improve our ability to detect or constrain modifications to general relativity, we repeat each of the previous experiments, but placing a very tight prior constraint on the coalescence time. Indeed, this parameter is extremely well constrained by ground based detectors, with a typical accuracy of a few milliseconds. We refer to the analysis mimicking multiband observations as *LISA+Earth*, and to the one using LISA alone as *LISA-only*. A proper multiband analysis will yield an even more significant impact on the parameter estimation, by providing valuable constraints on intrinsic parameters such as the mass ratio and the spins, which could be poorly constrained by observations with LISA only, as we saw in the previous chapter. For this reason, our results in the *LISA+Earth* case can be considered as conservative. We consider only one modification at the time (either dipole radiation or mass of graviton), and, as mentioned above, we neglect modifications to the amplitude of gravitational waves.

Signal generation

We generate data and parametrise SBHBs as described in section 3.1. Recall that we consider quasicircular binaries consisting of spinning black holes with aligned or anti-aligned spins with respect to the orbital angular momentum, and generate only the $(2, \pm 2)$ harmonic (using PhenomD). Modifications to general relativity are added to $\tilde{h}_{2\pm2}$ as described in section 4.1.1. We assume a four years mission duration, and an ideal 100% duty cycle. We use the LISA proposal power spectral density [29], including the confusion noise due to GBs [315].

We consider three different astrophysical systems. System 1 one is similar to GW150914. Systems 2 and 3 were chosen to be significantly different from GW150914 to evaluate the dis-

Variable	System 1			System 2	System 3
m_1 ($\mathrm{M}_\odot$)	38			60	50
m_2 ($\mathrm{M}_\odot$)	32			50	40
$m_{1,s}$ ($\mathrm{M}_\odot$)	35.2			53.1	45.8
$m_{2,s}$ ($\mathrm{M}_\odot$)	29.6			44.2	36.7
t_c (yrs)	8.3	4	2.5	4	5.2
f_0 (mHz)	12.4765	16.4265	19.5265	12.3826	12.783
χ_1	0.05			0.10	0.78
χ_2	0.02			0.33	0.22
λ (rad)	3.5064			0.2283	2.9966
β (rad)	0.1777			-0.431	-0.577
ψ (rad)	1.1			2.8	1.5
φ (rad)	5.4			6.0	0.88
ι (rad)	2.77			0.52	0.34
D_L (Mpc)	380			640	420
z	0.08			0.13	0.09
T_{obs} (yrs)	4				
SNR	10.5	13.2	10.9	13.1	15.0

Table 4.1: Systems for which we simulate data and that we use to constrain modifications to general relativity.

persion of constraints/measurements of non-general relativity parameters between different systems. Since low mass systems are less likely to be detected by LISA, we opted for heavier systems. The distances were chosen to keep the SNR at a comparable level for all systems, so that it does not bias our results. Notice that System 3 has quite high spins, and as we will discuss in section 4.1.5 this can bias the measurement of deviations from general relativity. In addition, for System 1 we consider three different values of the initial frequency, so that the time to coalescence (from the start of LISA observations) takes values of 8.3 years, 4 years and 2.5 years. The choice of the initial gravitational wave frequency strongly affects the parameter estimation (as discussed in the previous chapter), and allows us to explore constraints on general relativity modifications as a function of the signal's "chirpiness". The parameters of the systems are given in table 4.1. We also provide the time to coalescence and the SNR for each system.

4.1.3 Bayesian analysis

We deploy the full Bayesian framework described in the previous chapters to explore the accuracy with which LISA can estimate the parameters of the source and put constraints on modifications to general relativity. In the *LISA-only* scenario, we use the *Fiducial* prior described in section 3.3.2 for general relativity parameters, and assume a flat prior for the coefficients parametrising deviations from general relativity. We assume $B \geq 0$ and $m_g \geq 0$, corresponding to positive extra gravitational wave fluxes (besides the general relativity ones)

and real positive masses respectively. In the *LISA+Earth* case we use a Gaussian prior with standard deviation $\sigma_{t_c} = 1$ ms centred around the true value of the coalescence time instead of a flat prior on f_0.

We sample the posterior distribution using our MHMCMC algorithm, described in section 3.2. In the *LISA+Earth* scenario we use t_c as a sampling parameter rather than f_0. Instead of m_g, we use $\frac{D_0 m_g}{(1+z)D_L}$, in order to avoid the computation of D_0 (see equation (4.9)) at every point, thus saving computational time. Posteriors are reweighed at the end. From equations (4.5) and (4.9), we expect non-general relativity parameters to correlate with intrinsic parameters, therefore they are added to the first group of parameters (intrinsic parameters) during the burn-in phase. Finally, it is noteworthy that when sampling the posterior, we allow the chains to explore negative values of $B_{\rm BH}$ and m_g too and impose the cut a posteriori. This procedure reduces the number of effective points that we obtain out of a chain, but it allows for better sampling of the region close to the prior boundary. In order to cross-check our results we also used the parallel tempering code `PTMCMC` [363]. We obtained an excellent agreement between the two samplers, and especially for the $B_{\rm BH}$ and m_g marginalised distributions.

4.1.4 Putting upper bounds on non-general relativity parameters

We assume that the gravitational wave signal follows general relativity (simulated data) and we use non-general relativity templates as a search model for each system given in table 4.1. The aim here is to set an upper limit on the phenomenological deviations from general relativity. In the left panel of figure 4.1 we show the marginalised distribution of $B_{\rm BH}$ for System 1 ($t_c = 4.0$ years) both in the *LISA* and *LISA+Earth* scenario. The distribution peaks at the true value of the dipolar amplitude (i.e. 0) and has a compact support extending up to the maximum $B_{\rm BH}$ compatible with observations.

For most of the cases/systems considered here (except for System 3, to which we will come back when discussing the possibility of detecting modifications to general relativity in 4.1.5), we obtain similar distributions for $B_{\rm BH}$ and for m_g, as displayed in the left panel of figure 4.1. This allows us to place upper limits as 90% credible interval (0.9 quantile of the corresponding marginalised distribution). We present the upper bounds on $B_{\rm BH}$ and m_g obtained with each system and in each scenario in tables 4.2 and 4.3 respectively. We also provide the currently available constraints for comparison. The best constraints on dipole radiation in binary systems come from binary pulsars (see section 1.3). However, since the value of the dipolar amplitude might depend on the nature of the system, as argued in section 1.3, we only consider here current bounds for systems containing at least one black hole. For those, the most stringent current bound comes from the observation of a low mass X-ray binary [364]. This constraint is slightly better than the one obtained with current gravitational wave detections [340]. For m_g, we show the constraint obtained by the LVC after the first half of the third observational run [13]. A somewhat better upper bound on the mass of the graviton was obtained from Solar System observations [361], but it is unclear that a constraint from such a static configuration should be the same as for highly dynamical systems like BBHs.

The results presented in tables 4.2 and 4.3 show that the best constraints are given by the systems which are observed during the whole four years mission duration before passing

	$B_{\rm BH}$	
	LISA-only	*LISA+Earth*
System 1($t_c = 8.3$ years)	$< 1.1\ 10^{-7}$	$< 1.1\ 10^{-7}$
System 1($t_c = 4.0$ years)	$< 9.2\ 10^{-9}$	$< 3.2\ 10^{-9}$
System 1($t_c = 2.5$ years)	$< 6.8\ 10^{-8}$	$< 7.2\ 10^{-9}$
System 2	$< 1.5\ 10^{-8}$	$< 4.6\ 10^{-9}$
System 3	$< 1.9\ 10^{-7}$	$< 2.5\ 10^{-8}$
Current constraints	$< 4 \times 10^{-2}$	

Table 4.2: 90% confidence constraints on $B_{\rm BH}$ obtained with each system, in both the *LISA-only* and *LISA+Earth* scenario. Improvements by one of order of magnitude can be achieved when restricting t_c. Already in the *LISA-only* scenario, all the systems considered here would allow us to improve current constraints for black hole systems.

	m_g (eV)	
	LISA-only	*LISA+Earth*
System 1($t_c = 8.3$ years)	$< 9.3\ 10^{-23}$	$< 2.5\ 10^{-23}$
System 1($t_c = 4.0$ years)	$< 2.0\ 10^{-23}$	$< 1.5\ 10^{-23}$
System 1($t_c = 2.5$ years)	$< 3.1\ 10^{-23}$	$< 2.5\ 10^{-23}$
System 2	$< 1.2\ 10^{-23}$	$< 1.2\ 10^{-23}$
System 3	$< 3.5\ 10^{-23}$	$< 2.0\ 10^{-23}$
Current constraints	$< 1.8 \times 10^{-23}$	

Table 4.3: 90% confidence constraints on m_g obtained with each system, in both the *LISA-only* and *LISA+Earth* scenario. As explained in the main text, restricting t_c thanks to a multiband detection improves the bounds. System 1 ($t_c = 4.0$ years) and System 2 would allow to slightly improve on current bounds, but we expect that by the time LISA flies ground-based detectors will have placed a more stringent constraint on m_g.

out of band (System 2 and System 1 ($t_c = 4.0$ years)). In addition, System 1 ($t_c = 2.5$ years) gives better constraints than System 3 and System 1 ($t_c = 8.3$ years). Those results are in very good agreement with the finding discussed in the previous chapter, i.e. that most of the constraining power (on intrinsic parameters) comes from the chirp of the system. Although this might seem counterintuitive for low-frequency modifications such as dipole radiation, it can be explained by the correlation of non-general relativity parameters with intrinsic

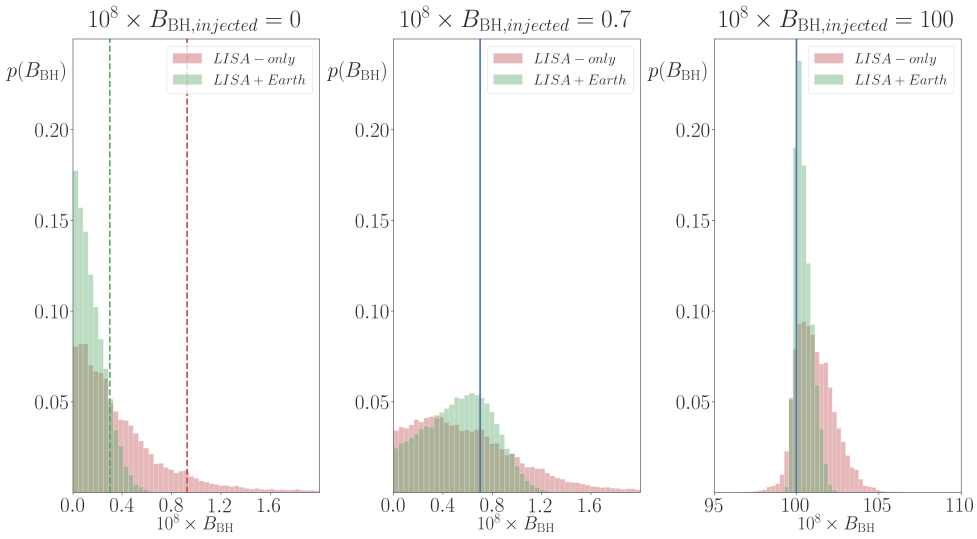

Figure 4.1: Distribution of the dipolar amplitude for System 1 (merging in 4 years), when using *LISA-only* (red) and *LISA+Earth* (green). In the left panel, the injected value is zero and the dashed lines indicate the upper bound that we can put on $B_{\rm BH}$ (corresponding to the 90% confidence interval). In both scenarios the upper bound is much below the current constraint (4×10^{-2}). In the middle and right panels the injected value is 0.7×10^{-8} and 1.0×10^{-6} respectively, indicated by the blue solid line. These values were chosen so that one is far above the bound that we can put on $B_{\rm BH}$ in the *LISA+Earth* scenario, and the other is of the same order. Since zero is not in the support of the posterior in the right panel, in this case we could safely claim the detection of a modification to general relativity, unlike for the posterior in the middle panel.

parameters such as mass ratio and spins. Large uncertainties in the symmetric mass ratio and in the effective spin lead to larger errors on parameters correlated to them, such as the chirp mass and non-general relativity parameters.

Overall, restricting t_c improves the constraints on non-general relativity parameters, but it does not have the same impact for all systems. An interesting observation is that although System 3 gives a slightly worse constraint on $B_{\rm BH}$ than System 1 ($t_c = 8.3$ years) in the *LISA-only* scenario, that constraint improves by an order of magnitude in the *LISA+Earth* scenario, whereas the constraint from System 1 ($t_c = 8.3$ years) remains unchanged. To understand this, we transformed the samples obtained in the *LISA-only* case to infer the time to coalescence of the systems (using the stationary phase approximation, equation (1.70)), and we found that for all systems except System 1 ($t_c = 8.3$ years) there is a very strong correlation between $B_{\rm BH}$, $\mathcal{M}_c$ and t_c. This is why restricting t_c helps to improve the bound on $B_{\rm BH}$. Because we are observing System 1 ($t_c = 8.3$ years) at lower frequencies, the correlation between $B_{\rm BH}$ and $\mathcal{M}_c$ is dominant. Thus restricting t_c does not have much impact on the estimation of either parameter, and in particular the bound on $B_{\rm BH}$ does not improve. However, a real multiband detection would yield additional constraints on the parameters of the source and most likely improve the constraint on $B_{\rm BH}$ for System 1 ($t_c = 8.3$ years). We see that the impact of restricting t_c on the upper bound of m_g is opposite:

we get the best improvement for the systems that start the farthest from merger (System 1 ($t_c = 8.3$ years) and System 3). The reason is similar: LISA observes a gravitational wave signal at quite low frequency, while the effects of mass ratio, spins and m_g appear beyond the leading post-Newtonian order terms, and therefore they are (relatively) poorly constrained (as explicitly shown in the previous chapter). Restricting t_c to be in a narrow interval imposes an additional constraint on those parameters, which allows one to improve the bound on m_g. For systems closer to coalescence, the frequency evolution during LISA observations is sufficient to set tight bounds, and the additional constraint coming from restricting t_c only moderately improves the results.

Our projected constraints on $B_{\rm BH}$ are in good agreement with [340, 337] and should improve current bounds for black hole systems by at most seven orders of magnitude. For m_g, we observe that multiband observations of System 1 ($t_c = 8.3$ years) and System 2 should slightly improve the current constraints. However, we expect that by the time LISA flies ground-based detectors will have improved their constraint on m_g. Our bounds are somewhat better than the ones obtained with GW150914-like systems in [341, 342]. One possible explanation for this difference is the higher SNR of our systems. Finally, the reported upper bounds are worse than the projected bounds obtained from the observation of supermassive black holes binaries by LISA in [341], due to a significant difference in the SNR and in the distance to those sources. We stress again that a real multiband analysis would not only restrict t_c, but also put additional constraints on all intrinsic parameters, improving parameter estimation as a whole. As a consequence, bounds on non-general relativity parameters from SBHBs observed with LISA and ground detectors could be more stringent than those presented here in the *LISA+Earth* scenario.

4.1.5 Detecting modifications to general relativity

We now turn to the case where the injected signal has a nonzero value of either $B_{\rm BH}$ or m_g. Based on the results presented in tables 4.2 and 4.3, we choose $B_{\rm BH}$ well above the bounds presented there, but still below currents constraints ($B_{{\rm BH},injected} = 100 \times 10^{-8}$), as well as $B_{\rm BH}$ and m_g of the same order as those bounds ($B_{{\rm BH},injected} = 0.7 \times 10^{-8}$ and $m_{g,injected} = 1.0 \times 10^{-23}$ eV). We choose a single value for m_g because there is less room between our projected bounds and the currents constraints.

In the middle and right panels of figure 4.1, we show the marginalised distribution of $B_{\rm BH}$ for System 1 ($t_c = 4.0$ years) both in the *LISA* and *LISA+Earth* scenario, when the injected value is $B_{{\rm BH},injected} = 0.7 \times 10^{-9}$ and $B_{{\rm BH},injected} = 100 \times 10^{-8}$ (respectively), denoted by the blue solid line. For the higher $B_{\rm BH}$, the distribution peaks around the injected value and is not compatible with zero, clearly indicating the presence of the effect. For the lower $B_{\rm BH}$, the distribution is very flat in the *LISA-only* scenario and more peaked in the *LISA+Earth* scenario. Similarly, in figure 4.2 we show the distribution of m_g for System 2 and for an injected value of 10^{-23} eV. For the reasons explained above, the impact of restricting t_c is milder, but it still slightly improves the sharpness of the posterior around the injected value. Although the peak of the posterior distribution is away from zero (and centred on the true value), as seen in figure 4.1 and figure 4.2 for the *LISA+Earth* scenario, we cannot still rule out general relativity (a vanishing deviation from general relativity is compatible with the data), and we cannot safely claim the detection of a deviation from general relativity.

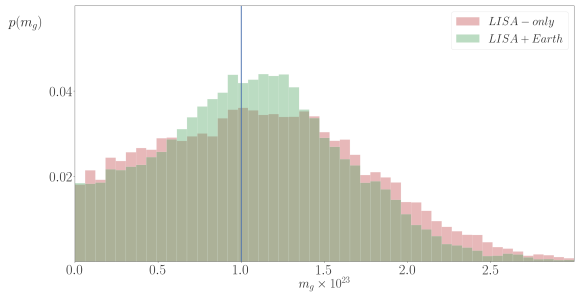

Figure 4.2: Distribution of the mass of the graviton for System 2, when using *LISA-only* (red) and *LISA+Earth* (green). The injected value is 1×10^{-23} eV, indicated by the blue solid line, below the current constraint 5×10^{-23}. This value was chosen to be close to the upper bound that we can put in the *LISA+Earth* scenario. Despite the peak around the injected value, zero is in the support of the distribution, so we cannot safely claim the detection of a non-general relativity effect.

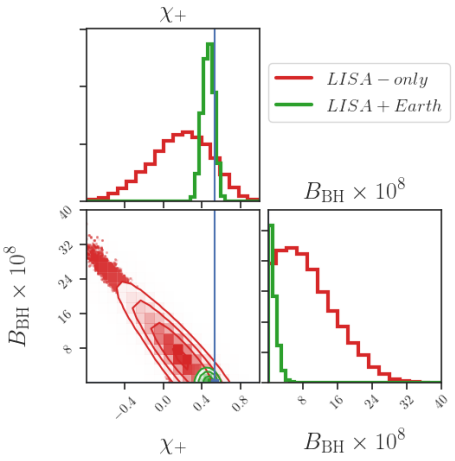

Figure 4.3: Distribution of the dipolar amplitude for System 3, when using *LISA-only* (red) and *LISA+Earth* (green). The injected value is 0 and dashed lines indicate the upper bound that we can put on B (corresponding to the 90% confidence interval). Notice that in the *LISA-only* case the distribution peaks away from 0, which would seem to indicate the presence of a nonzero modification, but this feature disappears in the *LISA+Earth* case. This is due to the poor determination of intrinsic parameters such as the spins, which leads to a bias in correlated parameters such as $B_{\rm BH}$. When constraining t_c, the determination of the intrinsic parameters improves, suppressing this bias.

Detailed analysis reveals that while analysing the general relativity signal, the peak of the distribution for $B_{\rm BH}$ could be away from zero even in the noise-free approximation. The corner plot presented in figure 4.3 shows the distributions of χ_+ and $B_{\rm BH}$ and the correlation between them for System 3. Note that the true value of $B_{\rm BH}$ here is zero, however, in the *LISA-only* scenario the distribution peaks at a nonzero value, mimicking a deviation from general relativity. Since we do not observe the chirp of this system, the likelihood is very

	$10^8 \times B_{\rm BH,injected} = 0.7$		$10^8 \times B_{\rm BH,injected} = 100$		$10^{23} \times m_{g,injected} = 1.0$	
	LISA-only	*LISA+Earth*	*LISA-only*	*LISA+Earth*	*LISA-only*	*LISA+Earth*
System 1($t_c = 8.3$ years)	$5.1\pm^{+6.8}_{-5.1}$	$5.1^{+6.8}_{-5.1}$	$105.0^{+15.5}_{-12.1}$	$102.8^{+12.8}_{-11.3}$	$4.5\pm^{+5.3}_{-4.5}$	$1.7^{+2.0}_{-1.7}$
System 1($t_c = 4.0$ years)	$0.5^{+0.7}_{-0.5}$	$0.54^{+0.3}_{-0.5}$	$101.0^{+2.2}_{-1.4}$	$100.3^{+1.1}_{-0.6}$	$1.6^{+1.4}_{-1.6}$	$1.1^{+1.0}_{-1.1}$
System 1($t_c = 2.5$ years)	$1.6^{+4.8}_{-1.6}$	$0.6^{+0.6}_{-0.6}$	$101.5^{+6.7}_{-6.4}$	$100.6^{+2.0}_{-1.0}$	$2.9^{+2.4}_{-2.9}$	$1.29^{+1.3}_{-1.3}$
System 2	$0.7^{+1}_{-0.7}$	$0.6^{+0.5}_{-0.6}$	$101.1^{+2.8}_{-1.9}$	$100.3^{+1.0}_{-0.6}$	$1.1^{+0.9}_{-1.1}$	$1.1^{+0.7}_{-1.1}$
System 3	$8.8^{+11}_{-8.8}$	$1.2^{+1.7}_{-1.2}$	$109.3^{+15.8}_{-11.8}$	$103.4^{+4.6}_{-4.2}$	$2.1^{+2.3}_{-2.1}$	$1.9^{+2.0}_{-1.9}$

Table 4.4: Recovered 90% confidence interval for non-general relativity parameters for different injected nonzero values. For a strong modification $B = 100 \times 10^8$ the posterior peaks around the injected value, and zero is not in the support of the distribution, as in the right panel of figure 4.1. Thus, we could safely claim the detection of a modification to general relativity. In the case of smaller modifications, e.g. $B_{\rm BH,injected} = 0.7 \times 10^8$ or $m_{g,injected} = 1.0 \times 10^{-23}$ eV, the posterior is compatible with 0. Therefore, even in cases where the distribution peaks around the true value, like in figure 4.2 and in the middle panel of figure 4.1, we could not safely claim the detection of a non-general relativity effect.

shallow across the allowed range of χ_+, and the prior, which peaks at $\chi_+ = 0$, dominates. The high spins of the black holes entering System 3 produce a rather high value of χ_+, for which the prior has little support. Thus, we are biased in our estimate of χ_+, and the strong correlation between χ_+ and $B_{\rm BH}$ shifts the peak of the posterior distribution for $B_{\rm BH}$ away from zero. In other words, our prior beliefs are stronger than the information (likelihood) provided by the data itself. This is a similar situation to the *SpinUp* system discussed in the previous chapter (see discussion in section 3.4.1). Restricting t_c puts some constraint on χ_+, suppressing the bias in $B_{\rm BH}$. This bias for the *LISA-only* scenario is much less obvious if the black holes' spins are low like in System 1.

The exercise above indicates the importance of multiband observations. At the same time (especially in the presence of noise) we should be careful and claim the detection of a modification to general relativity only if the distribution of non-general relativity parameters is incompatible with zero. For that reason, whenever the posterior distribution is compatible with zero, we define the 90% confidence interval of $B_{\rm BH}$ and m_g as the values between the 0 and the 0.9 quantiles. Otherwise, in situations as in the right panel of figure 4.1, we define the confidence interval as the values between the 0.05 and 0.95 quantiles, and we report the median as a point estimate. The 90% confidence interval on $B_{\rm BH}$ and m_g are given for each case considered in table 4.4.

The errors on non-general relativity parameters in all systems and scenarios considered are coherent with upper bounds: the cases giving the more stringent bounds are the ones that could detect modifications with higher precision. For completeness, we add that, for systems where the injected value is much lower than the calculated upper bound (e.g. when $B_{\rm BH,injected} = 0.7 \times 10^{-8}$ for System 1 ($t_c = 8.3$ years) or System 3), we cannot distinguish a peak away from zero, and the distribution is very similar to the one in the left panel of

figure 4.1.

In order to further investigate the presence of a modification to general relativity one could compute Bayes factors given by the ratio of evidences of two models : $\mathcal{B}_{M_1,M_2} = \frac{p(d|M_1)}{p(d|M_2)}$. As an example, Bayes factors much larger than 1 would suggest that model M_1 describes data better than model M_2. In our case the difference between models would be the presence (or absence) of some modification to general relativity in the gravitational wave templates. To carry this study we would need to use different samplers, e.g. nested sampling [365]. Additionally, the evidences could be used to weigh the individual posteriors and combine observations. Because the dipolar amplitude will in general be system dependent, stacking events in order to improve the constraint on $B_{\rm BH}$ may not be meaningful. On the other hand, combined observations could definitely improve the constraint on the mass of the graviton [11, 13]. We leave these investigations for future work.

Here, we have considered only perturbative deviations from the BBH signal predicted by general relativity, but we might expect more extreme modifications near the merger, in particular in the case of binaries made of ECOs as we will see next.

4.2 Modelling gravitational waves from exotic compact objects

4.2.1 State of the art

In a sense, the current state of knowledge for the gravitational wave signal emitted by ECO binaries, illustrated in figure 4.4, resembles the situation in the early 2000s for BBHs within general relativity[2]. At that epoch, only the early inspiral and post-merger phases had been reasonably modelled, while no numerical simulations for the merger phase were available until [94, 95, 96] and the large body of work since then.

One expects that for ECO binaries a post-Newtonian description furnishes a fairly good representation of the binary's behaviour in the early inspiral. Gravitational wave signals should be well described by the point-particle binary model until tidal effects become apparent. After coalescence, it is natural to expect either an object of the same nature as the initial bodies or a black hole. The gravitational waves emitted in this regime would be related to fundamental properties of the corresponding object and/or the dynamics of the merger. However, the details of the coalescence phase, which contains precious information on the properties of the original bodies (see section 4.2.2), are unknown. Up to date, few full numerical results are available, and only for some specific models of BBSs [344, 345, 346]. For these reasons, studies on the possibility of distinguishing ECOs from standard compact objects with gravitational waves have focused mainly on these two regimes, e.g. through perturbative modifications to the inspiral signal [367, 368, 369, 370, 371, 372, 373, 374, 375, 376, 377, 378, 379], quasinormal modes of ECOs [380, 381, 382, 118, 383, 384] or echoes after the merger [385, 386, 387, 388, 389, 390, 391, 392, 393, 394, 395, 396, 397, 398]. We start by discussing known features of the merger of non-black hole compact objects, which we utilise to construct our toy model for the full gravitational wave signal of ECO binaries.

[2]Figure 4.4 is largely inspired from figure 9 in [366].

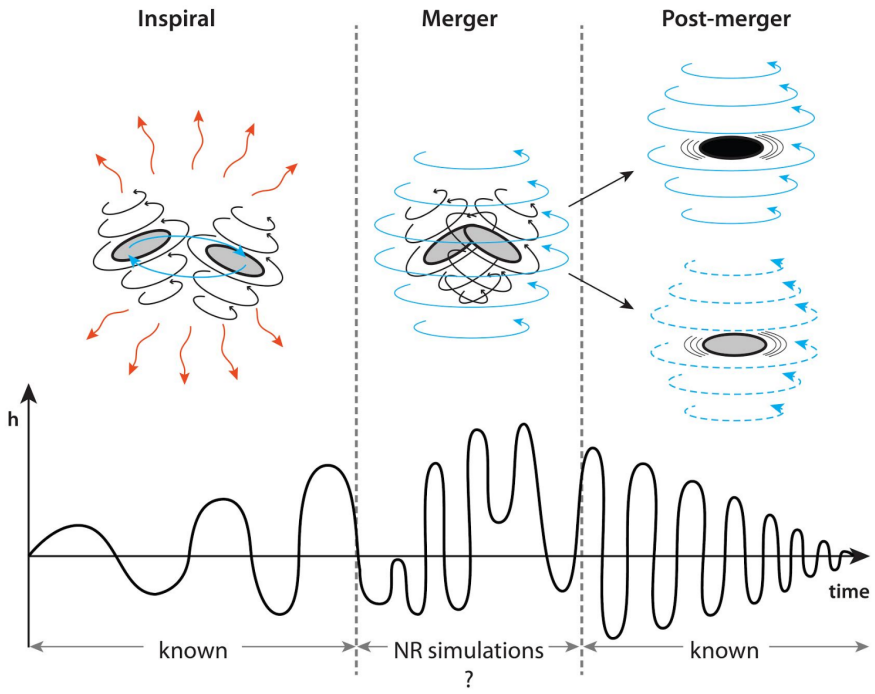

Figure 4.4: Schematic representation of our knowledge of the gravitational wave signal emitted by an ECO binary: within general relativity we have a good idea of the qualitative features of the inspiral and post-merger, but the connection between these two regimes is still largely unknown. We expect that the merger leads to the formation of either a black hole or an (excited) object of the same nature as the initial ECOs, possibly rotating. The remnant relaxes through emission of gravitational waves, which are related to its fundamental properties and/or the dynamics of the merger.

4.2.2 Coalescence of compact objects other than black holes

To construct our model, we will rely on our understanding of BBHs together with BNSs and BBSs. In particular, the differences of the latter two systems with BBHs will inform us how to implement in our model the particular phenomenology that general ECOs might display. For simplicity, we focus on binaries consisting of (nonspinning) identical objects (same nature and same mass) on quasicircular orbits. We denote by m_0 and r_0 the mass and radius of the bodies, and their compactness in isolation by $C_0 = m_0/r_0$.

During the inspiral phase of BNSs and BBSs, tidal effects lead to a correction in the gravitational wave phase at 5PN order relative to BBHs [114, 115, 116] (in general relativity). This correction is proportional to the dimensionless tidal polarisability: $\Lambda = \frac{2}{3}k_2 C_0^{-5}$ [115, 116], k_2 being the tidal Love number. The compactness and the tidal Love number are determined by the equation of state. Neutron stars typically have C_0 in the range $0.14 - 0.2$ (see figure 7 of [65]). To date, proposed models for nonspinning boson stars give similar values, but can reach higher compactness (so far, up to 0.3 [399, 400]). As for k_2, it is typically of the order of 0.1 for neutron stars and currently available models of boson stars [401, 402, 403, 369, 367].

The post-Newtonian description fails when the stars come in contact. This approximately

takes place at the "contact frequency"

$$f_c = \frac{C_0^{3/2}}{m_0}, \tag{4.11}$$

which depends on the equation of state through the compactness. For low enough values of C_0 ($\lesssim 0.29$), this frequency is lower than that of the ISCO for a BBH of the same mass. For this reason, we will employ the terminology "post-contact" rather than merger/post-merger whenever appropriate. For ultracompact exotic objects, $C_0 \sim 0.5$ and the objects reach the ISCO before touching. We thus expect the merger to proceed in a fashion more similar to BBHs, with no post-contact stage. However, no numerical simulations in this regime are available so far to confirm this expectation. Moreover, it is possible that such objects do not exist in nature as they might be nonlinearly unstable [404]. After contact, a rather complex behaviour is displayed by BNSs and BBSs (and thus potentially also by ECO binaries), while the system's evolution is comparatively simpler in the case of BBHs. This behaviour is only explorable through numerical simulations.

After the stars touch, the least bound material might be disrupted (and a portion of it might even be ejected), whereas the remaining part gives rise to an envelope containing the inner cores of the original bodies [405, 344]. Gravitational interaction acts to bring the cores together, but internal restoring forces (whose exact nature depends on the objects) and angular momentum oppose it. As a result, collapse to a black hole can be prevented, forming instead a hypermassive star [406, 344]. As these effects compete, the cores oscillate [405, 344]. Eventually, collapse to a black hole or formation of a stable star ensues. The exact outcome is determined by the total mass of the system, the equation of state and any further relevant physics at play (e.g. microphysics, electromagnetic effects and gravitational cooling) [407, 408, 409, 346].

These different scenarios leave distinct imprints in the waveform, as can be seen in figure 4.5. There, we display the gravitational wave signal produced by the merger of two neutron stars with initial masses $m_0 = 1.35\ M_\odot$, for different choices of the equation of state: 2B [410], ALF2 [410] and DD2 [411]. The merger happens at $t = 0$. The waveforms that we show were taken from the `CoRe` database [3] [412]. The system in the upper panel collapses immediately to a black hole following contact, whereas the other two form a hypermassive neutron star. The system in the middle panel collapses to a black hole after ~ 7 ms, and the one in the lower panel does not collapse for the simulation duration, seemingly forming a stable neutron star. In the last two cases, the difference with a BBH signal is visible with naked eye. Figure 4.6 shows the decomposition of the signal obtained with the ALF2 equation of state (middle panel of figure 4.5) into amplitude and frequency. We note that the post-contact signal is characterised by oscillations in the gravitational wave amplitude and frequency.

Remarkably, for some models of boson stars, if the outcome of the merger is a boson star, angular momentum is entirely radiated immediately after contact, with very little mass ejected [344, 345, 413, 414]. The hypermassive boson star radiates gravitational waves primarily at the fundamental quasinormal frequency of the star [344]. On the other hand,

[3] http://www.computational-relativity.org/.

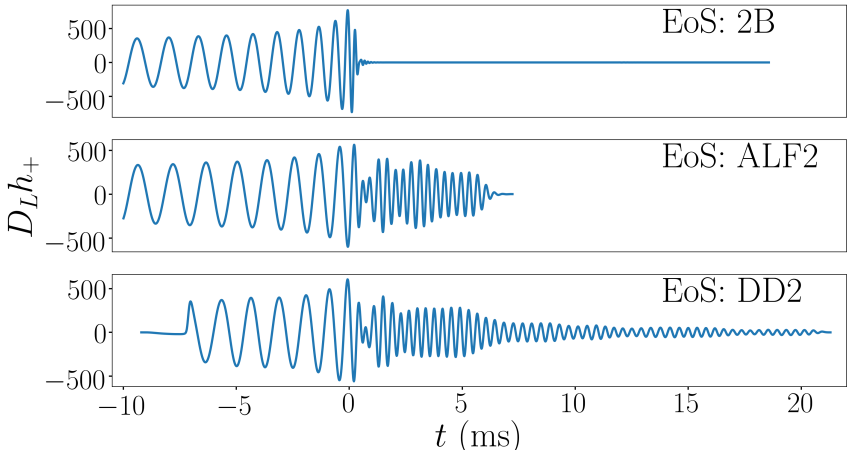

Figure 4.5: Numerical simulations of BNS waveforms for different equations of state. For the 2B equation of state, the system promptly collapses to a black hole after contact. For the ALF2 and the DD2 equation of state, a hypermassive neutron star is formed following contact. In the former case the hypermassive neutron star ends up collapsing to a black hole after $\simeq$ 7 ms, whereas in the latter case it does not collapse for the duration of the simulation, seemingly relaxing to a stable neutron star.

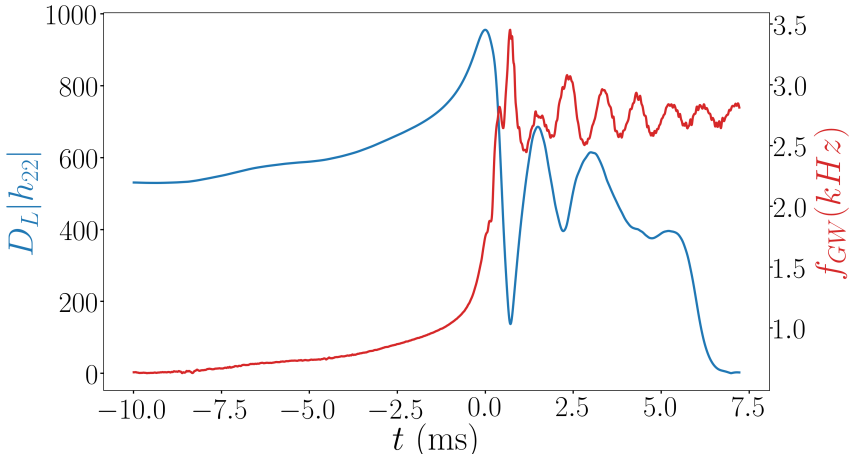

Figure 4.6: Amplitude-frequency decomposition of the gravitational wave signal emitted by a BNS following the ALF2 equation of state. The signal is characterised by the oscillations in amplitude (blue) and frequency (red) in the post-contact stage.

for BNSs the main frequencies in the post-contact stage are determined by the dynamics of the binary [415, 416, 417, 418].

With these observations in mind, we propose that the coalescence of ECO binaries should consist of (i) an inspiral phase with tidal effects (ii) a post-contact evolution with three possible scenarios:

- prompt collapse to a black hole,
- formation of a hypermassive ECO that ultimately collapses to a black hole,

- formation of a hypermassive ECO that settles into a stable remnant of the same nature as the original bodies.

Moreover, we expect the amount of angular momentum retained in the post-contact evolution to depend on the nature of the original bodies. We introduce a parameter $0 \leq \kappa \leq 1$ that represents the fraction of angular momentum retained at the onset of the post-contact phase. This parameter depends on the nature of the compact objects, and it is related to the ability of a given compact object to sustain rotation. For instance, it would be ~ 1 (~ 0) in case a stable remnant forms from the coalescence of a BNS (some models of BBS). This generic classification allows for a model agnostic phenomenological description of the coalescence of ECO binaries, irrespective of the exact nature of the involved bodies. We focus on the last two scenarios, and consider only extremal values of κ: we take $\kappa = 1$ for the scenario where a black hole is formed as the result of the collapse of a hypermassive ECO, and $\kappa = 1$ or $\kappa = 0$ for the scenario where a stable remnant is formed. Thus, we consider three types of behaviour in the post-contact stage:

- *RBH*: *rotating* systems that collapse to a *black hole*
- *RS*: *rotating* systems that form a *stable* remnant
- *NRS*: *non-rotating* systems that form a *stable* remnant

We focus on bodies with compactness in the range $0.14 \lesssim C_0 \lesssim 0.2$, which contains the typical values of many models of stable compact objects other than black holes. For high values of C_0, the toy model that we present next predicts a prompt collapse to a black hole, a scenario on which we do not focus. This is in agreement with the numerical simulations available so far, which suggest that for C_0 higher than ~ 0.18, the coalescence of BBSs leads to a black hole [344, 345, 346]. However, one should keep in mind that for equations of state that have not been explored yet, or for different setups, it might be possible to form more compact remnants. In particular, stable boson stars can reach compactnesses of ~ 0.3 [399, 400], suggesting such end states might be viable. Objects with higher compactness, however, might not be stable [404], in which case they would not be a possible coalescence end product. Our framework could be modified to account for these cases, e.g. by attaching a rotating bar instead of the toy model used here.

4.2.3 Toy model

Our starting point is the toy model introduced in [419] to describe the post-contact dynamics of BNSs. We model the inner cores of the ECOs by point particles interacting gravitationally, but also through an effective spring. The latter mimics the effect of the restoring forces, making the cores bounce. The disrupted material is modelled by a disk containing the two point particles, as shown in figure 4.7. For *RBH* and *RS* systems the disk and the cores corotate, for *NRS* systems neither the disk nor the cores rotate.

The toy model is characterised by four free parameters: the radius of the disk (R), the mass of the cores ($m/2$), the spring constant (k) and its length at rest $2\rho_0$. We assume mass conservation (i.e. no ejection of mass following contact) and that the two point particles have the same mass $m/2$. Therefore, the mass of the disk is $M = 2m_0 - m$, and its radius

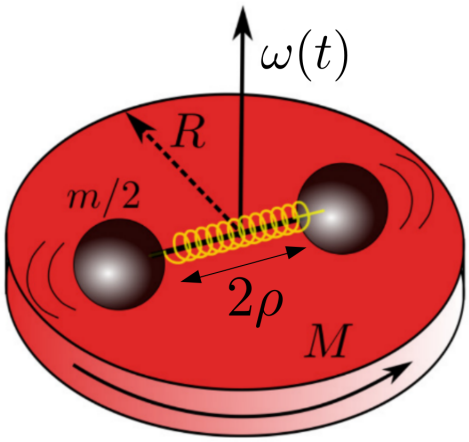

Figure 4.7: Illustration of the setup we use to model the dynamics of the post-contact stage, adapted from [419]. The hypermassive ECO is treated as a disk containing two point particles that interact gravitationally, but also through an effective spring. The latter mimics the effect of the restoring forces, making the cores bounce.

satisfies $r_0 \leq R \leq 2r_0$. We define the characteristic frequency of the spring as $\omega_0 = \sqrt{k/m}$. These free parameters should be related to the equation of state of the ECOs in the binary, e.g. higher values of k correspond to stiffer equations of state (see [420] for a discussion in the case of BNSs). Within this toy model, the three types of post-contact evolution (*RBH*, *RS* and *NRS*) are distinguished by the choice of free parameters and the prescription for the angular momentum.

The dynamics is governed by four variables: the distance of each core to the centre (ρ); the orbital angle (ϕ), out of which we define the orbital angular velocity ($\omega = \dot{\phi}$); the total energy (E); and the total angular momentum along the rotation axis (J). Quantities labelled by c refer to the time of first contact, and those labelled by i refer to the beginning of the toy model. We assume that, due to the finite shock-propagation speed, after the two objects touch, only their inner parts are compressed, whereas the outer layers keep their original sizes. We can therefore write $\rho_i = R - r_0$. We assume energy conservation and $J_i = \kappa J_c$, where κ is 0 for *NRS* systems and 1 otherwise. The initial orbital phase plays no role in the dynamics, and will be used later to match the post-contact stage to the inspiral.

We map the dynamics to that of an effective particle of mass given by the system's reduced mass, evolving in a potential well $V_{\rm eff} = V_{\rm centrifugal} + V_{\rm spring} + V_{\rm gravitational}$. The gravitational term was not accounted for in [419], it includes the interaction between the cores, the one between the cores and the disk and the rest energy of the disk:

$$V_{\rm gravitational} = -\frac{m^2}{8\rho} - \frac{mM\rho}{R^2} - \frac{2M^2}{3R}. \tag{4.12}$$

. The centrifugal and spring terms are given by

$$V_{\rm centrifugal} = \frac{1}{2} I\omega^2 = \frac{1}{2}\frac{J^2}{\frac{MR^2}{2} + m\rho^2}, \tag{4.13}$$

$$V_{\rm spring} = 2k(\rho - \rho_0)^2. \tag{4.14}$$

The addition of the gravitational term allows for a wider variety of post-contact behaviours, and helps provide a natural description of collapse to a black hole. Moreover, the treatment of [419] can be seen as a particular case of ours, in the limit of high values of k (stiffer objects), where the spring term dominates over the gravitational one. The shape of the effective potential is determined by the free parameters of the model. In figure 4.8 we display by dark-red lines the effective potential and the energy (in rescaled dimensionless units) at the start of the post-contact stage, for a given choice of the free parameters (corresponding to an *RS* system). The effective particle is trapped between an inner and an outer turning point, reproducing the oscillatory behaviour described in section 4.2.2. As the system evolves, energy and angular momentum are dissipated through radiation of gravitational waves. Due to the dependence of the centrifugal potential on the angular momentum, the effective potential changes during the evolution, as illustrated by the solid dark-blue line in figure 4.8.

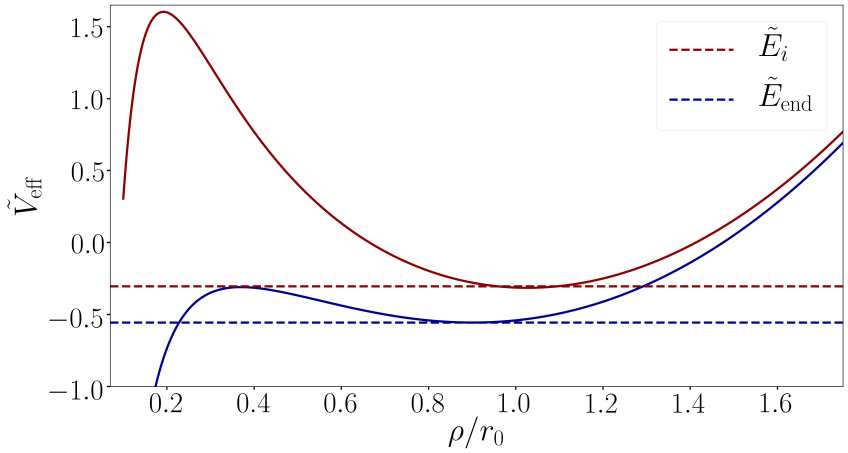

Figure 4.8: Evolution of the effective potential and the energy for an *RS* system. As the evolution proceeds, the energy reaches the minimum of the potential, leading to a "circularisation" of the orbit.

The evolution of the effective particle is governed by

$$\dot{\varphi} = \omega = \frac{J}{I} = \frac{J}{\frac{MR^2}{2} + m\rho^2}, \tag{4.15}$$

$$\dot{\rho} = \pm\sqrt{\frac{2}{m}}\sqrt{E - V_{\rm eff}(\rho)}, \tag{4.16}$$

$$\dot{E} = -P_{\rm GW}, \tag{4.17}$$

$$\dot{J} = -\dot{J}_{\rm GW}. \tag{4.18}$$

We compute the energy ($P_{\rm GW}$) and angular momentum ($\dot{J}_{\rm GW}$) carried away by gravitational waves consistently, using the adiabatic approximation and averaging over an entire period of the radial motion. Details of the computation are given in appendix A.1. We integrate the adiabatic equations of motion, equations (4.15), (4.16), (4.17) and (4.18), over successive periods, see appendices A.2 and A.3 for details. The evolution proceeds differently for each type of ECO binary:

- For *NRS* systems, one has $J = 0$ and thus the potential is fixed. As the evolution proceeds, the effective particle loses energy and sinks to the bottom of the potential. Physically, this corresponds to the formation of a stable object of the same nature as the binary's ECOs, with zero angular momentum. We fix the parameters of the toy model to match the frequency of the radial oscillations to numerical simulations of BBSs [344] (in principle we could also use quasinormal modes of different ECO models, although numerical simulations are needed in order to check that these are the relevant frequencies in this regime, as was explicitly done in [344].)

- For *RS* systems, the effective particle sinks to the bottom of the potential and the orbit "circularises" (see figure 4.8 and appendix A.3). The system keeps emitting gravitational waves as it settles into an equilibrium state, corresponding to the formation of a stable object of the same nature as the original ECOs.

- For *RBH* systems, the energy eventually becomes larger than the potential height, leading to a "plunge" and subsequent formation of a black hole. Following the hoop conjecture [421], we assume that a black hole is formed when the compactness of the system becomes larger than 0.5 (the minimum compactness of a black hole). The compactness of the system is defined as

$$C_\rho = \frac{M_\rho}{\rho}, \tag{4.19}$$

  where $M_\rho = m + M(\rho/R)^2$ is the total mass within the radius ρ. The black hole thus formed has mass $M_f = M_\rho$ and dimensionless spin parameter $\chi_f = J_\rho/M_\rho^2$, where $J_\rho = (m + M(\rho/R)^2)\rho^2\omega$ is the angular momentum of the collapsing matter out of which the black hole forms.

We display examples of the post-contact dynamics of an *RBH* and an *RS* system in appendix A.4. We found the results of this toy model to be more sensitive to the compactness rather than to the exact values of the free parameters. We present results obtained with choices of the free parameters that we consider to be representative of each type of ECO binary.

4.2.4 Waveform

Time domain

We focus on the dominant $(2, \pm 2)$ harmonic of the gravitational wave signal emitted by an ECO binary and match smoothly its amplitude and phase across the different stages of the evolution. We recall that for a gravitational wave signal emitted along the direction of the orbital angular momentum ($\iota = 0$), one has $h_{22} = \sqrt{\frac{4\pi}{5}}(h_+ - ih_\times)$. Writing $h(t) = \hat{A}_{22}(t)e^{-i\hat{\Psi}_{22}(t)}$, the instantaneous gravitational wave frequency is given by $\hat{f} = \frac{1}{2\pi}\frac{\mathrm{d}\hat{\Psi}_{22}}{\mathrm{d}t}$.

Inspiral

For the inspiral, we use the EOB waveform SEOBNRv4T, an extension of SEOBNRv4 [100] accounting for tidal effects[4], and take $k_2 = 0.1$. We stop the inspiral waveform at contact, i.e. when $\hat{f} = 2f_c$. We assume that the formation of the hypermassive star happens over a time interval $\Delta t = 1/2f_c$, which corresponds to half a period after contact. For $m_0 = 1.35\ M_\odot$, this gives $\Delta t \simeq 0.7$ ms, in good agreement with numerical simulations of BNSs. The inspiral is matched to the post-contact waveform over this interval, using cubic functions to ensure smoothness of the amplitude and the instantaneous gravitational wave frequency.

Post-contact

During this stage the waveform is computed using the quadrupole formula, see appendix A.1. For a wave propagating along the orbital angular momentum direction, it yields

$$h_+ = \frac{2}{D_L}(\gamma_2 \cos(2\phi) - \gamma_1 \sin(2\phi)), \tag{4.20}$$

$$h_\times = \frac{2}{D_L}(\gamma_1 \cos(2\phi) + \gamma_2 \sin(2\phi)), \tag{4.21}$$

where

$$\gamma_1 = \frac{2m\rho\dot{\rho}\omega(MR^2 + m\rho^2)}{\frac{MR^2}{2} + m\rho^2}, \tag{4.22}$$

$$\gamma_2 = m\left(\dot{\rho}^2 - \rho^2\omega^2 - 4\omega_0^2\rho(\rho - \rho_0) - \frac{m}{8\rho} + \frac{M\rho}{R^2}\right). \tag{4.23}$$

The phase and amplitude of the (2,2) harmonic are given by

$$\hat{A}_{22}(t) = \sqrt{\frac{16\pi}{5}}\frac{1}{D_L}\sqrt{\gamma_1^2 + \gamma_2^2}, \tag{4.24}$$

$$\hat{\Psi}_{22}(t) = 2\phi - \arctan(\gamma_1/\gamma_2). \tag{4.25}$$

The initial orbital phase (ϕ_i) is fixed by matching to the inspiral. For *NRS* systems one has $\gamma_1 = 0$ and $\phi = \phi_i$; therefore, with our definition, the instantaneous frequency would vanish in the post-contact phase. In this particular case, we define it instead as the frequency of radial oscillations.

Ringdown

For *RBH* systems, we model the ringdown signal of the final black hole using the model presented in [100, 101],

$$h_{22}^{\rm RD}(t) = \eta\, \check{A}_{22}(t)\, e^{i\check{\phi}_{22}(t)}\, e^{-i\sigma_{220}(t - t^{22}_{\rm match})}, \tag{4.26}$$

[4]This approximant is available in the LIGO Algorithm Library [422].

where $t^{22}_{\rm match}$ is the matching time and $\sigma_{220} = -\sigma^I + i\sigma^R$ is the least damped quasinormal frequency of a perturbed Kerr black hole, computed by [92]. The black hole mass and spin are computed as described below equation (4.19). The functions $\hat{A}_{22}(t)$ and $\hat{\phi}_{22}(t)$ are defined by

$$\check{A}_{22,\rm RD}(t) \equiv c_1^c \tanh\left[c_1^f(t - t^{22}_{\rm match}) + c_2^f\right] + c_2^c, \tag{4.27}$$

and

$$\check{\phi}_{22}(t) = \phi_1 - d_1^c \ln\left[\frac{1 + d_2^f e^{-d_1^f (t - t^{22}_{\rm match})}}{1 + d_2^f}\right]. \tag{4.28}$$

Coefficients with superscripts f are calibrated against numerical simulations (the expressions are given in [100, 101]). Those with superscripts c are used to ensure continuity of the amplitude, phase and their first derivatives at the matching time, while ϕ_1 is the phase at the start of the ringdown. With these matching prescriptions, the phase and the amplitude are $\mathcal{C}^1$ functions.

Our model could also incorporate different behaviours for the final stage, such as resonant modes of excited stars for *RS* systems, but we do not explore this possibility here.

Full waveform

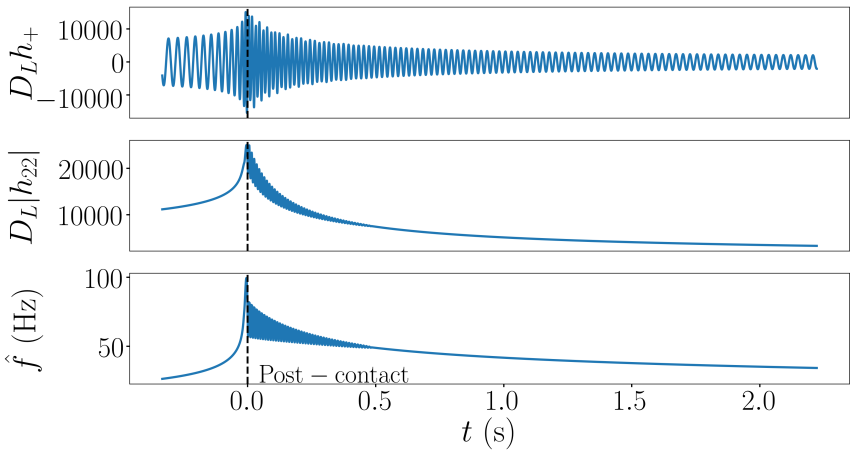

Figure 4.9: Waveform for an *RS* system with $m_0 = 30\ M_\odot$ and $C_0 = 0.17$. We show the real part of the (2,2) harmonic and its decomposition into amplitude and frequency. The black dashed lines indicate the start of the post-contact stage.

In figures 4.9 and 4.10 we display the real part of the (2,2) harmonic, together with its decomposition in amplitude and frequency for an *RS* and an *RBH* system with $m_0 = 30\ M_\odot$ and $C_0 = 0.17$. For the sake of clarity, we display only the last instants of the inspiral. The start of the post-contact signal is indicated with black dashed lines. Our model reproduces qualitatively the oscillatory behaviour of the gravitational wave amplitude and frequency in the post-contact stage. For the *RBH* system, $\hat{f}$ increases up to the ringdown frequency, whereas for the *RS* system it tends to zero as the system settles into a stable ECO. For completeness, in figure 4.11 we show the real part of the (2,2) harmonic for an *NRS* system with the same mass and compactness.

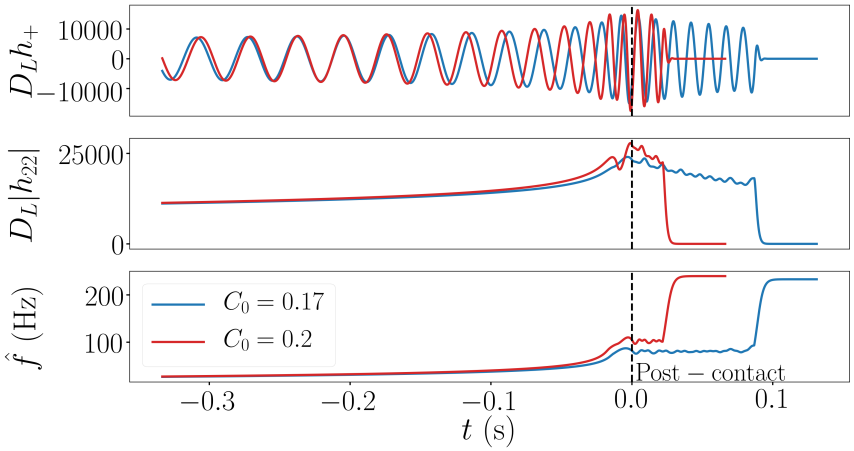

Figure 4.10: The same as figure 4.9, but for an *RBH* system with $m_0 = 30\ M_\odot$ and $C_0 = 0.17$ ($C_0 = 0.2$) in blue (red). After contact, the collapse to a black hole happens faster for more compact systems.

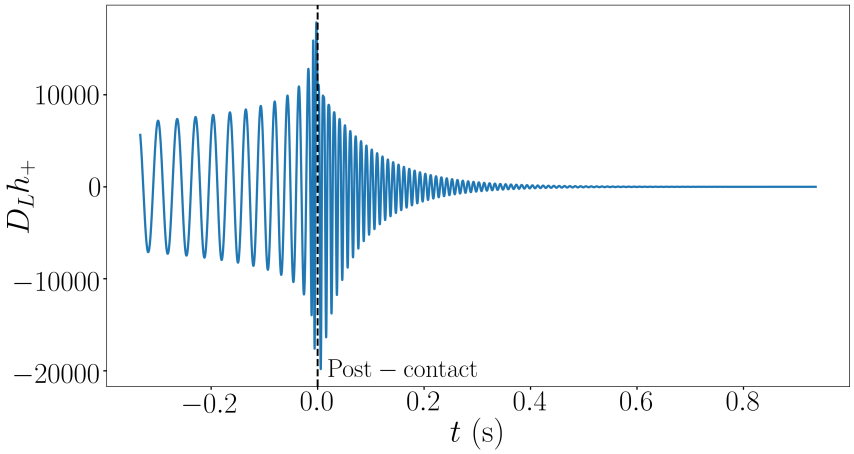

Figure 4.11: Real part of the (2,2) harmonic for an *NRS* system with $m_0 = 30\ M_\odot$ and $C_0 = 0.17$.

In figure 4.10 we overplot in red the evolution for a more compact system ($C_0 = 0.2$). This comparison has to be performed carefully: if we were to align the waveforms at the same reference frequency, the signal of the less compact binary would be shorter, because less compact objects touch earlier. Here, we aligned the waveforms at their respective contact frequencies to highlight the post-contact evolution (the apparent alignment ~ 0.25 s before the merger is coincidental). After contact, the collapse to a black hole happens faster for more compact objects. Moreover, more compact binaries emit gravitational waves in the post-contact stage at higher frequencies, as expected since their contact frequency is higher.

Frequency domain

We obtain the frequency domain signal $\tilde{h}_{22}$ by performing a discrete Fourier transform. In figure 4.12 we display the amplitude of $\tilde{h}_{22}$ for the three types of ECO binaries, taking

$m_0 = 30\ M_\odot$. Different colours correspond to different C_0, and the dashed lines indicate the corresponding gravitational wave frequency at contact. For comparison, we show the amplitude for a general relativity BBH with the same component masses and zero spins, obtained with PhenomD, in black dashed lines. Each type of ECO binary exhibits characteristic features in its signal:

- For *NRS* systems (upper panel), $|\tilde{h}_{22}|$ presents one main peak at the frequency of radial oscillations, and smaller peaks at the corresponding higher harmonics.
- For *RBH* systems (middle panel), we observe a main peak at the same frequency around which $\hat{f}$ oscillates in figure 4.10. Beatings between orbital and radial frequencies lead to significant power being emitted at higher and lower frequencies too. As a consequence, the inspiral and post-contact signal "interfere", leading to wiggles around the transition frequency $2f_c$. The beatings (and therefore the "interference") and the amplitude of the peak are reduced for more compact configurations, because the post-contact signal is shorter. Moreover, as the compactness increases the signal becomes more and more similar to a BBH signal.
- For *RS* systems (lower panel), $\hat{f}$ tends to zero (see figure 4.9), thus spreading the peak observed for *RBH* systems over lower frequencies. This leads to strong "interferences" between the inspiral and the post-contact signal, and a highly oscillatory behaviour ensues. We identify the repetition of an oscillatory pattern at different frequencies, corresponding to "harmonics" of the signal.

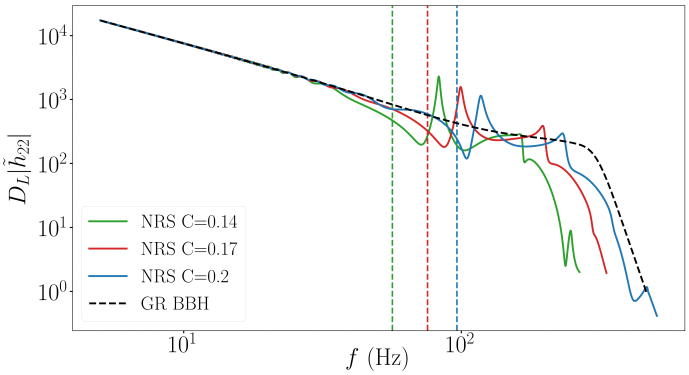

(a) In the post-contact stage, *NRS* systems emit almost exclusively at the frequency of radial oscillations and the corresponding higher harmonics.

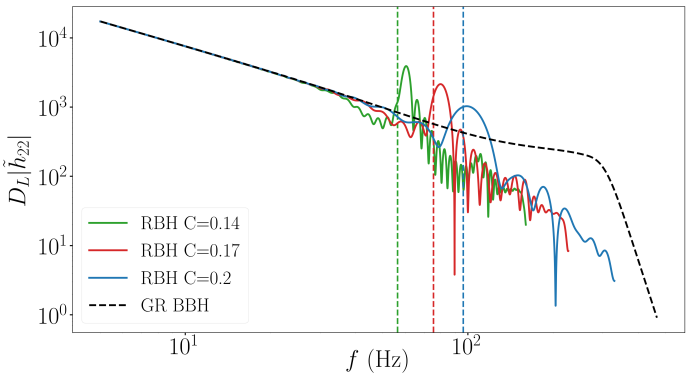

(b) For *RBH* systems, we observe a main peak at the frequency around which $\hat{f}$ oscillates in figure 4.10. There is also considerable power emitted at lower and higher frequencies. Thus, the inspiral and post-contact signals "interfere", leading to wiggles around $2f_c$.

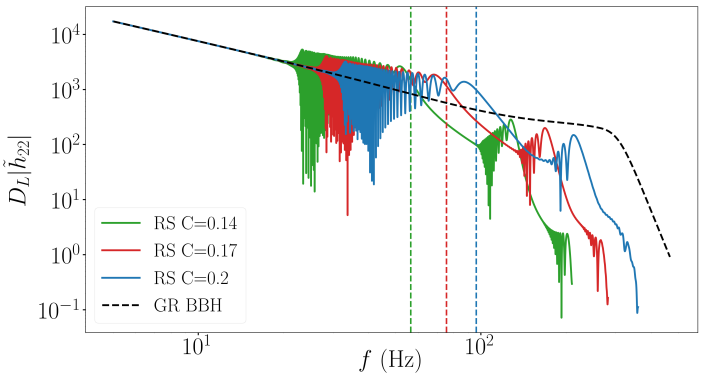

(c) For *RS* systems, $\hat{f}$ tends to zero (see figure 4.9), and the peak observed in *RBH* systems is therefore spread over lower frequencies, leading to significant "interference" with the inspiral signal. The repetition of an oscillatory pattern can be observed at higher frequencies.

Figure 4.12: Amplitude of the frequency-domain signal of the three types of ECO binaries, for different values of the initial compactness. The vertical dashed lines indicate the corresponding value of $2f_c$ for each C_0.

4.2.5 Data analysis

We can now assess the detectability of ECO binaries and how well we could distinguish them from BBHs with different gravitational wave detectors. We consider ECO binaries with source-frame masses in the ranges $[5M_\odot, 10^4 M_\odot]$ and $[10^3 M_\odot, 10^9 M_\odot]$, which could be probed by ground-based detectors and by LISA, respectively. In the following, it will be convenient to use both source-frame (subscript s) and detector-frame (subscript d) masses. We start by reviewing a few notions of data analysis and describing the specifics of the detectors.

Definitions

The strain measured by ground-based detectors can be written as

$$h = \mathcal{F}_+(\lambda, \beta, \psi, \iota) h_+ + \mathcal{F}_\times(\lambda, \beta, \psi, \iota) h_\times, \tag{4.29}$$

where $\mathcal{F}_+$ and $\mathcal{F}_\times$ are the extended antenna pattern functions of the detector, including the dependence on the inclination angle (ι) in addition to the longitude (λ), latitude (β) and polarisation (ψ) angles. We define the averaged SNR over λ, β, ψ and ι as

$$< \mathrm{SNR}^2 >= \int_{f_{\min}}^{f_{\max}} \frac{(< \mathcal{F}_+^2 > + < \mathcal{F}_\times^2 >)|\tilde{h}_{+,\times}(f)|^2}{S_n(f)} \, \mathrm{d}f, \tag{4.30}$$

where $<>$ denotes averaging over the angles and the integration limits $f_{\min}$ and $f_{\max}$ depend on the detector and the signal. Defining N as the number of noise-independent detectors and ϱ as the angle between the arms of a given detector, we have

$$< \mathcal{F}_+^2 > = \frac{7}{75} N \sin^2(\varrho), \tag{4.31}$$

$$< \mathcal{F}_\times^2 > = \frac{1}{15} N \sin^2(\varrho). \tag{4.32}$$

There is no contribution from polarisation mixing because $< \mathcal{F}_+ \mathcal{F}_\times >= 0$.

Detectors

We consider three ground-based detectors: LIGO Livingston at the time of GW170817 [9], advanced LIGO (aLIGO) at its design sensitivity [2] and ET. We take respectively $f_{\min} = 23, 10, 5$ Hz and $f_{\max} = 2000, 3000, 8000$ Hz for the integration limits. LIGO Livingston and aLIGO are single detectors with angle between the arms $\varrho = \pi/2$, while ET is made of three detectors with $\varrho = \pi/3$.

For LISA, the expression given in equation (4.29) is valid only in the long-wavelength approximation, to which we will stick. LISA can then be seen as consisting of two noise-independent detectors with $\varrho = \pi/3$. We use the LISA proposal noise level [29] including the confusion noise due to GBs [315], for more details on the calculation of angle-averaged SNRs in LISA, see [320]. We assume a mission duration of four years and adopt the frequency range $f_{\min} = \max(10^{-5}\ \mathrm{Hz}, f_{-4\mathrm{yrs}})$ and $f_{\max} = 0.1$ Hz, where $f_{-4\mathrm{yrs}}$ is the frequency of a BBH of same component masses 4 years before merger. This is an optimistic choice, as it allows for observing the inspiral during the whole mission duration, as well as the merger if it happens in band.

Detectability and distinguishability

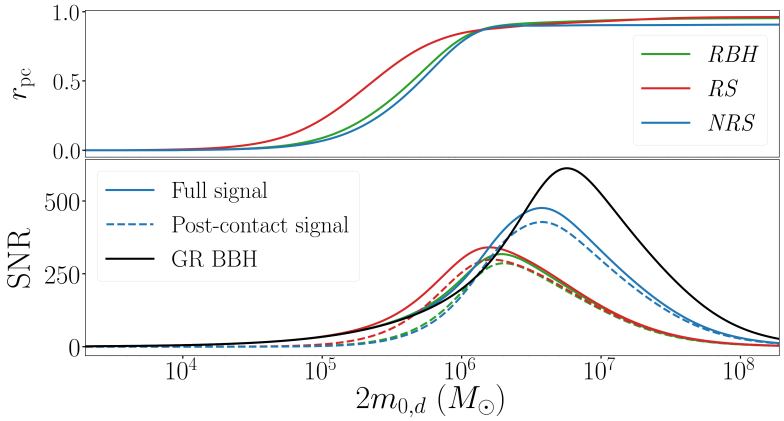

Figure 4.13: Lower panel: total and post-contact SNR in LISA as a function of the detector-frame mass, for the three types of ECO binaries. Upper panel: ratio of post-contact to total SNR. We take $C_0 = 0.17$ and place the sources at $z = 10$. As the total mass increases, LISA becomes more sensitive to the post-contact stage and less sensitive to the inspiral, and thence $r_{\rm pc}$ approaches unity.

We start by assessing the fraction of SNR coming from the post-contact signal. We define it as

$$r_{\rm pc} = \sqrt{\frac{<(\tilde{h}_{\rm pc}|\tilde{h}_{\rm pc})>}{<(\tilde{h}_{\rm tot}|\tilde{h}_{\rm tot})>}} = \frac{SNR_{\rm pc}}{SNR_{\rm tot}}, \tag{4.33}$$

where $\tilde{h}_{\rm tot}$ is the Fourier transform of the whole signal, and $\tilde{h}_{\rm pc}$ is that of the post-contact signal only. In the lower panel of figure 4.13, we display the total (full line) and post-contact (dashed line) SNR in LISA, for the three types of ECO binaries and as a function of the total mass in the detector frame. For comparison, in black we plot the SNR for a binary of nonspinning general relativity black holes, computed with PhenomD. We place the sources at $z = 10$. In the upper panel we plot $r_{\rm pc}$, which is independent of the redshift. As the total mass increases, LISA becomes more sensitive to the post-contact stage and less to the inspiral, thus $r_{\rm pc}$ approaches unity. The difference between the various types of systems can be understood from figure 4.12. The post-contact evolution of *RS* systems starts early (at lower frequencies), and the maximum of the SNR is shifted to lower masses than for the other systems. *NRS* systems can reach higher SNRs, because the amplitude of their frequency-domain signal is almost as high as for general relativity BBHs up to $\simeq 2f_c$, thus more SNR is accumulated in this frequency range as compared to *RS* and *RBH* systems, and significant power is emitted at the harmonics of the radial oscillation frequency (more than by BBHs at the same frequency). For lower masses, the total SNR of ECO binaries can even be larger than for BBHs, but it is smaller for higher masses because of the lower emitted power at high frequencies. The picture is similar for ECO binaries in the range $[5M_\odot, 10^4 M_\odot]$ in ground-based detectors.

To gauge our ability to identify these signals, i.e. to detect them and potentially distinguish them from BBHs, we define two thresholds: one for the whole signal and another one

for the post-contact signal. Based on studies of the detectability of post-merger signals from BNS coalescence [423, 424, 425], we require a minimum SNR for the post-contact signal of 4. Whereas for the overall detectability, we assume a threshold of 8. We define the horizon redshift for the identification of ECO binaries as the maximum redshift such that both thresholds are exceeded. We expect that if both thresholds are exceeded, we should be able to spot the presence of an ECO binary's post-contact signal in the residuals left after subtracting the best fit general relativity BBH template from data, and since it is very different from the post-merger signal of BBHs, we should be able to identify the merging objects as being ECOs. Figure 4.14 shows the horizon redshift for ECO binaries, as a function of the total mass in the source frame. The upper panel shows results for aLIGO, the middle one for ET and the lower for LISA. For comparison, we plot in black the horizon redshift for a binary of nonspinning general relativity black holes, computed with PhenomD. The abrupt cut for LISA is due to systems that accumulate a large SNR during their inspiral, but which merge outside the LISA frequency band. Because they can reach higher SNRs, *NRS* systems have the largest horizon among ECO binaries. The horizon distance typically increases with C_0, because the inspiral of more compact binaries lasts longer, allowing for the accumulation of more SNR. Our results show that aLIGO could identify ECO binaries only up to $z \simeq 1$, whereas ET and LISA could identify binaries with total mass $\mathcal{O}(10^2)\ M_\odot$ and $10^4 - 10^6\ M_\odot$ respectively, throughout the observable Universe.

Next, we investigate whether the detection of an ECO binary may be mistaken for a BBH. For a given ECO binary signal, we define its fitting factor (FF) [426] as the maximum overlap (defined in equation (2.3)) over general relativity BBH templates. The FF measures the *effectualness* [427] of a family of templates at reproducing a fiducial signal. The difference 1-FF yields the SNR fraction that would be lost as a result of the mismatch between the signal and the (best) template. We recall that template banks are built so that the overlap between neighbouring templates is no less than 0.97 (see section 2.1). For simplicity, we neglect the dependence on the longitude, latitude, right ascension and polarisation angles and work with the dominant $(2, \pm 2)$ harmonic. Moreover, we restrict ourselves to aligned (or anti-aligned) spins, and maximise over the merger time and the phase at merger as in [296]. Thus, we are left with four parameters over which to maximise: the masses and the spins. For this last step, we use `Multinest` [428] to search for the highest FFs. We compute BBH templates with PhenomD.

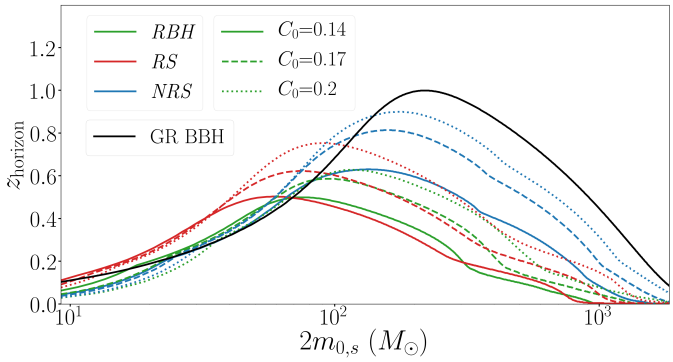

(a) aLIGO could detect ECO binaries up to $z \simeq 1$.

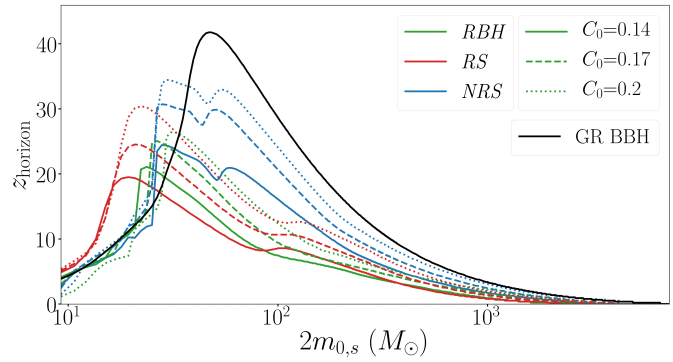

(b) ET could detect ECO binaries with total mass $\mathcal{O}(10^2)$ $M_\odot$ throughout the observable Universe. The double-peaked feature for the *NRS* system is due to the presence of two lines in the power spectral density, which damp the contribution of the secondary peak of the frequency-domain signal for masses in between the two maxima.

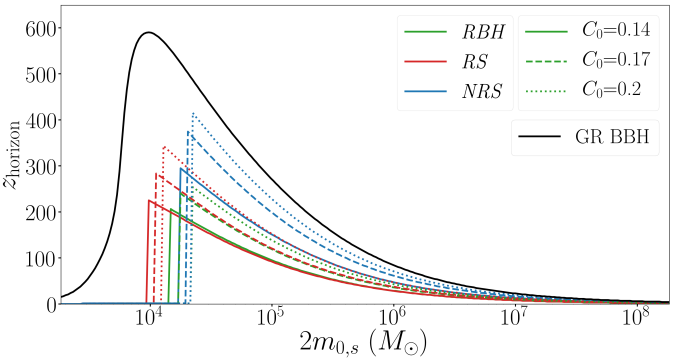

(c) LISA could detect ECO binaries with total mass $10^4 - 10^6$ $M_\odot$ throughout the observable Universe. The abrupt cut is due to systems that merge outside the LISA frequency band, but which accrue a large SNR during their inspiral.

Figure 4.14: Maximum redshift up to which we could observe and potentially distinguish different types of ECO binaries from BBHs, as a function of the total mass in the source frame. The threshold for observation and distinguishability is set at a total SNR of 8 and at a post-contact SNR of 4, respectively. The maximum redshift typically increases with C_0 and, among ECO binaries, is largest for *NRS* systems.

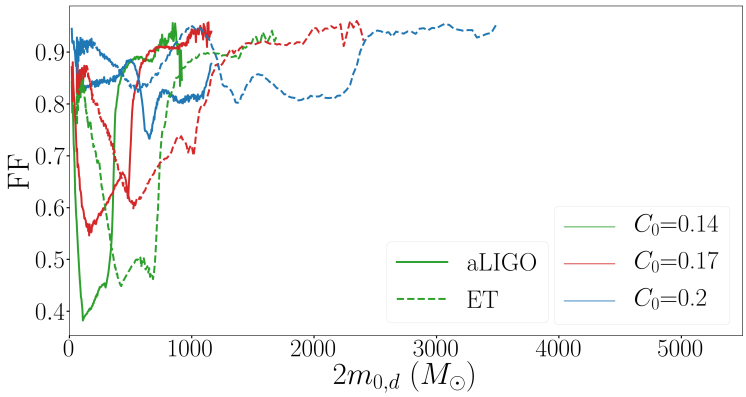

(a) FFs for *RBH* systems.

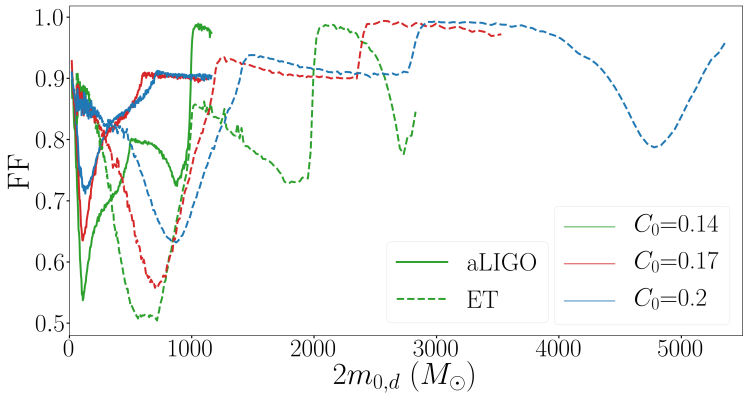

(b) FFs for *NRS* systems.

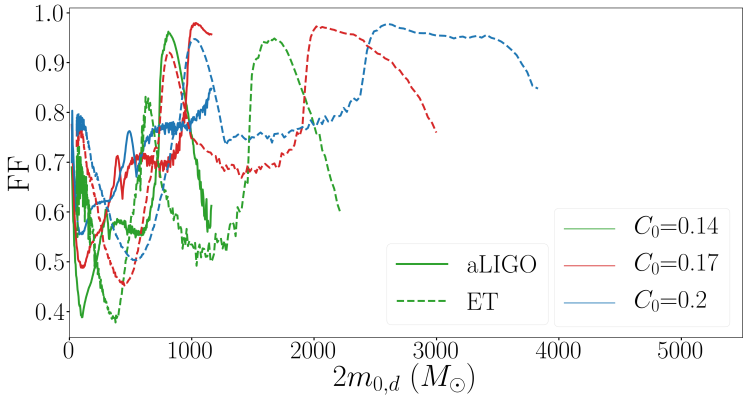

(c) FFs for *RS* systems.

Figure 4.15: FF as a function of the total mass in the detector frame, for the different types of ECO binaries (one in each panel) and different values of C_0 (distinguished by the colour) in aLIGO (full lines) and ET (dashed lines). Up to 60% of the SNR could be lost if ECO binaries are detected with BBH templates, potentially jeopardising detection of weaker signals.

Figure 4.15 shows FFs computed for each type of ECO binary. We use full (dashed) lines for aLIGO (ET). The key information in this figure is given by the range of FFs and the

Event	$\mathcal{M}_{c,s}$ ($M_\odot$)	$m_{0,s}$ ($M_\odot$)	$\mathrm{SNR}_{\mathrm{obs}}$	$C_0 = 0.14$			$C_0 = 0.17$			$C_0 = 0.2$		
				RBH	*RS*	*NRS*	*RBH*	*RS*	*NRS*	*RBH*	*RS*	*NRS*
GW150914	28.6	33	24.4	22.1	21.7	21.9	20.5	21.1	20.2	17.1	20.1	18.2
GW150112	15.2	17	10.0	8.0	8.3	7.2	6.9	8.0	6.5	5.2	7.5	5.6
GW151226	8.9	10	13.1	7.4	9.4	6.0	5.9	8.6	5.2	4.0	7.8	4.3
GW170104	21.4	25	13.0	11.2	11.3	11.0	10.3	11.0	10.1	8.3	10.4	8.9
GW170608	7.9	9	14.9	7.6	10.1	6.0	5.9	9.2	5.1	4.0	8.3	4.2
GW170729	35.4	41	10.8	10.3	10.4	10.4	10.0	9.8	9.9	8.8	9.3	9.1
GW170809	24.9	29	12.4	11.1	11.0	11.0	10.3	10.6	10.2	8.5	10.2	9.1
GW170814	24.1	28	15.9	13.7	14.0	13.7	12.8	13.4	12.6	10.4	12.8	11.1
GW170818	26.5	30	11.3	10.3	10.1	10.2	9.6	9.8	9.4	8.0	9.3	8.5
GW170823	29.2	33	11.5	10.8	10.4	10.8	10.2	10.2	10.1	8.7	9.7	9.2

Table 4.5: SNR of the post-contact signal for the LVC events, under the hypothesis that those were produced by ECO binaries. We assume equal masses and use the chirp mass and redshift reported in [7] to compute the masses of the binaries components; we also fix the total SNR to the network SNR reported by the LVC ($\mathrm{SNR}_{\mathrm{obs}}$).

masses for which the FF is minimum. We find that up to 60% of the SNR could be lost if only BBH templates were used in template-based searches, drastically decreasing our chances of detecting these exotic signals. The FF closely resembles inverted SNR (or equivalently the horizon redshift) as a function of the total mass (see figure 4.14), and is minimum for masses that maximise the post-contact SNR. This is why the minimum FF for ET is displaced with respect to aLIGO. The oscillations at higher masses are due to the most salient parts of these exotic signals lying within the most sensitive frequency window of the detector. *RS* and *NRS* systems have lower FFs in ET, whereas for *RBH* systems the minimum FF is lower in aLIGO. This might seem counterintuitive, but it can be understood as follows: (i) aLIGO observes only the very end of the inspiral, where tidal effects are more pronounced and dephasing with BBH templates grows fast; (ii) the post-contact signal of *RS* and *NRS* systems is "sufficiently different" from BBHs, unlike that of *RBH* systems; (iii) the noise level in ET is approximately flat over a broad frequency band, thus ET is more sensitive to the post-contact stage. Similarly, the FF is overall smaller for *RS* systems and higher for *RBH* systems (in agreement with the visual impression from figure 4.12). Finally, the FF increases with C_0, because ECOs become more similar to black holes as their compactness increases. Since the *effectualness* is always larger than the *faithfulness* [427], our results suggest that the estimation of the parameters of these exotic sources (including masses, spins, etc) could be significantly biased if only general relativity BBH templates are used.

Finally, we investigate the possibility that the detected BBH events in the first gravitational wave catalogue released by the LVC [7] may actually be ECO binaries. Because the chirp mass is one of the best constrained parameters, we make the assumption that its measurement is not significantly biased, and use the values reported by the LVC. Moreover, for each event we assume equal masses (all events in the catalogue are compatible with this

assumption). We estimate the SNR of the post-contact signal by fixing the total SNR to the value measured by the LIGO/Virgo network, and by using the sensitivity of LIGO Livingston at the time of GW170817. Let us stress that the noise level was not the same for all the events, and in particular, the power spectral density at the time of GW170817 corresponds to the highest sensitivity reached during the first two observing runs of the LVC. Therefore, our estimates serve as higher bounds on what the real post-contact SNR would have been. The values are reported in table 4.5. The post-contact SNR decreases with C_0, because the SNR accumulated during the inspiral is larger for more compact binaries and we have fixed the total SNR. Based on studies of the detectability of the post-contact signal of BNSs [424], our results suggest that the post-contact SNR would be sufficient for detection with wavelet-based pipelines, at least for the loudest sources. The compatibility of the residuals left after subtracting the best fit general relativity BBH template from data with Gaussian noise [11] makes it unlikely that these events were generated by ECO binaries as the ones we consider (i.e. made of identical objects with $C_0 \leq 0.2$ and which do not collapse promptly following contact). Our analysis could be extended to the second catalogue released by the LVC [8], including the noteworthy event GW190521 [190], which has been suggested to be compatible with a BBS signal [429].

4.3 Discussion

In this chapter we demonstrated the huge potential of gravitational wave observations in detecting deviations from general relativity. Working in the parametrised post-Einsteinian framework and performing a full Bayesian analysis, we assessed the ability of multiband observations to constrain the dipolar amplitude in BBHs and the mass of the graviton. The main result is that multiband observations of SBHBs could allow us to improve current bounds on dipolar amplitude by seven orders of magnitude. Furthermore, we argued that the merger of ECO binaries could be substantially different from the general relativity prediction for BBHs, offering a unique opportunity to identify these exotic objects. To enhance our chances of detecting exotic signals and properly extracting physical information from the data, we have proposed a simple model that captures the main features of the full gravitational wave signal from binaries consisting of identical ECOs with compactness below 0.2 and which do not collapse promptly following contact. We used this model to assess the detectability of these binaries with current and future detectors, and we showed that up to 60 % of the SNR could be lost when using BBH templates to search for these exotic signals, thus affecting our chances of observing them. Finally, we estimated that events in the first gravitational wave catalogue released by the LVC are unlikely to have been generated by such exotic binaries. Our model could serve to test different data analysis strategies. It could be particularly helpful for the design of algorithms looking for deviations from general relativity BBHs around the merger.

Multiband observations will also allow us to perform consistency tests between the part of the signal observed by LISA and the one observed by ground-detectors, probing the coherency of the signal across disconnected frequency bands [430]. An inconsistency between the signals would point to modifications appearing at either end of the signal. Moreover, the measurement of the time to coalescence with LISA could be used to inform ground-based

detectors and improve *black hole spectroscopy* [431]. Since general relativity predicts that the quasinormal modes depend only on the mass and spin of the final black hole, measuring at least two quasinormal modes allows us to perform very precise tests of the no-hair theorem and general relativity [432, 433, 434, 435]. There again, parametrised approaches [13, 436] offer a valuable alternative given that few computations of quasinormal modes in modified gravity theories have been performed to date.

The binaries we considered so far were assumed to be in vacuum, however in some circumstances their astrophysical environment could leave an imprint in the gravitational wave signal they emit. If not properly taken into account, this could spoil the aforementioned tests of general relativity. In the next chapter we will discuss of the signature of astrophysical effects in gravitational wave signals.

Chapter 5

The imprints of astrophysical effects on gravitational waves

The gravitational wave signal emitted by a binary system depends on its dynamics. The latter can be substantially modified if matter effects come at play, or by the presence of a third body. In this chapter we assess how can we use gravitational wave observations to obtain information on astrophysical effects in binary systems. We first consider astrophysical effects exterior to BBHs, called *environmental effects*, and then matter effects within a binary, more specifically the accretion from a white dwarf companion onto a black hole. We reproduce the analyses of [37, 36] and [38][1].

The detection of GW190521 [190] has been one of the highlights of the third observing run of the LVC. Besides challenging current formation channels and the existence of an upper mass gap, it might have provided the first multimessenger observation of a BBH. Indeed, the Zwicky Transient Facility observed an optical flare, interpreted as coming from the kicked GW190521 black hole merger remnant moving in an AGN disk [437]. The authors argue that the binary is most likely located in a disk migration trap, where gas torques vanish and binaries accumulate as they migrate inwards [438]. In fact, it had already been suggested that SBHBs and IMBHBs could reside in AGN disks [438, 439, 440, 441, 442, 443], and it has been argued since then that $\sim 25\%$ of the BBHs detected by the LVC could have formed in such an environment [444]. Binaries in AGN disks orbit the central massive black hole, and are expected to feel a drag force (dynamical friction) exerted by the surrounding gas, which could also be accreted onto the binary. Accretion onto binaries might also be possible for SBHBs formed in isolation (in the field-formation scenario) if gas is left following the common envelope phase [445]. Finally, accretion, in combination with mergers, is also thought to be the main channel via which black hole seeds evolve into the supermassive black holes we observe today [217]. To leading order, the effect of accretion, dynamical friction and the binary's peculiar acceleration on the waveform can be captured by a phase shift, similarly to the parametrised post-Einsteinian formalism, causing possible confusion in interpreting

[1] Among the results presented in the first section, I performed the Bayesian analyses and helped in the derivation of the effect of accretion from surrounding gas on the waveform. The computation of X-ray and radio emissions were originally performed by Laura Sberna and Andrea Caputo. Figure 5.10 is to be credited to Sylvain Marsat. Concerning the second section, the theoretical modelling was done jointly by Laura Sberna and I, under the supervision of Cole Miller. I performed the data analysis presented there.

data. As we will see in section 5.1.1, these effects lead to low-frequency modifications in the gravitational phase, thus LISA observations of SBHBs and IMBHBs during their early inspiral would be very sensitive to those. Working in a full Bayesian framework, we start by assessing the perspectives for detecting the effect of accretion in SBHBs and IMBHBs, and possible electromagnetic counterparts. Then, we focus on LISA and multiband observations of binary systems similar to GW190521 residing in AGN disks. Thanks to their high mass, these astrophysically motivated systems offer good perspectives for detection with LISA, and measuring environmental effects in their gravitational wave signal would help shed light on their origin and offer a unique probe of AGN properties. We do not rely on the association of GW190521 with the observation of the Zwicky Transient Facility, which is still debated [446], we only assume that GW190521-like binaries can be found in AGN disks.

In the second part of this chapter, we consider a specific example of GB: mass-transferring white dwarf-black hole binaries (WDBH). Population studies predict that tens of thousand of such binaries could form in the Milky Way (see, e.g., [447, 448]), but the rates are still uncertain by more than an order of magnitude. The expectation is that binaries containing a black hole will be subdominant in the range of frequencies relevant for LISA (see, e.g., [174]). Although [449] suggests that LISA might not see any detached (nonaccreting) WDBH in the Galaxy, [450] find that a few events could be possible if we account for binary interactions in Galactic globular clusters. Overall, these sources are often discarded in black hole population synthesis simulations (e.g. [451]) and further investigations are needed to predict the rate of their mass-transferring phase. There are no confirmed observations of WDBH binaries from electromagnetic surveys, although these binaries, like other mass-transferring systems, are expected to emit across a broad spectrum and have even been suggested to produce gamma-ray bursts [452]. The X-ray binary X-9, in the globular cluster 47 Tucanae, might host a white dwarf and a black hole [453, 454, 455], but the system is also consistent with a neutron star accretor. Other candidates include XMMU $122939.7 + 075333$ in a globular cluster of the Virgo Galaxy NGC 4472 [456]. We explore the ability of LISA to detect and characterise this virtually unexplored binary population. Using a semi-analytical model to describe the evolution of WDBH binaries, we derive two universal relations followed by these binaries in their evolution. We simulate LISA observations on which we perform a full Bayesian analysis, and using the universal relations we derived, we show that LISA could be the first observatory to unambiguously identify WDBH binaries.

5.1 Environmental effects

5.1.1 Perturbative corrections to the waveform

In order to compute how gravitational waves are modified due to environmental effects, we follow a similar path to section 4.1.1, i.e we compute the leading order correction to the dynamics of BBHs and then use the stationary phase approximation to obtain the Fourier domain deviation from vacuum BBHs. For sake of readability, we will not provide the full derivation for all three effects, we will briefly sketch them and provide the appropriate references. The effects are considered individually when deriving the modifications to the waveform. Let us first consider the example of accretion. We assume that the components

of a BBH embedded in a gaseous medium accrete at a same fraction of the Eddington ratio:

$$f_{\mathrm{Edd},i} = \frac{\dot{m}_i}{\dot{m}_{\mathrm{Edd}}}\,, \tag{5.1}$$

where $\dot{m}_{\mathrm{Edd}} \simeq 2.2\times10^{-8}\left(\frac{m_i}{M_\odot}\right) M_\odot\,\mathrm{yr}^{-1}$ is the Eddington accretion rate (obtained from the Eddington luminosity assuming radiative efficiency 0.1). The mass of the black holes then increases as

$$m_i(t) = m_{i,0}e^{-f_{\mathrm{Edd}}t/T_{\mathrm{Edd}}} \tag{5.2}$$

where $T_{\mathrm{Edd}} = 4.5\times10^7$ yr is the Salpeter time, and $m_{i,0}$ are the initial masses of the black holes. Considering that accretion proceeds adiabatically ($\dot{m}_i \ll m_i\omega_{\mathrm{orb}}$), the orbital angular momentum along the direction orthogonal to the orbital plane is invariant under accretion and the orbit remains circular (see, e.g., section 49 of [457] on adiabatic invariants). Thus, angular momentum is lost only through gravitational waves. Using Kepler's law, we have $J = \mathcal{M}_c^{5/3}\omega_{\mathrm{orb}}^{-1/3}$, and accounting for the time dependency of the chirp mass due to accretion, the angular momentum balance equation yields

$$\dot{\omega}_{\mathrm{orb}} = \frac{96}{5}\mathcal{M}_c^{5/3}\omega_{\mathrm{orb}}^{11/3} + 5\frac{\dot{\mathcal{M}}_c}{\mathcal{M}_c}\omega_{\mathrm{orb}}. \tag{5.3}$$

We then solve this equation and apply the stationary phase approximation, performing an expansion up to linear order in f_{Edd} [36]. To leading order, the phase shift for the (2,2) harmonic due to accretion reads

$$\Delta\Psi_{\mathrm{accretion}} = -f_{\mathrm{Edd}}\,\frac{1125\,\mathcal{M}_c}{851968(1+z)\tau_{\mathrm{Edd}}}\,(\pi\mathcal{M}_c f)^{-13/3}\,. \tag{5.4}$$

It will be implicit in the following that the masses appearing the waveform are the initial masses $m_{i,0}$. Accretion will in general be accompanied by a drag force due to the fact that the accreted material carries some angular momentum. This drag force yields an additional term in the angular momentum balance equation, and can either enhance or decrease the effect of accretion on the waveform. In our analysis we discard the terms due to this drag force, which would add a parameter in our waveform (strongly correlated to f_{Edd}), and require proper modelling of the dynamics of accretion. On the other hand, we include the dynamical friction due to the displacement of the binary in a gaseous medium.

Assuming a binary's centre of mass approximately comoving with the gas, dynamical friction exerts a drag force on each black hole (opposite to the black holes's velocity $\vec{v}_i$ in the centre of mass frame) given by

$$\vec{F}_{\mathrm{DF},i} = -\frac{4\pi\rho_g m_i^2 I(r_i,v_i)}{v_i^3}\vec{v}_i, \tag{5.5}$$

where ρ_g is the gas density in the AGN disk, r_i is the distance of the black hole from the centre of mass, and we assume $v_i \gg c_s$ (with c_s the sound speed; note that v_i is relativistic for binaries in the LISA band). For the "Coulomb logarithm" $I(r,v)$, we use the analytic expression of [458], which was validated against simulations for $v_i/c_s \lesssim 8$, but which we

extrapolate further (c.f. [459]). Following [458] (see also [460, 461, 462]), we only include the effect of the wake created by each black hole on itself, and neglect the companion's [463]. For $f \lesssim 0.3\,\mathrm{Hz}$ this is a good approximation, since the orbital separation of SBHBs and IMBHBs in the LISA band is larger than the wake's size. For the sound speed, we assume $c_s \approx v_g(H_d/a_g)$ [464], where a_g is the distance from the binary to the central massive black hole (i.e. the galactocentric radius), v_g is the galactocentric orbital velocity and H_d is the disk's height. The Zwicky Transient Facility measured a gas density surrounding the event of $\rho_{g,0} = 10^{-10}\,\mathrm{g\,cm^{-3}}$ and a disk aspect ratio $H_d/a_g \sim 0.01$ [437]. We will use the latter value to compute the sound speed, and treat the gas density as a free parameter. In presence of dynamical friction, the energy balance equation reads

$$\dot{E} = P_{\mathrm{GW}} - F_{\mathrm{DF},1} v_1 - F_{\mathrm{DF},1} v_2. \tag{5.6}$$

Solving for the orbital angular velocity and applying the stationary phase approximation leads to a -5.5PN modification in the phase, which at linear order in ρ_g reads

$$\Delta\Psi_{\mathrm{DF}} = -\rho_g \frac{25\pi(3\eta-1)\mathcal{M}^2}{739328(1+z)^2\eta^2}\,\gamma_{\mathrm{DF}}\,(\pi\mathcal{M}_c f)^{-16/3}\,, \tag{5.7}$$

with $\gamma_{\mathrm{DF}} = -247\ln(f/f_{\mathrm{DF}}) - 39 + 304\ln(20) + 38\ln(3125/8)$ and $f_{\mathrm{DF}} = c_s/[22\pi(m_1+m_2)]$.

Finally, the binary's centre of mass peculiar acceleration also modifies the waveform. It leads to a time dependent redshift for the source, which for a constant acceleration can be written to linear order as [465, 466]

$$1 + z(t_{\mathrm{obs}}) = (1+z_c)\left(1 - \frac{\dot{v}_g^{\parallel}(t_{c,\mathrm{src}})}{1+z_c}(t_{c,\mathrm{obs}} - t_{\mathrm{obs}})\right), \tag{5.8}$$

where z_c is the redshift at coalescence (which is absorbed in the definition of the redshifted mass), and $\dot{v}_g^{\parallel}(t_{c,\mathrm{src}})$ is the acceleration along the line of sight, computed at coalescence, dominating over the cosmological acceleration (which we neglect). The peculiar motion of the observer is accounted for in the response of the detector. The time dependency of the redshift translates into a phase shift when relating source frame to detector frame quantities in the stationary phase approximation, which reads [465, 467, 466]

$$\Delta\Psi_{\mathrm{acceleration}} = \frac{25\,\mathcal{M}_c}{65536}\dot{v}_g^{\parallel}(t_c)\;(\pi\mathcal{M}_c f)^{-13/3}\,, \tag{5.9}$$

In the case of a binary on a circular orbit around the AGN, $\dot{v}_g^{\parallel} \approx (3.2\times10^{-11}\mathrm{m/s^2})\,\epsilon$, where [465]

$$\epsilon = \left(\frac{v_{\mathrm{g}}}{100\,\mathrm{km/s}}\right)^2 \frac{10\,\mathrm{kpc}}{a_g}\cos(\psi_g)\,, \tag{5.10}$$

with ψ_g the angle between line of sight and acceleration. Note that ϵ could have either sign, depending on whether the binary is moving towards or away from the observer. Since $\cos(\psi_g) = \cos\iota_g \sin(\Omega_g t + \phi_{g,0})$ (with ι_g the inclination angle of the line of sight relative to the AGN disk, $\Omega_g = \sqrt{M}/a_g^{3/2}$, and $\phi_{g,0}$ the initial phase), the assumption of constant acceleration only holds at sufficiently large galactocentric distances a_g (i.e. low Ω_g). We will verify this assumption a posteriori (and relax it) later.

Equations (5.4) and (5.9) show that accretion and (constant) acceleration are degenerate, since they both appear at -4PN order [468, 469, 465, 36] (though accretion always yields a negative phase contribution, while acceleration can give contributions of either sign). Both effects can be included in the waveform via a phenomenological post-Newtonian term $\Delta\Psi_{-4\mathrm{PN}} = \Psi_{-4}\left(\pi\mathcal{M}_c f\right)^{-13/3}$, with Ψ_{-4} related to f_{Edd} and ϵ for accretion and acceleration, respectively.

We generate data and parametrise SBHBs as described in section 3.1. We consider only the $(2, \pm 2)$ harmonic, and include the effect of constant acceleration, accretion and dynamical friction by adding their respective phase shifts to PhenomD waveforms.

5.1.2 Accretion in SBHBs and IMBHBs

We start by evaluating the possibility of observing the effect of accretion in SBHBs and IMBHBs, working in the Bayesian framework presented in the previous chapters. We perform two different analyses: in the first one we generate data with a nonzero value for f_{Edd} and include it as a free parameter in the Bayesian analysis, in order to estimate with what precision it can be recovered. In the second case, data is also generated with a nonzero value of f_{Edd}, but when doing the analysis we set $f_{\mathrm{Edd}} = 0$ in the templates, in order to measure the bias in the parameter estimation. Then, we discuss of the possibility of detecting electromagnetic counterparts to these accreting binaries. We consider the two same scenarios as in section 4.1: *LISA-only* and *LISA+Earth*. We recall that in the latter case we set a narrow prior on the time to coalescence in order to simulate a multiband detection. We assume a ten years mission duration, a 100% duty cycle, and use the LISA proposal noise level [29], including the confusion noise due to GBs [315]. The parameter estimation is performed with our MHMCMC sampler, using $f_{\mathrm{Edd}}/(1+z)$ as a sampling parameter that we add to the first group of parameters (intrinsic parameters) during the burn-in phase. We take a flat prior on f_{Edd}, restricted to positive values, and the *Fiducial* prior for the remaining parameters (see section 3.3.2). We have also performed these analyses with `Multinest`, a public nested sampling algorithm [428, 365], for cross-validating our results .

In [36] we generated a synthetic astrophysical catalogue of SBHBs on which we performed a Fisher analysis to estimate the detectability of these sources and our ability to measure f_{Edd}. We found that for a LISA mission of ten years, the Eddington ratio could be measured with an error less than 100 % for a few systems. This computation was performed with angle averaged waveforms (see section 4.2.5). When including the source location, different realisations of the angles for the same astrophysical system yield different SNRs. This affects the precision within which one can recover the parameters of the source, including the sky position itself and f_{Edd}. Moreover, even for a fixed SNR level, the sky localisation provided by LISA depends on the position of the source. In order to cross-check results obtained with our Fisher matrix analysis and to quantify this variability, we select from the catalogue an astrophysical system for which the accretion parameter can be measured precisely through the Fisher matrix approach, and draw three different realisations of (λ, β, ψ, φ ,ι) yielding a low SNR (~ 9), a medium SNR (~ 15), and a high SNR (~ 20), respectively.

We also choose two optimistic IMBHB systems on the basis of a Fisher matrix analysis spanning the parameter space, i.e. the errors on f_{Edd} provided by the chosen IMBHBs are roughly the smallest throughout the parameter space. In more details, the systems that we

consider are

- An SBHB with $m_1 = 42.1\ M_\odot$, $m_2 = 39.8\ M_\odot$, $\chi_1 = 0.008$, $\chi_2 = 0.44$, at a distance $d_L = 416$ Mpc;
- An IMBHB with $m_{1,s} = 315\ M_\odot$, $m_{2,s} = 284\ M_\odot$, $\chi_1 = 0.9$, $\chi_2 = 0.85$, referred to as "light IMBHB";
- Another IMBHB with $m_{1,s} = 1000\ M_\odot$, $m_{2,s} = 900\ M_\odot$, $\chi_1 = 0.9$, $\chi_2 = 0.85$, referred to as "heavy IMBHB".

Optimistically, we take the sources to be chirping and set the time to coalescence to the mission's duration. We study the IMBHB systems at two different redshifts, $z = 0.1$ and $z = 0.5$, in order to estimate up to what distance the presence of accretion in the binary would be detectable. Note that the masses of the IMBHBs are given in the source frame. We use the same set of angles for the two IMBHBs, which were drawn randomly. The light and heavy IMBHBs have respectively SNRs of 218 and 593 at $z = 0.1$, and 46 and 126 at $z = 0.5$. We work only in the *LISA-only* scenario when considering IMBHBs.

Measuring accretion and sky localisation

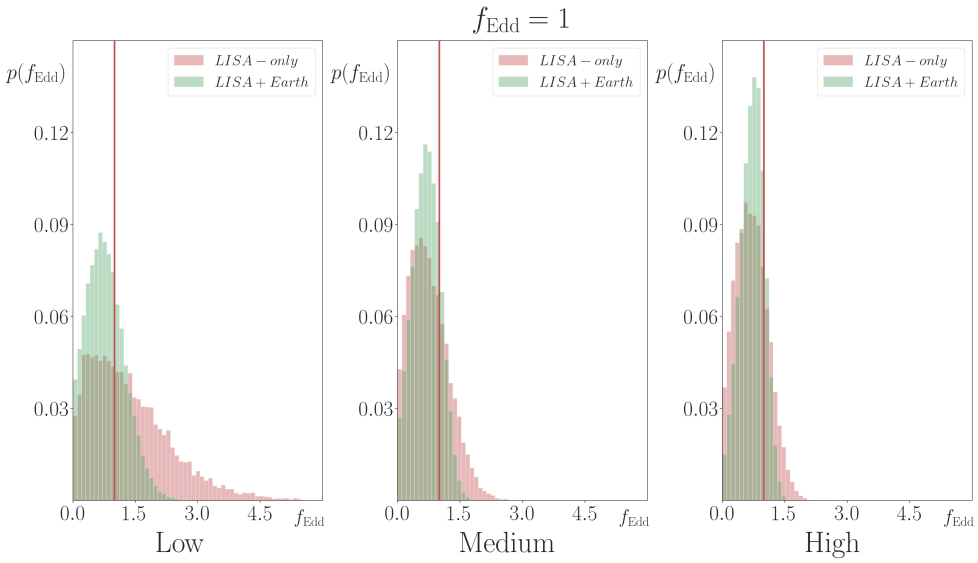

Figure 5.1: Marginalised distributions of $f_{\rm Edd}$ for the considered SBHB for various realisations of the angles, in the scenarios *LISA+Earth* (green) and *LISA-only* (red). Red lines indicate the injected value of the accretion rate, $f_{\rm Edd} = 1$. In the *LISA+Earth* scenario and for higher SNR the marginalised distribution is strongly peaked but still consistent with $f_{\rm Edd} = 0$.

In figure 5.1 we show the marginalised distributions of $f_{\rm Edd}$ for the chosen SBHB system, for various SNRs and for an injected value of $f_{\rm Edd} = 1$. For the high and the medium SNR

cases, already in the *LISA-only* scenario the posteriors indicate the presence of accretion. The marginalised distribution for $f_{\rm Edd}$ can be compared with those obtained when constraining modifications of general relativity in the parametrised post-Einsteinian framework. There, we saw that when generating data with no deviation from general relativity, the marginalised distribution of the non-general relativity parameters was mostly flat up to a threshold (representing the upper bound that can be placed on the parameters under scrutiny), and then went to 0 (see section 4.1.4). In contrast, we see in figure 5.1 that for high and medium SNR in the *LISA-only* scenario, the distribution peaks at some nonvanishing value, favouring the presence of a nonzero modification to the vacuum waveform. However, as discussed in section 4.1.5, correlations with intrinsic parameters could also make the posterior peak away from zero in the absence of modifications, therefore the support of the posterior provides the best argument for claiming a detection. In figure 5.2 we show the same as in figure 5.1, but for an injected value of $f_{\rm Edd} = 10$. This high accretion rate can be clearly detected even in the low SNR case and in the *LISA-only* scenario, since in this case $f_{\rm Edd} = 0$ is outside the support of the distribution. Thus, for super-Eddington accreting binaries in the LISA band, there is a concrete chance to detect the effect of high rates of accretion on the waveform for most SBHB events.

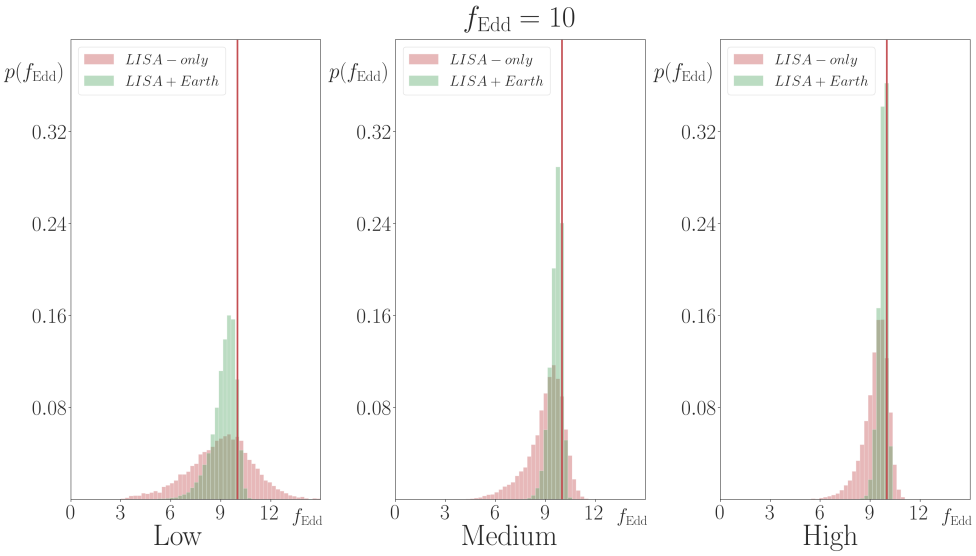

Figure 5.2: Same as figure 5.1 but for an injected value of $f_{\rm Edd} = 10$. Accretion is detected in all scenarios and for any angle realisation.

In table 5.1 we show the recovered 90% confidence intervals and median values for $f_{\rm Edd}$ and the sky localisation. In the $f_{\rm Edd} = 1$ case, since the distribution is leaning against the boundary of the prior (see figure 5.1), we define the 90% confidence interval for $f_{\rm Edd}$ by taking the lower 90% values. Instead, in the $f_{\rm Edd} = 10$ case, the interval is centred around the median values. We give the median value as point estimate. The 90% confidence sky localisation is defined as in equation (3.17). We show the same quantities for our IMBHB events in table 5.2. There, in the case $f_{\rm Edd} = 1$, we define the 90% confidence interval for $f_{\rm Edd}$ centred on the median, and in the case $f_{\rm Edd} = 0.1$ we define it by taking the lower

90% values. Except for the low SNR system, the error on the sky location is smaller than the nominal field of view of future X-ray and radio missions, potentially allowing for the detection of electromagnetic counterparts. We will discuss this possibility next.

	$f_{\rm Edd}^{\rm injected}=1$		$f_{\rm Edd}^{\rm injected}=10$	
	$f_{\rm Edd}$	$\Delta\Omega$ (deg^2)	$f_{\rm Edd}$	$\Delta\Omega$ (deg^2)
High SNR	$0.73^{+0.34}_{-0.73}$	0.32	$9.81^{+0.29}_{-0.54}$	0.32
Medium SNR	$0.69^{+0.43}_{-0.69}$	0.14	$9.23^{+0.42}_{-0.76}$	0.14
Low SNR	$0.75^{+0.66}_{-0.75}$	0.76	$9.33^{+0.79}_{-1.61}$	0.76

Table 5.1: Recovered 90% confidence interval on the accretion parameter $f_{\rm Edd}$ and on the sky location $\Delta\Omega$ for the considered SBHBs in the *LISA+Earth* scenario. The presence of accretion should be detected for super-Eddington accreting systems. The error on the sky position is within the field of view of Athena and SKA for the medium and high SNR systems, allowing (potentially) for electromagnetic followup.

	$f_{\rm Edd}^{\rm injected}=0.1$		$f_{\rm Edd}^{\rm injected}=1$	
	$f_{\rm Edd}$	$\Delta\Omega$ (deg^2)	$f_{\rm Edd}$	$\Delta\Omega$ (deg^2)
Light IMBHB	$0.14^{+0.12}_{-0.14}$	0.02	$1.05^{+0.12}_{-0.92}$	0.02
Heavy IMBHB	$0.17^{+0.17}_{-0.17}$	0.02	$1.04^{+0.20}_{-0.72}$	0.01

Table 5.2: Recovered 90% confidence interval on the accretion parameter $f_{\rm Edd}$ and on the sky location $\Delta\Omega$ for our two IMBHB systems, at redshift $z=0.1$. The statistical error estimated with our Fisher-matrix analysis is similar for the two IMBHBs. The presence of accretion should be detected for Eddington accreting systems. The error on the sky position is always within the field of view of Athena and SKA.

In figure 5.3 we compare how well can we recover $f_{\rm Edd}$ for IMBHBs at different redshifts, for injected $f_{\rm Edd}=1$. If the system is too far, the distribution tends to be flat and the effect of accretion is hardly noticeable. This is because of the lower SNR, but also because the detector-frame mass becomes larger at higher redshift, speeding up the evolution of the system and thus providing less information on negative post-Newtonian order modifications. Finally, in figure 5.4 we show how well can we recover $f_{\rm Edd}$ in IMBHBs for injected values of $f_{\rm Edd}=0.1$ at $z=0.1$. As in the case of SBHBs commented above, the marginalised distribution is compatible with $f_{\rm Edd}=0$, but the presence of a clear peak at $f_{\rm Edd}\neq 0$ favours the presence of accretion.

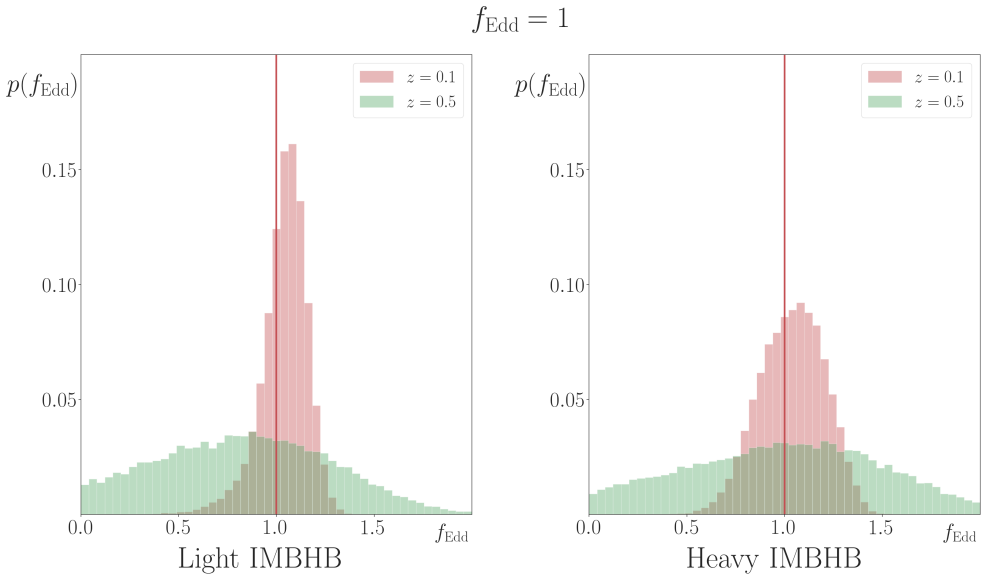

Figure 5.3: Marginalised distributions of $f_{\rm Edd}$ for our two IMBHB systems at redshifts $z = 0.1$ (red) and $z = 0.5$ (green) for an injected value of $f_{\rm Edd} = 1$. Accretion can be measured in both systems at $z = 0.1$, but not at higher redshift.

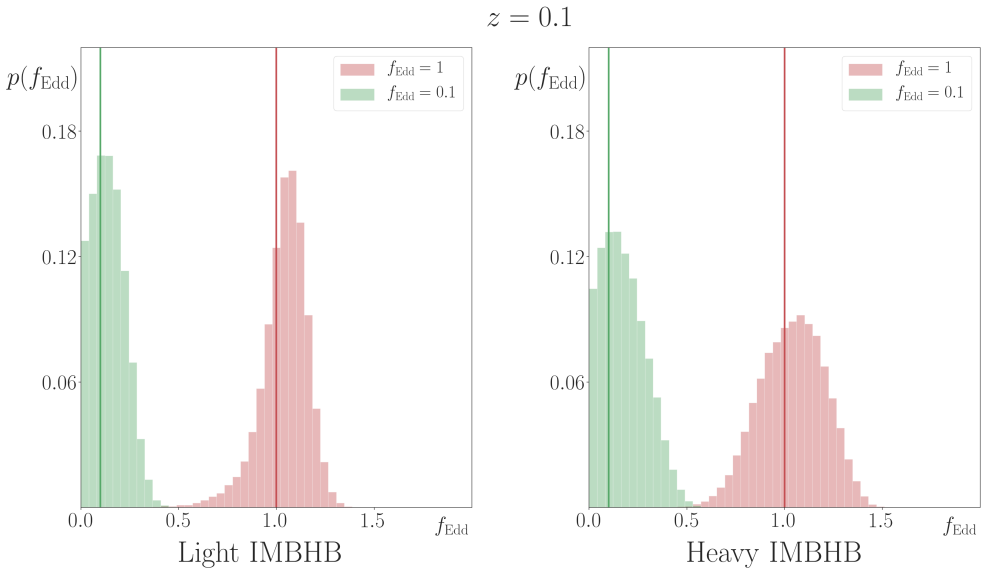

Figure 5.4: Marginalised distributions of $f_{\rm Edd}$ for our two IMBHB sources for injected values of $f_{\rm Edd} = 0.1$ and $f_{\rm Edd} = 1$ at $z = 0.1$. Accretion at this redshift needs to be approximately Eddington-level or stronger to be measured.

Estimating biases

The above results indicate that if accretion is present it could lead to a measurable change in the gravitational wave signal. Thus, if accretion is not taken into account, the estimation

of other source parameters could be significantly biased. Since $f_{\rm Edd}$ correlates mostly with the intrinsic parameters of the source, the latter should be the most affected.

For SBHBs in the *LISA-only* scenario, we find that in the three cases (high, medium, and low SNR), the signal can be recovered by an effectual template with $f_{\rm Edd} = 0$, i.e., we find a maximum for the posterior distribution which, in the worst cases, can be incompatible with the injected real value. The SNR of this effectual template is very similar to the injection's SNR ($\mathrm{SNR}_{\rm inj} - \mathrm{SNR}_{\rm eff} \lesssim 0.7$), and could thus trigger a detection. The bias in the parameter estimation and the relative drop in SNR is higher for higher SNR systems and for higher injected accretion rates. The effectual template, in particular, has a higher chirp mass and a higher mass ratio, while the initial frequency is shifted towards higher values. In figures 5.5 and 5.6 we show how this impacts the estimate of the masses and time to coalescence for two representative values, $f_{\rm Edd} = 1$ and $f_{\rm Edd} = 10$. In both cases, we compare to the recovered distribution of masses for vacuum general relativity. The mass of the primary black hole is shifted towards higher values, whereas the secondary mass gets lower. As a result, the time to coalescence is underestimated. For super-Eddington accretion, this shift in time to coalescence is at the level of tens of seconds. A multiband observation could then help identify a bias due to accretion in the parameter estimation, since ground-based detectors would measure very precisely the time to coalescence when the signal enters in their band [32].

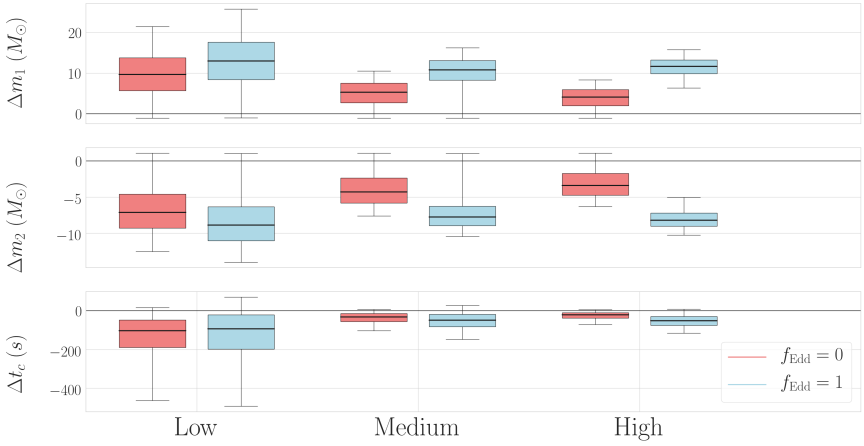

Figure 5.5: Bias in the SBHB binary masses and time to coalescence induced by ignoring the corrections due to accretion when $f_{\rm Edd} = 1$, for various angle realisations in the *LISA-only* scenario (blue) compared to the displacement found in vacuum systems (red). Boxes and whiskers delimit the 50% and 90% confidence intervals, respectively, and both are centred around the median, indicated by lines inside the boxes. For this level of accretion bias is not significant, even for the high SNR realisation.

In order to estimate this possibility, we repeat the above analysis in the *LISA+Earth* scenario. In this case the time to coalescence is constrained to within 1 ms from its true value, so no bias in t_c is possible. Nevertheless, signals can still be recovered by an effectual template, although with a larger mismatch from the true signal. In figure 5.7 we show the

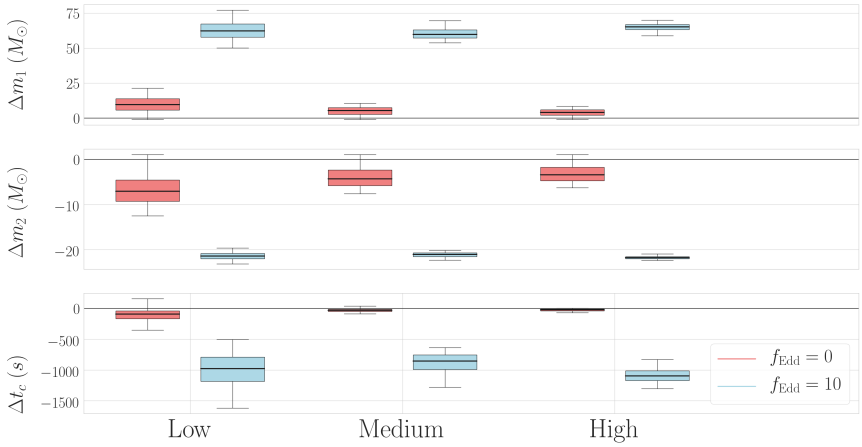

Figure 5.6: Same as in figure 5.5 but comparing $f_{\rm Edd} = 0$ with $f_{\rm Edd} = 10$. Bias here is significant for all SNR realisations.

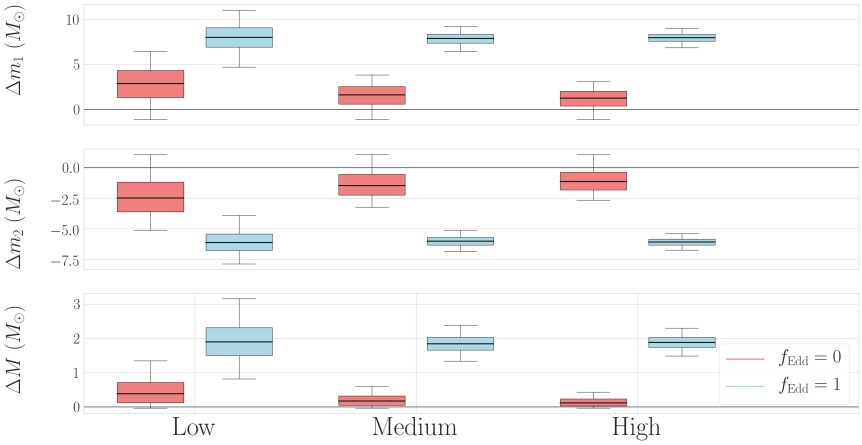

Figure 5.7: Same as in figure 5.5 but for the *LISA+Earth* scenario. We show M rather of t_c, the latter being fixed by the narrow prior in this scenario. Bias in the masses can still be significant for medium and high SNR realisations, despite the constraint provided by ground-based detectors.

difference between the recovered masses and total mass and the injected values. More in general, ground-based detectors should be largely insensitive to these low-frequency terms, as discussed in [342]. In this forecast study, the projected constraint on -4PN terms with the planned third generation detector CE is ten orders of magnitude worse than the projected constraint with LISA. We thus expect that observations with ground-based detectors should not be biased by omitting -4PN terms. Therefore, for values of $f_{\rm Edd}$ for which the LISA parameter estimation is significantly biased, the posterior distributions obtained with LISA

and with ground-based detectors might not even be compatible, which would hint at an unmodelled effect.

It is noteworthy that for the SBHB events the sky localisation is barely affected by accretion and remains excellent, as the distribution remains a Gaussian centred around the injected values with errors similar to the ones shown in table 5.1. In the case of IMBHBs, on the other hand, there is also a bias in the sky localisation, i.e. the injected value may lie outside the 90% confidence interval. This is due to the very small errors in sky position, and in fact the true localisation is very close to the recovered one, within $0.05\,\mathrm{deg}^2$. Therefore, for most realistic purposes the sky localisation is satisfactorily recovered. Since we did not consider any modification to the gravitational wave amplitude, when fixing $f_{\rm Edd} = 0$ as we did here, there is no bias on the estimation of D_L, contrary to the Fisher-matrix analysis in [466]. They also used waveforms modifying general relativity at -4PN order in phase, but included the leading-order modification to the amplitude too.

Prospects for electromagnetic counterparts

According to our MCMC analysis, both SBHBs and IMBHBs can typically be localised in the sky to within the fields of view of X-ray and radio instruments such as Athena and SKA, $\Delta\Omega_{\rm Athena} = 0.4\,\mathrm{deg}^2$, $\Delta\Omega_{\rm SKA} = 0.5\,\mathrm{deg}^2$ [327, 326]. This will allow the relevant region of the sky to be covered in a single viewing[2], thus potentially allowing for the coincident detection of an X-ray and/or radio counterpart to strongly-accreting BBHs. Even if the sky localisation was biased, as might be the case for IMBHBs, we estimated that the true position would still fall inside the field of view of the instruments. In the following, we compute the X-ray and radio emission of the binaries, and estimate the necessary integration time for detection by a single instrument viewing.

We start by estimating the X-ray flux. For this purpose, we assume that the accretion process has radiative efficiency $\varepsilon_{\rm rad} = 0.1$ (which is a good approximation at $f_{\rm Edd} < 1$), and that only a fraction 0.1 of the electromagnetic radiation is emitted in X-rays ("bolometric correction"). We find the X-ray flux from a single accreting black hole of mass m to be

$$F_X \simeq 1 \times 10^{-13} f_{\rm Edd} \left(\frac{m}{M_\odot}\right)\left(\frac{\mathrm{Mpc}}{D_L}\right)^2 \mathrm{erg\,cm^{-2}\,s^{-1}}\,. \tag{5.11}$$

This should be compared with the flux sensitivity of Athena for a given integration time, $T_{\rm int}$. Following [470], Athena's flux sensitivity for a 5σ detection is

$$F_X^{\rm Athena} = 1 \times 10^{-15} \left(\frac{10^3\,\mathrm{s}}{T_{\rm int}}\right)^{1/2} \mathrm{erg\,cm^{-2}\,s^{-1}}\,. \tag{5.12}$$

If both black holes are accreting, the minimum integration time for a binary where only one black hole is emitting is then given by

$$T_{\rm int} \simeq 8 \times 10^{-2}\, f_{\rm Edd}^{-2} \left(\frac{D_L}{\mathrm{Mpc}}\right)^4 \left(\frac{M_\odot}{M}\right)^2 \mathrm{s}\,. \tag{5.13}$$

[2]In some cases, the correlation between the sky position angles can imprint an asymmetric shape to the localised region, which might therefore partially fall outside the field of view. However, this would still only require $\mathcal{O}(1)$ viewings.

For the best-candidate SBHB event in our synthetic astrophysical catalogues, the required exposure time is $T_{\rm int} \gtrsim 4 \times 10^5 \, f_{\rm Edd}^{-2} \, {\rm s}$. Thus, even if we were to assume $f_{\rm Edd} \approx 1$, the integration time would have to be of several days. Assuming super-Eddington accretion $f_{\rm Edd} > 1$ is unlikely to help as the radiative efficiency is expected to be considerably lower than our assumed 0.1, i.e. the bolometric luminosity is not expected to significantly exceed the Eddington luminosity [471, 472, 473]. Moreover, high accretion rates in SBHBs likely require environments with large gas densities, such as AGNs, whose optical thickness further reduces the chances of an electromagnetic detection. For the considered IMBHB systems at $z = 0.1$, the required integration time is between 0.3 and 3 hours for Eddington-level accretion, for the heavy and light systems, respectively. This estimate suggests that detection of X-ray counterparts will be possible for (nearby) highly-accreting IMBHBs.

A binary system in external magnetic fields may also launch dual radio jets, which get amplified by the coalescence [474] relative to similar jets observed in isolated black holes [475]. See also [476] for simulations that yield ∼100 times larger (though less collimated) fluxes than [474]. Assuming a fiducial value $\varepsilon_{\rm rad} = 0.1$ for the radiative efficiency of the process and 0.1 for the fraction of emission in the radio band, the corresponding peak flux[3] is [474, 224]

$$F_{\rm flare} \simeq 2 \times 10^{-13} \, f_{\rm Edd} \, q^{-2} \left(\frac{D_L}{\rm Mpc} \right)^{-2} \left(\frac{M}{M_\odot} \right) \times {\rm erg \, cm^{-2} \, s^{-1}} \, . \tag{5.14}$$

Note that our definition of q is the inverse of [474, 224]. The flare flux can then be compared with the SKA sensitivity in the phase 1 implementation. The required sensitivity at frequency $\nu_{\rm SKA}$ for SKA,

$$F_{\rm SKA} = 5 \times 10^{-16} \left(\frac{10^{-2} \, {\rm s}}{T_{\rm obs}} \right)^{1/2} \left(\frac{\nu_{\rm SKA}}{\rm GHz} \right) \, {\rm erg \, cm^{-2} \, s^{-1}} \, , \tag{5.15}$$

is reached for an observation time $T_{\rm obs} \sim 10^{-2} \, {\rm s}$ for our best SBHB event. The observation time should be smaller than the duration of the merger (i.e., the duration of the flare) for the system [475], $T_{\rm flare} \sim 25 \, \frac{m}{100 M_\odot}$ ms. This condition is not satisfied for SBHBs. There is however the concrete possibility to detect a signal in the radio band for IMBHBs, for which for the light and heavy systems $T_{\rm obs} \approx 40 - 4$ ms $< T_{\rm flare}$. The performance of full SKA should improve by an order of magnitude with respect to equation (5.15), reducing the required integration time by a factor 100.

5.1.3 GW190521-like binaries

Finally, we turn to GW190521-like systems, i.e rather massive binaries, which could be labelled both as an SBHB or an IMBHB, residing in an AGN disk. We note $M_{\rm MBH}$ the mass of the central massive black hole, which in AGN J124942.3+344929, the candidate host for GW190521, is $M_{\rm MBH} \sim 10^8 - 10^9 \, M_\odot$. We assume a mission duration of six years, and consider two scenarios: *LISA-only* and *LISA+Ground*. In the latter case, we mimic a multiband detection by assuming that masses, spins, and merger time are measured by

[3]The peak sensitivity is reached when the orbital velocity is equal to that of the ISCO.

ground-based detectors, thus removing them from the analysis. Note this is a more optimistic assumption than in the *LISA+Earth* scenario previously considered. We assume a 100% duty cycle, and, in order to be more conservative, we use the SciRDv1 noise curve [314], including the confusion noise due to GBs [315].

In figure 5.8 we show the distribution of errors – produced with the augmented Fisher formalism described in section 3.4.3 – for the Eddington rate $f_{\rm Edd}$, the acceleration parameter ϵ, and the gas density ρ_g, (normalised to $\rho_{g,0} = 10^{-10}\,{\rm g\,cm^{-3}}$), considering modifications one by one. We use $f_{\rm Edd} = \rho_g = \epsilon = 0$ as injections, i.e. the distributions represent optimistic upper bounds on the parameters. We use the LVC masses, projections of spins on the orbital angular momentum, distance and inclination samples for the NRSur7dq4 model [106] and, for each sample, we set the time to coalescence to the mission's duration and draw sky location and polarisation randomly. We only perform the Fisher analysis for systems with SNR in the LISA band above 8. We find that LISA alone can detect super-Eddington accretion rates

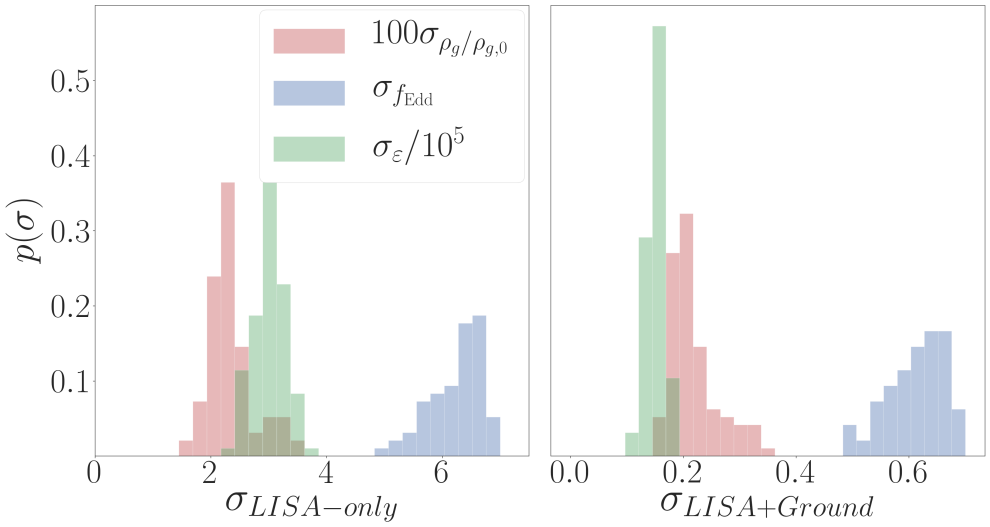

Figure 5.8: Distribution of Fisher-matrix errors on environmental effects for the LVC samples, with LISA alone or jointly with ground-based detectors.

($f_{\rm Edd} \gtrsim 6$), which may be typical in dense environments [477], and acceleration parameters $\epsilon \gtrsim 3 \times 10^5$, corresponding to $a_g \lesssim 1$ pc for $M_{\rm MBH} = 10^8 M_\odot$. The dynamical friction effect is even stronger, with $\rho_g/\rho_{g,0}$ constrained at percent level. All errors improve by about an order of magnitude in the *LISA+Ground* scenario (e.g., sub-Eddington accretion rates become measurable).

Next, we pick from the LVC posteriors the event with the highest SNR in the LISA band. The intrinsic parameters of this system are $m_{1,s} = 123\ M_\odot$, $m_{2,s} = 72\ M_\odot$, $\chi_1 = -0.40$ and $\chi_2 = -0.05$, it is at a distance $D_L = 1424$ Mpc ($z = 0.27$), and has an SNR in the LISA band of 9.6. We perform a full Bayesian analysis on this system, injecting nonzero values (plausible for sources in AGNs) for all environmental effects (considered simultaneously): $f_{\rm Edd} = 5$, $\epsilon = 3.2 \times 10^6$ (corresponding to $a_g \approx 0.4$ pc for $M_{\rm MBH} = 10^8\ M_\odot$) and $\rho_g = \rho_{g,0} = 10^{-10}\,{\rm g\,cm^{-3}}$. The effects of accretion and constant acceleration are accounted for by the effective parameter Ψ_{-4}. We assume a flat prior on Ψ_{-4} and ρ_g (we use $\rho_g/(1+z)^2$ as a sampling parameter).

Figure 5.9 shows the posterior distributions for the density ($\rho_g/\rho_{g,0}$) and the parameter Ψ_{-4} accounting for acceleration/accretion. Both parameters can be measured well, since they appear at different (negative) post-Newtonian orders. Note that the sign of Ψ_{-4} can help distinguish accretion ($\Psi_{-4} < 0$) from acceleration (Ψ_{-4} of either sign). Since this system is close to the LISA detection threshold (SNR ~ 8), we conclude that even for near-threshold events environmental effects are measurable, and their observation will only be limited by the event detectability.

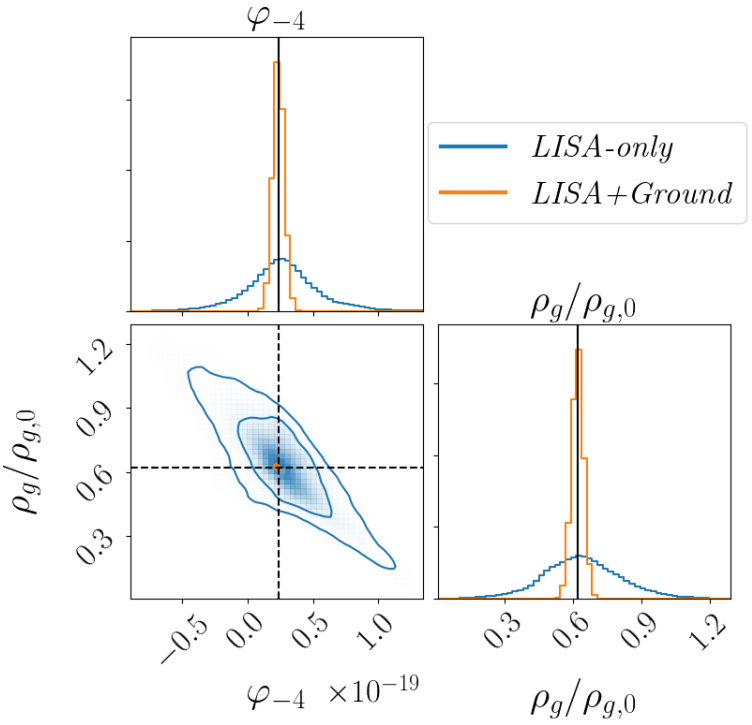

Figure 5.9: Posterior distribution of gas density and -4PN phase term (i.e. constant acceleration/accretion), with 68%, 95% and 99% confidence contours for a best-case event consistent with GW190521. Black lines indicate the injected values.

The assumption of constant acceleration breaks down if the systematic error produced by the variation of ϵ over the observation time $T_{\rm obs}$ is no longer negligible relative to the statistical error. Taylor-expanding ϵ in time, we compute its variation over the observation time: $\Delta\epsilon \sim M_{\rm MBH}^{3/2} T_{\rm obs}/a_g^{7/2}$. Requiring this variation to be smaller than the statistical error we obtained with our Fisher analysis, we get that the acceleration can no longer be considered constant for $a_g \lesssim 0.25\,{\rm pc}\,[M_{\rm MBH}/(10^8 M_\odot)]^{3/7}[T_{\rm obs}/(6{\rm yr})]^{2/7}$ (i.e. galactic orbital periods $T_g \lesssim 1200\,{\rm yr}\,[M_{\rm MBH}/(10^8 M_\odot)]^{1/7}[T_{\rm obs}/(6{\rm yr})]^{3/7}$). This is the case, e.g., if GW190521 lies in a disk migration trap. Reference [437] estimates the trap's distance from the central black hole as $a_g \sim 700M$, corresponding to $T_g \sim 1.8\,{\rm yr}$, i.e. the acceleration cannot be assumed constant over the observation time. In this situation, the Taylor-expansion leading to equation (5.9) breaks down, and the gravitational wave signal can be estimated as $s(t) = h(t + d^{\shortparallel}(t))$. The delay $d^{\shortparallel}(t)$ arises from the change in the source distance due to the orbital motion, and is given by the orbit's projection on the line of sight: $d^{\shortparallel}(t) = a_g \cos\iota_g \sin(\Omega_g t + \phi_{g,0})$. This time-

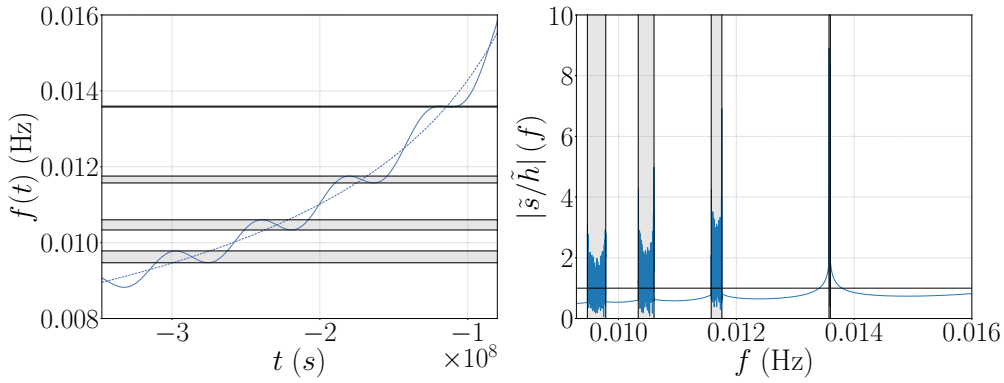

Figure 5.10: Doppler modulations of the gravitational wave signal due to the motion around the central black hole. The left panel shows the time-frequency track of the modulated signal (solid line) compared to the non-modulated one (dashed) (coalescence is at $t = 0$). The right panel shows the amplitude of the Fourier-domain transfer function $(\tilde{s}/\tilde{h})(f)$, with a horizontal line at 1. In both panels, the shaded bands show the frequency bands where the time-to-frequency map becomes multi-valued.

varying delay produces an oscillating Doppler modulation $\Psi_{\rm Doppler} \sim 2\pi f d^{\shortparallel}$ of the observed signal. The magnitude of this phase is approximately

$$2\pi f a_g \sim 2 \times 10^4 \,\mathrm{rad} \left(\frac{M_{\rm MBH}}{10^8 M_\odot}\right) \left(\frac{f}{10\,\mathrm{mHz}}\right) \left(\frac{a_g}{700M}\right) . \tag{5.16}$$

This effect strongly impacts the signal, dominating over the Doppler modulation produced by the LISA motion ($\approx 30\,\mathrm{rad}$), and happening on comparable timescales. The gravitational wave frequency suffers redshifts/blueshifts as the binary's centre of mass moves away/towards LISA; see figure 5.10. These modulations dominate over the gravitational wave-driven chirp rate, leading to a multi-valued time-to-frequency map in the shaded bands of figure 5.10, where chirping and anti-chirping parts of the signal overlap. This strongly affects the Fourier domain observed signal $\tilde{s}(f)$, with the transfer function amplitude $|\mathcal{T}(f)| = |\tilde{s}(f)/\tilde{h}(f)|$ showing interference patterns in the shaded bands. The impact on detection and parameter estimation is currently under study [478].

Finally, following section 5.1.2, we computed the emission due to X-rays from accretion onto the binary components and radio flares from jets. We find both effects difficult to observe even with Athena and SKA. Moreover, these emissions could be hidden by the intrinsic variability of the AGN. Emission by the merger remnant's emission in optical, as the Zwicky Transient Facility collaboration claims to have observed, is the best chance for observing a counterpart. Let us stress that the candidate counterpart was observed 34 days after the detection by the LVC, therefore even if we had to perform an archival search in the LISA data following the observation with ground-based detectors, the tight constraint on the sky localisation provided by LISA would still be helpful.

Let us now consider how accretion effects within a binary can affect the gravitational wave signal.

5.2 Accreting white dwarf-black hole binaries

5.2.1 Evolution of mass-transferring WDBH binaries

We consider WDBH binaries on a circular orbit with separation a. The binary's separation shrinks under the effect of gravitational waves, until the white dwarf gets close enough from the black hole so that the latter starts accreting from its companion. We model the evolution from the onset of mass transfer, when the white dwarf overfills its Roche lobe. Our treatment follows that of [479], with appropriate adjustments for the black hole component. In order to make notations more explicit, we note the mass of the black hole and the one of the white dwarf $M_{\rm BH}$ and $M_{\rm WD}$ respectively. We keep the notations $M = M_{\rm BH} + M_{\rm WD}$ and $q = M_{\rm BH}/M_{\rm WD}$ for the total mass and the mass ratio (note that our definition of the mass ratio is the inverse of one used in [38]). We use Eggleton's approximation for the zero-temperature mass-radius relation [480] of the white dwarf[4]

$$\begin{aligned}\frac{R_{\rm WD}}{R_\odot} =& 0.0114 \left[\left(\frac{M_{\rm WD}}{M_{\rm Ch}} \right)^{-2/3} - \left(\frac{M_{\rm WD}}{M_{\rm Ch}} \right)^{2/3} \right]^{1/2} \\ & \times \left[1 + 3.5 \left(\frac{M_{\rm WD}}{M_{\rm p}} \right)^{-2/3} + \left(\frac{M_{\rm WD}}{M_{\rm p}} \right)^{-1} \right]^{-2/3} ,\end{aligned} \tag{5.17}$$

where $M_{\rm Ch} = 1.44 M_\odot$ is the Chandrasekhar mass, and $M_{\rm p} = 0.00057 M_\odot$.

Mass transfer

The overfill factor indicates by how much the donor overfills its Roche lobe, $\Delta = R_{\rm WD} - R_L$. Mass transfer occurs when $\Delta > 0$ and increases monotonically with the overfill. We use the adiabatic approximation of [479] (see also [481])

$$\dot{M}_{\rm WD} = -F(M_{\rm BH}, M_{\rm WD}, a, R_{\rm WD}) \Delta^3 \, . \tag{5.18}$$

See [479] for the definition of F. We assume an accretion disk forms around the black hole and that matter is transferred from the ISCO at a radius $R_{\rm ISCO}$ [47]. We account for the limited efficiency of the black hole to accrete by setting

$$\dot{M}_{\rm BH} = \min \left(-\dot{M}_{\rm WD} \, \varepsilon_{\rm ISCO}, \dot{M}_{\rm Edd}(M_{\rm BH}) \right) , \tag{5.19}$$

where $\dot{M}_{\rm Edd}$ is the Eddington accretion rate (see section 5.1.1) and $\varepsilon_{\rm ISCO}$ is the specific mass-energy at the ISCO [47]. Therefore, mass is not necessarily conserved, accounting for possible loss through winds.

[4]Note that the accretion disk surrounding the black hole can heat the white dwarf. We will discuss this caveat in section 5.2.4.

Orbital separation

We assume that the variation of total angular momentum is due to gravitational wave emission and loss of matter:

$$\dot{J}_{\rm orb} + \dot{J}_{\rm BH} + \dot{J}_{\rm WD} = -\dot{J}_{\rm GW} - \dot{J}_{\rm loss}, \tag{5.20}$$

with $\dot{J}_{\rm GW} = \frac{32}{5}\frac{M_{\rm BH}M_{\rm WD}M}{a^4}J_{\rm orb}$. Following [482], we assume isotropic re-emission and take $\dot{J}_{\rm loss} = -q^{-1}\frac{\dot{M}}{M}J_{\rm orb}$. We neglect the angular momentum of the accretion disk surrounding the black hole, assuming that $M_{\rm disk} \ll M_{\rm BH}$ throughout the evolution.

We assume that the white dwarf is tidally locked. This is justified in high-mass-ratio systems such as WDBH binaries, since the synchronisation time-scale decreases as the inverted mass ratio squared [483]. Moreover, disk accretion can also contribute to synchronising the star rotation with the orbit [484]. The angular momentum of the donor can then be written as $J_{\rm WD} = I_{\rm WD}\Omega_{\rm WD}$, $\Omega_{\rm WD}$ being the orbital angular frequency and $I_{\rm WD} = k_{\rm WD}M_{\rm WD}R_{\rm WD}^2$ the momentum of inertia of the donor. The factor $k_{\rm WD}$ is a function of the white dwarf mass, for which we use the fit provided in [479]. Using Kepler's law, the variation in angular momentum of the donor is

$$\dot{J}_{\rm WD} = I_{\rm WD}\Omega_{\rm WD}\left(\Lambda_{\rm WD}\frac{\dot{M}_{\rm WD}}{M_{\rm WD}} - \frac{3}{2}\frac{\dot{a}}{a} + \frac{\dot{M}_{\rm BH}+\dot{M}_{\rm WD}}{M_{\rm WD}}\frac{1}{2\,(1+q)}\right), \tag{5.21}$$

where $\Lambda_{\rm WD} = 1+2\frac{{\rm d}\ln R_{\rm WD}}{{\rm d}\ln M_{\rm WD}}+\frac{{\rm d}\ln k_{\rm WD}}{{\rm d}\ln M_{\rm WD}}$. Note that the variation of the donor angular momentum was not included in the treatment of [479].

We assume no tidal torque acts on the black hole, so its angular momentum varies only as a result of the matter accreted at $R_{\rm ISCO}$,

$$\dot{J}_{\rm BH} = j_{\rm ISCO}\dot{M}_{\rm BH}, \tag{5.22}$$

where $j_{\rm ISCO}$ is the specific angular momentum at the ISCO [47]. The equation for the orbital separation of the binary can be derived from equations (5.20), (5.21) and (5.22) and reads

$$\begin{aligned}\frac{\dot{a}}{2a} = -\frac{1}{1-3\left(1+\frac{1}{q}\right)k_{\rm WD}r_{\rm WD}^2}\Bigg[&\frac{\dot{J}_{\rm GW}}{J_{\rm orb}} + \left(1-\frac{1}{2(1+q)}+\frac{k_{\rm WD}r_{\rm WD}^2}{2q}+\left(1+\frac{1}{q}\right)\Lambda_{\rm WD}k_{\rm WD}r_{\rm WD}^2\right)\frac{\dot{M}_{\rm WD}}{M_{\rm WD}}\\ &+\left(\frac{1}{q}-\frac{1}{2(1+q)}+\frac{k_{\rm WD}r_{\rm WD}^2}{2q}+\frac{j_{\rm ISCO}}{M_{\rm BH}}\sqrt{\frac{M}{a}}\right)\frac{\dot{M}_{\rm BH}}{M_{\rm WD}}\Bigg],\end{aligned} \tag{5.23}$$

where $r_i = R_i/a$.

Overfill and black hole spin

We evolve the over-fill factor according to

$$\dot{\Delta} = R_{\rm WD}\left[\left(\zeta_{\rm WD}-\zeta_{r_L}\right)\frac{\dot{M}_{\rm WD}}{M_{\rm WD}} - \frac{\dot{a}}{a}\right], \tag{5.24}$$

where $\zeta_{\rm WD} = \frac{\mathrm{d}\ln R_{\rm WD}}{\mathrm{d}\ln M_{\rm WD}}$ and $\zeta_{r_L} = \frac{\mathrm{d}\ln R_L/a}{\mathrm{d}\ln M_{\rm WD}}$ can be derived using Eggleton's approximation for the mass-radius relationship of cold white dwarves (equation (5.17)) and Eggleton's Roche lobe fitting formula [485], respectively. The latter reads:

$$R_L = \frac{0.49}{0.6 + q^{-2/3}\ln(1+q^{1/3})}\, a. \tag{5.25}$$

The angular momentum of the black hole can be written in terms of the dimensionless spin $\chi_{\rm BH}$,

$$J_{\rm BH} = M_{\rm BH}^2 \chi_{\rm BH}\,. \tag{5.26}$$

The accreting black hole will spin up according to equation (5.22), from which we obtain

$$\dot{\chi}_{\rm BH} = \left(\frac{j_{\rm ISCO}}{M_{\rm BH}} - 2\chi_{\rm BH}\right)\frac{\dot{M}_{\rm BH}}{M_{\rm BH}}\,. \tag{5.27}$$

The evolution of the black hole spin is not our main focus and has little effect on the overall evolution of the binary. We therefore neglect for simplicity other factors affecting the spin evolution, such as radiation emitted by the accretion disk and fix the initial black hole spin to $\chi_{\rm BH} = 0.1$.

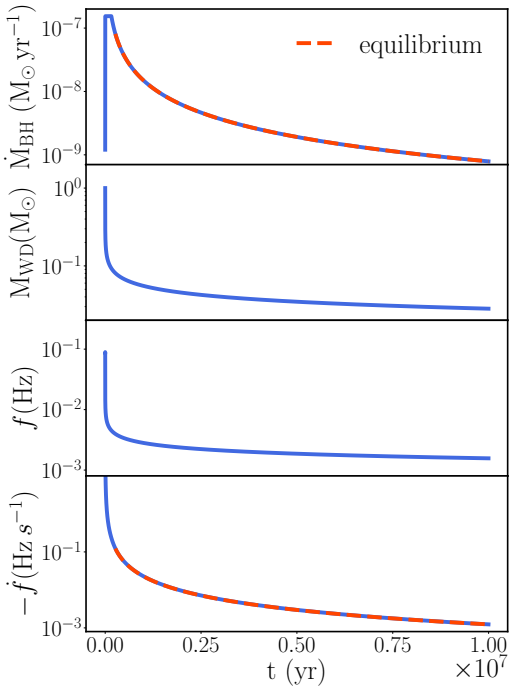

Figure 5.11: Evolution of the mass accretion rate, white dwarf's mass, gravitational wave frequency and its first derivative. The system has masses $M_{\rm WD} = 1\,M_\odot$ and $M_{\rm BH} = 7\,M_\odot$ at the time of first Roche lobe filling. The overlaid orange dashed line is the equilibrium solution described in appendix B.1.

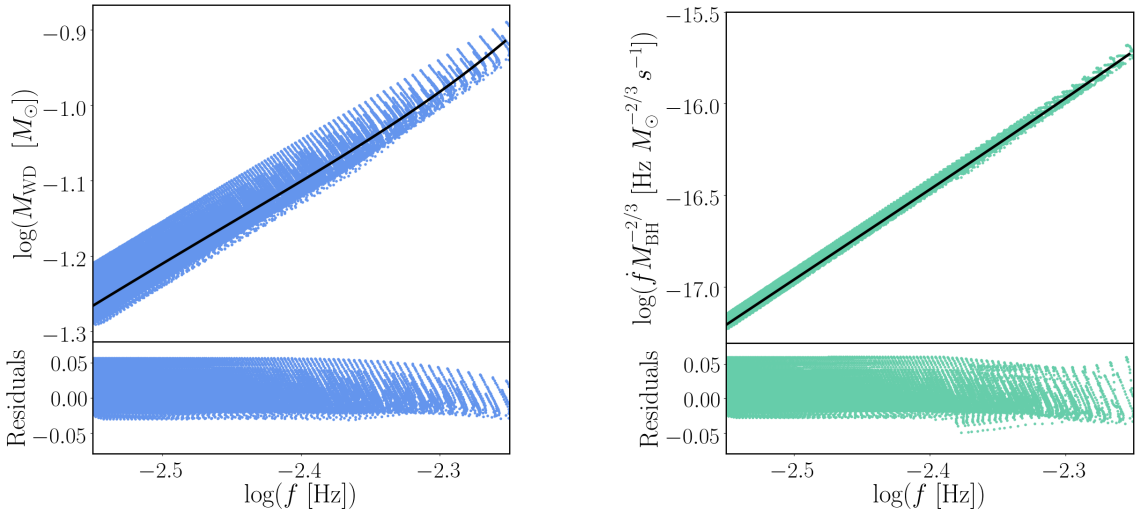

Figure 5.12: Evolutionary tracks of 400 WDBH binaries and their polynomial fits (black line). We focus on frequencies relevant to LISA.

5.2.2 Universal relations

We numerically integrate equations (5.18), (5.19), (5.20), (5.24) and (5.27), starting from the onset of mass transfer. The long term evolution of a typical WDBH binary is shown in figure 5.11. The cap in the black hole accretion rate in the top panel is due to accretion reaching the Eddington limit. As expected for mass-transfer dominated systems where the accretor is much more massive than the donor, the binary outspirals, giving a negative $\dot{f}$. Mass transfer proceeds rapidly at first, but quickly settles into an equilibrium rate. Equilibrium is attained when the increase in the Roche lobe matches the one in the white dwarf radius. Thus, we obtain the equilibrium mass transfer rate by setting the right-hand side of equation (5.24) to 0, see appendix B.1.

Across parameter space, the mass of the white dwarf follows an evolutionary track as a function of the gravitational wave frequency, which is approximately independent of the accretor mass and the initial conditions, as displayed in the left panel of figure 5.12. We span initial white dwarf masses between $[0.2, 1.2]\,M_\odot$, initial black hole masses in the range $[3, 20]\,M_\odot$ and only keep points from the equilibrium stage. These tracks can be compared with the ones traced by white dwarf accreting binaries in [176]. Our WDBH tracks follow a slightly different trajectory and show a more pronounced dependence on the accretor mass, resulting in a larger spread in the tracks (and hence fit residuals).

The absence of tidal torques acting on the white dwarf and the black hole yields an additional relation between $\dot{f} M_{\rm BH}^{-2/3}$ and f. We show this relation in the right panel of figure 5.12. Once again, the relation is roughly independent of the accretor mass and initial conditions. In appendix B.1 we explain how this relation can be derived from the equilibrium solution. We fit both evolutionary track relations with a quartic polynomial $\log_{10}(y) = \sum_{i=0}^{n} a_i \log_{10}(f[Hz])^i$ (figure 5.12). The fit coefficients are listed in appendix B.2.

5.2.3 Parameter estimation with LISA

In the case of almost monochromatic sources such as WDBH and double white dwarf binaries, the two gravitational wave polarisations can be obtained by using the quadrupole formula and Taylor-expanding in time the phase of the expressions given in equations (1.40) and (1.41), taking the simple form:

$$h_+ = A_0 \frac{1+\cos^2(\iota)}{2} \cos(\phi_0 + 2\pi f t + \pi \dot{f} t^2), \tag{5.28}$$

$$h_\times = A_0 \cos(\iota) \sin(\phi_0 + 2\pi f t + \pi \dot{f} t^2), \tag{5.29}$$

where $A_0 = \frac{\mathcal{M}_c}{D_L}(\pi \mathcal{M}_c f)^{2/3}$ is the amplitude of the signal, and ϕ_0 is the initial gravitational wave phase. Thus, gravitational wave observations provide us A_0, f and $\dot{f}$, and we cannot infer the individual masses and the distance without further assumptions. In order to assess how the universal relations we derived can be combined with LISA measurements, we consider an accreting WDBH system at two different stages of its evolution:

- "high frequency" (*HF*): $M_{\rm BH} = 7.02 M_\odot$, $M_{\rm WD} = 0.10\ M_\odot$, $f = 5$ mHz, $\dot{f} = -3.8 \times 10^{-16}$ Hz s^{-1};
- "low frequency" (*LF*): $M_{\rm BH} = 7.02 M_\odot$, $M_{\rm WD} = 0.06\ M_\odot$, $f = 3$ mHz, $\dot{f} = -3.2 \times 10^{-17}$ Hz s^{-1};

We compute LISA's response following [486, 487] to generate mock data and perform a full Bayesian analysis to infer the posterior distribution of the parameters of the source. For the noise level, we use the SciRdv1 curve [314], including the confusion noise due to the galactic foreground in addition to the instrument noise [315]. The parameter estimation is performed with the nested sampling algorithm `Multinest`. We assume a mission duration of six years and two values of the duty cycle: 100% and 75%. We set the distance to $D_L = 10$ kpc and simulate the effect of a reduced duty cycle by placing the source further. For almost monochromatic sources, the angles essentially affect the SNR and have little impact on our analysis. For a duty cycle of 100% (75%), the *HF* and *LF* systems have SNRs of 91 (68) and 26 (20) respectively. Systems at frequencies below 3 mHz, although more numerous, have little chance of being detected due to the galactic foreground. With a duty cycle of 75%, f and $\dot{f}$ are measured within 5×10^{-7} Hz and 5×10^{-18} Hz.s^{-1} for the *HF* system and an order of magnitude worse for the *LF* system.

In table 5.3 we report the estimates of the binary masses (normalised to the injected values) directly using the fits to the evolutionary tracks of figure 5.12. We can use these results to infer the chirp mass and, from the measurement of A_0, the distance to the source. We find a reasonable agreement with the injected values (within 5%). However, for the *HF* system, the injected values lie outside the 90% confidence intervals. This is because the systematics of the model dominate over the statistical uncertainty. In particular, the very narrow range for $M_{\rm WD}$ is due to the extremely good measurement of f. To correct for this, we estimate numerically the values of α_1 and α_2 that best align the evolutionary tracks, $M_{\rm WD}\, M_{\rm BH}^{-\alpha_1}$ and $\dot{f}_{\rm WD}\, M_{\rm BH}^{-2/3-\alpha_2}$ as functions of f. The exponents α_1 and α_2 are frequency dependent and are determined for each system in the frequency range of observation. We then convolve LISA posteriors with the aligned tracks to infer $M_{\rm BH}$ and $M_{\rm WD}$.

		HF			*LF*		
		$\tilde{M}_{\rm BH}$	$\tilde{M}_{\rm WD}$	$\tilde{D}_L$	$\tilde{M}_{\rm BH}$	$\tilde{M}_{\rm WD}$	$\tilde{D}_L$
100%	Fit	$0.99^{+0.01}_{-0.01}$	$0.99^{+5.7\times10^{-8}}_{-5.8\times10^{-8}}$	$1.05^{+0.11}_{-0.14}$	$1.04^{+0.40}_{-0.36}$	$0.97^{+2.8\times10^{-7}}_{-2.8\times10^{-7}}$	$0.98^{+0.35}_{-0.29}$
	Full	$1.01^{+0.08}_{-0.04}$	$0.99^{+0.02}_{-0.04}$	$1.06^{+0.11}_{-0.15}$	$1.03+0.44_{-0.38}$	$0.98^{+0.04}_{-0.05}$	$0.98^{+0.35}_{-0.29}$
75%	Fit	$0.99^{+0.01}_{-0.01}$	$0.99^{+7.7\times10^{-8}}_{-7.8\times10^{-8}}$	$1.39^{+0.16}_{-0.20}$	$1.05^{+0.55}_{-0.47}$	$0.97^{+3.8\times10^{-7}}_{-3.8\times10^{-7}}$	$1.28^{+0.59}_{-0.47}$
	Full	$1.01^{+0.08}_{-0.04}$	$0.99^{+0.02}_{-0.04}$	$1.05^{+0.13}_{-0.16}$	$1.03^{+0.61}_{-0.49}$	$0.98^{+0.05}_{-0.05}$	$0.96^{+0.44}_{-0.35}$

Table 5.3: Uncertainties on individual masses and distances normalised to the injected values, obtained with the fit to the global evolutionary tracks relations (Fit) and with the full results of numerical simulations (Full). The gravitational wave frequency f and $\dot{f}$ are measured within 5×10^{-7} Hz and 5×10^{-18} Hz s^{-1} for the *HF* system, assuming a duty cycle of 75%. These measurements are an order of magnitude worse for the *LF* system.

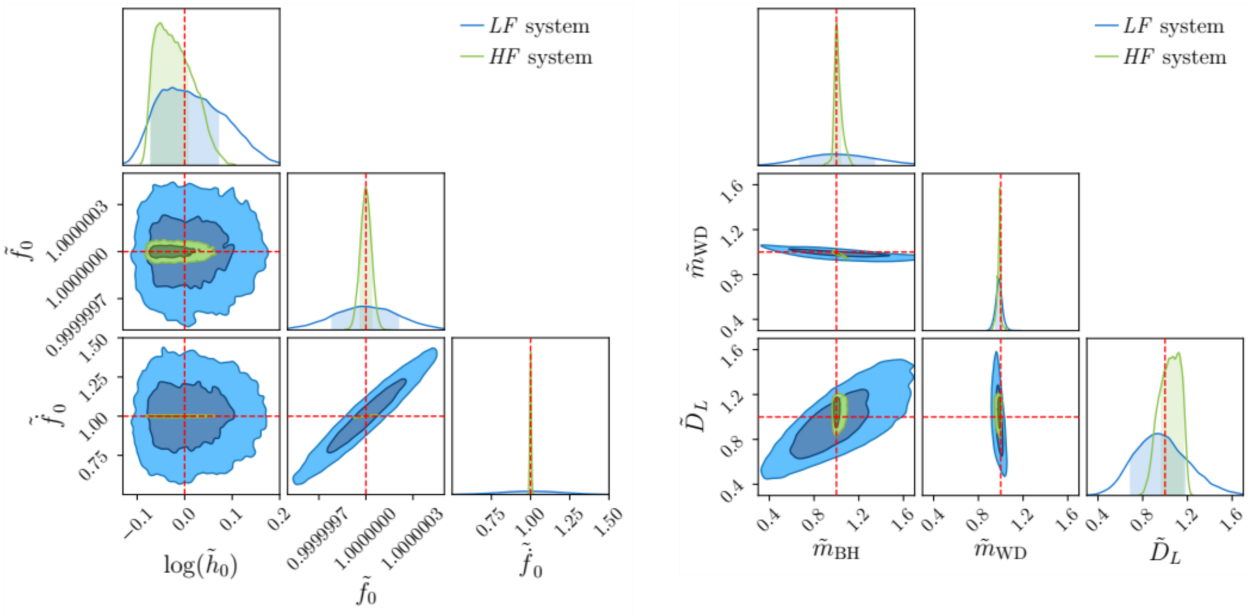

Figure 5.13: Left panel: posterior distribution for the gravitational wave amplitude, the gravitational wave frequency and its first derivative for the high and low frequency systems, obtained from LISA measurements at 75% duty cycle. Right panel: inferred posterior distributions for binary masses and luminosity distance, obtained applying the rescaled universal relations to LISA measurements, as described in section 5.2.3. We normalise to the injected values. The contours indicate the 50 and 90 % confidence intervals and the dashed lines represent the true values (equal to 1 in our normalisation).

In figure 5.13, we show how the measurement of h_0, f and $\dot{f}$ together with this procedure translates into a measurement of distance and the white dwarf and black hole masses for the two systems assuming a 75% duty cycle. We used the `ChainConsumer` library to

perform these plots [488]. Table 5.3 also shows the improvement as compared to fit-based measurements and the very good agreement between the injected and the inferred values obtained with this procedure. $M_{\rm BH}$ is less well constrained than $M_{\rm WD}$ because it relies on the measurement of $\dot{f}$. The measurement is worse for the *LF* system due to the lower value of $\dot{f}$ which results in it being measured not as well during the six years mission. We note that the results are less affected by a reduced duty cycle. Finally, even in the worst scenario the uncertainty on $M_{\rm BH}$ is sufficiently small to unambiguously identify the accretor as a black hole.

WDBH binaries are potential sources of electromagnetic radiation, in particular X-ray emission. The *HF* and *LF* systems would have respectively X-ray luminosity of $9 \times 10^{38}\,{\rm erg\,s^{-1}}$ and $1 \times 10^{38}\,{\rm erg\,s^{-1}}$ for $\varepsilon_{\rm rad} = 0.1$, well within the capabilities of current facilities. The fact that we are yet to convincingly identify WDBH binaries among X-ray sources could be explained by the lower rates of these systems, and the difficulty to classify the binary components from electromagnetic emission alone. Gravitational wave observations, on the other hand, could unequivocally identify the binary components. The very good localisation of the source by LISA ($\sim 1\,{\rm deg}^2$) could then provide the opportunity to observe an electromagnetic counterpart.

5.2.4 Temperature effects

So far we have assumed the companion white dwarf to be cold, by using the zero temperature mass-radius relation (5.17). However, hundreds of hot (effective surface temperature $T >$ 5000K) white dwarves have been observed [489, 490], and their temperature should be taken into account in describing their stellar structure. In particular, it could modify the mass-radius relation [491, 492, 493]. Besides being hot because they have not had time to cool after being formed, white dwarves in WDBH systems will be generically heated up by the emission of the black hole accretion disk. Let us estimate this effect. Assuming the black hole's disk emits isotropically and using Stefan-Boltzmann's law for the white dwarf, we get a balance equation

$$4\pi\sigma T_{\rm WD}^4 R_{\rm WD}^2 = \frac{L_{\rm BH}}{4\pi a^2}\pi R_{\rm WD}^2(1-A_{\rm WD}), \tag{5.30}$$

with $A_{\rm WD}$ the white dwarf albedo, and $T_{\rm WD}$ the temperature at the surface of the white dwarf. The luminosity of the black hole can be written as $L_{\rm BH} = \varepsilon_{\rm rad}\dot{M}_{\rm BH}$. Thus, we get

$$T_{\rm WD} = 3\times 10^5\,(1-A_{\rm WD})^{1/4}\left(\frac{\varepsilon_{\rm rad}}{0.1}\frac{M_{\rm BH}}{M_\odot}\frac{\dot{M}_{\rm BH}}{\dot{M}_{\rm Edd}}\right)^{1/4}\left(\frac{3R_\oplus}{a}\right)^{1/2}\,{\rm K}\,, \tag{5.31}$$

where $R_\oplus$ is the radius of the Earth. From this equation, we estimate that emission from the black hole disk could heat up the white dwarf to $\mathcal{O}(10^5)$ K. Relying on the efficient heat conduction in degenerate stars, we extrapolate this estimate to the core temperature of the white dwarf (T_c). Such low core temperatures, have little impact on the mass-radius relation, as illustrated in figure 5.14. In the temperature range 10^5-10^6 K, the relative variation in the white dwarf radius is less than 0.2%. A caveat is that these results were obtained for cooling sequences of isolated white dwarves [493]. More simulations of heated white dwarves as in [494] could provide further insight on the effect of illumination on the evolution of WDBH

binaries. White dwarves with masses lower than the ones considered in this work might also exhibit a stronger dependence on the temperature, see e.g. [491]. It would be interesting to extend our model to lighter white dwarves, in a mass range where finite temperature effects might become relevant.

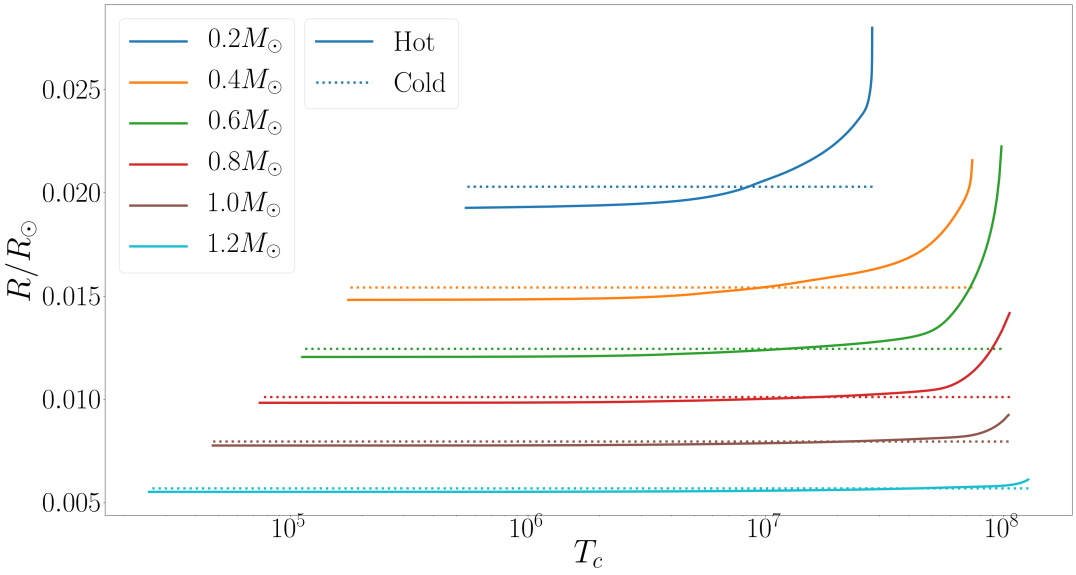

Figure 5.14: Evolution of the mass of a hot white dwarf with temperature for different masses. We use the cooling sequences of isolated white dwarves [493]. In the temperature range accessible for a white dwarf heated by the accretion disk to the black hole (10^5-10^6 K), the mass-radius relation varies very little with temperature. We overplot in dotted lines Eggleton's approximation for the zero-temperature mass-radius relation. There is some discrepancy between the two models and using an incorrect mass-radius relation could bias the results.

In figure 5.14 we overplot in dotted lines Eggleton's approximation for the zero-temperature mass-radius relation (equation (5.17)). Although the agreement is reasonable at low temperatures, there is some discrepancy between the models. The composition of the white dwarf (hydrogen, helium, carbon/oxygen) is also expected to play a role. A mismodelling of the mass-radius relation, together with the use of Eggleton's approximation for the Roche lobe radius, which was derived for stars made of incompressible fluids, could introduce a bias in our result. It would be interesting to quantify this potential bias by testing different relations. We leave this investigation for future work. Let us stress that our methodology is robust to changes in the mass-radius and Roche lobe radius relations, and we expect our main finding to hold, i.e., LISA could be the first observatory to unambiguously identify WDBH binaries.

Finally, we checked that the presence of tidal torques would not affect our results significantly for small synchronisation timescales ($\lesssim 100$ yrs). This study could therefore apply to broader classes of galactic binaries.

5.3 Discussion

In this chapter we assessed the potential of gravitational wave observations to inform us on astrophysical effects in binary systems. We showed that accretion from surrounding gas, dynamical friction and constant peculiar acceleration lead to perturbative modifications to vacuum BBH waveforms, and used this to infer to which accuracy can LISA and multiband observations measure these effects. We found that super-Eddington accretion is needed to have a measurable effect in SBHBs, while Eddington-level is enough in IMBHBs. In the later case, we computed that the X-ray and radio emissions due to accretion would be measurable by Athena and SKA. The detection of the counterpart would be eased by the precise sky localisation of LISA. Focusing on GW190521-like systems in AGN disks, we found that multiband observation would allow us to measure sub-Eddington accretion, gas densities much below the typical value in AGNs and the peculiar acceleration of the binary for orbits smaller than ~ 1 pc. We also showed that accelerations varying on a timescale comparable to the observation time cannot be treated perturbatively and have a strong impact on the waveform. We are currently assessing the impact of this effect, as well as relativistic effects such as lensing and Shapiro time delay, on parameter estimation and detection. Next, we considered the effect of accretion within a binary on the gravitational wave emission, focusing on systems made of black holes accreting from a companion white dwarf. We derived two universal relations between the masses of the objects, the gravitational wave frequency and its first derivative. We showed that combining LISA observations with these relations provides an estimate of the masses of both binary components and the distance to the source, which is information not usually accessible from gravitational wave observations of GBs. This additional piece of information would then allow us to unambiguously identify the binary components.

Astrophysical effects appear as a double-edged sword. On a one hand, they can manifest themselves in various different manners, which makes it hard to model them exhaustively, and could be mistaken for the manifestation of beyond general relativity physics. On the other hand, they provide us precious information on the environment of the source, which could be used to help us distinguish between different BBH formation scenarios, and the evolution of binary systems. LISA will typically provide a sky localisation for SBHBs, IMBHBs and GBs within 1 $\deg^2$. This will help localise potential electromagnetic counterparts (which would in turn help identify the host galaxy among the thousands – of which just a few AGNs – present within the LISA error-box). This is of great importance, because if deviations from vacuum general relativity BBH waveforms are measured, an electromagnetic counterpart in the LISA sky-position error-box would favour an environmental origin over a beyond general relativity one. Moreover, we expect deviations from general relativity to affect (to a varying degree) all systems, therefore they should be observed consistently across different events.

We saw how gravitational waves can be used to get astrophysical information from single events. As we accumulate observations, we become able to infer the population of compact objects in the Universe and constrain the astrophysical processes driving their formation and evolution. This is currently being done with the SBHBs observed by the LVC [202, 203, 204, 205]. In the next chapter we will see what can be learned from LISA observations of MBHBs.

Chapter 6

Inferring the population of massive black holes from LISA observations and constraining formation and evolution channels

Electromagnetic observations indicate that massive black holes are ubiquitously found in the centre of galaxies [213, 216], and that their properties are correlated with the ones of their host galaxies, suggesting a coeval growth [495, 496, 497, 498, 218]. Unfortunately, these observations are sensitive only to active massive black holes up to $z \sim 7$, or very nearby ones for which we can observe the gas/stellar dynamics. Gravitational waves will allow us to probe more distant and quieter massive black holes: LISA is expected to detect from a few tens to hundreds MBHBs up to $z \sim 20$ during the mission duration [30]. In this chapter we address the question of how these observations can be used to constrain scenarios for the formation and subsequent evolution of massive black holes. The results we present here are based on [39][1].

The population of MBHBs that LISA will observe is the result of a complex evolutionary path, of which the details are still largely unknown. Two open issues, of particular importance for LISA, can be highlighted. First, which astrophysical mechanisms provided the seeds that grew into massive black holes? Several scenarios have been proposed, suggesting seed masses ranging from 10^2 to 10^5 $M_\odot$, forming at $z \sim 15 - 20$ [216]. Once these intermediate mass black holes form, they are thought to grow via accretion of surrounding gas (and stars), and through successive mergers. Pictorially, following the merger of two galaxies hosting a black hole at their centre, dynamical friction makes the black holes sink to the centre of the resulting galaxy, where they form a bound binary system. Loss of energy through gravitational wave emission is not efficient enough to make the binary coalesce within a Hubble time, and other processes that extract energy from the binary are needed to bring the separation from parsec to milliparsec scales, where gravitational radiation takes over. This second issue is known as the "last parsec problem" [499]. These two crucial stages in the evolution of MBHBs affect the properties of the population of events that LISA will

[1] All the results presented here were obtained by me, with the help of my collaborators.

observe, such as the binary component masses and spins, the redshift and the rates. Thus, by accumulating observations with LISA, we can reverse engineer the problem, and shed light on these mechanisms.

We focus on the ability of LISA to distinguish between different seeding scenarios. We use the predictions of semi-analytical models for the evolution of galaxies and massive black holes to simulate LISA data. Each of these models has a light seed (LS) and a heavy seed (HS) variant, differing in the prescription for the initial masses of black holes. We consider the possibility that the population of massive black holes is described by a mixture between the LS and HS scenarios. We treat the mixing fraction between models as a *hyperparameter* controlling the population, and estimate it from simulated data sets using a hierarchical Bayesian framework. We test the robustness of our analysis by using the predictions of different semi-analytical simulations to generate data.

6.1 Data generation and parameter estimation

LISA will observe the last stages of the coalescence of MBHBs, where higher harmonics can be comparable in amplitude to the $(2, \pm 2)$ harmonics [500, 501, 502, 503, 284]. Therefore, we use PhenomHM to generate the signal and perform the parameter estimation. Differently from SBHBs, we parametrise MBHBs by their time to coalescence t_c and phase at coalescence φ_c. We use the SciRDv1 noise curve [314], including the confusion noise due to GBs [315]. We take 10^{-5} Hz as a lower limit for the LISA band. We assume a mission duration of four to ten years, and an ideal 100% duty cycle.

MBHBs will enter the LISA band from a few weeks to ~ 1 year before merging. For this reason, the modulations of the signal due to LISA's motion are less pronounced, and the posterior distribution for extrinsic parameters can be very degenerate and multimodal [284, 504]. This makes the posterior distribution much harder to sample. Therefore, we use the parallel tempering code `ptemcee` [505, 506] to perform the parameter estimation on many sources rather than our own MHMCMC. Let us stress that the focus of the study presented here is not the parameter estimation of MBHBs, we are only interested in obtaining realistic errors for the intrinsic parameters of the source and the distance. Thus, we do not perform a systematic check of the convergence of the chains (in particular for the sky location) and do not discuss the parameter estimation as extensively as for SBHBs in chapter 3.1. Moreover, as can be seen in figure 6.1, astrophysical models predict some events with large mass ratios and/or large spins, far outside the range of validity of current waveform models. Given the lack of viable alternatives for now, we will stick to the results obtained with PhenomHM. By running parameter estimation over the many systems needed to perform this study, we found some interesting cases which present an unexpected multimodality in intrinsic parameters. We discuss two examples of such in appendix C.

The chirp mass is the best measured parameter, and because we can observe the late inspiral and the merger-ringdown with high SNR (up to thousands), we can measure the mass ratio and the spins accurately. As for the distance measurement, the error due to weak lensing dominates over the statistical error at high redshifts. We use the (pessimistic) model

of [507], which estimates that the error due to lensing goes as

$$\sigma_{D_L,\text{lensing}}/D_L = 0.066 \left(\frac{1-(1+z)^{-0.25}}{0.25} \right)^{1.8} . \tag{6.1}$$

We include this error by convolving the measured LISA posterior distribution with a Gaussian of width $\sigma_{D_L,\text{lensing}}$. The error due to weak lensing propagates into the determination of source frame masses.

6.2 Massive black hole binaries population

Semi-analytical models provide a valuable tool for assessing the impact of different astrophysical mechanisms on the population of MBHBs that LISA will detect. They follow the coevolution of massive black holes and the baryonic structure in galaxies along dark matter halo merger trees, using astrophysically motivated prescriptions. The predictions of these models are compared with the observed evolution of galaxy morphology, star-formation rate and luminosity functions to test their robustness. We take the *Model-delayed* model of [508] (which builds on [509, 510, 511]) as our fiducial astrophysical model. It adopts the extended Press-Schechter formalism of [512] to describe merger trees. The Press-Schechter mass-function [513] predicts the number density of dark matter halos as a function of mass and redshift. The extended Press-Schechter formalism uses this mass-function to compute the merger history of a halo at present day by means of Monte-Carlo simulations [514]. In [512], the authors introduce phenomenological corrections to the Press-Schechter mass-function in order to reproduce the results of N-body simulations. In short, to perform these simulations we start by computing the merger tree of many halos distributed according to the Press-Schechter mass-function, we seed the relevant halos with a black hole according to some seeding model, compute the amount of hot gas initially present in halos (which will later form all the baryonic structure of the galaxy: stars, interstellar medium etc), and then follow the evolution of the black holes and the baryonic matter back to $z = 0$. During the evolution, interactions between the massive black holes and the baryonic structure (accretion, jets, tidal effects etc) are taken into account. These simulations yield a rate of merging MBHBs per comoving volume that we transform into catalogues of annual events for LISA.

In the LS variant of the model, massive black holes form from the collapse of Pop III stars at $z \sim 20$ [515], the first stars in the Universe, yielding initial masses right above the upper mass gap $\sim 150\ M_\odot$. In the HS variant, they form from the collapse of proto-galactic disks due to bar instabilities at redshift $z \sim 15-20$ [516], yielding initial masses $\sim 10^5\ M_\odot$. In both scenarios, the merger of massive black holes can be triggered by interaction either with gas, stars, or a third/fourth massive black hole. We use the masses, spins and redshift distribution of coalescing MBHBs predicted by the simulations. It is worth noting that the eccentricity of a binary, as well as the degree of alignment of the component spins, depend on the mechanism that triggers the merger. For instance, triple/quadruple interactions between massive black holes can lead to large eccentricities due to Kozai-Lidov resonances [517, 518]. Binaries merging in a gas-rich environment tend to have aligned spins, due to the gravitomagnetic torques exerted by the circumbinary disk (the so-called Bardeen-Petterson effect [519]). Because PhenomHM covers only quasicircular binaries with component spins aligned

or anti-aligned with the orbital angular momentum, we cannot fully exploit this valuable information. We simply take the projection of spins along the orbital angular momentum and neglect the eccentricity. Nevertheless, the information on the spins alignment is partially contained in the effective spin of the binary. To complete the set of parameters θ needed to describe LISA events, we draw the sky location uniformly on the sphere, the phase at coalescence and the polarisation uniformly in $[0, 2\pi]$ and $\cos(\iota)$ uniformly in $[-1, 1]$. We assume a time to coalescence of at most one year, and we do not consider the part of the signal below 10^{-5} Hz.

When running the simulations, only one of the seeding prescriptions is used. However, the population of massive black holes in the Universe is unlikely to be described by any of these "pure" models, but rather by a mixture of models. Following [520], we introduce a mixing fraction α between the LS and HS scenarios. In practice this is done by defining the (unnormalised) MBHB population distribution to be

$$N_{\rm pop}(\theta|\alpha) = \alpha N_{\rm pop}(\theta|{\rm LS}) + (1-\alpha) N_{\rm pop}(\theta|{\rm HS}). \tag{6.2}$$

In the following, we denote the normalised population distribution by $p_{\rm pop}(\theta|\alpha)$ and the predicted rate by $N_{\rm ev}$ (in $\rm yr^{-1}$), such that $N_{\rm pop}(\theta|\alpha) = N_{\rm ev}(\alpha) p_{\rm pop}(\theta|\alpha)$. The rate for a given value of the mixing fraction is obtained through linear interpolation between the value predicted by the LS ($\alpha = 1$) and HS ($\alpha = 0$) scenarios. The normalised population distribution is then given by

$$p_{\rm pop}(\theta|\alpha) = \frac{\alpha N_{\rm ev}({\rm LS})}{\alpha N_{\rm ev}({\rm LS}) + (1-\alpha) N_{\rm ev}({\rm HS})} p_{\rm pop}(\theta|{\rm LS}) + \frac{(1-\alpha) N_{\rm ev}({\rm HS})}{\alpha N_{\rm ev}({\rm LS}) + (1-\alpha) N_{\rm ev}({\rm HS})} p_{\rm pop}(\theta|{\rm HS}). \tag{6.3}$$

For a given SNR threshold, we denote by $N_{\rm det}(\alpha, {\rm SNR})$ the number of events (per year) above this threshold. In table 6.1 we provide the annual rates for the LS and HS scenarios[2], as well as the number of detectable events by LISA assuming an SNR threshold of 10 or 20. The LS scenario predicts many more events than the HS one because more dark matter halos are initially seeded with a black hole in that scenario. However, many of these events have low SNR and could not be detected with LISA. On the contrary, almost all events in the HS scenario could be detected.

[2]Note that we use a different noise curve and SNR threshold than [508, 225], hence the difference in the rates of detectable events.

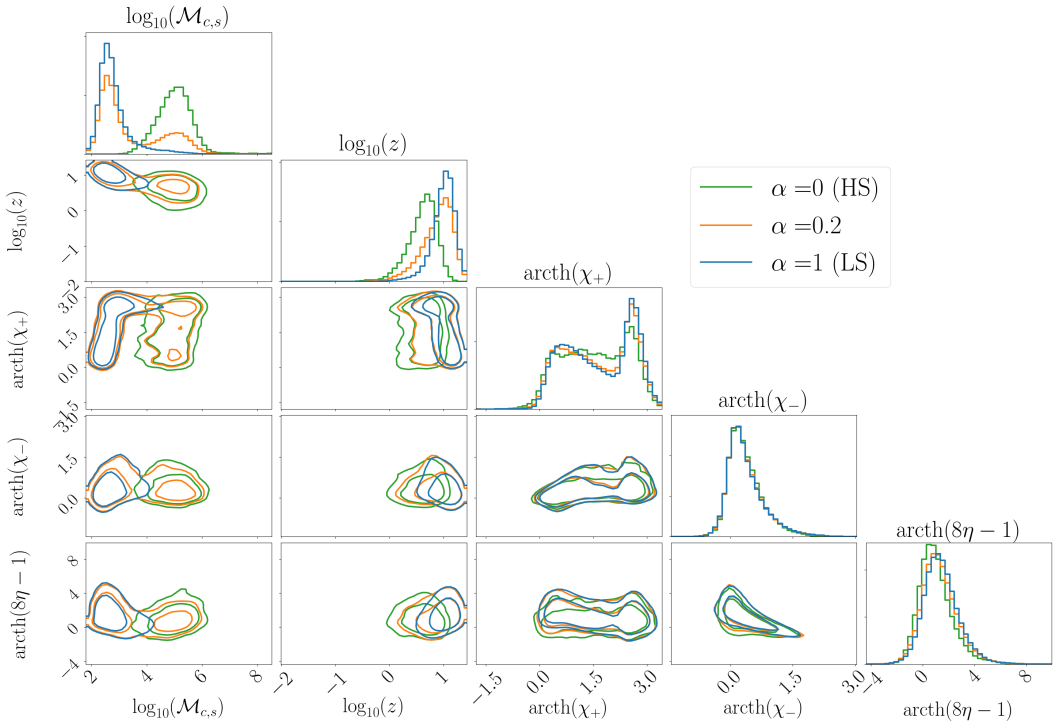

(a) Without SNR threshold.

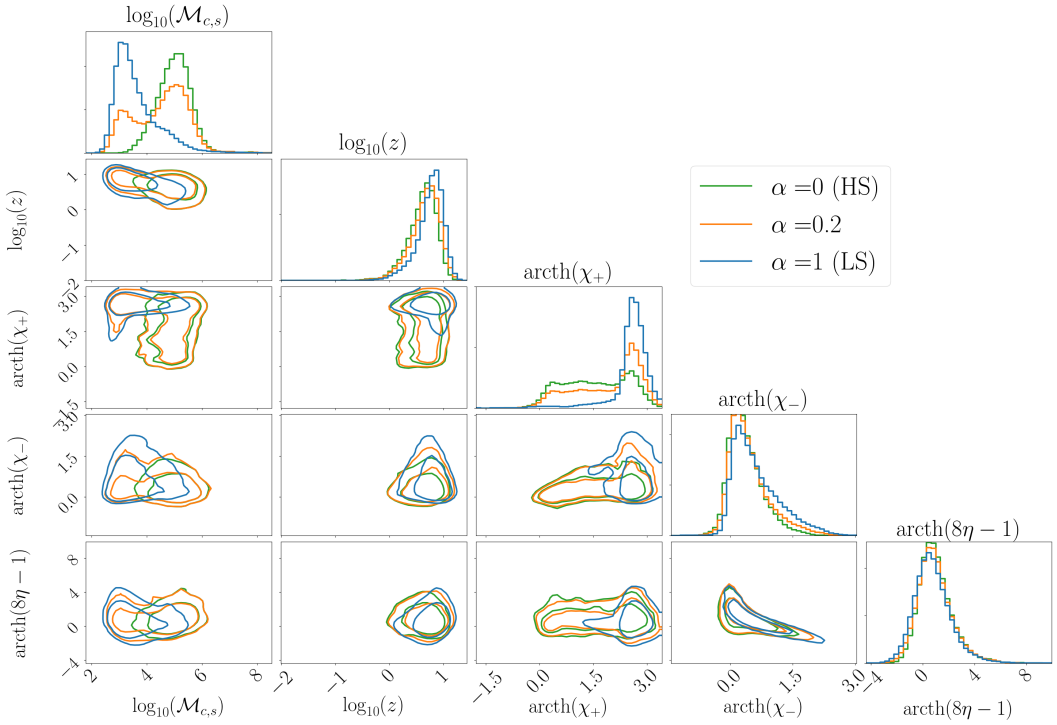

(b) With an SNR threshold of 10.

Figure 6.1: Normalised population distribution for different values of the mixing fraction between the LS and HS variants of our fiducial astrophysical model. The (source-frame) chirp mass distribution is the most sensitive to α. After the SNR cut, the redshift distributions look much more similar, unlike the effective spin distributions, as discussed in the main text.

In figure 6.1 we show the normalised population distribution for different values of α. In the lower panel we show only events that have an SNR above 10. We use "transformed" parameters (e.g. $\log_{10}(\mathcal{M}_{c,s}), \mathrm{arcth}(\chi_+)$) to make the salient features of the distributions more evident. As expected, the HS variant predicts binaries with higher masses than the LS one. When mixing between them, we get a double-peaked distribution, whose relative weights depend on the value of α. After imposing an SNR cut, lighter events are suppressed, and the relative weights change due to the fact that many LS events are not detectable. The effect of the SNR cut can be clearly seen in the redshift distribution: distant events predicted in the LS scenario are highly suppressed, and as a consequence the LS and HS redshift distributions after the cut look much more similar. On the contrary, after imposing the SNR cut the effective spin distributions can be better distinguished. This is due to the three-way correlation with redshift and chirp mass, which can be seen in the upper panel. The physical explanation is that the events that survive the SNR cut in the LS scenario tend to be closer and more massive (both because of the SNR threshold and because the black holes had more time to grow via accretion and mergers). Accretion also leads to larger spins for this subset of the population. Moreover, the presence of gas around binaries tends to align the spins through the Bardeen-Petterson effect, which in turn translates into larger values of the effective spin.

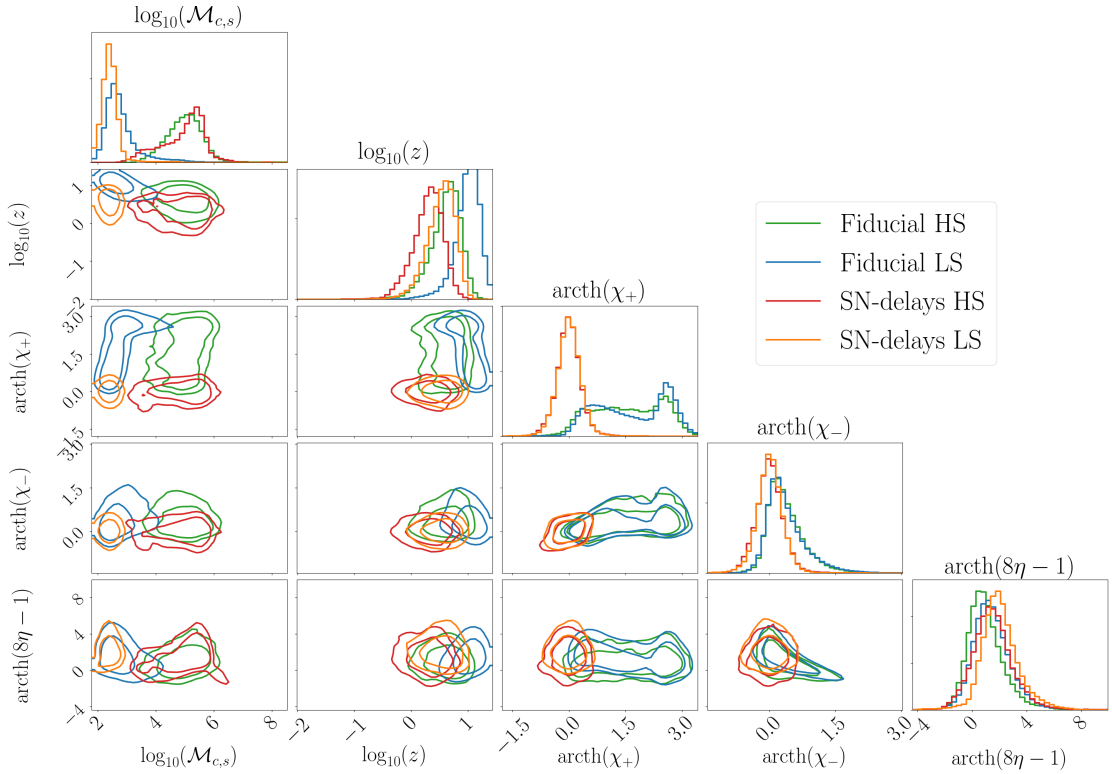

Figure 6.2: Comparison between the normalised population distributions predicted by our fiducial model and the SN-delays models, both in the LS and HS scenario. The chirp mass distributions are reasonably similar between the two models, but not the ones of redshift and effective spin.

As will be further detailed in section 6.5, we are also interested in the compatibility

		LS	HS
Fiducial	$N_{\rm ev}$ ($\rm yr^{-1}$)	234.3	23.98
	$N_{\rm det}(10)$ ($\rm yr^{-1}$)	53.01	23.89
	$N_{\rm det}(20)$ ($\rm yr^{-1}$)	29.85	23.67
SN-delays	$N_{\rm ev}$ ($\rm yr^{-1}$)	11.82	5.94
	$N_{\rm det}(10)$ ($\rm yr^{-1}$)	1.11	5.92
	$N_{\rm det}(20)$ ($\rm yr^{-1}$)	0.29	5.73

Table 6.1: Annual rate of events and number of detectable events with LISA per year. We consider an SNR threshold of 10 or 20. The LS scenario predicts more events than the HS one, but many of them could not be detected by LISA. The rate of events varies substantially between our fiducial model and the SN-delays models.

between astrophysical models for LISA data analysis. For this reason, we also consider a more recent class of models, more specifically the SN-delays model of [225]. This model uses the same seeding prescriptions as our fiducial model, but includes supernovae feedback, which can eject matter around the black holes and quench their growth, and implements additional delays between when dark matter halos merge and MBHBs form in addition to the dynamical friction timescale. In figure 6.2 we compare the normalised population distribution predicted by the SN-delays model to our fiducial model, both in the LS and HS cases, without any SNR threshold. Notice that the chirp mass distributions of the fiducial and SN-delays models are reasonably similar, but the redshift and effective spin ones are very different. The glaring difference in redshift distributions is due to the additional delays included in the SN-delays model, whereas the one in spin distributions is due to supernova feedback, which expels the gas surrounding the black holes in shallow potential wells, resulting in binaries with more isotropic spin orientations and smaller component spin magnitudes. In table 6.1 we also provide the rates predicted by the SN-delays model. Although the rates differ substantially between the LS and HS scenarios, comparison between the fiducial and SN-delays models shows that it is not a robust prediction of semi-analytical models, therefore we will not use rate information when estimating the mixing fraction.

6.3 Hierarchical Bayesian analysis

Assuming that MBHB events are distributed following the mixing prescription of equation (6.2), α can be treated as a hyperparameter controlling the population distribution. By observing many events, we will learn how the parameters θ (masses, spins, redshifts etc) of MBHBs are distributed, and therefore we will be able to infer the mixing fraction. Working in a Bayesian framework, our goal is to estimate the posterior distribution of α from a set of observed MBHB events $\mathbf{d}$. To do so, we follow a similar approach to the "bottom-up"

derivation of [521]. We assume that MBHB events are drawn from a population distribution $p_{\rm pop}(\theta|\alpha)$, and that their signals are statistically independent. This latter point is a highly non-trivial assumption about the LISA data stream since we expect to receive many signals at the same time (extreme mass ratio inspirals, GBs, MBHBs etc). Nevertheless, given the predicted event rate for MBHBs (see table 6.1), it is unlikely that MBHB signals will be overlapping in time-frequency bins. Moreover, their signal has a very different morphology from the other LISA sources, as they will be merging and rapidly evolving. Therefore, it is reasonable to assume the parameter estimation to be independent for each MBHB event.

The posterior distribution for α is given by Bayes' theorem:

$$p(\alpha|\mathbf{d}) = \frac{p(\mathbf{d}|\alpha)p(\alpha)}{p(\mathbf{d})}. \tag{6.4}$$

For $N_{\rm obs}$ statistically-independent signals, the hyperlikelihood can be written as

$$p(\mathbf{d}|\alpha) = \prod_{i=1}^{N_{\rm obs}} p(d_i|\alpha). \tag{6.5}$$

We must take into account that not all data will be detectable, due to the intrinsic loudness of a given signal, but also to noise fluctuations in the detector. We use the SNR as a detection statistic, and for each possible data d we define

$$I(d) = \begin{cases} 1 \text{ if } \mathrm{SNR}[d] > \mathrm{SNR}_{\rm threshold} \\ 0 \text{ otherwise.} \end{cases} \tag{6.6}$$

The individual hyperlikelihood for an event can then be written as

$$p(d|\alpha) = \frac{1}{\Xi(\alpha)} \int \mathrm{d}\theta \; p(d|\theta) p_{\rm pop}(\theta|\alpha) I(d). \tag{6.7}$$

The normalisation factor $\Xi(\alpha)$ (sometimes called selection function) is given by

$$\Xi(\alpha) = \int\int \mathrm{d}\theta \; \mathrm{d}d \; p(d|\theta) p_{\rm pop}(\theta|\alpha) I(d) \tag{6.8}$$

$$= \int \mathrm{d}\theta \; p_{\rm pop}(\theta|\alpha) \int_{d,\rm detectable} \mathrm{d}d \; p(d|\theta) \tag{6.9}$$

$$= \int \mathrm{d}\theta \; p_{\rm pop}(\theta|\alpha) p_{\rm det}(\theta), \tag{6.10}$$

where $p_{\rm det}(\theta)$ is the probability of detecting an event generated by an event with parameters θ. Since we work in the zero-noise approximation, we use the optimal SNR to decide of the detectability of a source. The selection function can then be computed as the fraction of events predicted by the population model that are above the threshold: $\Xi(\alpha) = N_{\rm det}(\alpha, \mathrm{SNR})/N_{\rm ev}(\alpha)$. In our case, it is given by

$$\Xi(\alpha) = \frac{\alpha N_{\rm ev}(\mathrm{LS})}{\alpha N_{\rm ev}(\mathrm{LS}) + (1-\alpha) N_{\rm ev}(\mathrm{HS})} \Xi(\mathrm{LS}) + \frac{(1-\alpha) N_{\rm ev}(\mathrm{HS})}{\alpha N_{\rm ev}(\mathrm{LS}) + (1-\alpha) N_{\rm ev}(\mathrm{HS})} \Xi(\mathrm{HS}). \tag{6.11}$$

By definition, all observed events have $I(d_i) = 1$, thus

$$p(\mathbf{d}|\alpha) = \prod_{i=1}^{N_{\rm obs}} \frac{\int \mathrm{d}\theta\ p(d_i|\theta) p_{\rm pop}(\theta|\alpha)}{\Xi(\alpha)}. \tag{6.12}$$

Usually, when performing parameter estimation on an event, we collect samples from the posterior distribution. We can use Bayes' theorem to express the events' likelihoods in terms of the events' posteriors, and use a Monte Carlo averaging to substitute the integral by a sum over the N_i collected samples. Finally, we get for the posterior distribution of the mixing fraction

$$p(\alpha|\mathbf{d}) = p(\alpha) \frac{\prod_{i=1}^{N_{\rm obs}} p(d_i)}{p(\mathbf{d})} \prod_{i=1}^{N_{\rm obs}} \left[\frac{1}{N_i} \sum_{j=1}^{N_i} \frac{p_{\rm pop}(\theta_j|\alpha)}{p_i(\theta_j)\Xi(\alpha)} \right]_{\theta_j \sim p(\theta|d_i)}. \tag{6.13}$$

In the above equation, the $p_i(\theta)$ are the priors used to perform parameter estimation on each single event, and the $p(d_i)$ are the events' evidence. Since we do not perform model selection, we discard the latter term, as well as the model evidence, $p(\mathbf{d})$, from our analysis. For the prior on α, we take a flat distribution in $[0, 1]$. Note that the population distribution $p_{\rm pop}(\theta|\alpha)$ is the intrinsic one, i.e. without applying any SNR cut, and that selection effects are entirely contained in the selection function $\Xi(\alpha)$. The rates information could be included in this formalism by assuming $N_{\rm obs}$ to follow a Poisson distribution of mean $N_{\rm det}(\alpha, \mathrm{SNR})$, and including this term on the right-hand side of equation (6.13). Given the large disparity in rates estimates between different models (see table 6.1), we will not use this information.

The measurement of α can be used to infer the population distribution by computing the predictive posterior distribution

$$\mathrm{PPD}(\theta|\mathbf{d}) = \int \mathrm{d}\alpha\ p_{\rm pop}(\theta|\alpha) p(\alpha|\mathbf{d}). \tag{6.14}$$

It encodes our prediction on the distribution of population observables (θ) given an observed data set. When performing simulations, comparing the posterior predictive distribution with the population distribution used to generate data gives us a sense of the quality of our inference.

6.4 Estimating the probability density function

From equation (6.13), we can see that the hierarchical Bayesian analysis requires being able to evaluate the probability density function of the population distribution. But semi-analytical models only provide samples from the population distribution, not the analytic probability density function. In this work, we use a kernel density estimation (KDE) [522, 523] to approximate the population probability density function from the samples. From a set of n_s samples drawn from the distribution $p_{\rm pop}(\theta|\alpha)$, the KDE approximates its probability density function as

$$\hat{p}_{\rm pop}(\theta|\alpha) = \frac{1}{n_s} \sum_{i=1}^{n_s} K_H(\theta - \theta_i), \tag{6.15}$$

where K_H is the *kernel function*. We choose to work with Gaussian KDEs, where, denoting by n_d the dimensionality of the parameter space,

$$K_H(y) = \frac{1}{(2\pi)^{-n_d/2}}(\det(H))^{-1/2}e^{-\frac{1}{2}y^T H^{-1}y}. \tag{6.16}$$

We use the KDE implementation of `scipy` [524], where H is taken to be proportional to the identity matrix. The proportionality constant is called the *bandwidth* of the KDE, and is a very important parameter, since it defines the smoothing scale of the approximation to the target probability density function. In figure 6.3 we show the approximations to the population probability density function of $\log_{10}(\mathcal{M}_{c,s})$ that we obtain using different values of the bandwidth (noted bw). For too large values of the bandwidth we cannot resolve

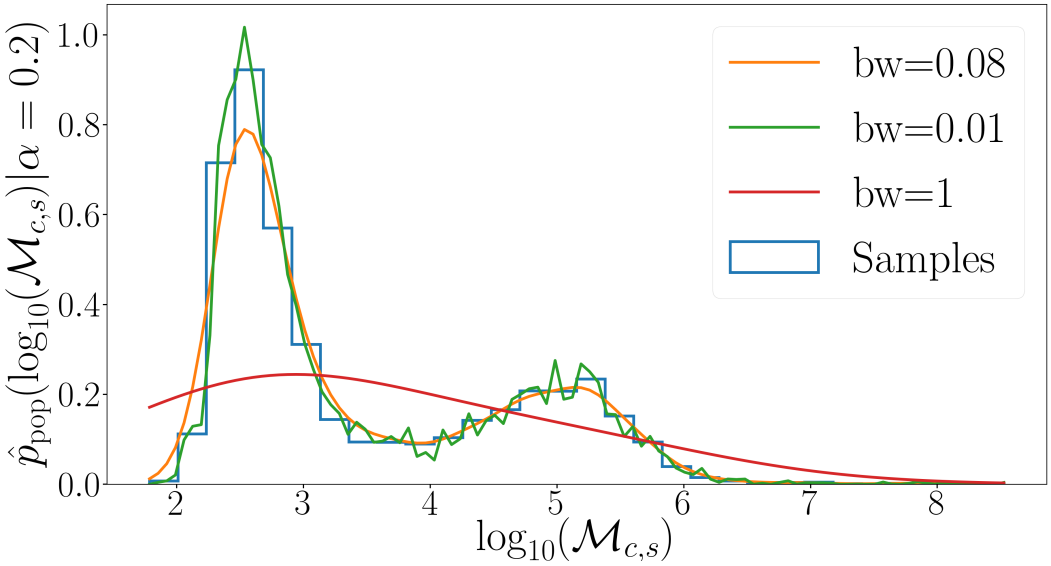

Figure 6.3: Comparison between different KDE approximations to the population probability density function of $\log_{10}(\mathcal{M}_{c,s})$, using different values of the bandwidth. By taking too small values of the bandwidth, the KDE is not smooth, and by taking too large values, we cannot resolve the features of the distribution. For the case shown here, a bandwidth of 0.08 is a good choice. This value was obtained by minimising the integrated squared error, as described in the main text.

the features of the distribution, and for too small values the resulting probability density function is not smooth. We deal with this issue by choosing the bandwidth that minimises the integrated squared error $\int \mathrm{d}\theta(p_{\rm pop}(\theta|\alpha) - \hat{p}_{\rm pop}(\theta|\alpha))^2$. In practice, it is estimated using a Monte Carlo averaging, and the quantity we seek to minimise is [525]

$$\int \mathrm{d}\theta \hat{p}_{\rm pop}(\theta|\alpha)^2 - \frac{2}{n_s}\sum_{i=1}^{n_s}\hat{p}_{\rm pop,-i}(\theta_i|\alpha), \tag{6.17}$$

where the sum runs over the n_s samples drawn from $p_{\rm pop}(\theta|\alpha)$ used to approximate the integral, and $\hat{p}_{\rm pop,-i}(\theta|\alpha)$ is the KDE obtained using all n_s samples but the i^{th} one. The value of 0.08 used in figure 6.3 was obtained with this method.

The required accuracy on the estimation of the probability density function increases with the number of observed events. Unfortunately, the accuracy of the KDE is limited by the number of simulation points at our disposal, in particular for the HS variant of our fiducial astrophysical model (~ 2500 points). This leads to a systematic error, which dominates over statistical errors when increasing the number of observed events, and leads to systematic biases in the hierarchical Bayesian analysis. Similarly, from equation (6.13) it can be seen that the error on $\ln(p(\alpha|\mathbf{d}))$ due to a misevaluation of the selection function increases linearly with the number of observed events. In our case, the accuracy to which the selection function is computed depends on the accuracy of the selection function for the LS and HS models (see equation (6.11)). In appendix D, we show that using too few points to compute these terms also leads to systematic biases. To mitigate these issues, we will make an approximation: we will take the probability density function computed from the KDE to be the "true" probability density function of our fiducial astrophysical model, and use it to generate mock data. By doing this, the data generation process is fully consistent with the probability density function used in the hierarchical Bayesian analysis, avoiding systematic biases. We compute the selection function for the LS and HS variants of our fiducial astrophysical model by generating many ($\sim 10^6$) events from the KDE and computing the fraction of detectable events. We then use equation (6.11) to evaluate the selection function for any value of α. This approximation should be seen as the limit where we have enough simulation points to build very accurate KDEs and compute the selection function to high precision. In figure 6.4 we compare the population distribution of the LS and HS variants of the fiducial astrophysical model computed from numerical simulations to the one obtained from the KDE. The bandwidth is chosen by minimising the integrated squared error, as described above. Note that, when building the KDE that will serve as our fiducial astrophysical model, we use $\mathrm{arcth}(\chi_{1,2})$ and instead of $\mathrm{arcth}(\chi_{+,-})$ in order to ensure the spins are in the physically allowed range. The distributions are overall in very good agreement, so we expect the results we will present here to be very similar to the ones we would obtain without doing any approximation.

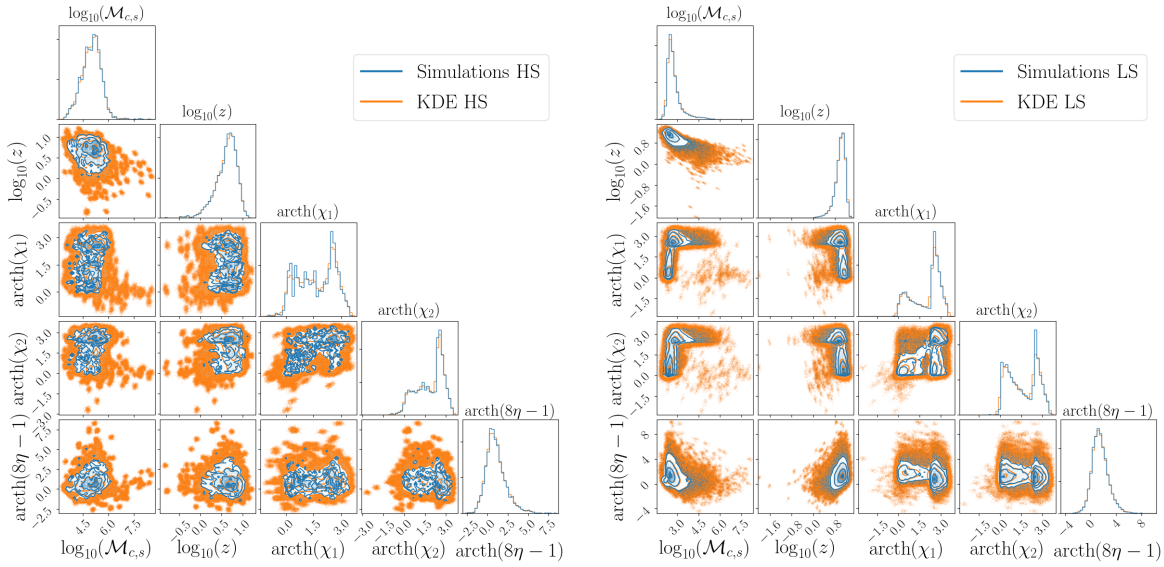

(a) LS variant.

(b) HS variant.

Figure 6.4: Comparison between the population distributions obtained from numerical simulations and the KDE we build from it. We purposefully did not smooth the corner plot in order to reflect the real level of agreement between the two distributions. When building the KDE, we use $\mathrm{arcth}(\chi_{1,2})$ instead of $\mathrm{arcth}(\chi_{+,-})$ in order to ensure the spins are in the physically allowed range. The bumpy histograms obtained from simulations of the HS variant (and in particular the spin ones) put in evidence that we lack points to build a KDE accurate enough for our purposes. Nevertheless, the two distributions are overall in good agreement, so using the KDE as our "true" fiducial astrophysical model should yield very similar results to the ones we would obtain without doing such an approximation.

6.5 Results

We consider two kinds of experiments. In the first one, we generate mock observation sets using the predictions of our fiducial astrophysical model (computed from the KDE), and use this same model in the hierarchical Bayesian analysis (the $p_{\mathrm{pop}}(\theta|\alpha)$ in equation (6.13)). In the second experiment, we use the SN-delays model to generate mock observation sets, but still use our fiducial astrophysical model in the hierarchical Bayesian analysis. The goal of this second experiment is to test if we could still draw meaningful conclusions if the population of MBHBs in the Universe is different from the one used in the data analysis pipeline. The results we will present here were obtained using an SNR threshold for detection of 10. Moreover, we do not take into account measurement errors, i.e. $p(d_i|\theta) = \delta(\theta - \theta_i)$ in equation (6.12).

6.5.1 Model-consistent inference

We start by investigating how the inference on α improves with the number of events. Although we do not use information on the rates in the inference, we make sure that the

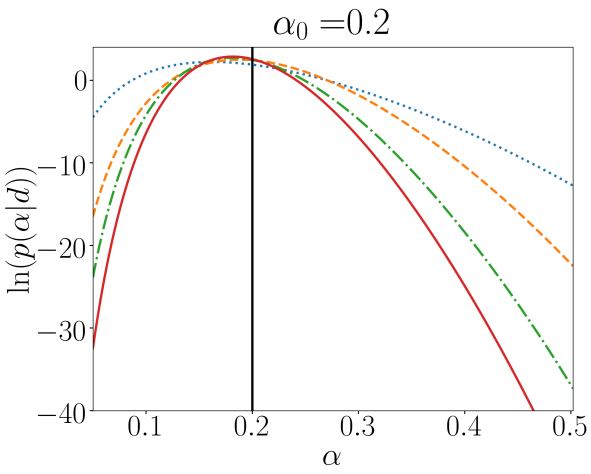

(a)

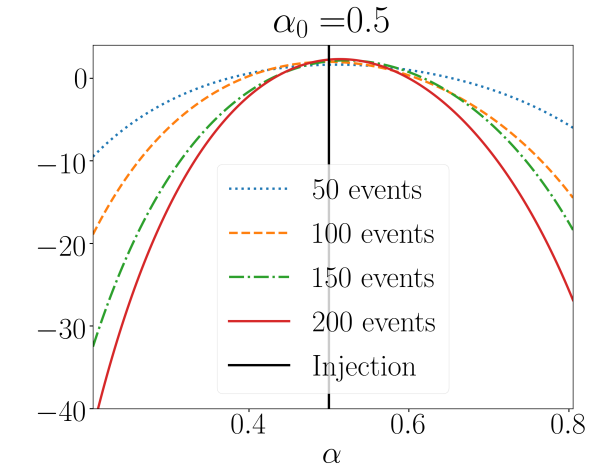

(b)

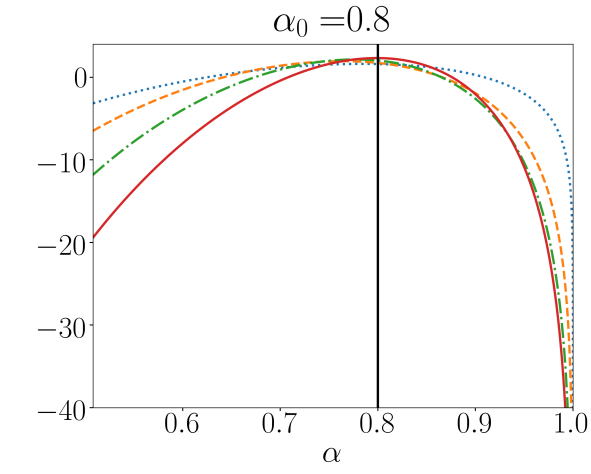

(c)

Figure 6.5: Posterior distribution on α for observation sets with an increasing number of observed events, generated using different values of the mixing fraction. The posteriors peak near the true value and become narrower as we increase the number of events.

number of events in the data sets is realistic for a LISA mission duration of four to ten years given the predicted rates (see table 6.1). In figure 6.5, we plot the log-posterior on α for observation sets with an increasing number of events. In the upper panel, the data set was generated with a mixing fraction $\alpha_0 = 0.2$ between the LS and HS variants of our fiducial astrophysical model, in the middle panel with $\alpha_0 = 0.5$, and in the lower panel with $\alpha_0 = 0.8$. The posteriors peak near the true value and become narrower as we increase the number of events. We observe a sharp drop in the posterior close to the extremal values. This is because as α approaches 0 (1) the resulting population is no longer compatible with the lightest (heaviest) events. Moreover, due to our choice of mixing prescription (see equations (6.2) and (6.3)) and to the higher rate of events of the LS variant, the shape of the population distribution changes faster for small values of α, so the posterior is narrower for α_0 close to 0 than for α_0 close to 1. In order to have a more global view, we generate several observation

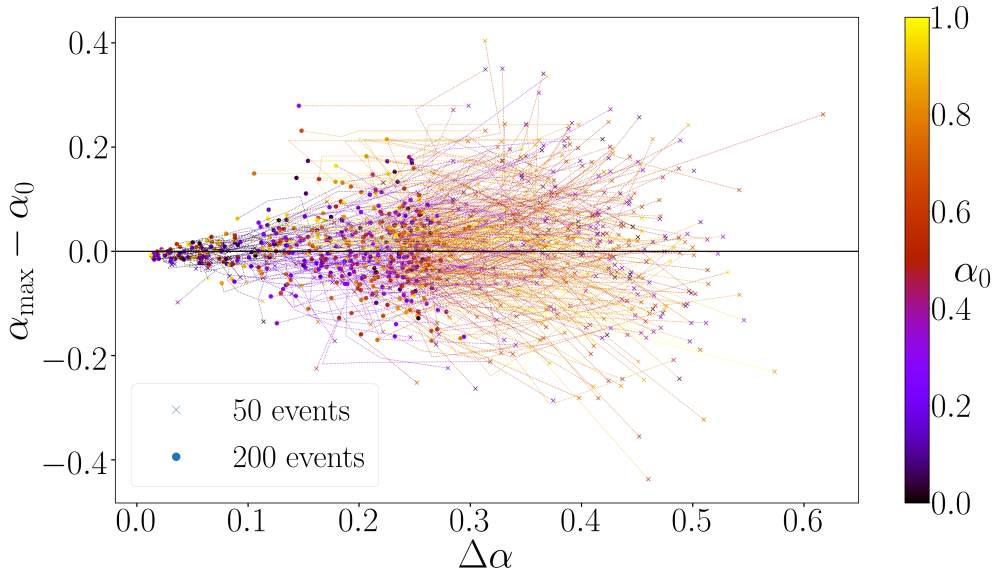

Figure 6.6: Evolution of the shift and the error on α (90% confidence interval) with the number of observed events. The observation sets start with 50 events (crosses) and end with 200 events (dots). The colour scale indicates the value of α_0. As expected, they tend do decrease as we observe more events. The fact that the points are equally distributed on both sides of the $\alpha_{\max} = \alpha_0$ line indicates that there is no systematic bias in our analysis.

sets with an increasing number of events, drawing the mixing fraction uniformly in $[0, 1]$, and plot the evolution of the shift and the error on α with the number of observed events in figure 6.6. We estimate the shift as the difference between the maximum-posterior point and the injection value, and the error on the mixing fraction ($\Delta\alpha$) as the 90% confidence interval centred around the median value. The colour scale indicates the value of the injected mixing fraction for each observation set. As expected, both tend to decrease as we observe more events. Also, note that the points are equally distributed on both sides of the $\alpha_{\max} = \alpha_0$ line, indicating that there is no systematic bias in our analysis. We find that the error on α tends to be smaller for injected values close to 0 or 1 and for small values of α_0, in agreement with our discussion on the shape of the posterior above.

Next, we assess our ability to infer the population distribution from an observed data

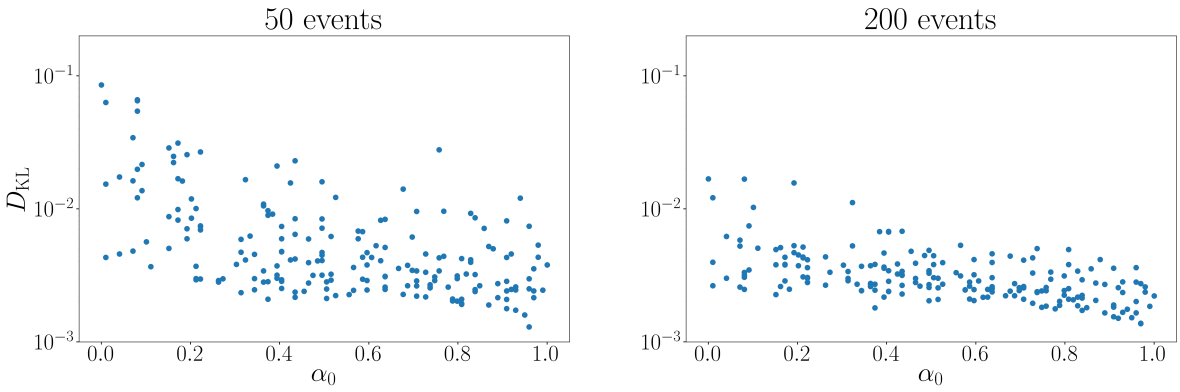

(a) 50 events.

(b) 200 events.

Figure 6.7: Kullback-Leibler divergence between the posterior predictive distribution and the population distribution for different observation sets generated with different values of α_0. In the left (right) panel the observation sets contain 50 (200) events. The smaller the KL divergence, the better our inference of the population distribution. Increasing the number of events tends to improve the inference, as expected.

set, using the posterior predictive distribution defined in equation (6.14). In figure 6.7, we plot the KL divergence (see equation (3.7)) between the posterior predictive distribution and the population distribution for data sets of 50 and 200 events. The KL divergence tends to be smaller for larger data sets, meaning that our inference on the population distribution improves. We observe that the largest values of the KL divergence are reached for $\alpha_0 \sim 0$. This is because the population distribution varies faster for small α, so even small (statistical) shifts in the estimation of the mixing fraction lead to larger discrepancies between the posterior predictive distribution and the population distribution for $\alpha_0 \sim 0$. Nevertheless, as can be seen in the upper-left panel of figure 6.8, even in the worse case (the largest value of the KL divergence among the cases shown in figure 6.7) we can reconstruct the population distribution reasonably well. The other panels show the comparison between the posterior predictive and the population distributions for data sets of 100 events yielding mid-range values of the KL divergence and for the data set yielding the smallest one. Overall, this pipeline allows us to infer the population distribution accurately when the model used to generate data is the same as the one used in the pipeline. We will now test the robustness of this pipeline by using different models in the two stages.

6.5.2 Robustness

We mix between the HS and LS variants of the SN-delays model as described in equation (6.2), and generate data sets of 20 events for $\alpha_0 = 0$, $\alpha_0 = 0.5$ and $\alpha_0 = 1$. We run our pipeline on these observation sets and compare the posterior predictive distribution to the population distribution. The results are shown in figures 6.9, 6.10 and 6.11. In each case, we show both the intrinsic distribution and the one after imposing an SNR threshold of 10.

For $\alpha_0 = 0$ (figure 6.9), we can reasonably well reproduce the chirp mass distribution of the detectable population, but we overestimate the fraction of light events in the intrinsic

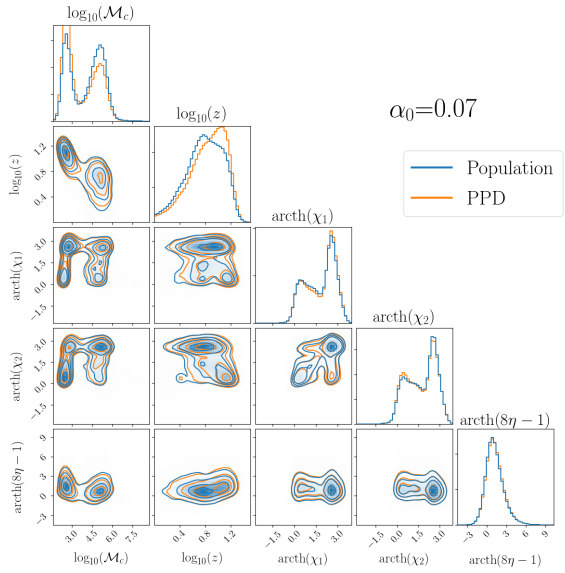

(a) Worse case.

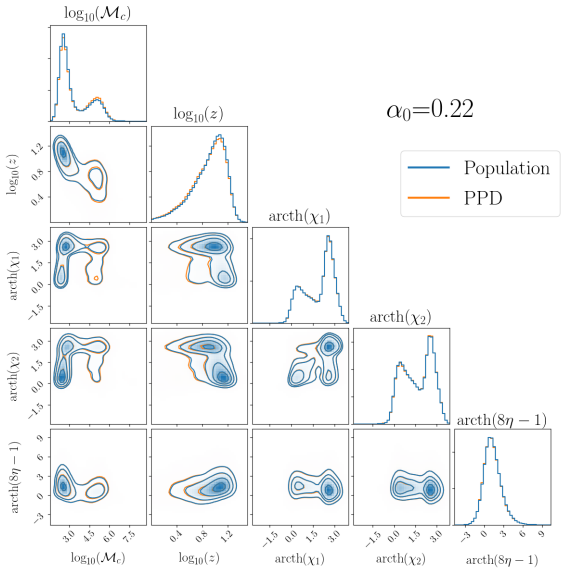

(b) Mid-range case.

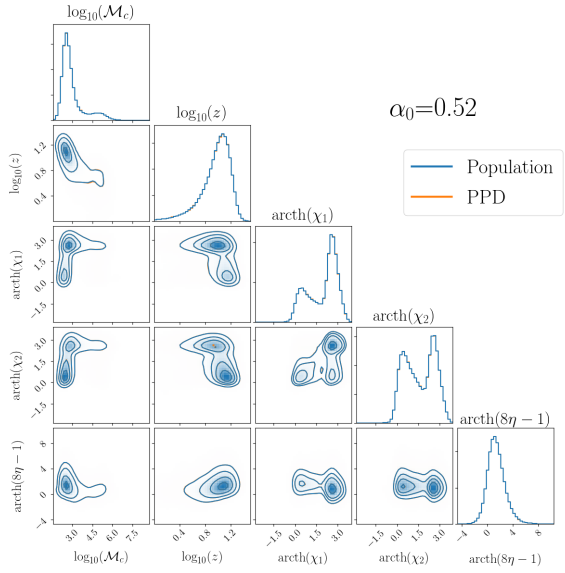

(c) Mid-range case.

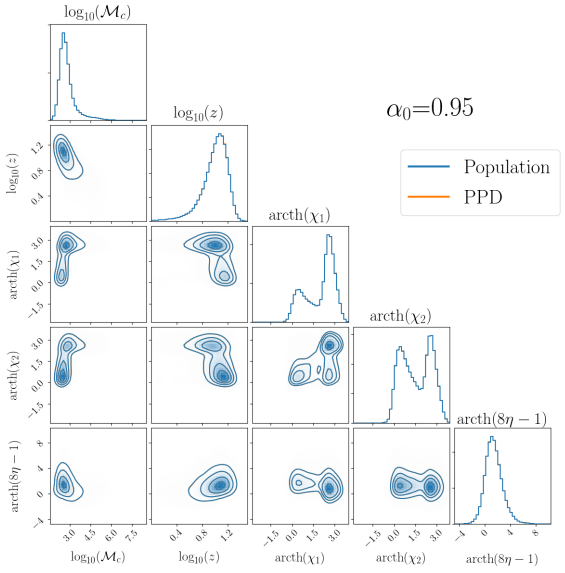

(d) Best case.

Figure 6.8: Comparison between the population distribution and the posterior predictive distribution for four observation sets generated with different values of α_0. Each observation set contains 100 events. In the upper-left and lower-right panels we show the cases that yield the larger and smaller values of the KL divergence among the cases shown in figure 6.7. The other two panels show cases yielding mid-range values of the KL divergence.

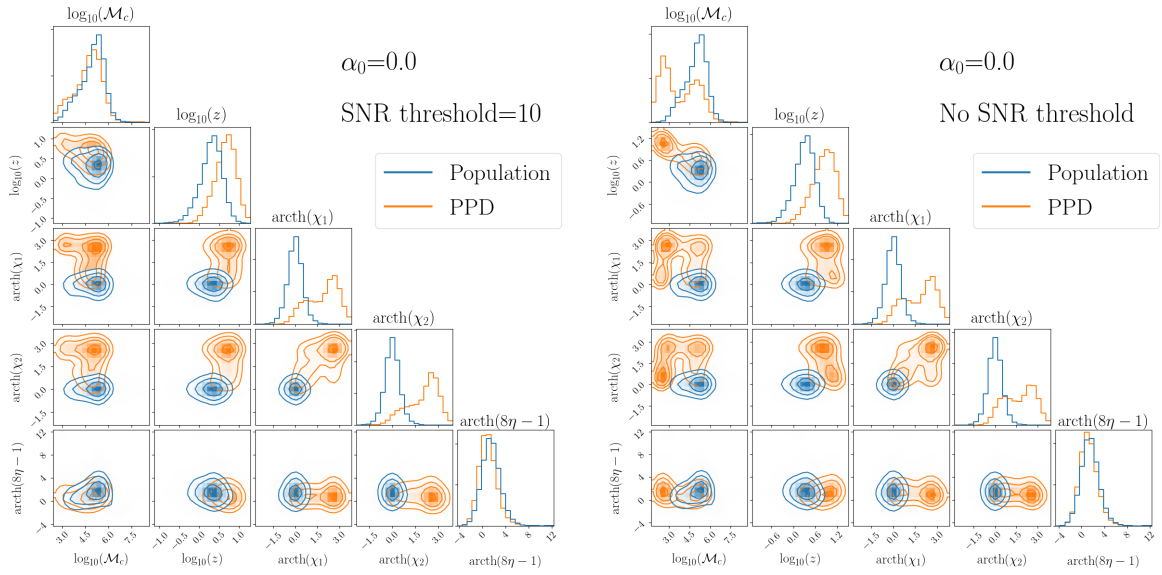

(a) Detectable population.

(b) Intrinsic population.

Figure 6.9: Comparison between the population distribution for the HS variant of the SN-delays model and the posterior predictive distribution for an observation set containing 20 events from the HS SN-delays catalogue. In the left panel we show the distribution of detectable events and in the right panel we show the intrinsic population.

population. This is because the HS variant of the SN-delays model has a tail extending to lighter values than the HS variant of the fiducial model. Our pipeline compensates for this by adding events from the LS variant, and since only $\sim 25\%$ of LS events are detectable, the fraction of light events in the intrinsic population is overestimated. Similarly, for $\alpha_0 = 0.5$ (figure 6.10) the posterior predictive distribution agrees reasonably well with the population distribution of chirp mass for detectable events, but this time the fraction of light events in the intrinsic population is underestimated. This is due to the difference in the fraction of detectable events between the LS variants of our fiducial model and the SN-delays model (see table 6.1). For a given number of detected light events, the latter predicts twice as many light events in the intrinsic population as our fiducial model. Finally, for $\alpha_0 = 1$ (figure 6.11) even the chirp mass distribution of detectable events is wrongly estimated. This is due to a tail of heavy events predicted by the LS variant of the SN-delays model, which causes our pipeline to estimate α_0 to be different from 1. In all three cases, due to the differences in the fiducial and SN-delays population, redshift and spins distributions are poorly reconstructed.

These results show that this pipeline would lead to erroneous predictions if the population of MBHBs is too different from the one predicted by our astrophysical models. Note that in the LS SN-delays model we do not expect to observe 20 events even for a ten years mission duration, but this does not change our previous conclusion.

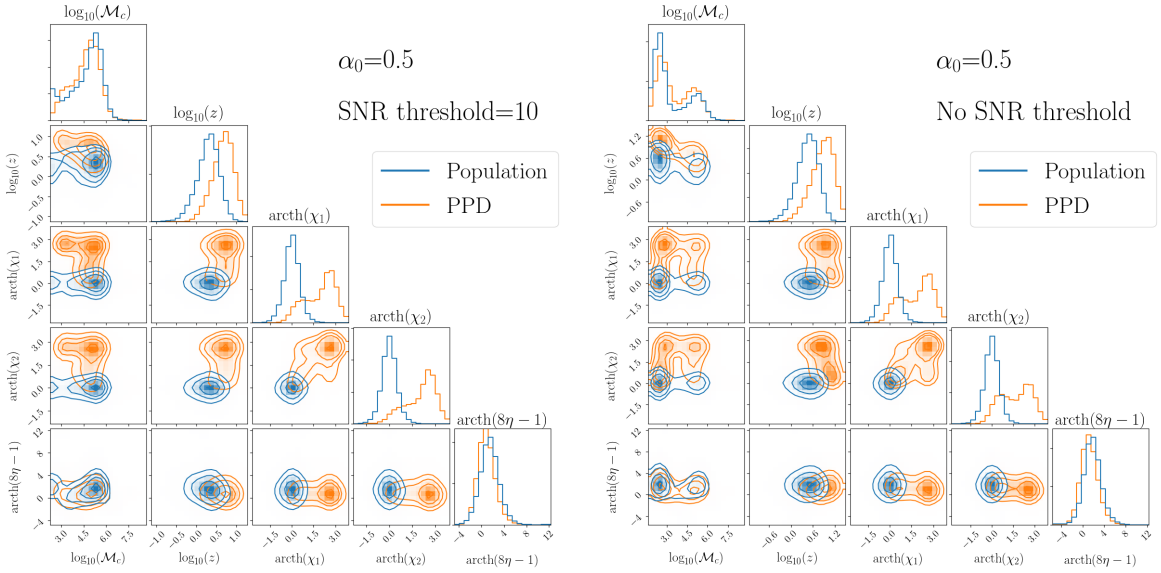

(a) Detectable population. (b) Intrinsic population.

Figure 6.10: Same as figure 6.9 for a mixing fraction between the HS and LS variants of the SN-delays model of 0.5.

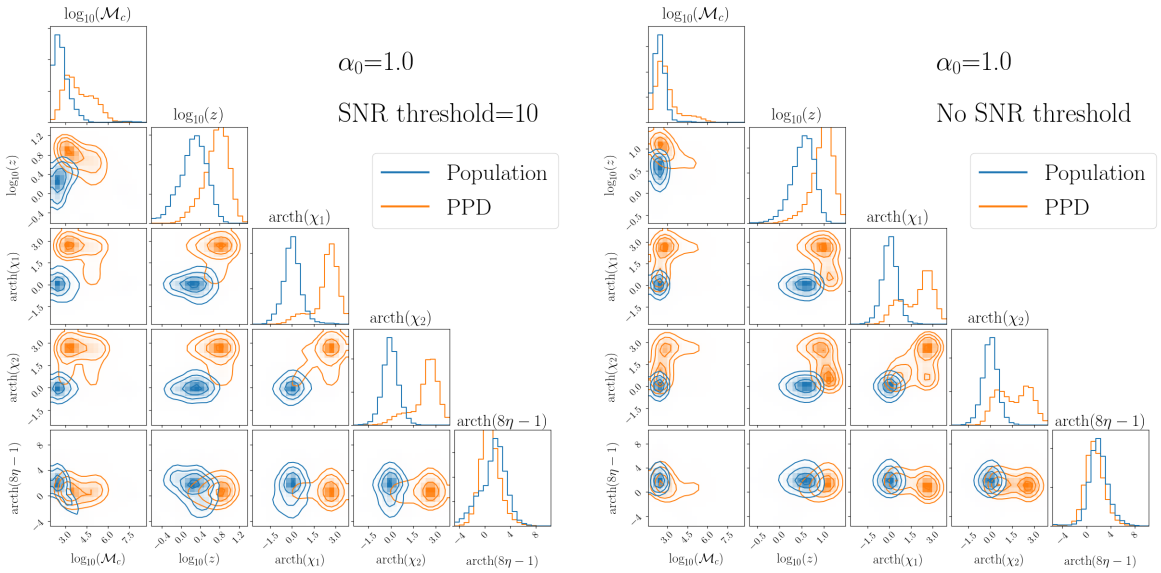

(a) Detectable population. (b) Intrinsic population.

Figure 6.11: Same as figure 6.9 for the LS variant of the SN-delays model.

6.6 Discussion

In this chapter we discussed of the ability of LISA to distinguish between different astrophysical models for the formation and evolution of massive black holes by inferring the population of MBHBs. We introduced a mixing fraction between astrophysical models to account for the possibility that the population of MBHBs in the Universe cannot be described by one single model. More specifically, we mixed between two variants of a same model: one that predicts that massive black holes form from light seeds and another from heavy seeds. We built a pipeline based on the hierarchical Bayesian framework to measure the mixing fraction from LISA observations, and infer the population of massive black holes. We have shown that this pipeline allows us to reconstruct accurately the population of MBHBs if it is similar to the one used in the pipeline, but not if the populations are too different.

This problem could potentially be mitigated by introducing additional mixing fractions: one could in principle mix between as many models as desired. Nevertheless, given the large uncertainty surrounding astrophysical models, we believe a better alternative is to use a theory-agnostic approach. We are currently working on a simplified astrophysical model for the formation and evolution of massive black holes where the population of MBHBs depends on physically-meaningful hyperparameters controlling the initial mass distribution, the delay between dark matter halo mergers and MBHB mergers etc. We could then perform a hierarchical Bayesian analysis to infer these hyperparameters from LISA observations, using this same model to generate data, or more complex ones, such as the ones we used in this work. In appendix D, we emphasise another important issue: we will need many more points from numerical simulations in order to avoid systematic biases.

The results presented here did not take into account measurement errors. We are currently working on this point, but we do not expect our main conclusions to change. On a longer timescale, it will also be necessary to use waveforms including eccentricity and precession effects, since those contain a fair amount of information on the mechanisms that trigger the coalescence of MBHBs. We expect that including this information should help solve the "last parsec problem".

Chapter 7

Conclusion and perspectives

In only six years, gravitational waves have already provided an incredible amount of information on our Universe. For instance, they have allowed us to infer for the first time the properties of the population of compact binaries and provided new tests of general relativity. They have also triggered many questions, and the future of gravitational wave astronomy promises to be very exciting. The sensitivity improvement of current detectors will increase the detection rate and our ability to extract the source parameters. Moreover, the next generation of detectors is already being planned. Among them, the space-based interferometer LISA will complement ground-based detectors and allow us to observe a yet unexplored population of compact binaries. In this thesis, we have proposed tools to exploit the full potential of gravitational wave observations, and assessed what could be learned on astrophysics and fundamental physics from these observations, with a special focus on the LISA mission.

We have performed for the first time a full Bayesian analysis on simulated LISA data of SBHBs, using an MCMC sampler that we designed for this purpose. Restraining ourselves to quasicircular binaries with component spins aligned or anti-aligned with the orbital angular momentum, we performed parameter estimation for several systems, exploring the parameter space of these sources. We have determined the accuracy to which the source parameters could be measured and explained the correlations between them. This study will be very helpful in building tools to search for these sources in the LISA data stream, a highly nontrivial task. Moreover, we have shown that such observations would allow us to measure to high precision low-frequency modifications to the gravitational wave signal arising due to modified gravity or environmental effects. For instance, constraints on dipolar radiation, a generic prediction of beyond general relativity theories, could be improved by six orders of magnitude with LISA, and seven with multiband observations. Inspired by the detection of GW190521, we considered LISA observations of systems with total mass $\sim 150\ M_\odot$ residing in AGN disks. We have shown that these observations would allow us to measure the effect of acceleration around the central massive black hole, accretion and dynamical friction, providing an unique probe of AGN properties. These environmental effects are degenerate with modified gravity ones, potentially spoiling tests of general relativity. If a low-frequency deviation from vacuum general relativity waveforms is detected, the very precise sky localisation provided by LISA could help disentangle between these effects, since the observation of an electromagnetic counterpart would favour the astrophysical origin. We

also expect that modifications to general relativity should be observed consistently across all detections, providing other means to identify them. These studies have confirmed the scientific potential of LISA observations of SBHBs, but many important extensions to our work are to be considered. First of all it is necessary to include precession and, more importantly, eccentricity effects. Indeed, we expect SBHBs to have a nonzero eccentricity when in the LISA band, and measuring it would help discriminate between different formation scenarios. Moreover, in our work we mimicked multiband observations by adding by hand constraints on the intrinsic parameters of the source, to include the information provided by ground-based detectors. We are now carrying a full study of multiband observations, in order to better characterise its benefits and ready this analysis involving very different detectors.

Next, we have shown that future gravitational wave observations could allow us to observe new classes of systems. On the fundamental physics side, we proposed a model for the full gravitational wave signal of ECO binaries. This theory-agnostic model relies on simple assumptions based on results obtained from theoretical computations and numerical simulations. With this model in hand, we estimated that, together, ET and LISA will allow us to observe virtually all ECO binaries in the Universe. However, their detection might be almost impossible with current data analysis pipelines, and in particular if only BBH waveforms are used in template-based searches. Our model provides a theoretically-motivated waveform on which we can test data analysis pipelines looking for nonperturbative deviations to general relativity BBHs. It could easily be modified to account for other types of behaviours in the merger/post-merger regime and for all relevant modifications to the inspiral part of the signal. On the astrophysics side, we showed that LISA could be the first instrument to confirm the existence of binaries made of a black hole accreting from a white dwarf. Indeed, by combining LISA measurements with the semi-analytical evolution model for WDBH binaries that we proposed, we could infer the masses of both binary components and the distance to the source. This important piece of information, which could usually not be obtained with gravitational wave observations of GBs, would allow us to unambiguously identify the binary components. Our model relies on a few analytic approximations, such as the Eggleton's mass-radius relation and Eggleton's Roche lobe fitting formula. Although we expect that these should not affect qualitatively our conclusions, we plan on assessing their quantitative impact in the estimation of the parameters of the source.

Finally, we have built a pipeline for inferring the population of MBHBs from LISA observations, and discriminating between different scenarios for the formation and evolution of massive black holes. Our pipeline uses the hierarchical Bayesian framework to measure the hyperparameters controlling the population of MBHBs, comparing the observed population to theoretical predictions. In our study we had a single hyperparameter: the mixing fraction between two distinct models. It allows us to partially account for the large uncertainty surrounding astrophysical models. We have found that our pipeline would allow us to correctly infer the population of MBHBs, but only if the observed data set is similar enough to the predictions of the model we compare it against. Given that this will most likely not be true, we believe a theory-agnostic approach is necessary. Therefore, we are currently working on a simplified model, where the population of MBHBs is governed by astrophysically meaningful hyperparameters, such as the time delay between dark matter halos and MBHBs mergers or the median mass of black hole seeds. We have also pointed

at another important issue: population studies based on results from numerical simulations, which require some approximation method for evaluating the probability density function of the population distributions, need a large number of points. Otherwise, systematic biases will appear due to the poor approximation to the probability density function and/or the selection function. These biases could already be important for the few tens to hundreds observations of MBHBs we expect with LISA, and even more for the thousands that we expect with ground-based detectors. Last, motivated by our findings on the unexpected multimodality between intrinsic parameters in Bayesian analysis of MBHBs, we are now carrying an extensive study of the parameter estimation of MBHBs. We expect it to shed light on the yet unexplained multimodalities, and help characterise the scientific potential of MBHB observations with LISA. In the next few years, it will also be necessary to include precession and eccentricity effects in order to solve the "final parsec problem".

Thus, in this thesis I have done my best to provide an answer to a few questions I believed were relevant to the gravitational waves community. In this process many additional, interesting and challenging questions were raised that I hope to be able to address in the near future.

Appendices

Appendix A

Modelling gravitational waves from exotic compact objects

A.1 Gravitational waves feedback

The conservative equations of motions (for $P_{\rm GW} = \dot{J}_{\rm GW} = 0$) are obtained by taking the derivatives of (4.16) and (4.15) and making use of (4.17) and (4.18). They read

$$\ddot{\rho} = \rho\omega^2 - 4\omega_0^2(\rho - \rho_0) - \frac{m^2}{8\rho^2} + \frac{M}{R^2}, \tag{A.1}$$

$$\dot{\omega} = -\frac{2m\rho\dot{\rho}\omega}{\frac{MR^2}{2} + m\rho^2}. \tag{A.2}$$

The quadrupole moment of the system is given by $Q_{ij} = M_{ij} - \frac{1}{2}\delta_{ij}M_{kk}$, where

$$\begin{aligned} M_{ij} =& \frac{m\rho^2}{2}\begin{pmatrix} \cos(2\phi) & \sin(2\phi) & 0 \\ \sin(2\phi) & -\cos(2\phi) & 0 \\ 0 & 0 & 0 \end{pmatrix} \\ &+ \frac{m\rho^2}{6}\begin{pmatrix} 1 & 0 & 0 \\ 0 & 1 & 0 \\ 0 & 0 & -2 \end{pmatrix}. \end{aligned} \tag{A.3}$$

Making use of the conservative equations of motion, (A.1) and (A.2), we compute the two polarisations of a gravitational wave propagating along the orbital axis:

$$\begin{aligned} h_+ &= \frac{\ddot{Q}_{11} - \ddot{Q}_{22}}{D_L} \\ &= \frac{2}{D_L}(\gamma_2\cos(2\phi) - \gamma_1\sin(2\phi)), \end{aligned} \tag{A.4}$$

$$\begin{aligned} h_\times &= \frac{2\ddot{Q}_{12}}{D_L} \\ &= \frac{2}{D_L}(\gamma_1\cos(2\phi) + \gamma_2\sin(2\phi)), \end{aligned} \tag{A.5}$$

where γ_1 and γ_2 have been defined in equations (4.22) and (4.23). We recall that the radiated power and angular momentum (equations 1.30 and 1.31) are given by

$$P_{\rm GW} = \frac{1}{5} < \dddot{Q}_{ij} \dddot{Q}_{ij} >, \tag{A.6}$$

$$\dot{J}_{\rm GW} = \frac{2}{5} \epsilon^{3kl} < \dddot{Q}_{ka} \ddot{Q}_{la} >, \tag{A.7}$$

where the average is performed over one period of radial oscillation. Using the conservative equations of motion and defining

$$\begin{aligned} g_2 =& \dot{\gamma_1} + 2\omega\gamma_2 \\ =& - m\dot{\rho} \left(\frac{4MR^2\omega^2\rho}{\frac{MR^2}{2} + m\rho^2} + 4\omega_0^2(4\rho - 3\rho_0) + \frac{m}{8\rho^2} - \frac{3M}{R^2} \right), \\ g_1 =& \dot{\gamma_2} - 2\omega\gamma_1 \end{aligned} \tag{A.8}$$

$$\begin{aligned} =& \frac{2m}{\frac{MR^2}{2} + m\rho^2} \left[- \frac{m\rho^2\dot{\rho}^2\omega(3MR^2 + 2m\rho^2)}{\frac{MR^2}{2} + m\rho^2} \right. \\ & + \omega \left(\left(\dot{\rho}^2 - 4\omega_0^2(\rho - \rho_0)\rho + \frac{M\rho}{R^2} - \frac{m}{8\rho} \right) \left(\frac{3MR^2}{2} + 2m\rho^2 \right) \right. \\ & \left. \left. + \rho^2\omega^2 \frac{MR^2}{2} \right) \right], \end{aligned} \tag{A.9}$$

we get

$$P_{\rm GW} = \frac{2}{5} < g_1^2 + g_2^2 >, \tag{A.10}$$

$$\dot{J}_{\rm GW} = \frac{4}{5} < \gamma_2 g_1 - \gamma_1 g_2 > . \tag{A.11}$$

The averaged energy and angular momentum loss are recomputed at the beginning of each cycle.

A.2 Quasi-eccentric orbit

Inspired by the equations for eccentric motion, we introduce the phase angle υ such that

$$\rho = \frac{p}{1 + e\cos(\upsilon)}. \tag{A.12}$$

The parameter p and the "eccentricity' e of the orbit can be computed from the turning points ρ_+ and ρ_-

$$p = 2\frac{\rho_+\rho_-}{\rho_+ + \rho_-} \tag{A.13}$$

$$e = \frac{\rho_+ - \rho_-}{\rho_+ + \rho_-}. \tag{A.14}$$

Assuming the adiabatic approximation for e and p holds, i.e.

$$\frac{\dot{e}}{e} \ll \frac{1}{T}, \tag{A.15}$$

$$\frac{\dot{p}}{p} \ll \frac{1}{T}, \tag{A.16}$$

the derivative of equation (A.12) gives

$$\dot{\rho} = \frac{pe\sin(\upsilon)\dot{\upsilon}}{(1+e\cos(\upsilon))^2}. \tag{A.17}$$

The change of sign in $\dot{\rho}$ is accounted for by $\sin(\upsilon)$ and the evolution of υ is monotonic. The sign of $\dot{\upsilon}$ is determined by the initial conditions. For instance, if $\upsilon_i > 0$, equation (4.16) becomes

$$\dot{\upsilon} = \frac{(1+e\cos(\upsilon))^2}{pe|\sin\upsilon|}\sqrt{\frac{2}{m}}\sqrt{E - V_{eff}(\rho)}. \tag{A.18}$$

The term under the rightmost square root can be written

$$E - V_{eff} = \frac{-2km(\rho-\rho_+)(\rho-\rho_-)(\rho-\rho_3)(\rho-\rho_4)(\rho-\rho_5)}{\rho(\frac{MR^2}{2}+m\rho^2)}, \tag{A.19}$$

where ρ_3, ρ_4 and ρ_5 are the remaining (possibly complex) roots of $E - V_{\text{eff}} = 0$. Noticing that

$$\rho - \rho_+ = \frac{-pe(1+\cos(\upsilon))}{(1-e)(1+e\cos(\upsilon))},$$
$$\rho - \rho_- = \frac{pe(1-\cos(\upsilon))}{(1-e)(1+e\cos(\upsilon))},$$

the equation for υ can be recast as

$$\dot{\upsilon} = \frac{2\omega_0(1+e\cos(\upsilon))}{\sqrt{1-e^2}}\sqrt{\frac{(\rho-\rho_3)(\rho-\rho_4)(\rho-\rho_5)}{\rho(\frac{MR^2}{2m}+\rho^2)}}. \tag{A.20}$$

Thus, we evolve numerically equations (A.12) and (A.20) rather than equation (4.16).

For *RBH* systems, when the energy becomes larger than the effective potential height, the inner turning point ceases to exist, so we cannot use equation (A.12) anymore, and we turn back to equation (4.16) to describe the final moments of the evolution before the collapse to a black hole.

A.3 Quasi-circular orbit

For *RS* systems, after reaching the bottom of the potential the evolution proceeds, unlike for *NRS* systems. This is because the system still has angular momentum to radiate. However,

the separation between the cores ceases to oscillate, and the orbit becomes "quasicircular". Thus, e becomes very small and the adiabatic approximation (equation (A.15)) is no longer valid. Mathematically, this regime corresponds to $V'_{\rm eff}(\rho) = 0$. This condition allows us to express ω as a function of ρ, and we get the new conservative equations of motion

$$\dot{\rho} = 0, \tag{A.21}$$

$$\omega^2 = \frac{1}{\rho}\left(4\omega_0^2(\rho-\rho_0) + \frac{m}{8\rho^2} - \frac{M}{R^2}\right). \tag{A.22}$$

These expressions are used in equations (A.10) and (A.11) to write $P_{\rm GW}$ and $\dot{J}_{\rm GW}$ as functions of ρ only. Accounting for the dissipation of energy and angular momentum, the equation for ρ is given by

$$\dot{\rho} = \frac{\dot{E}}{\frac{\partial E}{\partial \rho}} = \frac{\dot{J}}{\frac{\partial J}{\partial \rho}}. \tag{A.23}$$

As a sanity check, we verified that the expressions using the angular momentum and the one using the energy give the same equation. Finally, the equations of motion become

$$\begin{aligned}\dot{\rho} = &-\frac{32}{5}m^2\omega^2\rho^2\left(4\omega_0^2\rho^2(\rho-\rho_0) + \frac{m}{8} - \frac{M\rho^2}{R^2}\right)^2 \\ &\times\left[2m\omega_0^2\rho^2\left(4(\rho-\rho_0)\rho^2 + \rho_0\left(\rho^2 + \frac{MR^2}{2m}\right)\right)\right. \\ &\left.+\frac{M}{2R^2\rho^2}\left(\frac{MR^2}{2} - 3m\rho^2\right) - \frac{m}{16}\left(\frac{3MR^2}{2} - m\rho^2\right)\right]^{-1},\end{aligned} \tag{A.24}$$

$$\omega = \sqrt{\frac{1}{\rho}\left(4\omega_0^2(\rho-\rho_0) + \frac{m}{8\rho^2} - \frac{M}{R^2}\right)}, \tag{A.25}$$

$$\begin{aligned}E = &\,2m\omega_0^2\left(\left(\frac{MR^2}{2m} + \rho^2\right)\left(1 - \frac{\rho_0}{\rho}\right) + (\rho-\rho_0)^2\right) \\ &+ \frac{m}{16\rho^3}\left(\frac{MR^2}{2} + m\rho^2\right) - \frac{M}{2R^2\rho}\left(\frac{MR^2}{2} + 3m\rho^2\right) - \frac{2}{3}\frac{M^2}{R},\end{aligned} \tag{A.26}$$

$$J = \left(\frac{MR^2}{2} + m\rho^2\right)\omega. \tag{A.27}$$

Note that taking the $M, k \to 0$ limit we recover the equations for a quasicircular binary at separation 2ρ. Once the orbit "circularises", ρ tends to an equilibrium value corresponding to one of the roots of equation (A.22), and ω goes to 0. To ensure numerical stability, we switch to this description when $e < 10^{-5}$.

A.4 Post-contact dynamics

Figure A.1 shows the post-contact evolution of an *RBH* (upper panel) and an *RS* (lower panel) system with $m_0 = 30\ M_\odot$ and $C_0 = 0.17$. In the left panel we display the distance of the cores to the centre of mass, which is half the separation between the cores, and in

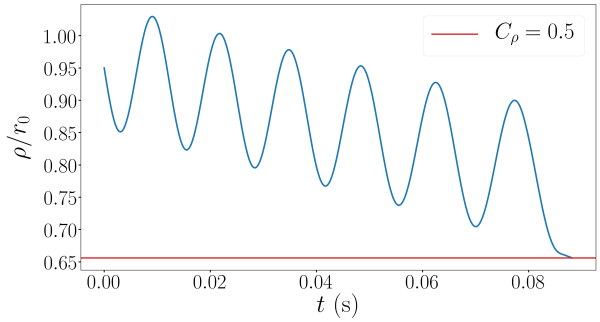

(a) The distance to the centre of mass oscillates around a decreasing mean value, untill it reaches a value such that $C_\rho = 0.5$, leading to the formation of a black hole.

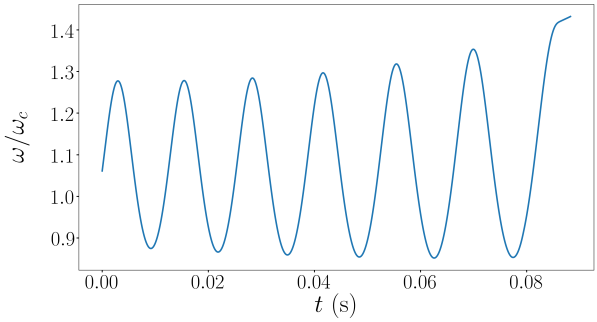

(b) The orbital angular velocity oscillates around a stable mean value and increases right before the formation of the black hole.

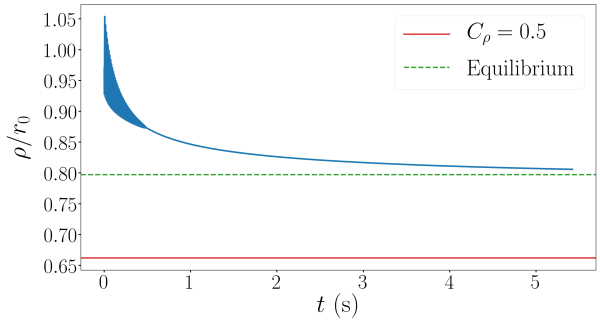

(c) Initially, the distance to the centre of mass oscillates around a decreasing mean value. Once the orbit "circularises", ρ decreases while tending to an equilibrium value, corresponding to the formation of a stable ECO.

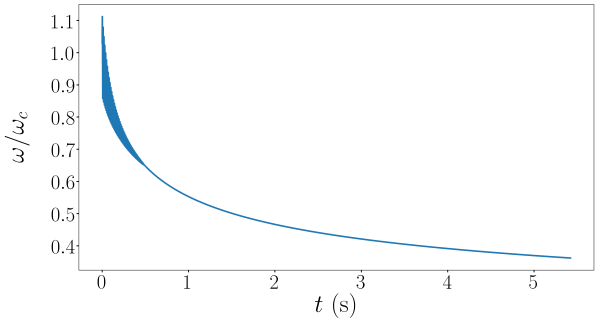

(d) The orbital angular velocity first oscillates around a decreasing mean value and once the orbit "circularises", ω decreases while tending to 0 (not shown in the figure).

Figure A.1: Evolution of the distance of the cores to the centre of mass (half the distance between the cores) and the orbital angular velocity for an *RBH* (upper panel) and an *RS* (lower panel) system.

the right panel the orbital angular velocity. Red solid lines indicate the threshold value of ρ below which a black hole is formed, i.e. such that C_ρ, defined in equations (4.19), is 0.5. For the *RBH* system, ρ oscillates around a decreasing mean value and, eventually, reaches the threshold value, leading to the formation of a black hole. ω oscillates around a stable mean value and increases right before the formation of the black hole. This is related to the increase in the gravitational wave frequency before the ringdown stage in figure 4.10. For the system we show, the final black hole has total mass $M_f = 58\ M_\odot$ and dimensionless spin $\chi_f = 0.39$. In the case of the *RS* system, ρ and ω initially oscillate around a decreasing mean value. The orbit then "circularises", from which point both decrease, while the system tends to an equilibrium configuration. The equilibrium value of ρ, indicated by the green dashed line, is higher than the threshold value for collapse. Therefore, a stable ECO is formed. The equilibrium value of ω is 0, this cannot be seen from figure A.1 because we do not display the long-term evolution for sake of clarity. The evolution of ρ for *NRS* systems is similar to the one of the *RS* system.

Appendix B

Accreting white dwarf-black hole binaries

B.1 Equilibrium solutions

After the initial phase of mass accretion, a very good approximation of the mass transfer rate can be obtained by setting the right-hand side of equation (5.24) to 0 [479] and $\dot{M}_{\rm BH} = -\epsilon_{\rm ISCO}\dot{M}_{\rm WD}$. We find for the equilibrium mass-transfer rate

$$\frac{\dot{M}_{\rm WD,\,eq}}{M_{\rm WD}} = -\frac{\dot{J}_{\rm GW}/J_{\rm orb}}{K_{\rm eq}}, \tag{B.1}$$

where

$$\begin{aligned} K_{\rm eq} =& \frac{\zeta_{\rm WD} - \zeta_{r_L}}{2}\left(1 - 3\left(1+\frac{1}{q}\right)k_{\rm WD}r_{\rm WD}^2\right) \\ &+ \left(1+\frac{1}{q}\right)\Lambda_{\rm WD}k_{\rm WD}r_{\rm WD}^2(1-\epsilon_{\rm ISCO})\left(\frac{1}{2q}k_{\rm WD}r_{\rm WD}^2 - \frac{1}{2(1+q)}\right) + 1 - \epsilon_{\rm ISCO}\left(\frac{1}{q} + \frac{j_{\rm ISCO}}{M_{\rm BH}}\sqrt{\frac{M}{a}}\right). \end{aligned} \tag{B.2}$$

Using Kepler's law, $\frac{\dot{f}}{2f} = -\frac{3\dot{a}}{2a}$, and replacing equation (B.1) in equation (5.23) gives, at equilibrium,

$$\begin{aligned} \frac{\dot{f}}{2f} = \frac{3\dot{J}_{\rm GW}/J_{\rm orb}}{K_{\rm eq}\left(1-3\left(1+\frac{1}{q}\right)k_{\rm WD}r_{\rm WD}^2\right)}\Bigg[1 &+ \left(\frac{1}{q} - \frac{1}{2(1+q)} + \frac{1}{2q}k_{\rm WD}r_{\rm WD}^2 + \frac{j_{\rm ISCO}}{M_{\rm BH}}\sqrt{\frac{M}{a}}\right)\epsilon_{\rm ISCO} \\ &- \left(1 + \frac{1}{2(1+q)} + \frac{1}{2q}k_{\rm WD}r_{\rm WD}^2 + \left(1+\frac{1}{q}\right)\Lambda_{\rm WD}k_{\rm WD}r_{\rm WD}^2\right)\Bigg]. \end{aligned} \tag{B.3}$$

Furthermore,

$$\frac{\dot{J}_{\rm GW}}{J_{\rm orb}} = \frac{32}{5}\frac{M_{\rm BH}M_{\rm WD}M}{a^4} \propto M_{\rm BH}M_{\rm WD}M\left(\frac{M}{f^2}\right)^{-4/3} \simeq M_{\rm BH}^{2/3}M_{\rm WD}f^{8/3}, \tag{B.4}$$

where in the last step we used $M_{\rm WD} \ll M_{\rm BH}$, so that $M \simeq M_{\rm BH}$. Finally, the late time evolution of the other terms in equation (B.3) happens to have a weak dependence on $M_{\rm BH}$, so $\dot{f} M_{\rm BH}^{-2/3}$ is an almost $M_{\rm BH}$-independent quantity as verified in the right panel of figure 5.12.

B.2 Fits to the evolutionary tracks

The coefficients for the evolutionary tracks fits described in the main text are summarised in table B.1.

	a_0	a_1	a_2	a_3	a_4
$y = M_{\rm WD}[M_\odot]$	319.7593186	509.0101135	303.8011829	80.7077869	8.0347503
$y = \dot{f} M_{\rm BH}^{-2/3}[{\rm Hz}\, M_\odot^{-2/3} s^{-1}]$	142.6384491	236.4026829	136.2183828	35.5719325	3.4778346

Table B.1: Coefficients for the fits in figure 5.12.

Appendix C

Multimodal parameter estimation of massive black hole binaries

While performing parameter estimation for the many systems used in the population study of section 6, we found that in some cases the posterior distribution of intrinsic parameters presents an unexpected multimodality. We have found this to happen for systems with near equal masses, and for systems with low and unequal masses and large spins, when including higher harmonics in the parameter estimation. We will discuss one example of each. The results presented here were checked using our MHMCMC sampler, `PTMCMC` [363] and `ptemcee` [505, 506][1].

C.1 Near equal mass system

We focus on a system with q close to 1 that we label *Equalq*. Its properties are listed in table C.1, together with the SNR of the (2,2) and (2,1) harmonics, as well as the total SNR. When including higher harmonics in the parameter estimation of this system, the χ_- distribution has a secondary maximum at $\chi_- = -\chi_{-,0}$, as illustrated in figure C.1, where we compare the results obtained with PhenomD and PhenomHM (the same waveform model is used for the injection and the parameter estimation). We do not show extrinsic parameters for more clarity, since there is no correlation with intrinsic parameters for this system.

By performing parameter estimation using the dominant (2,2) harmonic and one additional harmonic at a time, we find it is the (2,1) harmonic that is responsible for this secondary maximum. In the other cases, the two maxima are enfolded within one single mode. The reason for this is made clear in figure C.2, where we show the characteristic strain of several harmonics ($f|\tilde{h}|$, without the LISA response) of the *Equalq* system and of the same system but with $\chi_- = -\chi_{-,0}$. Only the (2,1) harmonic is substantially different between the two systems, showing a "dip" for positive χ_-. We have verified that when keeping the total SNR fixed while increasing the SNR of the (2,1) harmonic (by varying the inclination), the secondary is suppressed, whereas if we instead decrease the SNR in the

[1]These results are part of an ongoing project in collaboration with V. Baibhav, E. Berti, R. Cotesta, M. Katz and S. Marsat. All the results presented here were obtained by me.

(2,1) harmonic, the posterior is unimodal, enclosing the two maxima. The same happens if instead we fix the relative contribution of the (2,1) mode and vary the total SNR.

This can be further understood by examining the post-Newtonian expansion of the (2,2) and (2,1) harmonics [526]:

$$\tilde{h}_{\ell m}(f) = \frac{M^2}{D_L}\pi\sqrt{\frac{2\eta}{3}}\,V_m^{-7/2}\,e^{-i(m\,\Psi_{\rm SPA}(V_m)+\pi/4)}\,\hat{H}_{lm}(V_m), \tag{C.1a}$$

$$\begin{aligned}\hat{H}_{22} &= -1+\left(\frac{323}{224}-\frac{451\eta}{168}\right)V_2^2+\left[-\frac{27}{8}\delta_m\,\chi_a+\chi_s\left(-\frac{27}{8}+\frac{11}{6}\eta\right)\right]V_2^3\\ &+\left[\frac{27312085}{8128512}+\frac{1975055}{338688}\eta-\frac{105271}{24192}\eta^2+\chi_a^2\left(\frac{113}{32}-14\eta\right)\right.\\ &+\left.\frac{113}{16}\delta_m\,\chi_a\chi_s+\chi_s^2\left(\frac{113}{32}-\frac{\eta}{8}\right)\right]V_2^4+\mathcal{O}(V_2^5)\,,\end{aligned} \tag{C.1b}$$

$$\begin{aligned}\hat{H}_{21} &= -\frac{\sqrt{2}}{3}\left\{\delta_m V_1-\frac{3}{2}\left(\chi_a+\delta_m\,\chi_s\right)V_1^2+\delta_m\left(\frac{335}{672}+\frac{117}{56}\eta\right)V_1^3\right.\\ &+\left[\chi_a\left(\frac{3427}{1344}-\frac{2101}{336}\eta\right)+\delta_m\chi_s\left(\frac{3427}{1344}-\frac{965}{336}\eta\right)\right.\\ &+\left.\left.\delta_m\left(-\frac{i}{2}-\pi-2i\log(2)\right)\right]V_1^4\right\}+\mathcal{O}(V_2^5)\,,\end{aligned} \tag{C.1c}$$

where $V_m=(2\pi Mf/m)^{1/3}$, $\chi_{s,a}=(\chi_1\pm\chi_2)/2$ and SPA stands for stationary phase approximation. Note that we corrected for a typo in the 2PN term of the (2,1) harmonic in [526]. In the near equal mass case considered here, $\chi_{\rm s,a}\sim\chi_{+,-}$. It is clear from these expressions that in the equal mass case ($\delta_m=0$), the change $\chi_-\to-\chi_-$ leaves the (2,2) harmonic invariant while the (2,1) harmonic is multiplied by -1. This multiplicative factor can be compensated by a shift of π in the phase at coalescence. Therefore, we expect that the phase at coalescence of the secondary mode should be shifted by π with respect to the injection, but we do not find that.

In figure C.3 we plot the posterior distribution of χ_-, φ_c for systems with the same mass ratio as the *Equalq* system ($q=1.02$, left panel) and with $q=1.0004$ (right panel), for different values of χ_-. The secondary maximum is enhanced in the latter case, in agreement with equation (C.1c), since in the exact $q=1$ case we expect them to have the same weight as the main mode. However, although φ_c is slightly shifted, we do not find the expected shift by π. The very negative value of the log-likelihood at the point $\chi_-=-\chi_{-,0}$, $\varphi_c=\varphi_{c,0}+\pi$ ($\ln\mathcal{L}<-10$) reinforces our belief that it is not a secondary maximum.

To investigate this behaviour, we perform some waveform comparisons. In figure C.4, we plot the amplitudes of the (2,2) and (2,1) harmonics for systems with $M=10^6M_\odot$, $q=1$ and $\chi_-=\pm0.05$, and the difference in phase between the two systems for the (2,2) and (2,1) harmonics, using PhenomHM (upper panel) and the NRHybSur3dq8 surrogate waveform [107] (lower panel). In the latter case, we find the expected shift of π in the phase, whereas for PhenomHM the phase difference is identically 0. These results suggest that the phase

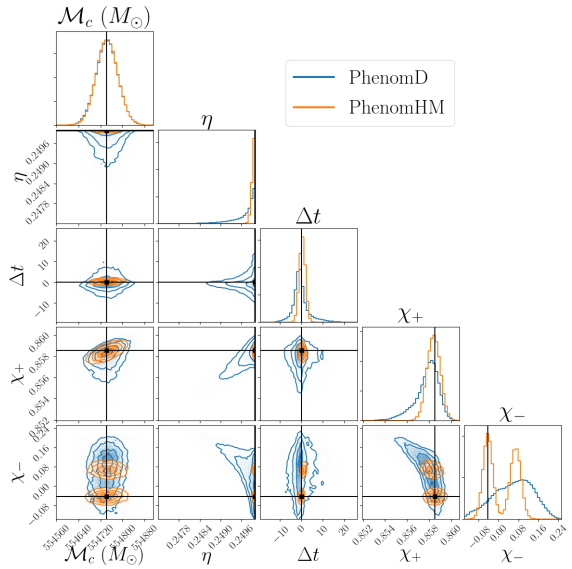

(a) Distribution of sampling parameters.

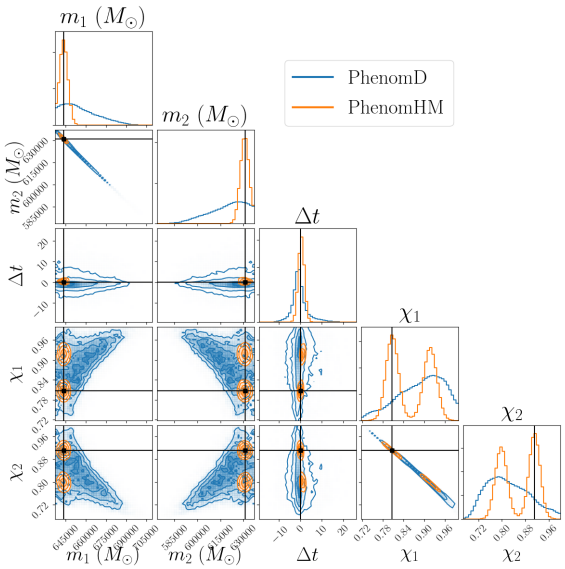

(b) Distribution of parameters entering the waveform computation.

Figure C.1: Comparison of inferred distributions for the *Equalq* system when using PhenomD and PhenomHM. In the left panel we show the distribution of parameteters used in the sampling, and in the right panel of the original waveform parameters. When including higher harmonics, we find a secondary maximum at $\chi_- = -\chi_{-,0}$, which results in two maxima for individual spins. Black lines indicate the injection.

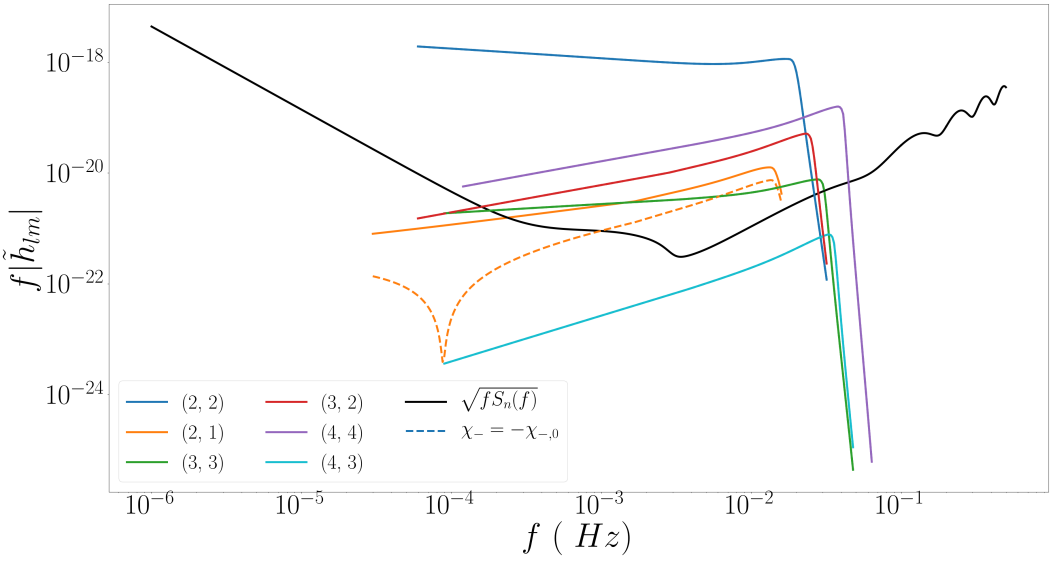

Figure C.2: Characteristic strain of several harmonics for the *Equalq* system and for a system with the opposite value of χ_-. The LISA response is not taken into account. The dark line shows the SciRDv1 noise strain. Only the (2,1) harmonic is substantially different between the two systems, and allows one to partially distinguish between them.

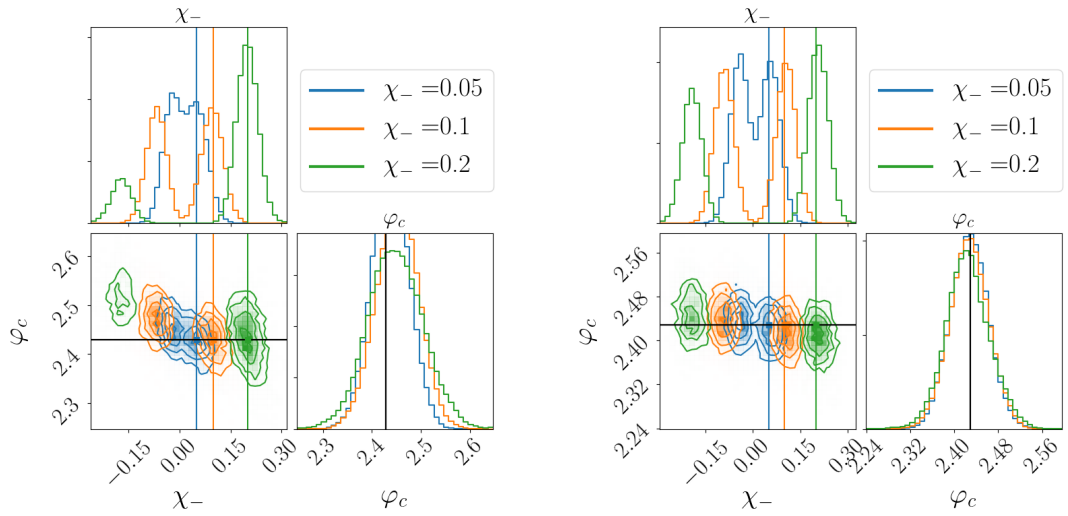

(a) $q = 1.02$.

(b) $q = 1.0004$.

Figure C.3: Inferred distribution on χ_- and φ_c for systems with the same mass ratio as the *Equalq* system ($q = 1.02$, left panel) and with $q = 1.0004$ (right panel), for different values of χ_-. The weight of the secondary mode increases as q gets closer to 1. Against our expectations, we do not find that φ_c is shifted by π in the secondary mode.

of the harmonics other than the (2,2) in PhenomHM might be ill-defined. However, the bimodality in χ_- should be physical, not simply a waveform artefact, as we argued above based on the post-Newtonian expansions.

C.2 Low and unequal masses, large spins system

The majority of the cases where we found a multimodal distribution for intrinsic parameters is for systems with moderately low masses, large mass ratio ($\sim 2 - 10$) and large spins ($\gtrsim 0.95$) or large mass ratio ($\gtrsim 10$) and moderately large spins ~ 0.7. Given that the validity of PhenomHM is limited to $q \leq 18$ and $\chi_{1,2} \leq 0.85$, some caution is needed in interpreting these results. We will focus on a system with moderately high mass ratio ($q = 5.3$), which we label *Highq*. We list its properties in table C.2. The results we will present here were obtained using the LISA proposal noise curve [29]. Higher harmonics, especially the (3,3) harmonic, have a relatively high SNR due to the moderately large mass ratio of the system. In figure C.6, we show the parameter estimation using PhenomD and PhenomHM. In the latter case, the distribution of intrinsic parameters shows three maxima, which are encompassed within a single mode when considering only the $(2, \pm 2)$ harmonics.

Performing parameter estimation including only the $(2, \pm 2)$ harmonics and one additional harmonic at a time, we find that the multimodality is due to the $(3, 3)$ and $(4, 4)$ harmonics. As in the near equal mass case, we find that if we increase the SNR of these modes (by varying the inclination or the total SNR), the multimodality disappears, whereas if we decrease it, we obtain one single mode encompassing the three maxima. We observe the same behaviour

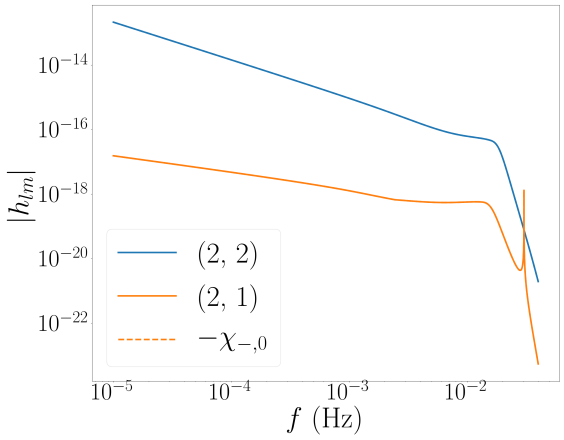

(a) Amplitude with PhenomHM.

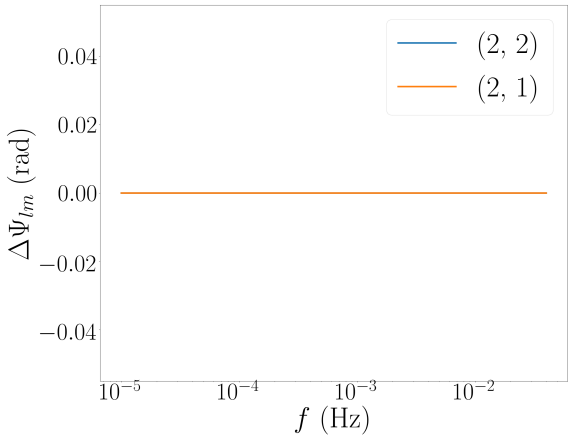

(b) Phase difference with PhenomHM.

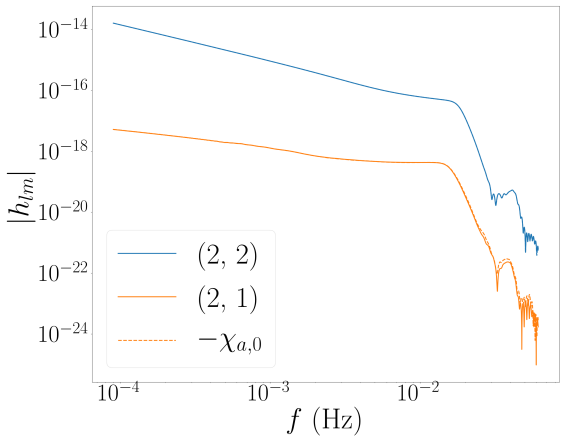

(c) Amplitude with NRHybSur3dq8.

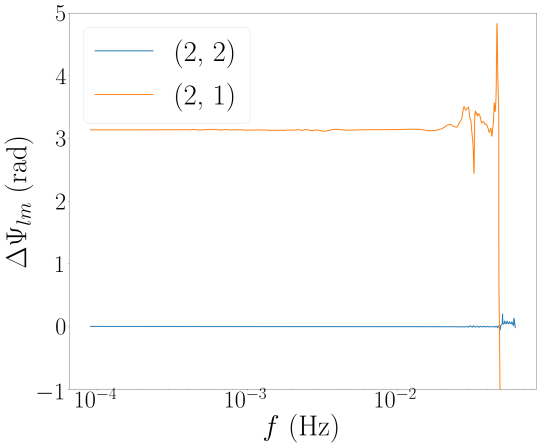

(d) Phase difference with NRHybSur3dq8.

Figure C.4: In the left panels we plot the amplitude of the (2,2) and (2,1) harmonics for systems with $M = 10^6 M_\odot$, $q = 1$ and $\chi_a = \pm 0.05$, and in the right panels we plot the difference in phase between the two signals for both harmonics. In the upper panels we use PhenomHM, whereas in the lower panels we use the NRHybSur3dq8 surrogate waveform. Only in the latter case we find the expected shift of π in the phase, suggesting that the phase of the harmonics other than the (2,2) in PhenomHM might be ill-defined.

if we vary the mass ratio (keeping the total SNR fixed): increasing q the SNR in higher harmonics increases, and we obtain one single mode, whereas as we decrease q, the three modes are "blurred". Finally, notice that this system has a rather low chirp mass, so it is merging in the high frequency end of LISA, as can be seen in figure C.6. If we increase the chirp mass of the system (keeping the total SNR fixed), the secondary maxima disappear. We have also checked that if we cut the signal before the merger (the cut is performed in time domain), the parameter estimation is barely affected. These last two points show that this multimodality is due to the inspiral portion of the signal and that it is resolved if we have enough SNR in the merger.

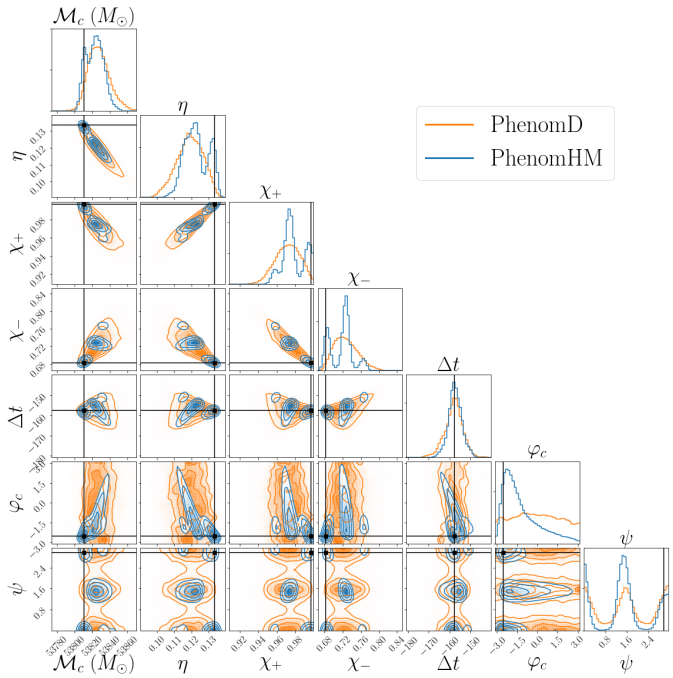

(a) Distribution of sampling parameters.

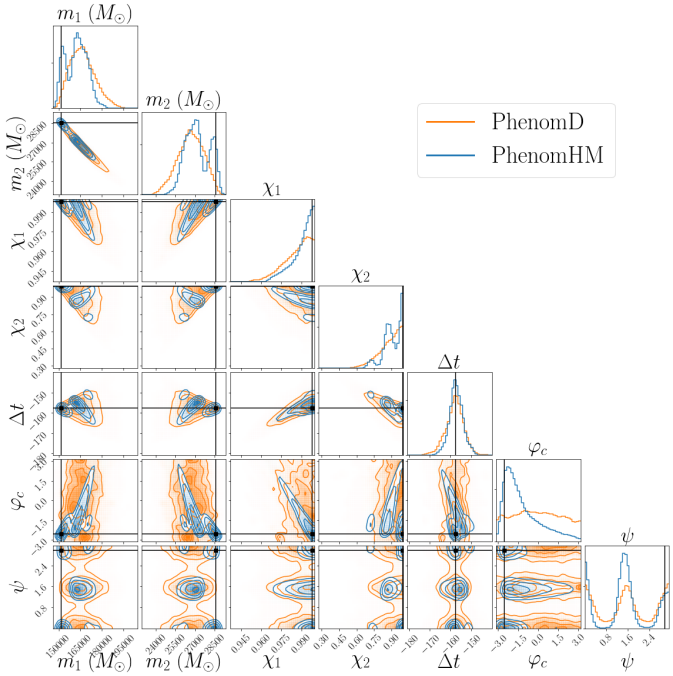

(b) Distribution of parameters entering the waveform computation.

Figure C.5: Comparison of inferred distributions for the *Highq* system when using PhenomD and PhenomHM. In the upper panel we show the distribution of parameteters used in the sampling, and in the lower panel of the original waveform parameters. When including higher harmonics, we find find two secondary maxima in intrinsic parameters in addition to the main mode, which are strongly correlated with φ_c and ψ. Black lines indicate the injection.

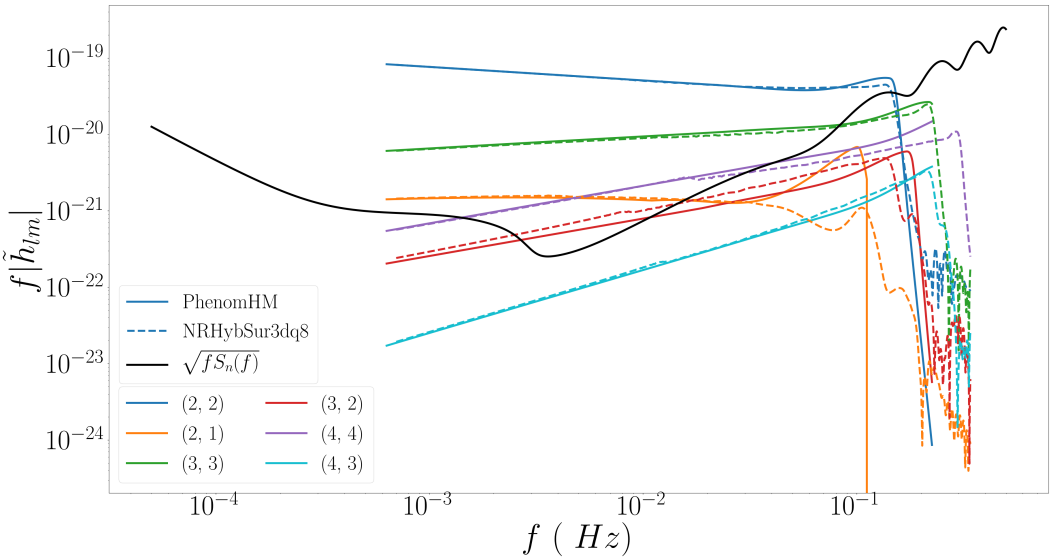

Figure C.6: Characteristic strain of several harmonics for the *Highq* system predicted by PhenomHM and the NRHybSur3dq8 surrogate waveform. The LISA response is not taken into account. The dark line shows the Proposal noise strain. Except for the (3,2) harmonic, the inspiral portion if the signal is in good agreement between the two waveforms.

We currently have no analytical explanation for this multimodality, but it seems to be related to correlations of masses and spins with the time to coalescence, the phase at coalescence and the polarisation. Indeed, if, as a test, we keep these three parameters fixed in the Bayesian analysis, we find no multimodality. When we include the time to coalescence and/or the phase at coalescence, the smaller mode (the leftmost in terms of χ_+) appears in addition to the true mode, and when we include any of these parameters together with the polarisation the central mode also appears.

We have verified that the multimodality is not due to the LISA response, so in order to check if this multimodality is not a waveform artefact, we intend to compute the faithfulness between the injection and surrounding points using different families of templates (e.g. PhenomXHM [527], EOB waveforms etc.), and check if that same multimodality is seen. The comparison between PhenomHM and the NRHybSur3dq8 surrogate waveform in figure C.6 shows clear discrepancies between the two models around the merger, but a reasonable agreement in the inspiral portion of the signal (except for the $(3, 2)$ harmonic), which is where the multimodality comes from. We cannot conclude how would the parameter estimation change using the NRHybSur3dq8 surrogate waveform, and it is yet to be understood if this multimodality is truly physical.

The two cases we have discussed are similar in the sense that the multimodality is due to higher harmonics having enough SNR to improve the parameter estimation relative to when using the $(2, \pm 2)$ harmonics only, but not enough to completely resolve partial degeneracies. We expect that third generation ground-based detectors could observe a similar multimodality to the first one we discussed, since SBHBs tend to have $q \sim 1$ and they will be observed with SNR figures of hundreds, as in the case we discussed. The second example stresses the importance of having trustable waveform models for binaries with large spins and unequal

	Equalq
m_1 ($M_\odot$)	6.4×10^5
m_2 ($M_\odot$)	6.3×10^5
$\mathcal{M}_c$ ($M_\odot$)	5.5×10^5
q	1.02
η	0.24998
χ_1	0.81
χ_2	0.91
χ_+	0.86
χ_-	-0.04
λ (rad)	5.5
β (rad)	0.6
ψ (rad)	2.1
φ (rad)	2.4
ι (rad)	2.5
D_L (Gpc)	40
z	4.2
SNR	654
$\text{SNR}_{(2,2}$	653
$\text{SNR}_{(2,1)}$	3

Table C.1: Properties of the *Equalq* system, together with the total SNR and the SNR of the (2,2) and (2,1) harmonics. Note that the total SNR is not the quadratic sum of the individual harmonics' SNRs due to nonzero inner products between different harmonics.

masses. Indeed, numerical simulations suggest that we might observe many such MBHBs (see section 6.2), and it has to be determined if the second example of multimodality we found is physical or a waveform artefact. Let us stress that performing parameter estimation for ~ 450 MBHB systems predicted by numerical simulations, we found a similar multimodality in ~ 10 cases.

	Highq
m_1 ($M_\odot$)	1.5×10^5
m_2 ($M_\odot$)	2.8×10^4
$\mathcal{M}_c$ ($M_\odot$)	5.3×10^4
q	5.3
η	0.13
χ_1	0.99797
χ_2	0.99311
χ_+	0.9972
χ_-	0.68
λ (rad)	5.0
β (rad)	0.007
ψ (rad)	1.95
φ (rad)	3.74
ι (rad)	1.755
D_L (Gpc)	88
z	8.5
SNR	29
$\text{SNR}_{(2,2}$	29
$\text{SNR}_{(3,3)}$	7
$\text{SNR}_{(4,4)}$	2

Table C.2: Properties of the *Highq* system, together with the total SNR and the SNR of the (2,2) and (3,3) and (4,4) harmonics.

Appendix D

Systematic biases due to a misevaluation of the selection function

The selection function used to obtain the results of section 6 was computed with equation (6.11). We generated 8×10^5 events for the LS and HS variants from the KDE and computed the terms Ξ(LS) and Ξ(HS) individually. In figure D.1 we compare this selection function with one obtained using only 2×10^3 points to compute each term. There is a clear discrepancy between the two functions, which reflects on the population inference, as can be seen in figure D.2. There, we compare the bias versus error on α plots obtained using each of these selection functions. Clearly, using too few points to compute the selection function leads to systematic biases, as can be seen by the fact that many more point are below the $\alpha_{\rm max} = \alpha_0$ line than above. We do not expect to observe thousands of MBHBs with LISA, but we have chosen this large number of events to emphasise this effect. Even for fewer events we could be biased due to a misevaluation of the selection function, and a large number of points from numerical simulations will be needed to mitigate this effect (see also [528]). Moreover, third generation ground-based detectors are expected to detect thousands of events, and will face this same issue.

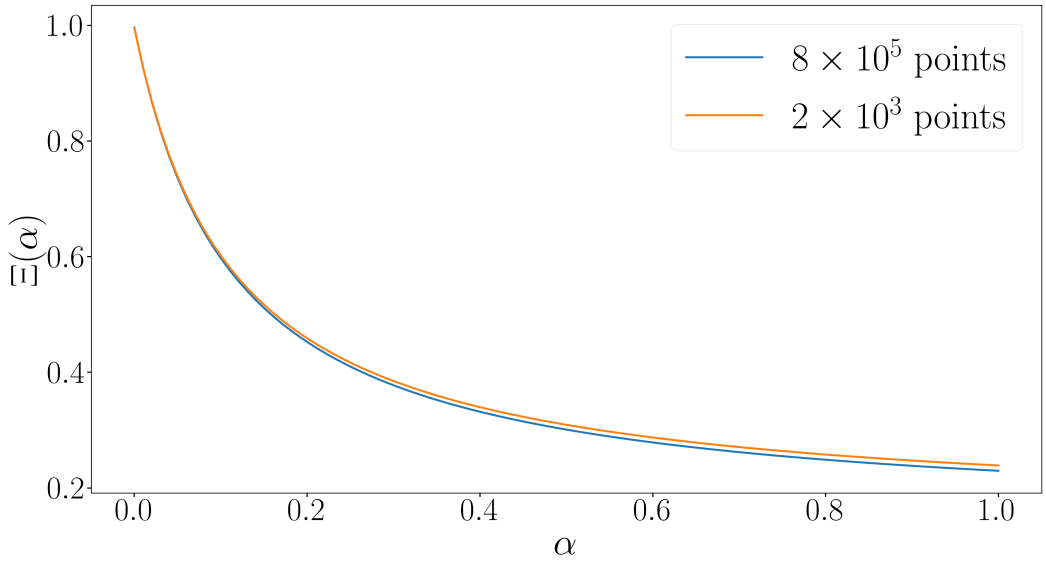

Figure D.1: Comparison between the selection functions obtained using different numbers of points to compute Ξ(LS) and Ξ(HS).

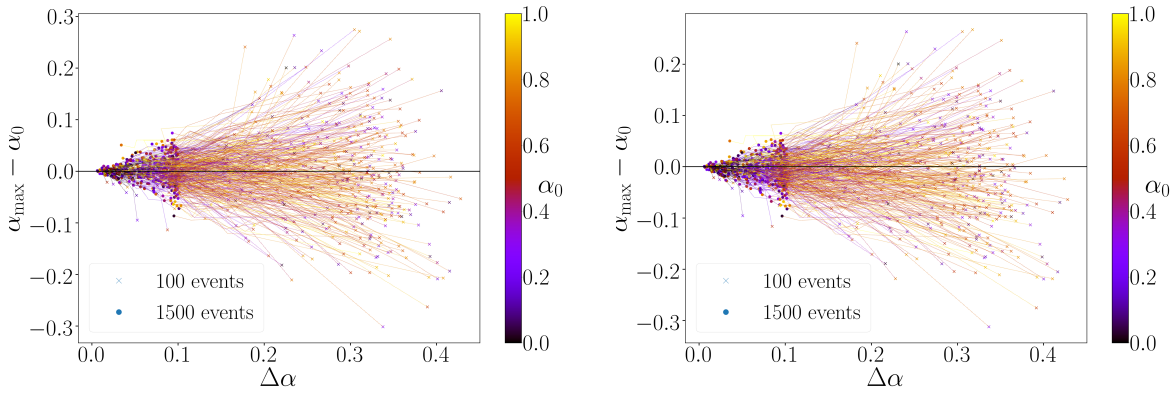

(a) We use 8×10^5 points to evaluate the selection function of the LS and HS variants.

(b) We use 2×10^3 points to evaluate the selection function of the LS and HS variants.

Figure D.2: Evolution of the bias and the error on α using the selection function in blue in figure D.1 (left panel) and the one in orange (right panel). We can clearly observe a systematic bias in the latter case, due to a misevaluation of the selection function.

Bibliography

[1] N. Aghanim *et al.*, "Planck 2018 results. VI. Cosmological parameters," 2018.

[2] J. Aasi *et al.*, "Advanced LIGO," *Class. Quant. Grav.*, vol. 32, p. 074001, 2015.

[3] B. P. Abbott *et al.*, "Observation of Gravitational Waves from a Binary Black Hole Merger," *Phys. Rev. Lett.*, vol. 116, no. 6, p. 061102, 2016.

[4] J. H. Taylor, L. A. Fowler, and P. M. McCulloch, "Measurements of general relativistic effects in the binary pulsar PSR 1913+16," *Nature*, vol. 277, pp. 437–440, 1979.

[5] A. Einstein, "Approximative Integration of the Field Equations of Gravitation," *Sitzungsber. Preuss. Akad. Wiss. Berlin (Math. Phys.)*, vol. 1916, pp. 688–696, 1916.

[6] F. Acernese *et al.*, "Advanced Virgo: a second-generation interferometric gravitational wave detector," *Class. Quant. Grav.*, vol. 32, no. 2, p. 024001, 2015.

[7] B. Abbott *et al.*, "GWTC-1: A Gravitational-Wave Transient Catalog of Compact Binary Mergers Observed by LIGO and Virgo during the First and Second Observing Runs," *Phys. Rev. X*, vol. 9, no. 3, p. 031040, 2019.

[8] R. Abbott *et al.*, "GWTC-2: Compact Binary Coalescences Observed by LIGO and Virgo During the First Half of the Third Observing Run," 10 2020.

[9] B. Abbott *et al.*, "GW170817: Observation of Gravitational Waves from a Binary Neutron Star Inspiral," *Phys. Rev. Lett.*, vol. 119, no. 16, p. 161101, 2017.

[10] B. P. Abbott *et al.*, "Multi-messenger Observations of a Binary Neutron Star Merger," *Astrophys. J. Lett.*, vol. 848, no. 2, p. L12, 2017.

[11] B. Abbott *et al.*, "Tests of General Relativity with the Binary Black Hole Signals from the LIGO-Virgo Catalog GWTC-1," *Phys. Rev. D*, vol. 100, no. 10, p. 104036, 2019.

[12] B. P. Abbott *et al.*, "Tests of general relativity with GW150914," *Phys. Rev. Lett.*, vol. 116, no. 22, p. 221101, 2016. [Erratum: Phys. Rev. Lett.121,no.12,129902(2018)].

[13] R. Abbott *et al.*, "Tests of General Relativity with Binary Black Holes from the second LIGO-Virgo Gravitational-Wave Transient Catalog," 10 2020.

[14] B. P. Abbott *et al.*, "Binary Black Hole Population Properties Inferred from the First and Second Observing Runs of Advanced LIGO and Advanced Virgo," *Astrophys. J. Lett.*, vol. 882, no. 2, p. L24, 2019.

[15] R. Abbott *et al.*, "Population Properties of Compact Objects from the Second LIGO-Virgo Gravitational-Wave Transient Catalog," *Astrophys. J. Lett.*, vol. 913, no. 1, p. L7, 2021.

[16] K. Popper, *The Logic of Scientific Discovery*. ISSR library, Routledge, 2002.

[17] K. Somiya, "Detector configuration of KAGRA: The Japanese cryogenic gravitational-wave detector," *Class. Quant. Grav.*, vol. 29, p. 124007, 2012.

[18] Y. Aso, Y. Michimura, K. Somiya, M. Ando, O. Miyakawa, T. Sekiguchi, D. Tatsumi, and H. Yamamoto, "Interferometer design of the KAGRA gravitational wave detector," *Phys. Rev. D*, vol. 88, no. 4, p. 043007, 2013.

[19] C. S. Unnikrishnan, "IndIGO and LIGO-India: Scope and plans for gravitational wave research and precision metrology in India," *Int. J. Mod. Phys. D*, vol. 22, p. 1341010, 2013.

[20] S. Hild *et al.*, "Sensitivity Studies for Third-Generation Gravitational Wave Observatories," *Class. Quant. Grav.*, vol. 28, p. 094013, 2011.

[21] M. Punturo *et al.*, "The Einstein Telescope: A third-generation gravitational wave observatory," *Class. Quant. Grav.*, vol. 27, p. 194002, 2010.

[22] S. Ballmer and V. Mandic, "New Technologies in Gravitational-Wave Detection," *Ann. Rev. Nucl. Part. Sci.*, vol. 65, pp. 555–577, 2015.

[23] B. P. Abbott *et al.*, "Exploring the Sensitivity of Next Generation Gravitational Wave Detectors," *Class. Quant. Grav.*, vol. 34, no. 4, p. 044001, 2017.

[24] R. S. Foster and D. C. Backer, "Constructing a Pulsar Timing Array," *Astrophys. J.*, vol. 361, p. 300, 1990.

[25] G. Hobbs *et al.*, "The international pulsar timing array project: using pulsars as a gravitational wave detector," *Class. Quant. Grav.*, vol. 27, p. 084013, 2010.

[26] A. Sesana, A. Vecchio, and C. N. Colacino, "The stochastic gravitational-wave background from massive black hole binary systems: implications for observations with Pulsar Timing Arrays," *Mon. Not. Roy. Astron. Soc.*, vol. 390, p. 192, 2008.

[27] Z. Arzoumanian *et al.*, "The NANOGrav 12.5 yr Data Set: Search for an Isotropic Stochastic Gravitational-wave Background," *Astrophys. J. Lett.*, vol. 905, no. 2, p. L34, 2020.

[28] G. Janssen *et al.*, "Gravitational wave astronomy with the SKA," *PoS*, vol. AASKA14, p. 037, 2015.

[29] H. Audley *et al.*, "Laser Interferometer Space Antenna," 2017.

[30] A. Klein *et al.*, "Science with the space-based interferometer eLISA: Supermassive black hole binaries," *Phys. Rev.*, vol. D93, no. 2, p. 024003, 2016.

[31] V. Korol, E. M. Rossi, P. J. Groot, G. Nelemans, S. Toonen, and A. G. Brown, "Prospects for detection of detached double white dwarf binaries with Gaia, LSST and LISA," *Mon. Not. Roy. Astron. Soc.*, vol. 470, no. 2, pp. 1894–1910, 2017.

[32] A. Sesana, "Prospects for Multiband Gravitational-Wave Astronomy after GW150914," *Phys. Rev. Lett.*, vol. 116, no. 23, p. 231102, 2016.

[33] A. Toubiana, S. Marsat, S. Babak, J. Baker, and T. Dal Canton, "Parameter estimation of stellar-mass black hole binaries with LISA," *Phys. Rev. D*, vol. 102, p. 124037, 2020.

[34] A. Toubiana, S. Marsat, S. Babak, E. Barausse, and J. Baker, "Tests of general relativity with stellar-mass black hole binaries observed by LISA," *Phys. Rev. D*, vol. 101, no. 10, p. 104038, 2020.

[35] A. Toubiana, S. Babak, E. Barausse, and L. Lehner, "Modeling gravitational waves from exotic compact objects," *Phys. Rev. D*, vol. 103, no. 6, p. 064042, 2021.

[36] A. Caputo, L. Sberna, A. Toubiana, S. Babak, E. Barausse, S. Marsat, and P. Pani, "Gravitational-wave detection and parameter estimation for accreting black-hole binaries and their electromagnetic counterpart," *Astrophys. J.*, vol. 892, no. 2, p. 90, 2020.

[37] A. Toubiana *et al.*, "Detectable environmental effects in GW190521-like black-hole binaries with LISA," *Phys. Rev. Lett.*, vol. 126, no. 10, p. 101105, 2021.

[38] L. Sberna, A. Toubiana, and M. C. Miller, "Golden galactic binaries for LISA: mass-transferring white dwarf black hole binaries," *Astrophys. J.*, vol. 908, no. 1, p. 1, 2021.

[39] A. Toubiana, K. W. K. Wong, S. Babak, E. Barausse, E. Berti, J. R. Gair, S. Marsat, and S. R. Taylor, "Discriminating between different scenarios for the formation and evolution of massive black holes with LISA," *Phys. Rev. D*, vol. 104, no. 8, p. 083027, 2021.

[40] Z. Carson, "Probing Fundamental Physics with Gravitational Waves," other thesis, 10 2020.

[41] P. S. Laplace, *A Treatise in Celestial Mechanics*. 1822.

[42] A. Einstein, "On the electrodynamics of moving bodies," *Annalen Phys.*, vol. 17, pp. 891–921, 1905.

[43] A. Einstein, "Grundgedanken der allgemeinen relativitätstheorie und anwendung dieser theorie in astronomie.," pp. 315–315, 1915.

[44] J. Wheeler and K. Ford, "Geons, black holes and quantum foam: A life in physics," *American Journal of Physics*, vol. 68, 06 2000.

[45] A. Einstein, "The Field Equations of Gravitation," *Sitzungsber. Preuss. Akad. Wiss. Berlin (Math. Phys.)*, vol. 1915, pp. 844–847, 1915.

[46] C. W. Misner, K. S. Thorne, and J. A. Wheeler, *Gravitation*. San Francisco: W. H. Freeman, 1973.

[47] S. Chandrasekhar, *The mathematical theory of black holes*. 1985.

[48] M. Maggiore, *Gravitational Waves. Vol. 1: Theory and Experiments*. Oxford Master Series in Physics, Oxford University Press, 2007.

[49] A. Einstein, "The Foundation of the General Theory of Relativity," *Annalen Phys.*, vol. 49, no. 7, pp. 769–822, 1916.

[50] A. Einstein, "Explanation of the Perihelion Motion of Mercury from the General Theory of Relativity," *Sitzungsber. Preuss. Akad. Wiss. Berlin (Math. Phys.)*, vol. 1915, pp. 831–839, 1915.

[51] F. W. Dyson, A. S. Eddington, and C. Davidson, "A Determination of the Deflection of Light by the Sun's Gravitational Field, from Observations Made at the Total Eclipse of May 29, 1919," *Phil. Trans. Roy. Soc. Lond. A*, vol. 220, pp. 291–333, 1920.

[52] C. M. Will, "The Confrontation between General Relativity and Experiment," *Living Rev. Rel.*, vol. 17, p. 4, 2014.

[53] E. Berti *et al.*, "Testing General Relativity with Present and Future Astrophysical Observations," *Class. Quant. Grav.*, vol. 32, p. 243001, 2015.

[54] K. Koyama, "Cosmological Tests of Modified Gravity," *Rept. Prog. Phys.*, vol. 79, no. 4, p. 046902, 2016.

[55] F. Zwicky, "On the Masses of Nebulae and of Clusters of Nebulae," *Astrophys. J.*, vol. 86, pp. 217–246, 1937.

[56] A. G. Riess *et al.*, "Observational evidence from supernovae for an accelerating universe and a cosmological constant," *Astron. J.*, vol. 116, pp. 1009–1038, 1998.

[57] S. W. Hawking, "Breakdown of Predictability in Gravitational Collapse," *Phys. Rev. D*, vol. 14, pp. 2460–2473, 1976.

[58] D. Marolf, "The black hole information problem: past, present, and future," *Reports on Progress in Physics*, vol. 80, p. 092001, Jul 2017.

[59] A. Einstein, "Über Gravitationswellen," *Sitzungsber. Preuss. Akad. Wiss. Berlin (Math. Phys.)*, vol. 1918, pp. 154–167, 1918.

[60] H. Bondi, "Plane gravitational waves in general relativity," *Nature*, vol. 179, pp. 1072–1073, 1957.

[61] H. Bondi, F. A. E. Pirani, and I. Robinson, "Gravitational waves in general relativity. 3. Exact plane waves," *Proc. Roy. Soc. Lond. A*, vol. 251, pp. 519–533, 1959.

[62] F. A. E. Pirani, "Invariant formulation of gravitational radiation theory," *Phys. Rev.*, vol. 105, pp. 1089–1099, 1957.

[63] R. A. Hulse and J. H. Taylor, "Discovery of a pulsar in a binary system," *Astrophys. J. Lett.*, vol. 195, pp. L51–L53, 1975.

[64] R. N. Manchester, G. B. Hobbs, A. Teoh, and M. Hobbs, "The Australia Telescope National Facility pulsar catalogue," *Astron. J.*, vol. 129, p. 1993, 2005.

[65] F. Özel and P. Freire, "Masses, Radii, and the Equation of State of Neutron Stars," *Ann. Rev. Astron. Astrophys.*, vol. 54, pp. 401–440, 2016.

[66] K. Schwarzschild, "On the gravitational field of a mass point according to Einstein's theory," *Sitzungsber. Preuss. Akad. Wiss. Berlin (Math. Phys.)*, vol. 1916, pp. 189–196, 1916.

[67] J. Michell, "On the Means of Discovering the Distance, Magnitude, &c. of the Fixed Stars, in Consequence of the Diminution of the Velocity of Their Light, in Case Such a Diminution Should be Found to Take Place in any of Them, and Such Other Data Should be Procured from Observations, as Would be Farther Necessary for That Purpose.," *Phil. Trans. Roy. Soc. Lond.*, vol. 74, pp. 35–57, 1784.

[68] S. Chandrasekhar, "The maximum mass of ideal white dwarfs," *Astrophys. J.*, vol. 74, pp. 81–82, 1931.

[69] J. R. Oppenheimer and G. M. Volkoff, "On Massive neutron cores," *Phys. Rev.*, vol. 55, pp. 374–381, 1939.

[70] R. C. Tolman, "Static solutions of Einstein's field equations for spheres of fluid," *Phys. Rev.*, vol. 55, pp. 364–373, 1939.

[71] M. Schmidt, "3C 273 : A Star-Like Object with Large Red-Shift," *Nature*, vol. 197, no. 4872, p. 1040, 1963.

[72] D. Lynden-Bell, "Galactic nuclei as collapsed old quasars," *Nature*, vol. 223, p. 690, 1969.

[73] R. P. Kerr, "Gravitational field of a spinning mass as an example of algebraically special metrics," *Phys. Rev. Lett.*, vol. 11, pp. 237–238, 1963.

[74] S. W. Hawking and R. Penrose, "The Singularities of gravitational collapse and cosmology," *Proc. Roy. Soc. Lond. A*, vol. 314, pp. 529–548, 1970.

[75] A. Eckart and R. Genzel, "Observations of stellar proper motions near the Galactic Centre," *Nature*, vol. 383, pp. 415–417, 1996.

[76] A. M. Ghez, B. L. Klein, M. Morris, and E. E. Becklin, "High proper motion stars in the vicinity of Sgr A*: Evidence for a supermassive black hole at the center of our galaxy," *Astrophys. J.*, vol. 509, pp. 678–686, 1998.

[77] M. Bauböck *et al.*, "Modeling the orbital motion of Sgr A*'s near-infrared flares," *Astron. Astrophys.*, vol. 635, p. A143, 2020.

[78] K. Akiyama *et al.*, "First M87 Event Horizon Telescope Results. IV. Imaging the Central Supermassive Black Hole," *Astrophys. J. Lett.*, vol. 875, no. 1, p. L4, 2019.

[79] A. Le Tiec and J. Novak, *Theory of Gravitational Waves*, pp. 1–41. 2017.

[80] V. Baibhav, E. Berti, V. Cardoso, and G. Khanna, "Black Hole Spectroscopy: Systematic Errors and Ringdown Energy Estimates," *Phys. Rev. D*, vol. 97, no. 4, p. 044048, 2018.

[81] M. Giesler, M. Isi, M. A. Scheel, and S. Teukolsky, "Black Hole Ringdown: The Importance of Overtones," *Phys. Rev. X*, vol. 9, no. 4, p. 041060, 2019.

[82] X. Jiménez Forteza, S. Bhagwat, P. Pani, and V. Ferrari, "Spectroscopy of binary black hole ringdown using overtones and angular modes," *Phys. Rev. D*, vol. 102, no. 4, p. 044053, 2020.

[83] S. Bhagwat, M. Okounkova, S. W. Ballmer, D. A. Brown, M. Giesler, M. A. Scheel, and S. A. Teukolsky, "On choosing the start time of binary black hole ringdowns," *Phys. Rev. D*, vol. 97, no. 10, p. 104065, 2018.

[84] L. Blanchet, "Gravitational Radiation from Post-Newtonian Sources and Inspiralling Compact Binaries," *Living Rev. Rel.*, vol. 17, p. 2, 2014.

[85] C. Cutler and E. E. Flanagan, "Gravitational waves from merging compact binaries: How accurately can one extract the binary's parameters from the inspiral wave form?," *Phys. Rev.*, vol. D49, pp. 2658–2697, 1994.

[86] A. Buonanno, "Gravitational waves," in *Les Houches Summer School - Session 86: Particle Physics and Cosmology: The Fabric of Spacetime Les Houches, France, July 31-August 25, 2006*, 2007.

[87] B. Mulgrew, "The Stationary Phase Approximation, Time-Frequency Decomposition and Auditory Processing," *IEEE Transactions on Signal Processing*, vol. 62, pp. 56–68, Jan 2014.

[88] H. A. Lorentz and J. Droste, *The Motion of a System of Bodies under the Influence of their Mutual Attraction, According to Einstein's Theory*, pp. 330–355. Dordrecht: Springer Netherlands, 1937.

[89] C. M. Will, *Theory and Experiment in Gravitational Physics*. Cambridge University Press, 9 2018.

[90] S. A. Teukolsky, "Rotating black holes - separable wave equations for gravitational and electromagnetic perturbations," *Phys. Rev. Lett.*, vol. 29, pp. 1114–1118, 1972.

[91] E. Seidel and S. Iyer, "BLACK HOLE NORMAL MODES: A WKB APPROACH. 4. KERR BLACK HOLES," *Phys. Rev. D*, vol. 41, pp. 374–382, 1990.

[92] E. Berti, V. Cardoso, and A. O. Starinets, "Quasinormal modes of black holes and black branes," *Class. Quant. Grav.*, vol. 26, p. 163001, 2009.

[93] V. Cardoso, L. Gualtieri, C. Herdeiro, and U. Sperhake, "Exploring New Physics Frontiers Through Numerical Relativity," *Living Rev. Relativity*, vol. 18, p. 1, 2015.

[94] F. Pretorius, "Evolution of binary black hole spacetimes," *Phys. Rev. Lett.*, vol. 95, p. 121101, 2005.

[95] M. Campanelli, C. O. Lousto, P. Marronetti, and Y. Zlochower, "Accurate evolutions of orbiting black-hole binaries without excision," *Phys. Rev. Lett.*, vol. 96, p. 111101, 2006.

[96] J. G. Baker, J. Centrella, D.-I. Choi, M. Koppitz, and J. van Meter, "Gravitational wave extraction from an inspiraling configuration of merging black holes," *Phys. Rev. Lett.*, vol. 96, p. 111102, 2006.

[97] B. Szilágyi, J. Blackman, A. Buonanno, A. Taracchini, H. P. Pfeiffer, M. A. Scheel, T. Chu, L. E. Kidder, and Y. Pan, "Approaching the Post-Newtonian Regime with Numerical Relativity: A Compact-Object Binary Simulation Spanning 350 Gravitational-Wave Cycles," *Phys. Rev. Lett.*, vol. 115, no. 3, p. 031102, 2015.

[98] A. Buonanno and T. Damour, "Effective one-body approach to general relativistic two-body dynamics," *Phys. Rev. D*, vol. 59, p. 084006, 1999.

[99] A. Buonanno and T. Damour, "Transition from inspiral to plunge in binary black hole coalescences," *Phys. Rev. D*, vol. 62, p. 064015, 2000.

[100] A. Bohé *et al.*, "Improved effective-one-body model of spinning, nonprecessing binary black holes for the era of gravitational-wave astrophysics with advanced detectors," *Phys. Rev.*, vol. D95, no. 4, p. 044028, 2017.

[101] T. Damour and A. Nagar, "A new analytic representation of the ringdown waveform of coalescing spinning black hole binaries," *Phys. Rev.*, vol. D90, no. 2, p. 024054, 2014.

[102] T. Damour, B. R. Iyer, P. Jaranowski, and B. S. Sathyaprakash, "Gravitational waves from black hole binary inspiral and merger: The Span of third postNewtonian effective one-body templates," *Phys. Rev. D*, vol. 67, p. 064028, 2003.

[103] A. Buonanno, Y. Pan, J. G. Baker, J. Centrella, B. J. Kelly, S. T. McWilliams, and J. R. van Meter, "Toward faithful templates for non-spinning binary black holes using the effective-one-body approach," *Phys. Rev. D*, vol. 76, p. 104049, 2007.

[104] S. Ossokine *et al.*, "Multipolar Effective-One-Body Waveforms for Precessing Binary Black Holes: Construction and Validation," *Phys. Rev. D*, vol. 102, no. 4, p. 044055, 2020.

[105] J. Blackman, S. E. Field, C. R. Galley, B. Szilágyi, M. A. Scheel, M. Tiglio, and D. A. Hemberger, "Fast and Accurate Prediction of Numerical Relativity Waveforms from Binary Black Hole Coalescences Using Surrogate Models," *Phys. Rev. Lett.*, vol. 115, no. 12, p. 121102, 2015.

[106] V. Varma, S. E. Field, M. A. Scheel, J. Blackman, D. Gerosa, L. C. Stein, L. E. Kidder, and H. P. Pfeiffer, "Surrogate models for precessing binary black hole simulations with unequal masses," *Phys. Rev. Research.*, vol. 1, p. 033015, 2019.

[107] V. Varma, S. E. Field, M. A. Scheel, J. Blackman, L. E. Kidder, and H. P. Pfeiffer, "Surrogate model of hybridized numerical relativity binary black hole waveforms," *Phys. Rev. D*, vol. 99, no. 6, p. 064045, 2019.

[108] P. Ajith *et al.*, "A Template bank for gravitational waveforms from coalescing binary black holes. I. Non-spinning binaries," *Phys. Rev. D*, vol. 77, p. 104017, 2008. [Erratum: Phys.Rev.D 79, 129901 (2009)].

[109] P. Ajith *et al.*, "Inspiral-merger-ringdown waveforms for black-hole binaries with non-precessing spins," *Phys. Rev. Lett.*, vol. 106, p. 241101, 2011.

[110] L. Santamaria *et al.*, "Matching post-Newtonian and numerical relativity waveforms: systematic errors and a new phenomenological model for non-precessing black hole binaries," *Phys. Rev. D*, vol. 82, p. 064016, 2010.

[111] S. Husa, S. Khan, M. Hannam, M. Pürrer, F. Ohme, X. Jiménez Forteza, and A. Bohé, "Frequency-domain gravitational waves from nonprecessing black-hole binaries. I. New numerical waveforms and anatomy of the signal," *Phys. Rev.*, vol. D93, no. 4, p. 044006, 2016.

[112] S. Khan, S. Husa, M. Hannam, F. Ohme, M. Pürrer, X. Jiménez Forteza, and A. Bohé, "Frequency-domain gravitational waves from nonprecessing black-hole binaries. II. A phenomenological model for the advanced detector era," *Phys. Rev.*, vol. D93, no. 4, p. 044007, 2016.

[113] L. London, S. Khan, E. Fauchon-Jones, C. García, M. Hannam, S. Husa, X. Jiménez-Forteza, C. Kalaghatgi, F. Ohme, and F. Pannarale, "First higher-multipole model of gravitational waves from spinning and coalescing black-hole binaries," *Phys. Rev. Lett.*, vol. 120, no. 16, p. 161102, 2018.

[114] T. Damour, "The Motion of Compact Bodies and Gravitational Radiation," *Fundam. Theor. Phys.*, vol. 9, pp. 89–106, 1984.

[115] E. E. Flanagan and T. Hinderer, "Constraining neutron star tidal Love numbers with gravitational wave detectors," *Phys. Rev. D*, vol. 77, p. 021502, 2008.

[116] L. Wade, J. D. Creighton, E. Ochsner, B. D. Lackey, B. F. Farr, T. B. Littenberg, and V. Raymond, "Systematic and statistical errors in a bayesian approach to the estimation of the neutron-star equation of state using advanced gravitational wave detectors," *Phys. Rev. D*, vol. 89, no. 10, p. 103012, 2014.

[117] B. P. Abbott *et al.*, "GW151226: Observation of Gravitational Waves from a 22-Solar-Mass Binary Black Hole Coalescence," *Phys. Rev. Lett.*, vol. 116, no. 24, p. 241103, 2016.

[118] N. Yunes, K. Yagi, and F. Pretorius, "Theoretical Physics Implications of the Binary Black-Hole Mergers GW150914 and GW151226," *Phys. Rev.*, vol. D94, no. 8, p. 084002, 2016.

[119] D. Lovelock, "The Einstein tensor and its generalizations," *J. Math. Phys.*, vol. 12, pp. 498–501, 1971.

[120] D. Lovelock, "The four-dimensionality of space and the einstein tensor," *J. Math. Phys.*, vol. 13, pp. 874–876, 1972.

[121] M. Fierz, "On the physical interpretation of P.Jordan's extended theory of gravitation," *Helv. Phys. Acta*, vol. 29, pp. 128–134, 1956.

[122] P. Jordan, "The present state of Dirac's cosmological hypothesis," *Z. Phys.*, vol. 157, pp. 112–121, 1959.

[123] C. Brans and R. H. Dicke, "Mach's principle and a relativistic theory of gravitation," *Phys. Rev.*, vol. 124, pp. 925–935, 1961. [,142(1961)].

[124] B. Bertotti, L. Iess, and P. Tortora, "A test of general relativity using radio links with the Cassini spacecraft," *Nature*, vol. 425, pp. 374–376, 2003.

[125] C. M. Will and H. W. Zaglauer, "Gravitational Radiation, Close Binary Systems, and the Brans-dicke Theory of Gravity," *Astrophys. J.*, vol. 346, p. 366, 1989.

[126] T. Damour and G. Esposito-Farese, "Tensor multiscalar theories of gravitation," *Class. Quant. Grav.*, vol. 9, pp. 2093–2176, 1992.

[127] Y. Fujii and K. Maeda, *The scalar-tensor theory of gravitation*. Cambridge Monographs on Mathematical Physics, Cambridge University Press, 7 2007.

[128] D. M. Eardley, "Observable effects of a scalar gravitational field in a binary pulsar.," *Astrophys. J. Lett.*, vol. 196, pp. L59–L62, 1975.

[129] K. Nordtvedt, "Equivalence Principle for Massive Bodies Including Rotational Energy and Radiation Pressure," *Phys. Rev.*, vol. 180, pp. 1293–1298, 1969.

[130] P. G. Roll, R. Krotkov, and R. H. Dicke, "The Equivalence of inertial and passive gravitational mass," *Annals Phys.*, vol. 26, pp. 442–517, 1964.

[131] T. Damour and G. Esposito-Farese, "Nonperturbative strong field effects in tensor - scalar theories of gravitation," *Phys. Rev. Lett.*, vol. 70, pp. 2220–2223, 1993.

[132] T. Damour and G. Esposito-Farese, "Tensor - scalar gravity and binary pulsar experiments," *Phys. Rev.*, vol. D54, pp. 1474–1491, 1996.

[133] P. C. C. Freire, N. Wex, G. Esposito-Farese, J. P. W. Verbiest, M. Bailes, B. A. Jacoby, M. Kramer, I. H. Stairs, J. Antoniadis, and G. H. Janssen, "The relativistic pulsar-white dwarf binary PSR J1738+0333 II. The most stringent test of scalar-tensor gravity," *Mon. Not. Roy. Astron. Soc.*, vol. 423, p. 3328, 2012.

[134] N. Wex, "Testing Relativistic Gravity with Radio Pulsars," 2 2014.

[135] S. W. Hawking, "Black holes in the Brans-Dicke theory of gravitation," *Commun. Math. Phys.*, vol. 25, pp. 167–171, 1972.

[136] J. D. Bekenstein, "Novel ''no-scalar-hair'' theorem for black holes," *Phys. Rev. D*, vol. 51, no. 12, p. 6608, 1995.

[137] T. P. Sotiriou and S.-Y. Zhou, "Black hole hair in generalized scalar-tensor gravity," *Phys. Rev. Lett.*, vol. 112, p. 251102, 2014.

[138] K. Yagi, L. C. Stein, and N. Yunes, "Challenging the Presence of Scalar Charge and Dipolar Radiation in Binary Pulsars," *Phys. Rev.*, vol. D93, no. 2, p. 024010, 2016.

[139] E. Barausse and K. Yagi, "Gravitation-Wave Emission in Shift-Symmetric Horndeski Theories," *Phys. Rev. Lett.*, vol. 115, no. 21, p. 211105, 2015.

[140] H. O. Silva, J. Sakstein, L. Gualtieri, T. P. Sotiriou, and E. Berti, "Spontaneous scalarization of black holes and compact stars from a Gauss-Bonnet coupling," *Phys. Rev. Lett.*, vol. 120, no. 13, p. 131104, 2018.

[141] C. A. R. Herdeiro, E. Radu, N. Sanchis-Gual, and J. A. Font, "Spontaneous Scalarization of Charged Black Holes," *Phys. Rev. Lett.*, vol. 121, no. 10, p. 101102, 2018.

[142] F.-L. Julié, "Gravitational radiation from compact binary systems in Einstein-Maxwell-dilaton theories," *JCAP*, vol. 1810, p. 033, 2018.

[143] F.-L. Julié and E. Berti, "Post-Newtonian dynamics and black hole thermodynamics in Einstein-scalar-Gauss-Bonnet gravity," *Phys. Rev. D*, vol. 100, no. 10, p. 104061, 2019.

[144] J. Healy, T. Bode, R. Haas, E. Pazos, P. Laguna, D. Shoemaker, and N. Yunes, "Late Inspiral and Merger of Binary Black Holes in Scalar-Tensor Theories of Gravity," *Class. Quant. Grav.*, vol. 29, p. 232002, 2012.

[145] M. W. Horbatsch and C. P. Burgess, "Cosmic Black-Hole Hair Growth and Quasar OJ287," *JCAP*, vol. 1205, p. 010, 2012.

[146] E. Berti, V. Cardoso, L. Gualtieri, M. Horbatsch, and U. Sperhake, "Numerical simulations of single and binary black holes in scalar-tensor theories: circumventing the no-hair theorem," *Phys. Rev.*, vol. D87, no. 12, p. 124020, 2013.

[147] Z. Cao, P. Galaviz, and L.-F. Li, "Binary black hole mergers in $f(R)$ theory," *Phys. Rev. D*, vol. 87, no. 10, p. 104029, 2013.

[148] E. W. Hirschmann, L. Lehner, S. L. Liebling, and C. Palenzuela, "Black Hole Dynamics in Einstein-Maxwell-Dilaton Theory," *Phys. Rev. D*, vol. 97, no. 6, p. 064032, 2018.

[149] H. Witek, L. Gualtieri, P. Pani, and T. P. Sotiriou, "Black holes and binary mergers in scalar Gauss-Bonnet gravity: scalar field dynamics," *Phys. Rev. D*, vol. 99, no. 6, p. 064035, 2019.

[150] M. Okounkova, "Numerical relativity simulation of GW150914 in Einstein dilaton Gauss-Bonnet gravity," *Phys. Rev. D*, vol. 102, no. 8, p. 084046, 2020.

[151] M. Okounkova, L. C. Stein, J. Moxon, M. A. Scheel, and S. A. Teukolsky, "Numerical relativity simulation of GW150914 beyond general relativity," *Phys. Rev. D*, vol. 101, no. 10, p. 104016, 2020.

[152] J. L. Blázquez-Salcedo, F. S. Khoo, and J. Kunz, "Quasinormal modes of Einstein-Gauss-Bonnet-dilaton black holes," *Phys. Rev. D*, vol. 96, no. 6, p. 064008, 2017.

[153] J. L. Blázquez-Salcedo, C. F. B. Macedo, V. Cardoso, V. Ferrari, L. Gualtieri, F. S. Khoo, J. Kunz, and P. Pani, "Perturbed black holes in Einstein-dilaton-Gauss-Bonnet gravity: Stability, ringdown, and gravitational-wave emission," *Phys. Rev. D*, vol. 94, no. 10, p. 104024, 2016.

[154] C. Molina, P. Pani, V. Cardoso, and L. Gualtieri, "Gravitational signature of Schwarzschild black holes in dynamical Chern-Simons gravity," *Phys. Rev. D*, vol. 81, p. 124021, 2010.

[155] V. Cardoso and L. Gualtieri, "Perturbations of Schwarzschild black holes in Dynamical Chern-Simons modified gravity," *Phys. Rev. D*, vol. 80, p. 064008, 2009. [Erratum: Phys.Rev.D 81, 089903 (2010)].

[156] R. N. Lang, "Compact binary systems in scalar-tensor gravity. II. Tensor gravitational waves to second post-Newtonian order," *Phys. Rev. D*, vol. 89, no. 8, p. 084014, 2014.

[157] N. Sennett, S. Marsat, and A. Buonanno, "Gravitational waveforms in scalar-tensor gravity at 2PN relative order," *Phys. Rev. D*, vol. 94, no. 8, p. 084003, 2016.

[158] A. Vilenkin and E. P. S. Shellard, *Cosmic Strings and Other Topological Defects*. Cambridge University Press, 7 2000.

[159] M. B. Hindmarsh and T. W. B. Kibble, "Cosmic strings," *Rept. Prog. Phys.*, vol. 58, pp. 477–562, 1995.

[160] C. Caprini and D. G. Figueroa, "Cosmological Backgrounds of Gravitational Waves," *Class. Quant. Grav.*, vol. 35, no. 16, p. 163001, 2018.

[161] G. Boileau, N. Christensen, R. Meyer, and N. J. Cornish, "Spectral separation of the stochastic gravitational-wave background for LISA: observing both cosmological and astrophysical backgrounds," 11 2020.

[162] R. Abbott *et al.*, "Upper Limits on the Isotropic Gravitational-Wave Background from Advanced LIGO's and Advanced Virgo's Third Observing Run," 1 2021.

[163] R. Abbott *et al.*, "Constraints on cosmic strings using data from the third Advanced LIGO-Virgo observing run," 1 2021.

[164] B. P. Abbott *et al.*, "Search for the isotropic stochastic background using data from Advanced LIGO's second observing run," *Phys. Rev. D*, vol. 100, no. 6, p. 061101, 2019.

[165] Z. Arzoumanian *et al.*, "The NANOGrav 11-year Data Set: Pulsar-timing Constraints On The Stochastic Gravitational-wave Background," *Astrophys. J.*, vol. 859, no. 1, p. 47, 2018.

[166] J. Ellis and M. Lewicki, "Cosmic String Interpretation of NANOGrav Pulsar Timing Data," *Phys. Rev. Lett.*, vol. 126, no. 4, p. 041304, 2021.

[167] S. Blasi, V. Brdar, and K. Schmitz, "Has NANOGrav found first evidence for cosmic strings?," *Phys. Rev. Lett.*, vol. 126, no. 4, p. 041305, 2021.

[168] W. Buchmuller, V. Domcke, and K. Schmitz, "From NANOGrav to LIGO with metastable cosmic strings," *Phys. Lett. B*, vol. 811, p. 135914, 2020.

[169] C. J. Moore, R. H. Cole, and C. P. L. Berry, "Gravitational-wave sensitivity curves," *Class. Quant. Grav.*, vol. 32, no. 1, p. 015014, 2015.

[170] "Gwplotter." `http://gwplotter.com/`.

[171] M. Sieniawska and M. Bejger, "Continuous gravitational waves from neutron stars: current status and prospects," *Universe*, vol. 5, no. 11, p. 217, 2019.

[172] R. Abbott *et al.*, "All-sky search in early O3 LIGO data for continuous gravitational-wave signals from unknown neutron stars in binary systems," 12 2020.

[173] B. P. Abbott *et al.*, "All-sky search for continuous gravitational waves from isolated neutron stars using Advanced LIGO O2 data," *Phys. Rev. D*, vol. 100, no. 2, p. 024004, 2019.

[174] G. Nelemans, L. R. Yungelson, and S. F. Portegies Zwart, "The gravitational wave signal from the galactic disk population of binaries containing two compact objects," *Astron. Astrophys.*, vol. 375, pp. 890–898, 2001.

[175] T. Kupfer, V. Korol, S. Shah, G. Nelemans, T. R. Marsh, G. Ramsay, P. J. Groot, D. T. H. Steeghs, and E. M. Rossi, "LISA verification binaries with updated distances from Gaia Data Release 2," *Mon. Not. Roy. Astron. Soc.*, vol. 480, no. 1, pp. 302–309, 2018.

[176] K. Breivik, K. Kremer, M. Bueno, S. L. Larson, S. Coughlin, and V. Kalogera, "Characterizing Accreting Double White Dwarf Binaries with the Laser Interferometer Space Antenna and Gaia," *Astrophys. J. Lett.*, vol. 854, no. 1, p. L1, 2018.

[177] M. R. Adams, N. J. Cornish, and T. B. Littenberg, "Astrophysical Model Selection in Gravitational Wave Astronomy," *Phys. Rev. D*, vol. 86, p. 124032, 2012.

[178] V. Korol, E. M. Rossi, and E. Barausse, "A multimessenger study of the Milky Way's stellar disc and bulge with LISA, Gaia, and LSST," *Mon. Not. Roy. Astron. Soc.*, vol. 483, no. 4, pp. 5518–5533, 2019.

[179] K. Breivik, C. M. Mingarelli, and S. L. Larson, "Constraining Galactic Structure with the LISA White Dwarf Foreground," *Astrophys. J.*, vol. 901, no. 1, p. 4, 2020.

[180] V. Korol *et al.*, "Populations of double white dwarfs in Milky Way satellites and their detectability with LISA," *Astron. Astrophys.*, vol. 638, p. A153, 2020.

[181] E. Roebber *et al.*, "Milky Way Satellites Shining Bright in Gravitational Waves," *Astrophys. J. Lett.*, vol. 894, no. 2, p. L15, 2020.

[182] J. Fuller and D. Lai, "Dynamical Tides in Compact White Dwarf Binaries: Influence of Rotation," *Mon. Not. Roy. Astron. Soc.*, vol. 444, no. 4, pp. 3488–3500, 2014.

[183] S. Shah, S. L. Larson, and W. Brown, "Ultra-compact binaries as gravitational wave sources," *J. Phys. Conf. Ser.*, vol. 610, no. 1, p. 012003, 2015.

[184] S. Toonen, J. S. W. Claeys, N. Mennekens, and A. J. Ruiter, "PopCORN: Hunting down the differences between binary population synthesis codes," *Astron. Astrophys.*, vol. 562, p. A14, 2014.

[185] T. B. Littenberg and N. Yunes, "Binary White Dwarfs as Laboratories for Extreme Gravity with LISA," *Class. Quant. Grav.*, vol. 36, no. 9, p. 095017, 2019.

[186] Z. Barkat, G. Rakavy, and N. Sack, "Dynamics of Supernova Explosion Resulting from Pair Formation," *Phys. Rev. Lett.*, vol. 18, pp. 379–381, 1967.

[187] G. Rakavy and G. Shaviv, "Instabilities in Highly Evolved Stellar Models," *Astrophys. J.*, vol. 148, p. 803, 1967.

[188] D. Kasen, S. E. Woosley, and A. Heger, "Pair Instability Supernovae: Light Curves, Spectra, and Shock Breakout," *Astrophys. J.*, vol. 734, p. 102, 2011.

[189] M. Spera and M. Mapelli, "Very massive stars, pair-instability supernovae and intermediate-mass black holes with the SEVN code," *Mon. Not. Roy. Astron. Soc.*, vol. 470, no. 4, pp. 4739–4749, 2017.

[190] R. Abbott *et al.*, "GW190521: A Binary Black Hole Merger with a Total Mass of 150 $M_{\odot}$," *Phys. Rev. Lett.*, vol. 125, p. 101102, 2020.

[191] C. D. Bailyn, R. K. Jain, P. Coppi, and J. A. Orosz, "The Mass distribution of stellar black holes," *Astrophys. J.*, vol. 499, p. 367, 1998.

[192] F. Ozel, D. Psaltis, R. Narayan, and J. E. McClintock, "The Black Hole Mass Distribution in the Galaxy," *Astrophys. J.*, vol. 725, pp. 1918–1927, 2010.

[193] W. M. Farr, N. Sravan, A. Cantrell, L. Kreidberg, C. D. Bailyn, I. Mandel, and V. Kalogera, "The Mass Distribution of Stellar-Mass Black Holes," *Astrophys. J.*, vol. 741, p. 103, 2011.

[194] K. A. Postnov and L. R. Yungelson, "The Evolution of Compact Binary Star Systems," *Living Rev. Rel.*, vol. 17, p. 3, 2014.

[195] M. J. Benacquista and J. M. B. Downing, "Relativistic Binaries in Globular Clusters," *Living Rev. Rel.*, vol. 16, p. 4, 2013.

[196] S. Bird, I. Cholis, J. B. Muñoz, Y. Ali-Haïmoud, M. Kamionkowski, E. D. Kovetz, A. Raccanelli, and A. G. Riess, "Did LIGO detect dark matter?," *Phys. Rev. Lett.*, vol. 116, no. 20, p. 201301, 2016.

[197] G. Franciolini, V. Baibhav, V. De Luca, K. K. Y. Ng, K. W. K. Wong, E. Berti, P. Pani, A. Riotto, and S. Vitale, "Evidence for primordial black holes in LIGO/Virgo gravitational-wave data," 5 2021.

[198] D. Gerosa, E. Berti, R. O'Shaughnessy, K. Belczynski, M. Kesden, D. Wysocki, and W. Gladysz, "Spin orientations of merging black holes formed from the evolution of stellar binaries," *Phys. Rev.*, vol. D98, no. 8, p. 084036, 2018.

[199] F. Antonini and H. B. Perets, "Secular evolution of compact binaries near massive black holes: Gravitational wave sources and other exotica," *Astrophys. J.*, vol. 757, p. 27, 2012.

[200] J. Samsing, "Eccentric Black Hole Mergers Forming in Globular Clusters," *Phys. Rev.*, vol. D97, no. 10, p. 103014, 2018.

[201] V. De Luca, V. Desjacques, G. Franciolini, A. Malhotra, and A. Riotto, "The initial spin probability distribution of primordial black holes," *JCAP*, vol. 05, p. 018, 2019.

[202] K. W. K. Wong, K. Breivik, K. Kremer, and T. Callister, "Joint constraints on the field-cluster mixing fraction, common envelope efficiency, and globular cluster radii from a population of binary hole mergers via deep learning," *Phys. Rev. D*, vol. 103, no. 8, p. 083021, 2021.

[203] M. Zevin, S. S. Bavera, C. P. L. Berry, V. Kalogera, T. Fragos, P. Marchant, C. L. Rodriguez, F. Antonini, D. E. Holz, and C. Pankow, "One Channel to Rule Them All? Constraining the Origins of Binary Black Holes Using Multiple Formation Pathways," *Astrophys. J.*, vol. 910, no. 2, p. 152, 2021.

[204] Y. Bouffanais, M. Mapelli, F. Santoliquido, N. Giacobbo, U. N. Di Carlo, S. Rastello, M. C. Artale, and G. Iorio, "New insights on binary black hole formation channels after GWTC-2: young star clusters versus isolated binaries," 2 2021.

[205] V. De Luca, G. Franciolini, P. Pani, and A. Riotto, "Bayesian Evidence for Both Astrophysical and Primordial Black Holes: Mapping the GWTC-2 Catalog to Third-Generation Detectors," 2 2021.

[206] D. Gerosa, S. Ma, K. W. K. Wong, E. Berti, R. O'Shaughnessy, Y. Chen, and K. Belczynski, "Multiband gravitational-wave event rates and stellar physics," *Phys. Rev.*, vol. D99, no. 10, p. 103004, 2019.

[207] J. Samsing and D. J. D'Orazio, "Black Hole Mergers From Globular Clusters Observable by LISA I: Eccentric Sources Originating From Relativistic N-body Dynamics," *Mon. Not. Roy. Astron. Soc.*, vol. 481, no. 4, pp. 5445–5450, 2018.

[208] A. Nishizawa, E. Berti, A. Klein, and A. Sesana, "eLISA eccentricity measurements as tracers of binary black hole formation," *Phys. Rev.*, vol. D94, no. 6, p. 064020, 2016.

[209] A. Nishizawa, A. Sesana, E. Berti, and A. Klein, "Constraining stellar binary black hole formation scenarios with eLISA eccentricity measurements," *Mon. Not. Roy. Astron. Soc.*, vol. 465, no. 4, pp. 4375–4380, 2017.

[210] K. Breivik, C. L. Rodriguez, S. L. Larson, V. Kalogera, and F. A. Rasio, "Distinguishing Between Formation Channels for Binary Black Holes with LISA," *Astrophys. J.*, vol. 830, no. 1, p. L18, 2016.

[211] P. Amaro-Seoane and L. Santamaria, "Detection of IMBHs with ground-based gravitational wave observatories: A biography of a binary of black holes, from birth to death," *Astrophys. J.*, vol. 722, pp. 1197–1206, 2010.

[212] K. Jani, D. Shoemaker, and C. Cutler, "Detectability of Intermediate-Mass Black Holes in Multiband Gravitational Wave Astronomy," *Nature Astron.*, vol. 4, no. 3, pp. 260–265, 2019.

[213] M. Mezcua, "Observational evidence for intermediate-mass black holes," *Int. J. Mod. Phys. D*, vol. 26, no. 11, p. 1730021, 2017.

[214] J. M. Miller, A. C. Fabian, and M. C. Miller, "A Comparison of intermediate mass black hole candidate ULXs and stellar-mass black holes," *Astrophys. J. Lett.*, vol. 614, pp. L117–L120, 2004.

[215] R. Abbott *et al.*, "Properties and Astrophysical Implications of the 150 $M_\odot$ Binary Black Hole Merger GW190521," *Astrophys. J. Lett.*, vol. 900, no. 1, p. L13, 2020.

[216] M. A. Latif and A. Ferrara, "Formation of supermassive black hole seeds," *Publ. Astron. Soc. Austral.*, vol. 33, p. e051, 2016.

[217] M. Volonteri, "The Formation and Evolution of Massive Black Holes," *Science*, vol. 337, p. 544, 2012.

[218] J. Kormendy and L. C. Ho, "Coevolution (Or Not) of Supermassive Black Holes and Host Galaxies," *Ann. Rev. Astron. Astrophys.*, vol. 51, pp. 511–653, 2013.

[219] P. Padovani *et al.*, "Active galactic nuclei: what's in a name?," *Astron. Astrophys. Rev.*, vol. 25, no. 1, p. 2, 2017.

[220] F. Wang, J. Yang, X. Fan, J. F. Hennawi, A. J. Barth, E. Banados, F. Bian, K. Boutsia, T. Connor, F. B. Davies, and et al., "A luminous quasar at redshift 7.642," *Astrophys. J.*, vol. 907, p. L1, Jan 2021.

[221] A. Sesana, F. Haardt, P. Madau, and M. Volonteri, "Low - frequency gravitational radiation from coalescing massive black hole binaries in hierarchical cosmologies," *Astrophys. J.*, vol. 611, pp. 623–632, 2004.

[222] P. J. Armitage and P. Natarajan, "Accretion during the merger of supermassive black holes," *Astrophys. J. Lett.*, vol. 567, pp. L9–L12, 2002.

[223] A. De Rosa *et al.*, "The quest for dual and binary supermassive black holes: A multi-messenger view," *New Astron. Rev.*, vol. 86, p. 101525, 2019.

[224] N. Tamanini, C. Caprini, E. Barausse, A. Sesana, A. Klein, and A. Petiteau, "Science with the space-based interferometer eLISA. III: Probing the expansion of the Universe using gravitational wave standard sirens," *JCAP*, vol. 04, p. 002, 2016.

[225] E. Barausse, I. Dvorkin, M. Tremmel, M. Volonteri, and M. Bonetti, "Massive Black Hole Merger Rates: The Effect of Kiloparsec Separation Wandering and Supernova Feedback," *Astrophys. J.*, vol. 904, no. 1, p. 16, 2020.

[226] S. Sigurdsson and M. J. Rees, "Capture of stellar mass compact objects by massive black holes in galactic cusps," *Mon. Not. Roy. Astron. Soc.*, vol. 284, p. 318, 1997.

[227] M. Bonetti and A. Sesana, "Gravitational wave background from extreme mass ratio inspirals," *Phys. Rev. D*, vol. 102, no. 10, p. 103023, 2020.

[228] S. Babak, J. Gair, A. Sesana, E. Barausse, C. F. Sopuerta, C. P. L. Berry, E. Berti, P. Amaro-Seoane, A. Petiteau, and A. Klein, "Science with the space-based interferometer LISA. V: Extreme mass-ratio inspirals," *Phys. Rev. D*, vol. 95, no. 10, p. 103012, 2017.

[229] L. S. Finn and K. S. Thorne, "Gravitational waves from a compact star in a circular, inspiral orbit, in the equatorial plane of a massive, spinning black hole, as observed by LISA," *Phys. Rev. D*, vol. 62, p. 124021, 2000.

[230] E. Poisson, A. Pound, and I. Vega, "The Motion of point particles in curved spacetime," *Living Rev. Rel.*, vol. 14, p. 7, 2011.

[231] J. R. Gair, M. Vallisneri, S. L. Larson, and J. G. Baker, "Testing General Relativity with Low-Frequency, Space-Based Gravitational-Wave Detectors," *Living Rev. Rel.*, vol. 16, p. 7, 2013.

[232] V. Kalogera, K. Belczynski, C. Kim, R. W. O'Shaughnessy, and B. Willems, "Formation of Double Compact Objects," *Phys. Rept.*, vol. 442, pp. 75–108, 2007.

[233] C. S. Ye, W.-f. Fong, K. Kremer, C. L. Rodriguez, S. Chatterjee, G. Fragione, and F. A. Rasio, "On the Rate of Neutron Star Binary Mergers from Globular Clusters," *Astrophys. J. Lett.*, vol. 888, no. 1, p. L10, 2020.

[234] B. P. Abbott *et al.*, "GW170817: Measurements of neutron star radii and equation of state," *Phys. Rev. Lett.*, vol. 121, no. 16, p. 161101, 2018.

[235] T. Dietrich, T. Hinderer, and A. Samajdar, "Interpreting Binary Neutron Star Mergers: Describing the Binary Neutron Star Dynamics, Modelling Gravitational Waveforms, and Analyzing Detections," 4 2020.

[236] K. Chatziioannou and W. M. Farr, "Inferring the maximum and minimum mass of merging neutron stars with gravitational waves," *Phys. Rev. D*, vol. 102, no. 6, p. 064063, 2020.

[237] S. I. Blinnikov, I. D. Novikov, T. V. Perevodchikova, and A. G. Polnarev, "Exploding neutron stars in close binaries," 8 2018.

[238] D. Eichler, M. Livio, T. Piran, and D. N. Schramm, "Nucleosynthesis, Neutrino Bursts and Gamma-Rays from Coalescing Neutron Stars," *Nature*, vol. 340, pp. 126–128, 1989.

[239] L.-X. Li and B. Paczynski, "Transient events from neutron star mergers," *Astrophys. J. Lett.*, vol. 507, p. L59, 1998.

[240] B. D. Metzger and E. Berger, "What is the Most Promising Electromagnetic Counterpart of a Neutron Star Binary Merger?," *Astrophys. J.*, vol. 746, p. 48, 2012.

[241] B. Abbott *et al.*, "GW190425: Observation of a Compact Binary Coalescence with Total Mass $\sim 3.4 M_\odot$," *Astrophys. J. Lett.*, vol. 892, p. L3, 2020.

[242] M. L. Chan, C. Messenger, I. S. Heng, and M. Hendry, "Binary Neutron Star Mergers and Third Generation Detectors: Localization and Early Warning," *Phys. Rev. D*, vol. 97, no. 12, p. 123014, 2018.

[243] E. Belgacem, Y. Dirian, S. Foffa, E. J. Howell, M. Maggiore, and T. Regimbau, "Cosmology and dark energy from joint gravitational wave-GRB observations," *JCAP*, vol. 08, p. 015, 2019.

[244] M. Mapelli and N. Giacobbo, "The cosmic merger rate of neutron stars and black holes," *Mon. Not. Roy. Astron. Soc.*, vol. 479, no. 4, pp. 4391–4398, 2018.

[245] K. Belczynski, S. Repetto, D. E. Holz, R. O'Shaughnessy, T. Bulik, E. Berti, C. Fryer, and M. Dominik, "Compact Binary Merger Rates: Comparison with LIGO/Virgo Upper Limits," *Astrophys. J.*, vol. 819, no. 2, p. 108, 2016.

[246] D. Clausen, S. Sigurdsson, and D. F. Chernoff, "Black Hole-Neutron Star Mergers in Globular Clusters," *Mon. Not. Roy. Astron. Soc.*, vol. 428, p. 3618, 2013.

[247] M. A. Sedda, "Dissecting the properties of neutron star - black hole mergers originating in dense star clusters," *Commun. Phys.*, vol. 3, p. 43, 2020.

[248] R. Abbott *et al.*, "GW190814: Gravitational Waves from the Coalescence of a 23 Solar Mass Black Hole with a 2.6 Solar Mass Compact Object," *Astrophys. J. Lett.*, vol. 896, no. 2, p. L44, 2020.

[249] C. Barbieri, O. S. Salafia, A. Perego, M. Colpi, and G. Ghirlanda, "Light-curve models of black hole – neutron star mergers: steps towards a multi-messenger parameter estimation," *Astron. Astrophys.*, vol. 625, p. A152, 2019.

[250] F. Foucart, "A brief overview of black hole-neutron star mergers," *Front. Astron. Space Sci.*, vol. 7, p. 46, 2020.

[251] S. L. Liebling and C. Palenzuela, "Dynamical Boson Stars," *Living Rev. Rel.*, vol. 20, no. 1, p. 5, 2017.

[252] P. O. Mazur and E. Mottola, "Gravitational condensate stars: An alternative to black holes," 9 2001.

[253] M. Visser and D. L. Wiltshire, "Stable gravastars: An Alternative to black holes?," *Class. Quant. Grav.*, vol. 21, pp. 1135–1152, 2004.

[254] M. Visser, *Lorentzian wormholes: From Einstein to Hawking*. 1995.

[255] K. Skenderis and M. Taylor, "The fuzzball proposal for black holes," *Phys. Rept.*, vol. 467, pp. 117–171, 2008.

[256] A. Almheiri, D. Marolf, J. Polchinski, and J. Sully, "Black Holes: Complementarity or Firewalls?," *JHEP*, vol. 02, p. 062, 2013.

[257] M. Saravani, N. Afshordi, and R. B. Mann, "Empty black holes, firewalls, and the origin of Bekenstein–Hawking entropy," *Int. J. Mod. Phys. D*, vol. 23, no. 13, p. 1443007, 2015.

[258] B. Holdom and J. Ren, "Not quite a black hole," *Phys. Rev. D*, vol. 95, no. 8, p. 084034, 2017.

[259] S. B. Giddings, "Possible observational windows for quantum effects from black holes," *Phys. Rev. D*, vol. 90, no. 12, p. 124033, 2014.

[260] J. Abedi, H. Dykaar, and N. Afshordi, "Echoes from the Abyss: Tentative evidence for Planck-scale structure at black hole horizons," *Phys. Rev. D*, vol. 96, no. 8, p. 082004, 2017.

[261] V. Cardoso and P. Pani, "Testing the nature of dark compact objects: a status report," *Living Rev. Rel.*, vol. 22, no. 1, p. 4, 2019.

[262] C. Ott, "The Gravitational Wave Signature of Core-Collapse Supernovae," *Class. Quant. Grav.*, vol. 26, p. 063001, 2009.

[263] S. E. Gossan, P. Sutton, A. Stuver, M. Zanolin, K. Gill, and C. D. Ott, "Observing Gravitational Waves from Core-Collapse Supernovae in the Advanced Detector Era," *Phys. Rev. D*, vol. 93, no. 4, p. 042002, 2016.

[264] C. Afle and D. A. Brown, "Inferring physical properties of stellar collapse by third-generation gravitational-wave detectors," *Phys. Rev. D*, vol. 103, no. 2, p. 023005, 2021.

[265] E. Abdikamalov, G. Pagliaroli, and D. Radice, "Gravitational Waves from Core-Collapse Supernovae," 10 2020.

[266] S. V. Bergh and G. A. Tammann, "Galactic and extragalactic supernova rates," *Ann. Rev. Astron. Astrophys.*, vol. 29, pp. 363–407, 1991.

[267] B. P. Abbott *et al.*, "Optically targeted search for gravitational waves emitted by core-collapse supernovae during the first and second observing runs of advanced LIGO and advanced Virgo," *Phys. Rev. D*, vol. 101, no. 8, p. 084002, 2020.

[268] T. Damour and A. Vilenkin, "Gravitational wave bursts from cosmic strings," *Phys. Rev. Lett.*, vol. 85, pp. 3761–3764, 2000.

[269] C. P. L. Berry and J. R. Gair, "Expectations for extreme-mass-ratio bursts from the Galactic Centre," *Mon. Not. Roy. Astron. Soc.*, vol. 435, pp. 3521–3540, 2013.

[270] J. Weber, "Detection and Generation of Gravitational Waves," *Phys. Rev.*, vol. 117, pp. 306–313, 1960.

[271] J. Weber, "Evidence for discovery of gravitational radiation," *Phys. Rev. Lett.*, vol. 22, pp. 1320–1324, 1969.

[272] D. W. Sciama, G. B. Field, and M. J. Rees, "Upper Limit to Radiation of Mass Energy Derived from Expansion of Galaxy," *Phys. Rev. Lett.*, vol. 23, pp. 1514–1515, 1969.

[273] M. Gertsenshtein and V. Pustovoit, "On the detection of low frequency gravitational waves," *JETP*, vol. 43, pp. 605–607, 1962.

[274] "A brief history of ligo." `https://www.ligo.caltech.edu/system/media_files/binaries/386/original/LIGOHistory.pdf`.

[275] M. Armano *et al.*, "The LISA Pathfinder Mission," *J. Phys. Conf. Ser.*, vol. 610, no. 1, p. 012005, 2015.

[276] M. Armano *et al.*, "Sub-Femto- g Free Fall for Space-Based Gravitational Wave Observatories: LISA Pathfinder Results," *Phys. Rev. Lett.*, vol. 116, no. 23, p. 231101, 2016.

[277] B. Abbott *et al.*, "Detector description and performance for the first coincidence observations between LIGO and GEO," *Nucl. Instrum. Meth. A*, vol. 517, pp. 154–179, 2004.

[278] B. F. Schutz and M. Tinto, "Antenna patterns of interferometric detectors of gravitational waves - I. Linearly polarized waves.," *Mon. Not. Roy. Astron. Soc.*, vol. 224, pp. 131–154, Jan. 1987.

[279] M. Tinto, "Antenna patterns of interferometric detectors of gravitational waves - II. Elliptically and randomly polarized waves.," *Mon. Not. Roy. Astron. Soc.*, vol. 226, pp. 829–848, June 1987.

[280] B. P. Abbott *et al.*, "A guide to LIGO–Virgo detector noise and extraction of transient gravitational-wave signals," *Class. Quant. Grav.*, vol. 37, no. 5, p. 055002, 2020.

[281] A. Nishizawa, A. Taruya, K. Hayama, S. Kawamura, and M.-a. Sakagami, "Probing non-tensorial polarizations of stochastic gravitational-wave backgrounds with ground-based laser interferometers," *Phys. Rev. D*, vol. 79, p. 082002, 2009.

[282] M. Tinto and S. V. Dhurandhar, "Time-delay interferometry," *Living Rev. Rel.*, vol. 8, p. 4, 2005.

[283] S. Marsat and J. G. Baker, "Fourier-domain modulations and delays of gravitational-wave signals," 6 2018.

[284] S. Marsat, J. G. Baker, and T. Dal Canton, "Exploring the Bayesian parameter estimation of binary black holes with LISA," *Phys. Rev. D*, vol. 103, no. 8, p. 083011, 2021.

[285] N. Wiener, *Extrapolation, Interpolation, and Smoothing of Stationary Time Series, with Engineering Applications*. 1949.

[286] L. A. Wainstein and V. D. Zubakov, *Extraction of Signals from Noise*. 1970.

[287] M. H. A. Davis, "A REVIEW OF THE STATISTICAL THEORY OF SIGNAL DETECTION," 1987.

[288] S. Babak, R. Balasubramanian, D. Churches, T. Cokelaer, and B. S. Sathyaprakash, "A Template bank to search for gravitational waves from inspiralling compact binaries. I. Physical models," *Class. Quant. Grav.*, vol. 23, pp. 5477–5504, 2006.

[289] I. W. Harry, B. Allen, and B. S. Sathyaprakash, "A Stochastic template placement algorithm for gravitational wave data analysis," *Phys. Rev. D*, vol. 80, p. 104014, 2009.

[290] S. Privitera, S. R. P. Mohapatra, P. Ajith, K. Cannon, N. Fotopoulos, M. A. Frei, C. Hanna, A. J. Weinstein, and J. T. Whelan, "Improving the sensitivity of a search for coalescing binary black holes with nonprecessing spins in gravitational wave data," *Phys. Rev. D*, vol. 89, no. 2, p. 024003, 2014.

[291] J. Abadie *et al.*, "Search for Gravitational Waves from Low Mass Compact Binary Coalescence in LIGO's Sixth Science Run and Virgo's Science Runs 2 and 3," *Phys. Rev. D*, vol. 85, p. 082002, 2012.

[292] J. Aasi *et al.*, "Search for gravitational waves from binary black hole inspiral, merger, and ringdown in LIGO-Virgo data from 2009–2010," *Phys. Rev. D*, vol. 87, no. 2, p. 022002, 2013.

[293] A. Buonanno, Y.-b. Chen, and M. Vallisneri, "Detection template families for gravitational waves from the final stages of binary–black-hole inspirals: Nonspinning case," *Phys. Rev. D*, vol. 67, p. 024016, 2003. [Erratum: Phys.Rev.D 74, 029903 (2006)].

[294] C. J. Moore, D. Gerosa, and A. Klein, "Are stellar-mass black-hole binaries too quiet for LISA?," *Mon. Not. Roy. Astron. Soc.*, vol. 488, no. 1, pp. L94–L98, 2019.

[295] B. P. Abbott *et al.*, "GW150914: First results from the search for binary black hole coalescence with Advanced LIGO," *Phys. Rev. D*, vol. 93, no. 12, p. 122003, 2016.

[296] B. Allen, W. G. Anderson, P. R. Brady, D. A. Brown, and J. D. E. Creighton, "FINDCHIRP: An Algorithm for detection of gravitational waves from inspiraling compact binaries," *Phys. Rev.*, vol. D85, p. 122006, 2012.

[297] S. A. Usman *et al.*, "The PyCBC search for gravitational waves from compact binary coalescence," *Class. Quant. Grav.*, vol. 33, no. 21, p. 215004, 2016.

[298] S. Sachdev *et al.*, "The GstLAL Search Analysis Methods for Compact Binary Mergers in Advanced LIGO's Second and Advanced Virgo's First Observing Runs," 1 2019.

[299] C. Messick *et al.*, "Analysis Framework for the Prompt Discovery of Compact Binary Mergers in Gravitational-wave Data," *Phys. Rev. D*, vol. 95, no. 4, p. 042001, 2017.

[300] B. Zackay, L. Dai, T. Venumadhav, J. Roulet, and M. Zaldarriaga, "Detecting Gravitational Waves With Disparate Detector Responses: Two New Binary Black Hole Mergers," 10 2019.

[301] B. P. Abbott *et al.*, "All-Sky Search for Short Gravitational-Wave Bursts in the Second Advanced LIGO and Advanced Virgo Run," *Phys. Rev. D*, vol. 100, no. 2, p. 024017, 2019.

[302] C. L. Rodriguez, B. Farr, V. Raymond, W. M. Farr, T. B. Littenberg, D. Fazi, and V. Kalogera, "Basic Parameter Estimation of Binary Neutron Star Systems by the Advanced LIGO/Virgo Network," *Astrophys. J.*, vol. 784, p. 119, 2014.

[303] R. L. Karandikar, "On the markov chain monte carlo (mcmc) method," *Sadhana*, vol. 31, pp. 81–104, Apr 2006.

[304] M. Vallisneri, "Use and abuse of the Fisher information matrix in the assessment of gravitational-wave parameter-estimation prospects," *Phys. Rev.*, vol. D77, p. 042001, 2008.

[305] S. E. Timpano, L. J. Rubbo, and N. J. Cornish, "Characterizing the galactic gravitational wave background with LISA," *Phys. Rev.*, vol. D73, p. 122001, 2006.

[306] C. Cutler, "Angular resolution of the LISA gravitational wave detector," *Phys. Rev.*, vol. D57, pp. 7089–7102, 1998.

[307] A. Vecchio and E. D. L. Wickham, "LISA response function and parameter estimation," *Class. Quant. Grav.*, vol. 21, no. 5, pp. S661–S664, 2004.

[308] A. Vecchio and E. D. L. Wickham, "The Effect of the LISA response function on observations of monochromatic sources," *Phys. Rev.*, vol. D70, p. 082002, 2004.

[309] S. Chib and E. Greenberg, "Understanding the metropolis-hastings algorithm," *The American Statistician*, vol. 49, no. 4, pp. 327–335, 1995.

[310] N. Metropolis, A. Rosenbluth, M. Rosenbluth, A. Teller, and E. Teller, "Equation of state calculations by fast computing machines," *J. Chem. Phys.*, vol. 21, pp. 1087–1092, 1953.

[311] A. Buonanno, G. B. Cook, and F. Pretorius, "Inspiral, merger and ring-down of equal-mass black-hole binaries," *Phys. Rev.*, vol. D75, p. 124018, 2007.

[312] A. Buonanno, B. Iyer, E. Ochsner, Y. Pan, and B. S. Sathyaprakash, "Comparison of post-Newtonian templates for compact binary inspiral signals in gravitational-wave detectors," *Phys. Rev.*, vol. D80, p. 084043, 2009.

[313] A. Gelman and D. B. Rubin, "Inference from Iterative Simulation Using Multiple Sequences," *Statist. Sci.*, vol. 7, pp. 457–472, 1992.

[314] LISA Science Study Team, "LISA Science Requirements Document." `https://www.cosmos.esa.int/documents/678316/1700384/SciRD.pdf/25831f6b-3c01-e215-5916-4ac6e4b306fb?t=1526479841000`, 2018.

[315] A. Mangiagli, A. Klein, M. Bonetti, M. L. Katz, A. Sesana, M. Volonteri, M. Colpi, S. Marsat, and S. Babak, "On the inspiral of coalescing massive black hole binaries with LISA in the era of Multi-Messenger Astrophysics," *Phys. Rev. D*, vol. 102, p. 084056, 2020.

[316] K. W. K. Wong, E. D. Kovetz, C. Cutler, and E. Berti, "Expanding the LISA Horizon from the Ground," *Phys. Rev. Lett.*, vol. 121, no. 25, p. 251102, 2018.

[317] A. Gupta, S. Datta, S. Kastha, S. Borhanian, K. Arun, and B. Sathyaprakash, "Multi-parameter tests of general relativity using multiband gravitational-wave observations," 5 2020.

[318] B. Ewing, S. Sachdev, S. Borhanian, and B. Sathyaprakash, "Archival searches for stellar-mass binary black holes in LISA," 11 2020.

[319] T. D. Abbott *et al.*, "Improved analysis of GW150914 using a fully spin-precessing waveform Model," *Phys. Rev.*, vol. X6, no. 4, p. 041014, 2016.

[320] T. Robson, N. J. Cornish, and C. Liu, "The construction and use of LISA sensitivity curves," *Class. Quant. Grav.*, vol. 36, no. 10, p. 105011, 2019.

[321] S. Kullback and R. A. Leibler, "On information and sufficiency," *Ann. Math. Statist.*, vol. 22, pp. 79–86, 03 1951.

[322] D. Foreman-Mackey, "corner.py: Scatterplot matrices in python," *The Journal of Open Source Software*, vol. 24, 2016.

[323] A. Mangiagli, A. Klein, A. Sesana, E. Barausse, and M. Colpi, "Post-Newtonian phase accuracy requirements for stellar black hole binaries with LISA," *Phys. Rev.*, vol. D99, no. 6, p. 064056, 2019.

[324] E. Poisson and C. M. Will, "Gravitational waves from inspiraling compact binaries: Parameter estimation using second postNewtonian wave forms," *Phys. Rev.*, vol. D52, pp. 848–855, 1995.

[325] L. S. Finn and D. F. Chernoff, "Observing binary inspiral in gravitational radiation: One interferometer," *Phys. Rev. D*, vol. 47, pp. 2198–2219, 1993.

[326] N. Meidinger, "The Wide Field Imager instrument for Athena," *Contributions of the Astronomical Observatory Skalnate Pleso*, vol. 48, pp. 498–505, Jul 2018.

[327] P. Dewdney *et al.*, "Square Kilometre Array White Paper." `https://www.skatelescope.org/wp-content/uploads/2014/03/SKA-TEL-SKO-0000308_SKA1_System_Baseline_v2_DescriptionRev01-part-1-signed.pdf`, 2015.

[328] S. Shah, M. van der Sluys, and G. Nelemans, "Using electromagnetic observations to aid gravitational-wave parameter estimation of compact binaries observed with LISA," *Astron. Astrophys.*, vol. 544, p. A153, 2012.

[329] Z. Cao and W.-B. Han, "Waveform model for an eccentric binary black hole based on the effective-one-body-numerical-relativity formalism," *Phys. Rev. D*, vol. 96, no. 4, p. 044028, 2017.

[330] B. Ireland, O. Birnholtz, H. Nakano, E. West, and M. Campanelli, "Eccentric Binary Black Holes with Spin via the Direct Integration of the Post-Newtonian Equations of Motion," *Phys. Rev. D*, vol. 100, no. 2, p. 024015, 2019.

[331] I. Hinder, L. E. Kidder, and H. P. Pfeiffer, "Eccentric binary black hole inspiral-merger-ringdown gravitational waveform model from numerical relativity and post-Newtonian theory," *Phys. Rev. D*, vol. 98, no. 4, p. 044015, 2018.

[332] T. Hinderer and S. Babak, "Foundations of an effective-one-body model for coalescing binaries on eccentric orbits," *Phys. Rev. D*, vol. 96, no. 10, p. 104048, 2017.

[333] E. Huerta *et al.*, "Eccentric, nonspinning, inspiral, Gaussian-process merger approximant for the detection and characterization of eccentric binary black hole mergers," *Phys. Rev. D*, vol. 97, no. 2, p. 024031, 2018.

[334] B. F. Schutz, "Determining the Hubble Constant from Gravitational Wave Observations," *Nature*, vol. 323, pp. 310–311, 1986.

[335] W. Del Pozzo, A. Sesana, and A. Klein, "Stellar binary black holes in the LISA band: a new class of standard sirens," *Mon. Not. Roy. Astron. Soc.*, vol. 475, no. 3, pp. 3485–3492, 2018.

[336] K. Kyutoku and N. Seto, "Gravitational-wave cosmography with LISA and the Hubble tension," *Phys. Rev.*, vol. D95, no. 8, p. 083525, 2017.

[337] G. Gnocchi, A. Maselli, T. Abdelsalhin, N. Giacobbo, and M. Mapelli, "Bounding alternative theories of gravity with multiband GW observations," *Phys. Rev. D*, vol. 100, no. 6, p. 064024, 2019.

[338] Z. Carson and K. Yagi, "Multi-band gravitational wave tests of general relativity," 2019.

[339] S. Vitale, "Multiband Gravitational-Wave Astronomy: Parameter Estimation and Tests of General Relativity with Space- and Ground-Based Detectors," *Phys. Rev. Lett.*, vol. 117, no. 5, p. 051102, 2016.

[340] E. Barausse, N. Yunes, and K. Chamberlain, "Theory-Agnostic Constraints on Black-Hole Dipole Radiation with Multiband Gravitational-Wave Astrophysics," *Phys. Rev. Lett.*, vol. 116, no. 24, p. 241104, 2016.

[341] K. Chamberlain and N. Yunes, "Theoretical Physics Implications of Gravitational Wave Observation with Future Detectors," *Phys. Rev.*, vol. D96, no. 8, p. 084039, 2017.

[342] Z. Carson and K. Yagi, "Parameterized and inspiral-merger-ringdown consistency tests of gravity with multi-band gravitational wave observations," *Phys. Rev.*, vol. D101, no. 4, p. 044047, 2020.

[343] N. Yunes and F. Pretorius, "Fundamental Theoretical Bias in Gravitational Wave Astrophysics and the Parameterized Post-Einsteinian Framework," *Phys. Rev.*, vol. D80, p. 122003, 2009.

[344] C. Palenzuela, P. Pani, M. Bezares, V. Cardoso, L. Lehner, and S. Liebling, "Gravitational Wave Signatures of Highly Compact Boson Star Binaries," *Phys. Rev.*, vol. D96, no. 10, p. 104058, 2017.

[345] M. Bezares, C. Palenzuela, and C. Bona, "Final fate of compact boson star mergers," *Phys. Rev.*, vol. D95, no. 12, p. 124005, 2017.

[346] M. Bezares and C. Palenzuela, "Gravitational Waves from Dark Boson Star binary mergers," *Class. Quant. Grav.*, vol. 35, no. 23, p. 234002, 2018.

[347] M. Agathos, W. Del Pozzo, T. G. F. Li, C. Van Den Broeck, J. Veitch, and S. Vitale, "TIGER: A data analysis pipeline for testing the strong-field dynamics of general relativity with gravitational wave signals from coalescing compact binaries," *Phys. Rev.*, vol. D89, no. 8, p. 082001, 2014.

[348] S. Tahura, K. Yagi, and Z. Carson, "Testing Gravity with Gravitational Waves from Binary Black Hole Mergers: Contributions from Amplitude Corrections," 2019.

[349] K. Yagi, L. C. Stein, N. Yunes, and T. Tanaka, "Post-Newtonian, Quasi-Circular Binary Inspirals in Quadratic Modified Gravity," *Phys. Rev.*, vol. D85, p. 064022, 2012. [Erratum: Phys. Rev.D93,no.2,029902(2016)].

[350] N. Yunes, F. Pretorius, and D. Spergel, "Constraining the evolutionary history of Newton's constant with gravitational wave observations," *Phys. Rev.*, vol. D81, p. 064018, 2010.

[351] N. Yunes, R. O'Shaughnessy, B. J. Owen, and S. Alexander, "Testing gravitational parity violation with coincident gravitational waves and short gamma-ray bursts," *Phys. Rev.*, vol. D82, p. 064017, 2010.

[352] K. Yagi, N. Tanahashi, and T. Tanaka, "Probing the size of extra dimension with gravitational wave astronomy," *Phys. Rev.*, vol. D83, p. 084036, 2011.

[353] N. Yunes and L. C. Stein, "Non-Spinning Black Holes in Alternative Theories of Gravity," *Phys. Rev.*, vol. D83, p. 104002, 2011.

[354] S. Vigeland, N. Yunes, and L. Stein, "Bumpy Black Holes in Alternate Theories of Gravity," *Phys. Rev.*, vol. D83, p. 104027, 2011.

[355] S. Mirshekari, N. Yunes, and C. M. Will, "Constraining Generic Lorentz Violation and the Speed of the Graviton with Gravitational Waves," *Phys. Rev.*, vol. D85, p. 024041, 2012.

[356] K. Chatziioannou, N. Yunes, and N. Cornish, "Model-Independent Test of General Relativity: An Extended post-Einsteinian Framework with Complete Polarization Content," *Phys. Rev. D*, vol. 86, p. 022004, 2012. [Erratum: Phys.Rev.D 95, 129901 (2017)].

[357] C. M. Will, "Bounding the mass of the graviton using gravitational wave observations of inspiralling compact binaries," *Phys. Rev.*, vol. D57, pp. 2061–2068, 1998.

[358] P. Horava, "Quantum Gravity at a Lifshitz Point," *Phys. Rev.*, vol. D79, p. 084008, 2009.

[359] M. Visser, "Lorentz symmetry breaking as a quantum field theory regulator," *Phys. Rev.*, vol. D80, p. 025011, 2009.

[360] B. P. Abbott *et al.*, "Gravitational Waves and Gamma-rays from a Binary Neutron Star Merger: GW170817 and GRB 170817A," *Astrophys. J.*, vol. 848, no. 2, p. L13, 2017.

[361] C. M. Will, "Solar system versus gravitational-wave bounds on the graviton mass," *Class. Quant. Grav.*, vol. 35, no. 17, p. 17LT01, 2018.

[362] B. P. Abbott *et al.*, "Tests of General Relativity with GW170817," *Phys. Rev. Lett.*, vol. 123, no. 1, p. 011102, 2019.

[363] J. Ellis and R. van Haasteren, "jellis18/PTMCMCSampler: Official Release," Oct. 2017.

[364] K. Yagi, "A New constraint on scalar Gauss-Bonnet gravity and a possible explanation for the excess of the orbital decay rate in a low-mass X-ray binary," *Phys. Rev.*, vol. D86, p. 081504, 2012.

[365] J. Skilling, "Nested sampling for general bayesian computation," *Bayesian Anal.*, vol. 1, pp. 833–859, 12 2006.

[366] K. Thorne, "Space-time warps and the quantum world: Speculations about the future," 2002.

[367] N. Sennett, T. Hinderer, J. Steinhoff, A. Buonanno, and S. Ossokine, "Distinguishing boson stars from black holes and neutron stars from tidal interactions in inspiraling binary systems," *Physical Review D*, vol. 96, Jul 2017.

[368] A. Maselli, P. Pani, V. Cardoso, T. Abdelsalhin, L. Gualtieri, and V. Ferrari, "Probing Planckian corrections at the horizon scale with LISA binaries," *Phys. Rev. Lett.*, vol. 120, no. 8, p. 081101, 2018.

[369] V. Cardoso, E. Franzin, A. Maselli, P. Pani, and G. Raposo, "Testing strong-field gravity with tidal Love numbers," *Phys. Rev. D*, vol. 95, no. 8, p. 084014, 2017. [Addendum: Phys.Rev.D 95, 089901 (2017)].

[370] G. F. Giudice, "Hunting for dark particles with gravitational waves," *EPJ Web Conf.*, vol. 164, p. 02004, 2017.

[371] N. Krishnendu, K. Arun, and C. K. Mishra, "Testing the binary black hole nature of a compact binary coalescence," *Phys. Rev. Lett.*, vol. 119, no. 9, p. 091101, 2017.

[372] N. Krishnendu, C. K. Mishra, and K. Arun, "Spin-induced deformations and tests of binary black hole nature using third-generation detectors," *Phys. Rev. D*, vol. 99, no. 6, p. 064008, 2019.

[373] N. K. Johnson-Mcdaniel, A. Mukherjee, R. Kashyap, P. Ajith, W. Del Pozzo, and S. Vitale, "Constraining black hole mimickers with gravitational wave observations," 4 2018.

[374] A. Addazi, A. Marciano, and N. Yunes, "Can we probe Planckian corrections at the horizon scale with gravitational waves?," *Phys. Rev. Lett.*, vol. 122, no. 8, p. 081301, 2019.

[375] S. Datta, R. Brito, S. Bose, P. Pani, and S. A. Hughes, "Tidal heating as a discriminator for horizons in extreme mass ratio inspirals," *Phys. Rev. D*, vol. 101, no. 4, p. 044004, 2020.

[376] S. Datta, K. S. Phukon, and S. Bose, "Recognizing black holes in gravitational-wave observations: Telling apart impostors in mass-gap binaries," 4 2020.

[377] Y. Asali, P. T. Pang, A. Samajdar, and C. Van Den Broeck, "Probing resonant excitations in exotic compact objects via gravitational waves," 4 2020.

[378] C. Chirenti, C. Posada, and V. Guedes, "Where is Love? Tidal deformability in the black hole compactness limit," 5 2020.

[379] C. Pacilio, M. Vaglio, A. Maselli, and P. Pani, "Gravitational-wave detectors as particle-physics laboratories: Constraining scalar interactions with boson-star binaries," 7 2020.

[380] C. F. Macedo, P. Pani, V. Cardoso, and L. C. B. Crispino, "Astrophysical signatures of boson stars: quasinormal modes and inspiral resonances," *Phys. Rev. D*, vol. 88, no. 6, p. 064046, 2013.

[381] V. Cardoso, E. Franzin, and P. Pani, "Is the gravitational-wave ringdown a probe of the event horizon?," *Phys. Rev. Lett.*, vol. 116, no. 17, p. 171101, 2016. [Erratum: Phys.Rev.Lett. 117, 089902 (2016)].

[382] C. F. B. Macedo, V. Cardoso, L. C. B. Crispino, and P. Pani, "Quasinormal modes of relativistic stars and interacting fields," *Phys. Rev. D*, vol. 93, no. 6, p. 064053, 2016.

[383] C. Chirenti and L. Rezzolla, "Did GW150914 produce a rotating gravastar?," *Phys. Rev. D*, vol. 94, no. 8, p. 084016, 2016.

[384] E. Maggio, L. Buoninfante, A. Mazumdar, and P. Pani, "How does a dark compact object ringdown?," 6 2020.

[385] V. Cardoso, S. Hopper, C. F. B. Macedo, C. Palenzuela, and P. Pani, "Gravitational-wave signatures of exotic compact objects and of quantum corrections at the horizon scale," *Phys. Rev. D*, vol. 94, no. 8, p. 084031, 2016.

[386] Z. Mark, A. Zimmerman, S. M. Du, and Y. Chen, "A recipe for echoes from exotic compact objects," *Phys. Rev. D*, vol. 96, no. 8, p. 084002, 2017.

[387] A. Maselli, S. H. Völkel, and K. D. Kokkotas, "Parameter estimation of gravitational wave echoes from exotic compact objects," *Phys. Rev. D*, vol. 96, no. 6, p. 064045, 2017.

[388] R. S. Conklin, B. Holdom, and J. Ren, "Gravitational wave echoes through new windows," *Phys. Rev. D*, vol. 98, no. 4, p. 044021, 2018.

[389] J. Westerweck, A. Nielsen, O. Fischer-Birnholtz, M. Cabero, C. Capano, T. Dent, B. Krishnan, G. Meadors, and A. H. Nitz, "Low significance of evidence for black hole echoes in gravitational wave data," *Phys. Rev. D*, vol. 97, no. 12, p. 124037, 2018.

[390] Q. Wang and N. Afshordi, "Black hole echology: The observer's manual," *Phys. Rev. D*, vol. 97, no. 12, p. 124044, 2018.

[391] A. Urbano and H. Veermäe, "On gravitational echoes from ultracompact exotic stars," *JCAP*, vol. 04, p. 011, 2019.

[392] R. Lo, T. Li, and A. Weinstein, "Template-based Gravitational-Wave Echoes Search Using Bayesian Model Selection," *Phys. Rev. D*, vol. 99, no. 8, p. 084052, 2019.

[393] A. B. Nielsen, C. D. Capano, O. Birnholtz, and J. Westerweck, "Parameter estimation and statistical significance of echoes following black hole signals in the first Advanced LIGO observing run," *Phys. Rev. D*, vol. 99, no. 10, p. 104012, 2019.

[394] K. W. Tsang, A. Ghosh, A. Samajdar, K. Chatziioannou, S. Mastrogiovanni, M. Agathos, and C. Van Den Broeck, "A morphology-independent search for gravitational wave echoes in data from the first and second observing runs of Advanced LIGO and Advanced Virgo," *Phys. Rev. D*, vol. 101, no. 6, p. 064012, 2020.

[395] E. Maggio, A. Testa, S. Bhagwat, and P. Pani, "Analytical model for gravitational-wave echoes from spinning remnants," *Phys. Rev. D*, vol. 100, no. 6, p. 064056, 2019.

[396] B. Chen, Y. Chen, Y. Ma, K.-L. R. Lo, and L. Sun, "Instability of Exotic Compact Objects and Its Implications for Gravitational-Wave Echoes," 2 2019.

[397] R. S. Conklin and B. Holdom, "Gravitational wave echo spectra," *Phys. Rev. D*, vol. 100, no. 12, p. 124030, 2019.

[398] L. F. L. Micchi, N. Afshordi, and C. Chirenti, "How loud are echoes from Exotic Compact Objects?," 10 2020.

[399] R. Friedberg, T. Lee, and Y. Pang, "Scalar Soliton Stars and Black Holes," *Phys. Rev. D*, vol. 35, p. 3658, 1987.

[400] M. Kesden, J. Gair, and M. Kamionkowski, "Gravitational-wave signature of an inspiral into a supermassive horizonless object," *Phys. Rev. D*, vol. 71, p. 044015, 2005.

[401] T. Damour and A. Nagar, "Relativistic tidal properties of neutron stars," *Phys. Rev. D*, vol. 80, p. 084035, 2009.

[402] T. Binnington and E. Poisson, "Relativistic theory of tidal Love numbers," *Phys. Rev. D*, vol. 80, p. 084018, 2009.

[403] T. Hinderer, "Tidal Love numbers of neutron stars," *Astrophys. J.*, vol. 677, pp. 1216–1220, 2008.

[404] V. Cardoso, L. C. B. Crispino, C. F. B. Macedo, H. Okawa, and P. Pani, "Light rings as observational evidence for event horizons: long-lived modes, ergoregions and nonlinear instabilities of ultracompact objects," *Phys. Rev. D*, vol. 90, no. 4, p. 044069, 2014.

[405] M. Shibata and K. Uryu, "Simulation of merging binary neutron stars in full general relativity: Gamma = two case," *Phys. Rev. D*, vol. 61, p. 064001, 2000.

[406] T. W. Baumgarte, S. L. Shapiro, and M. Shibata, "On the maximum mass of differentially rotating neutron stars," *Astrophys. J.*, vol. 528, p. L29, 2000.

[407] S. Bernuzzi, "Neutron Stars Merger Remnants," 4 2020.

[408] C. Palenzuela, I. Olabarrieta, L. Lehner, and S. L. Liebling, "Head-on collisions of boson stars," *Phys. Rev. D*, vol. 75, p. 064005, 2007.

[409] L. Lehner and F. Pretorius, "Numerical Relativity and Astrophysics," *Ann. Rev. Astron. Astrophys.*, vol. 52, pp. 661–694, 2014.

[410] J. S. Read, B. D. Lackey, B. J. Owen, and J. L. Friedman, "Constraints on a phenomenologically parameterized neutron-star equation of state," *Phys. Rev. D*, vol. 79, p. 124032, 2009.

[411] S. Typel, G. Ropke, T. Klahn, D. Blaschke, and H. Wolter, "Composition and thermodynamics of nuclear matter with light clusters," *Phys. Rev. C*, vol. 81, p. 015803, 2010.

[412] T. Dietrich, D. Radice, S. Bernuzzi, F. Zappa, A. Perego, B. Brügmann, S. V. Chaurasia, R. Dudi, W. Tichy, and M. Ujevic, "CoRe database of binary neutron star merger waveforms," *Class. Quant. Grav.*, vol. 35, no. 24, p. 24LT01, 2018.

[413] N. Sanchis-Gual, F. Di Giovanni, M. Zilhão, C. Herdeiro, P. Cerdá-Durán, J. A. Font, and E. Radu, "Non-linear dynamics of spinning bosonic stars: formation and stability," *Phys. Rev. Lett.*, vol. 123, no. 22, p. 221101, 2019.

[414] F. Di Giovanni, N. Sanchis-Gual, P. Cerdá-Durán, M. Zilhão, C. Herdeiro, J. A. Font, and E. Radu, "On the dynamical bar-mode instability in spinning bosonic stars," 10 2020.

[415] A. Bauswein and H. T. Janka, "Measuring neutron-star properties via gravitational waves from binary mergers," *Phys. Rev. Lett.*, vol. 108, p. 011101, 2012.

[416] A. Bauswein, H. T. Janka, K. Hebeler, and A. Schwenk, "Equation-of-state dependence of the gravitational-wave signal from the ring-down phase of neutron-star mergers," *Phys. Rev. D*, vol. 86, p. 063001, 2012.

[417] A. Bauswein and N. Stergioulas, "Unified picture of the post-merger dynamics and gravitational wave emission in neutron star mergers," *Phys. Rev. D*, vol. 91, no. 12, p. 124056, 2015.

[418] L. Lehner, S. L. Liebling, C. Palenzuela, O. L. Caballero, E. O'Connor, M. Anderson, and D. Neilsen, "Unequal mass binary neutron star mergers and multimessenger signals," *Class. Quant. Grav.*, vol. 33, no. 18, p. 184002, 2016.

[419] K. Takami, L. Rezzolla, and L. Baiotti, "Spectral properties of the post-merger gravitational-wave signal from binary neutron stars," *Phys. Rev.*, vol. D91, no. 6, p. 064001, 2015.

[420] M. Lucca, L. Sagunski, F. Guercilena, and C. M. Fromm, "Shedding light on the angular momentum evolution of binary neutron star merger remnants: a semi-analytic model," *JHEAp*, vol. 29, pp. 19–30, 2021.

[421] K. S. Thorne, *Magic without Magic: John Archibald Wheeler*. Oxford science publications, 1972.

[422] LIGO Scientific Collaboration, "LIGO Algorithm Library - LALSuite." free software (GPL), 2018.

[423] K. W. Tsang, T. Dietrich, and C. Van Den Broeck, "Modeling the postmerger gravitational wave signal and extracting binary properties from future binary neutron star detections," *Phys. Rev. D*, vol. 100, no. 4, p. 044047, 2019.

[424] K. Chatziioannou, J. A. Clark, A. Bauswein, M. Millhouse, T. B. Littenberg, and N. Cornish, "Inferring the post-merger gravitational wave emission from binary neutron star coalescences," *Phys. Rev. D*, vol. 96, no. 12, p. 124035, 2017.

[425] M. Breschi, S. Bernuzzi, F. Zappa, M. Agathos, A. Perego, D. Radice, and A. Nagar, "kiloHertz gravitational waves from binary neutron star remnants: time-domain model and constraints on extreme matter," *Phys. Rev. D*, vol. 100, no. 10, p. 104029, 2019.

[426] T. Apostolatos, "Search templates for gravitational waves from precessing, inspiraling binaries," *Phys. Rev. D*, vol. 52, pp. 605–620, 1995.

[427] T. Damour, B. R. Iyer, and B. Sathyaprakash, "Improved filters for gravitational waves from inspiralling compact binaries," *Phys. Rev. D*, vol. 57, pp. 885–907, 1998.

[428] F. Feroz, M. Hobson, and M. Bridges, "MultiNest: an efficient and robust Bayesian inference tool for cosmology and particle physics," *Mon. Not. Roy. Astron. Soc.*, vol. 398, pp. 1601–1614, 2009.

[429] J. Calderón Bustillo, N. Sanchis-Gual, A. Torres-Forné, J. A. Font, A. Vajpeyi, R. Smith, C. Herdeiro, E. Radu, and S. H. Leong, "The (ultra) light in the dark: A potential vector boson of 8.7×10^{-13} eV from GW190521," 9 2020.

[430] A. Ghosh *et al.*, "Testing general relativity using golden black-hole binaries," *Phys. Rev. D*, vol. 94, no. 2, p. 021101, 2016.

[431] R. Tso, D. Gerosa, and Y. Chen, "Optimizing LIGO with LISA forewarnings to improve black-hole spectroscopy," *Phys. Rev.*, vol. D99, no. 12, p. 124043, 2019.

[432] O. Dreyer, B. J. Kelly, B. Krishnan, L. S. Finn, D. Garrison, and R. Lopez-Aleman, "Black hole spectroscopy: Testing general relativity through gravitational wave observations," *Class. Quant. Grav.*, vol. 21, pp. 787–804, 2004.

[433] E. Berti, V. Cardoso, and C. M. Will, "On gravitational-wave spectroscopy of massive black holes with the space interferometer LISA," *Phys. Rev. D*, vol. 73, p. 064030, 2006.

[434] E. Berti, J. Cardoso, V. Cardoso, and M. Cavaglia, "Matched-filtering and parameter estimation of ringdown waveforms," *Phys. Rev. D*, vol. 76, p. 104044, 2007.

[435] E. Berti, K. Yagi, H. Yang, and N. Yunes, "Extreme Gravity Tests with Gravitational Waves from Compact Binary Coalescences: (II) Ringdown," *Gen. Rel. Grav.*, vol. 50, no. 5, p. 49, 2018.

[436] V. Cardoso, M. Kimura, A. Maselli, E. Berti, C. F. B. Macedo, and R. McManus, "Parametrized black hole quasinormal ringdown: Decoupled equations for nonrotating black holes," *Phys. Rev. D*, vol. 99, no. 10, p. 104077, 2019.

[437] M. J. Graham *et al.*, "Candidate Electromagnetic Counterpart to the Binary Black Hole Merger Gravitational Wave Event S190521g," *Phys. Rev. Lett.*, vol. 124, no. 25, p. 251102, 2020.

[438] J. M. Bellovary, M.-M. Mac Low, B. McKernan, and K. E. S. Ford, "Migration Traps in Disks Around Supermassive Black Holes," *Astrophys. J. Lett.*, vol. 819, no. 2, p. L17, 2016.

[439] I. Bartos, B. Kocsis, Z. Haiman, and S. Márka, "Rapid and Bright Stellar-mass Binary Black Hole Mergers in Active Galactic Nuclei," *Astrophys. J.*, vol. 835, no. 2, p. 165, 2017.

[440] N. C. Stone, B. D. Metzger, and Z. Haiman, "Assisted inspirals of stellar mass black holes embedded in AGN discs: solving the 'final au problem'," *Mon. Not. Roy. Astron. Soc.*, vol. 464, no. 1, pp. 946–954, 2017.

[441] A. Secunda, J. Bellovary, M.-M. Mac Low, K. E. Saavik Ford, B. McKernan, N. Leigh, W. Lyra, and Z. Sándor, "Orbital Migration of Interacting Stellar Mass Black Holes in Disks around Supermassive Black Holes," *Astrophys. J.*, vol. 878, no. 2, p. 85, 2019.

[442] B. McKernan, K. E. S. Ford, W. Lyra, and H. B. Perets, "Intermediate mass black holes in AGN disks: I. Production \& Growth," *Mon. Not. Roy. Astron. Soc.*, vol. 425, p. 460, 2012.

[443] B. McKernan, K. E. S. Ford, B. Kocsis, W. Lyra, and L. M. Winter, "Intermediate-mass black holes in AGN discs – II. Model predictions and observational constraints," *Mon. Not. Roy. Astron. Soc.*, vol. 441, no. 1, pp. 900–909, 2014.

[444] V. Gayathri, Y. Yang, H. Tagawa, Z. Haiman, and I. Bartos, "Black hole mergers of AGN origin in LIGO/Virgo's O1-O3a observing periods," 4 2021.

[445] N. Ivanova *et al.*, "Common Envelope Evolution: Where we stand and how we can move forward," *Astron. Astrophys. Rev.*, vol. 21, p. 59, 2013.

[446] G. Ashton, K. Ackley, I. M. n. Hernandez, and B. Piotrzkowski, "Current observations are insufficient to confidently associate the binary black hole merger GW190521 with AGN J124942.3+344929," 10 2020.

[447] J. R. Hurley, C. A. Tout, and O. R. Pols, "Evolution of binary stars and the effect of tides on binary populations," *Mon. Not. Roy. Astron. Soc.*, vol. 329, p. 897, 2002.

[448] L. R. Yungelson, J. P. Lasota, G. Nelemans, G. Dubus, E. P. J. van den Heuvel, J. Dewi, and S. Portegies Zwart, "The origin and fate of short-period low-mass black-hole binaries," *Astron. Astrophys.*, vol. 454, p. 559, 2006.

[449] K. Breivik *et al.*, "COSMIC Variance in Binary Population Synthesis," *Astrophys. J.*, vol. 898, no. 1, p. 71, 2020.

[450] K. Kremer, S. Chatterjee, K. Breivik, C. L. Rodriguez, S. L. Larson, and F. A. Rasio, "LISA Sources in Milky Way Globular Clusters," *Phys. Rev. Lett.*, vol. 120, no. 19, p. 191103, 2018.

[451] A. Lamberts, S. Garrison-Kimmel, P. Hopkins, E. Quataert, J. Bullock, C.-A. Faucher-Giguère, A. Wetzel, D. Keres, K. Drango, and R. Sanderson, "Predicting the binary black hole population of the Milky Way with cosmological simulations," *Mon. Not. Roy. Astron. Soc.*, vol. 480, no. 2, pp. 2704–2718, 2018.

[452] Y.-Z. Dong, W.-M. Gu, T. Liu, and J. Wang, "A black hole–white dwarf compact binary model for long gamma-ray bursts without supernova association," *Mon. Not. Roy. Astron. Soc.*, vol. 475, no. 1, pp. L101–L105, 2018.

[453] J. C. A. Miller-Jones *et al.*, "Deep radio imaging of 47 Tuc identifies the peculiar X-ray source X9 as a new black hole candidate," *Mon. Not. Roy. Astron. Soc.*, vol. 453, no. 4, pp. 3918–3931, 2015.

[454] V. Tudor *et al.*, "HST spectrum and timing of the ultracompact X-ray binary candidate 47 Tuc X9," *Mon. Not. Roy. Astron. Soc.*, vol. 476, no. 2, pp. 1889–1908, 2018.

[455] R. P. Church, J. Strader, M. B. Davies, and A. Bobrick, "Formation constraints indicate a black-hole accretor in 47 Tuc X9," *Astrophys. J. Lett.*, vol. 851, p. L4, 2017.

[456] T. J. Maccarone, A. Kundu, S. E. Zepf, and K. L. Rhode, "A black hole in a globular cluster," *Nature*, vol. 445, pp. 183–185, 2007.

[457] L. D. Landau and E. M. Lifshitz, *Course on theoretical physics: Mechanics*. Wiley, 1960.

[458] H. Kim and W.-T. Kim, "Dynamical Friction of a Circular-Orbit Perturber in a Gaseous Medium," *Astrophys. J.*, vol. 665, pp. 432–444, 2007.

[459] B. Kocsis, N. Yunes, and A. Loeb, "Observable Signatures of EMRI Black Hole Binaries Embedded in Thin Accretion Disks," *Phys. Rev. D*, vol. 84, p. 024032, 2011.

[460] E. C. Ostriker, "Dynamical friction in a gaseous medium," *Astrophys. J.*, vol. 513, p. 252, 1999.

[461] E. Barausse, "Relativistic dynamical friction in a collisional fluid," *Mon. Not. Roy. Astron. Soc.*, vol. 382, pp. 826–834, 2007.

[462] C. F. Macedo, P. Pani, V. Cardoso, and L. C. Crispino, "Into the lair: gravitational-wave signatures of dark matter," *Astrophys. J.*, vol. 774, p. 48, 2013.

[463] H. Kim, W.-T. Kim, and F. J. Sanchez-Salcedo, "Dynamical Friction of Double Perturbers in a Gaseous Medium," *Astrophys. J.*, vol. 679, p. L33, 2008.

[464] J. Frank, A. King, and D. J. Raine, *Accretion Power in Astrophysics: Third Edition*. Jan. 2002.

[465] C. Bonvin, C. Caprini, R. Sturani, and N. Tamanini, "Effect of matter structure on the gravitational waveform," *Phys. Rev. D*, vol. 95, no. 4, p. 044029, 2017.

[466] N. Tamanini, A. Klein, C. Bonvin, E. Barausse, and C. Caprini, "Peculiar acceleration of stellar-origin black hole binaries: Measurement and biases with LISA," *Phys. Rev. D*, vol. 101, no. 6, p. 063002, 2020.

[467] K. Inayoshi, N. Tamanini, C. Caprini, and Z. Haiman, "Probing stellar binary black hole formation in galactic nuclei via the imprint of their center of mass acceleration on their gravitational wave signal," *Phys. Rev. D*, vol. 96, no. 6, p. 063014, 2017.

[468] E. Barausse, V. Cardoso, and P. Pani, "Can environmental effects spoil precision gravitational-wave astrophysics?," *Phys. Rev.*, vol. D89, no. 10, p. 104059, 2014.

[469] V. Cardoso and A. Maselli, "Constraints on the astrophysical environment of binaries with gravitational-wave observations," 2019.

[470] S. McGee, A. Sesana, and A. Vecchio, "The assembly of cosmic structure from baryons to black holes with joint gravitational-wave and X-ray observations," 2018.

[471] N. I. Shakura and R. A. Sunyaev, "Black holes in binary systems. Observational appearance," *Astron. Astrophys.*, vol. 24, pp. 337–355, 1973.

[472] J. Poutanen, S. Fabrika, A. G. Butkevich, and P. Abolmasov, "Supercritically accreting stellar mass black holes as ultraluminous X-ray sources," *Mon. Not. Roy. Astron. Soc.*, vol. 377, pp. 1187–1194, 2007.

[473] A. Sadowski, "Slim accretion disks around black holes," other thesis, 8 2011.

[474] C. Palenzuela, L. Lehner, and S. L. Liebling, "Dual Jets from Binary Black Holes," *Science*, vol. 329, p. 927, 2010.

[475] J. F. Steiner, J. E. McClintock, and R. Narayan, "Jet Power and Black Hole Spin: Testing an Empirical Relationship and Using it to Predict the Spins of Six Black Holes," *Astrophys. J.*, vol. 762, p. 104, 2013.

[476] P. Moesta, D. Alic, L. Rezzolla, O. Zanotti, and C. Palenzuela, "On the detectability of dual jets from binary black holes," *Astrophys. J. Lett.*, vol. 749, p. L32, 2012.

[477] X. Li, P. Chang, Y. Levin, C. D. Matzner, and P. J. Armitage, "Simulation of a Compact Object with Outflows Moving Through a Gaseous Background," *Mon. Not. Roy. Astron. Soc.*, vol. 494, no. 2, pp. 2327–2336, 2020.

[478] A. Toubiana *et al.* In preparation.

[479] T. R. Marsh, G. Nelemans, and D. Steeghs, "Mass transfer between double white dwarfs," *Mon. Not. Roy. Astron. Soc.*, vol. 350, p. 113, 2004.

[480] F. Verbunt and S. Rappaport, "Mass Transfer Instabilities Due to Angular Momentum Flows in Close Binaries," *Astrophys. J.*, vol. 332, p. 193, 1988.

[481] R. F. Webbink, "Double white dwarfs as progenitors of R Coronae Borealis stars and Type I supernovae," *Astrophys. J.*, vol. 277, pp. 355–360, 1984.

[482] L. M. van Haaften, G. Nelemans, R. Voss, M. A. Wood, and J. Kuijpers, "The evolution of ultracompact X-ray binaries," *Astron. Astrophys.*, vol. 537, p. A104, 2012.

[483] C. G. Campbell, "Tidal effects in twin-degenerate binaries," *Monthly Notices of the Royal Astronomical Society*, vol. 207, pp. 433–443, 04 1984.

[484] J. P. Zahn, "Tidal friction in close binary stars," *Astron. Astrophys.*, vol. 57, pp. 383–394, 1977.

[485] P. P. Eggleton, "Aproximations to the radii of Roche lobes.," *Astrophys. J.*, vol. 268, pp. 368–369, 1983.

[486] N. J. Cornish and T. B. Littenberg, "Tests of Bayesian Model Selection Techniques for Gravitational Wave Astronomy," *Phys. Rev. D*, vol. 76, p. 083006, 2007.

[487] T. Robson and N. Cornish, "Impact of galactic foreground characterization on a global analysis for the LISA gravitational wave observatory," *Class. Quant. Grav.*, vol. 34, no. 24, p. 244002, 2017.

[488] S. R. Hinton, "ChainConsumer," *The Journal of Open Source Software*, p. 00045, 2016.

[489] W. B. Hubbard and R. L. Wagner, "Hot White Dwarfs," *Astrophys. J.*, vol. 159, p. 93, 1970.

[490] D. J. Eisenstein *et al.*, "A Catalog of Spectroscopically Confirmed White Dwarfs from the Sloan Digital Sky Survey Data Release 4," *Astrophys. J. Suppl.*, vol. 167, pp. 40–58, 2006.

[491] C. J. Deloye and L. Bildsten, "White dwarf donors in ultracompact binaries: The Stellar structure of finite entropy objects," *Astrophys. J.*, vol. 598, pp. 1217–1228, 2003.

[492] E. do A. Soares, "Constraining Effective Temperature, Mass and Radius of Hot White Dwarfs," 2017.

[493] A. Bédard, P. Bergeron, P. Brassard, and G. Fontaine, "On the Spectral Evolution of Hot White Dwarf Stars. I. A Detailed Model Atmosphere Analysis of Hot White Dwarfs from SDSS DR12," *Astrophys. J.*, vol. 901, p. 93, 2020.

[494] A. L. Piro, P. Arras, and L. Bildsten, "White dwarf heating and subsequent cooling in dwarf nova outbursts," *Astrophys. J.*, vol. 628, pp. 401–410, 2005.

[495] J. Kormendy and D. Richstone, "Inward bound: The Search for supermassive black holes in galactic nuclei," *Ann. Rev. Astron. Astrophys.*, vol. 33, p. 581, 1995.

[496] L. Ferrarese and D. Merritt, "A Fundamental relation between supermassive black holes and their host galaxies," *Astrophys. J. Lett.*, vol. 539, p. L9, 2000.

[497] N. J. McConnell and C.-P. Ma, "Revisiting the Scaling Relations of Black Hole Masses and Host Galaxy Properties," *Astrophys. J.*, vol. 764, p. 184, 2013.

[498] M. Schramm and J. D. Silverman, "The black hole - bulge mass relation of Active Galactic Nuclei in the Extended Chandra Deep Field - South Survey," *Astrophys. J.*, vol. 767, p. 13, 2013.

[499] M. Milosavljevic and D. Merritt, "The Final parsec problem," *AIP Conf. Proc.*, vol. 686, no. 1, pp. 201–210, 2003.

[500] K. G. Arun, B. R. Iyer, B. S. Sathyaprakash, S. Sinha, and C. Van Den Broeck, "Higher signal harmonics, LISA's angular resolution and dark energy," *Phys. Rev. D*, vol. 76, p. 104016, 2007. [Erratum: Phys.Rev.D 76, 129903 (2007)].

[501] M. Trias and A. M. Sintes, "LISA observations of supermassive black holes: Parameter estimation using full post-Newtonian inspiral waveforms," *Phys. Rev. D*, vol. 77, p. 024030, 2008.

[502] E. K. Porter and N. J. Cornish, "The Effect of Higher Harmonic Corrections on the Detection of massive black hole binaries with LISA," *Phys. Rev. D*, vol. 78, p. 064005, 2008.

[503] S. T. McWilliams, J. I. Thorpe, J. G. Baker, and B. J. Kelly, "Impact of mergers on LISA parameter estimation for nonspinning black hole binaries," *Phys. Rev. D*, vol. 81, p. 064014, 2010.

[504] M. L. Katz, S. Marsat, A. J. K. Chua, S. Babak, and S. L. Larson, "GPU-accelerated massive black hole binary parameter estimation with LISA," *Phys. Rev. D*, vol. 102, no. 2, p. 023033, 2020.

[505] W. D. Vousden, W. M. Farr, and I. Mandel, "Dynamic temperature selection for parallel tempering in Markov chain Monte Carlo simulations," *Monthly Notices of the Royal Astronomical Society*, vol. 455, p. 1919–1937, Nov 2015.

[506] D. Foreman-Mackey, D. W. Hogg, D. Lang, and J. Goodman, "emcee: The MCMC Hammer," *Publications of the Astronomical Society of the Pacific*, vol. 125, no. 925, p. 306–312, 2013.

[507] C. M. Hirata, D. E. Holz, and C. Cutler, "Reducing the weak lensing noise for the gravitational wave Hubble diagram using the non-Gaussianity of the magnification distribution," *Phys. Rev. D*, vol. 81, p. 124046, 2010.

[508] M. Bonetti, A. Sesana, F. Haardt, E. Barausse, and M. Colpi, "Post-Newtonian evolution of massive black hole triplets in galactic nuclei – IV. Implications for LISA," *Mon. Not. Roy. Astron. Soc.*, vol. 486, no. 3, pp. 4044–4060, 2019.

[509] E. Barausse, "The evolution of massive black holes and their spins in their galactic hosts," *Mon. Not. Roy. Astron. Soc.*, vol. 423, pp. 2533–2557, 2012.

[510] A. Sesana, E. Barausse, M. Dotti, and E. M. Rossi, "Linking the spin evolution of massive black holes to galaxy kinematics," *Astrophys. J.*, vol. 794, p. 104, 2014.

[511] F. Antonini, E. Barausse, and J. Silk, "The Coevolution of Nuclear Star Clusters, Massive Black Holes, and their Host Galaxies," *Astrophys. J.*, vol. 812, no. 1, p. 72, 2015.

[512] H. Parkinson, S. Cole, and J. Helly, "Generating Dark Matter Halo Merger Trees," *Mon. Not. Roy. Astron. Soc.*, vol. 383, p. 557, 2008.

[513] W. H. Press and P. Schechter, "Formation of galaxies and clusters of galaxies by self-similar gravitational condensation," *Astrophys. J.*, vol. 187, pp. 425–438, 1974.

[514] S. Cole, C. G. Lacey, C. M. Baugh, and C. S. Frenk, "Hierarchical galaxy formation," *Mon. Not. Roy. Astron. Soc.*, vol. 319, p. 168, 2000.

[515] P. Madau and M. J. Rees, "Massive black holes as Population III remnants," *Astrophys. J. Lett.*, vol. 551, pp. L27–L30, 2001.

[516] M. Volonteri, G. Lodato, and P. Natarajan, "The evolution of massive black hole seeds," *Mon. Not. Roy. Astron. Soc.*, vol. 383, p. 1079, 2008.

[517] Y. Kozai, "Secular perturbations of asteroids with high inclination and eccentricity," *Astron. J.*, vol. 67, pp. 591–598, 1962.

[518] M. L. Lidov, "The evolution of orbits of artificial satellites of planets under the action of gravitational perturbations of external bodies," *Planet. Space Sci.*, vol. 9, no. 10, pp. 719–759, 1962.

[519] J. M. Bardeen and J. A. Petterson, "The Lense-Thirring Effect and Accretion Disks around Kerr Black Holes," *Astrophys. J. Lett.*, vol. 195, p. L65, 1975.

[520] A. Sesana, J. Gair, E. Berti, and M. Volonteri, "Reconstructing the massive black hole cosmic history through gravitational waves," *Phys. Rev. D*, vol. 83, p. 044036, 2011.

[521] I. Mandel, W. M. Farr, and J. R. Gair, "Extracting distribution parameters from multiple uncertain observations with selection biases," *Mon. Not. Roy. Astron. Soc.*, vol. 486, no. 1, pp. 1086–1093, 2019.

[522] E. Parzen, "On Estimation of a Probability Density Function and Mode," *The Annals of Mathematical Statistics*, vol. 33, no. 3, pp. 1065 – 1076, 1962.

[523] M. Rosenblatt, "Remarks on Some Nonparametric Estimates of a Density Function," *The Annals of Mathematical Statistics*, vol. 27, no. 3, pp. 832 – 837, 1956.

[524] P. Virtanen, R. Gommers, T. E. Oliphant, M. Haberland, T. Reddy, D. Cournapeau, E. Burovski, P. Peterson, W. Weckesser, J. Bright, S. J. van der Walt, M. Brett, J. Wilson, K. J. Millman, N. Mayorov, A. R. J. Nelson, E. Jones, R. Kern, E. Larson, C. J. Carey, İ. Polat, Y. Feng, E. W. Moore, J. VanderPlas, D. Laxalde, J. Perktold, R. Cimrman, I. Henriksen, E. A. Quintero, C. R. Harris, A. M. Archibald, A. H. Ribeiro, F. Pedregosa, P. van Mulbregt, and SciPy 1.0 Contributors, "SciPy 1.0: Fundamental Algorithms for Scientific Computing in Python," *Nature Methods*, vol. 17, pp. 261–272, 2020.

[525] S.-T. Chiu, "Bandwidth Selection for Kernel Density Estimation," *The Annals of Statistics*, vol. 19, no. 4, pp. 1883 – 1905, 1991.

[526] C. K. Mishra, A. Kela, K. Arun, and G. Faye, "Ready-to-use post-Newtonian gravitational waveforms for binary black holes with nonprecessing spins: An update," *Phys. Rev. D*, vol. 93, no. 8, p. 084054, 2016.

[527] C. García-Quirós, M. Colleoni, S. Husa, H. Estellés, G. Pratten, A. Ramos-Buades, M. Mateu-Lucena, and R. Jaume, "Multimode frequency-domain model for the gravitational wave signal from nonprecessing black-hole binaries," *Phys. Rev. D*, vol. 102, no. 6, p. 064002, 2020.

[528] W. M. Farr, "Accuracy Requirements for Empirically Measured Selection Functions," *Research Notes of the AAS*, p. 66, May 2019.